Università degli Studi di Cagliari
Department of Civil, Environmental and Architecture Engineering

PHD DEGREE

Earth and Environmental Sciences and Technologies

Cycle XXXIII

TITLE OF THE PHD THESIS

MODELLING OF GEOGENIC RADON IN SARDINIA AND HEALTH RISK ASSESSMENT

Scientific Disciplinary Sectors

Applied Geology (GEO/05) and Environmental Technologies (ICAR/03)

PhD Student: Mirsina Mousavi Aghdam

Supervisors Professor Valentina Dentoni
Professor Stefania DaPelo
Professor Paolo Randaccio
Professor Alfredo Loi

Final exam. Academic Year 2019 – 2020
Thesis defence: April 2021 Session

"I found radon as a mysterious gaseous element which should be studied more, not only for identifying and mitigation of the adverse health effects of this radioactive gas to the public but also as a reliable tool for better understanding of physical and chemical process occurring in the universe"

ABSTRACT

Enhanced level of radon in indoor environments such as homes, schools, public buildings and workplaces is considered an important health issue. Provided that radon is responsible for about 3–14 percent of all lung cancers, governments and inter-governmental institutions have issued several rules in the field of radioprotection of people from exposure to radon and its progenies. As one of the main preventive measures in Europe, the 2013/59/EURATOM BSS Directive requires the member states countries to prepare an action plan to address the radon potential source and identify Radon Prone Areas (RPAs), where the radon concentration is expected to exceed the national threshold level (as annual average of 300 Bq m^{-3} for both residential and workplaces).

Following this directive, the work to be discussed here focuses on the preparation of a radon potential map of Sardinia according to the "Vast Area" approach and based on the use of literature derived geogenic data (e.g. lithological and geological types, U and Ra content, soil-gas radon, permeability and tectonics). As one of the main results of this thesis work, a predictive Geogenic Radon Potential (GRP) map expressing the radon potentials in ordinal categories was developed.

The produced GRP map has merit because 1) it doesn't depend on the anthropogenic factors (e.g. building material, ventilation rate and living habits); 2) it can be used for the estimation of the radon hazard of both existing buildings and future construction sites, thus for the land-use planning.

Complementary field and laboratory-based experiments were conducted to examine the predictive power of the proposed GRP map. Through the validation tests, we tried to answer three main questions; 1) considering the effect of radon anthropogenic factors, is it possible to use the GRP levels to estimate the indoor radon concentration for an area? 2) Do the results of real-time pilot tests in an area identified as RPA correlate with the category of radon potential predicted by the GRP map? And 3) is it possible to use the GRP map to justify the occurrence of enhanced levels of radon in closed spaces?

In general, the correlations between examination test results and the predicted radon potential by the GRP map showed that the proposed map can address the major source of indoor radon in Sardinia. Besides, the radon emanation potential and natural radioactivity of the building material, the second major contributor to the indoor radon activity, was also investigated in detail parallel to the GRP mapping. The application of radon is not limited to addressing the health hazard. Radon monitoring coupled with natural

radioactivity detection can be used as a tool for radiogenic assessments. This application was investigated in an area that consists of heavy mineral placer deposits in South-Eastern Sardinia. Through this experiment, the natural radioactive characteristics and radon-related behaviors of studied formations were well-distinguished

The last year of the Ph.D. programme was carried out at Trinity College of Dublin, where the primary purpose of the study was to evaluate in detail the radon and thoron potential in an area with complex geology. Data obtained from radiometric surveys, geochemical measurements and indoor radon concentrations were used to distinguish radon and thoron release from different geo formations and soil types. To aim this, a set of samples were collected from selected geo types and radon/thoron exhalation rates were estimated through laboratory experiments. As a result, radon and thoron potential maps were developed. In the next step, a detailed investigation of soil gas radon concentrations was considered in a radon priority area identified through the potential maps. As a result of the second investigation, a geostatistical model was built to estimate the GRPs with higher accuracy. The key findings from the research carried out in Ireland were 1) Geology was found to be the controlling factor to distinguish between the radon-related behaviors of different rock types. However, using a soil type classification system, better correlations were found between thoron exhalation rates and the activity concentration of parent element Thorium. 2) By developing a geospatial model based on radiometric data (i.e. equivalent uranium and thorium), soil gas radon monitoring and permeability measurements, it would be possible to produce accurate and high-resolution geogenic radon maps.

The GRP maps produced through this thesis work give an insight into a better understanding of radon potential in Sardinia and Ireland. As the secondary result of this research, the field and laboratory-based experiments bring more specific information on natural radioactivity levels and radon/thoron potential of studied areas. Both produced maps and the published research papers from the results of these experiments can guide governmental authorities and policymakers for decision-making about the protection of the public against radiation risk. The maps can be also used as a base for targeting the hot spots for additional testing of radon in Sardinia and Ireland. More generally, this work aimed to create a communication strategy conveying radon potential and the associated radiological risk to the public, academic bodies, professionals and directors.

ACKNOWLEDGMENTS

I would first like to thank my supervisor, Professor Valentina Dentoni, whose support was invaluable in developing my own research idea and methodology. I am extremely grateful to Professor Quentin Crowley for his insightful feedback pushed me to sharpen my thinking and brought my work to a higher level. I would also like to thank my tutor, Professor Paolo Randaccio, for his valuable guidance throughout my studies and for providing me the instruments I needed.

I would like to acknowledge my colleagues from both my home university and Trinity College of Dublin, where I spent my research period abroad, for their wonderful collaboration. I would particularly like to single out Professor Rocha who provided me with the tools that I needed to choose the right direction and successfully complete my research. I want to thank the Environmental Protection Agency and the Geological Survey Ireland for their support and for all of the opportunities I was given to further my research.

I would also like to thank Professor Alfredo Loi, Professor Viviana Fanti, Dr. Alessandra Bernardini, Dr. Stefano Naitza, Dr. Nicola Careddu and Dr. Mattia Meloni for their valuable geological, petrological and radiological guidance throughout my studies.

In addition, I would like to thank my wife for her wise counsel and sympathetic understanding. Finally, I could not have completed this dissertation without the support of my friends, Dr. Brian Conry, Maxime Savatier, Sean O'Dubhlain, Stefano Fanari, Giulio Sogos and Francesco Pinna. It is their kind help and support that have made my study and life in Italy and Ireland a wonderful time.

CONTENTS

LIST OF TABLES

LIST OF FIGURES

1 INTRODUCTION

1.1 Natural Radioactivity

In recent decades, much has been learned about the nature and sources of human exposure to naturally-occurring radiation and radionuclides. The radiation dose received by the population may come from a variety of sources of both natural and artificial radioactivity. Figure 1-1 shows the distribution of sources, which is based on estimates of worldwide annual exposures (Kovler et al., 2017). Natural sources of radioactivity are responsible for the majority of the radiation exposure. The most important sources include external radiation coming from outer space (cosmic radiation); external radiation produced by naturally occurring radioactive elements contained in the Earth's crust (terrestrial radiation); the radioactive gases of radon and thoron which can accumulate in buildings; and radioactivity transferred to consumable food and water (O'Connor et al., 2014).

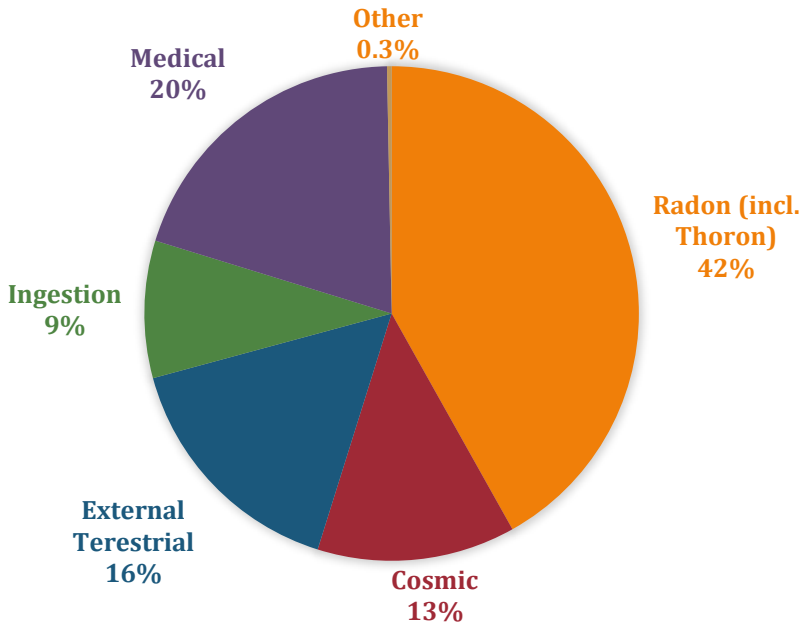

Figure 1-1 Distribution of the sources of human radiation exposure (Kovler et al., 2017)

1.1.1 Terrestrial Radiation

Naturally occurring radionuclides with half-lives comparable with the age of the Earth, such as ^{238}U, ^{232}Th and ^{40}K and their intensely radioactive decay products are the primary sources of terrestrial gamma radiation (NRC, 1999). The concentration of these primordial radioelements depends primarily on the geological conditions (Karadeniz et

al., 2015). Moreover, trace elements of the primordial radioelements can also be found in building materials used in the construction of houses and other structures and thus can also cause indoor radiation exposure.

1.1.2 Natural Radioactivity in the Geologic Environment

Radioactive decay processes of Uranium–radium, Thorium and Potassium, occurring in natural rocks, produce the only source of measurable quantities of gamma rays. Mean values and the ranges of ^{238}U, ^{232}Th and ^{40}K contents for different rock types are shown in Table 1-1. These elements form large positive ions (cations); therefore, they require minerals with large crystal structure openings to fit into. Such minerals are most common in certain types of rocks that evolved through processes in the Earth's crust. These rocks may have evolved by either the distillation of molten magma or stiffing by sedimentation (Hurley, 2009). Generally, the radioactivity of igneous rocks increases from mafic (basic) to felsic (acid) rocks and also, the radioactivity of sedimentary rocks increases from clean to shaly rocks, i.e., with increasing clay content. In the case of Uranium, high contents are generally associated with acid (and intermediate) rocks (e.g., granites) —their average concentration is about 4.65 ppm. As a result of weathering and alteration, Uranium forms soluble salts. Similar to Uranium, Thorium can also be found in acid (and intermediate) rocks, but unlike Uranium, it is very stable and will not dissolve in a solution. Potassium is chemically combined in three main groups of potassium-containing minerals such as clay minerals, where potassium occurs either in the mineral structure or adsorbed to the clay particles, rock-forming minerals, where potassium is chemically combined in the mineral structure and evaporites, where potassium occurs chemically as salt (Jürgen H.Schön, 2015).

Soils are produced as a result of the weathering of materials on Earth's surface, including the mechanical breakup of rocks and the chemical weathering of minerals. From radiological aspects, studying the radioactivity of soils is very important because soils not only behave as a source of continuous radiation exposure to humans but also as a medium for the migration of radionuclides to other environmental compartments such as water, air, sediments and biological systems. The contents of radionuclides in surface soils may not only be influenced by their content in the bedrocks, but also by the abiotic and biotic factors that originated the soils. Changes in the radionuclide contents of a soil may be promoted by the processes of soil formation as additions, losses, transformations and translocations, which depend on factors such as topography, climate, organisms and time (Ribeiro et al., 2018; UNSCEAR, 2000).

Table 1-1 Ranges and/or averages of concentrations of ^{40}K, ^{232}Th and ^{238}U in typical rocks and soils. Based on data from (NRC, 1999; Hazen et al., 2009; Wedepohl et al., 1969)

Material	^{40}K % total K	^{232}Th ppm	^{238}U ppm
Igneous rocks			
Syenites and phonolites	3–6	0.7–35 [typically >10]	0.1–26
Granites and rhyolites	2.5–4.5	8–56	2–50
Intermediate igneous rocks			1–6
Basalts and other mafic rocks	1–2	0.1–4	0.1–1
Ultramafic rocks	<1 [av.* ~0.6]	<0.1	0.001–1
Sedimentary rocks			
Shales, clays, mudrocks	<0.01–7.1	10–13	1–5
Black shales (organic-rich)	2.6	10.9	2–1250
Phosphorite-black shales	–	–	≤700
Phosphorite	–	1–5	
Sandstones	<0.01–5.6	1–7	0.5–4
Limestones, dolomites	<0.01–5 [av. limestone ~0.3] [av. dolomite ~0.6]	<0.05–3	<0.1–9
Pure evaporites	Variable	–	<0.1
Metamorphic Rocks			
Low-grade	Dependent on parent rock (i.e., igneous and sedimentary)	Highly variable, typically 6–10	<1–5
Medium-grade			<1–5
High-grade			<1–7
All rocks	0.3–4.5	2–20	0.5–4.7
Continental crust (average)	2.8	10.7	2.8
Soils (global average)	1.5	9	1.8

* Average

1.2 Radon

Radon has received the most attention among the scientific community over recent decades since it is the major contributor to the ionizing radiation dose received by the

general population. (See also Figure 1-1). Radon is the second leading cause of lung cancer after smoking and is classified as a human carcinogen (WHO, 2009). In addition to being a health hazard, it also has extensive applications in atmospheric science, marine and environmental sciences, earthquake studies, geochemical exploration studies (including uranium and hydrocarbon), organic pollutant studies in groundwater and noble gas geochemistry (Baskaran, 2016).

1.2.1 Physicochemical Properties

Radon is a noble radioactive gas that is chemically inert and does not react with other elements or often with compounds. It has no color, odor, or taste. The most important isotopes of radon are ^{222}Rn, ^{220}Rn and ^{219}Rn, which are intermediate radioactive decay of the ^{238}U, ^{232}Th and ^{235}U series, respectively. Among the radioisotopes, ^{222}Rn (also known as radon) and ^{220}Rn (also known as thoron) have greater half-lives (3.82 days for ^{222}Rn and 56.83 seconds for ^{220} Rn) and therefore they are commonly considered in radiological studies.

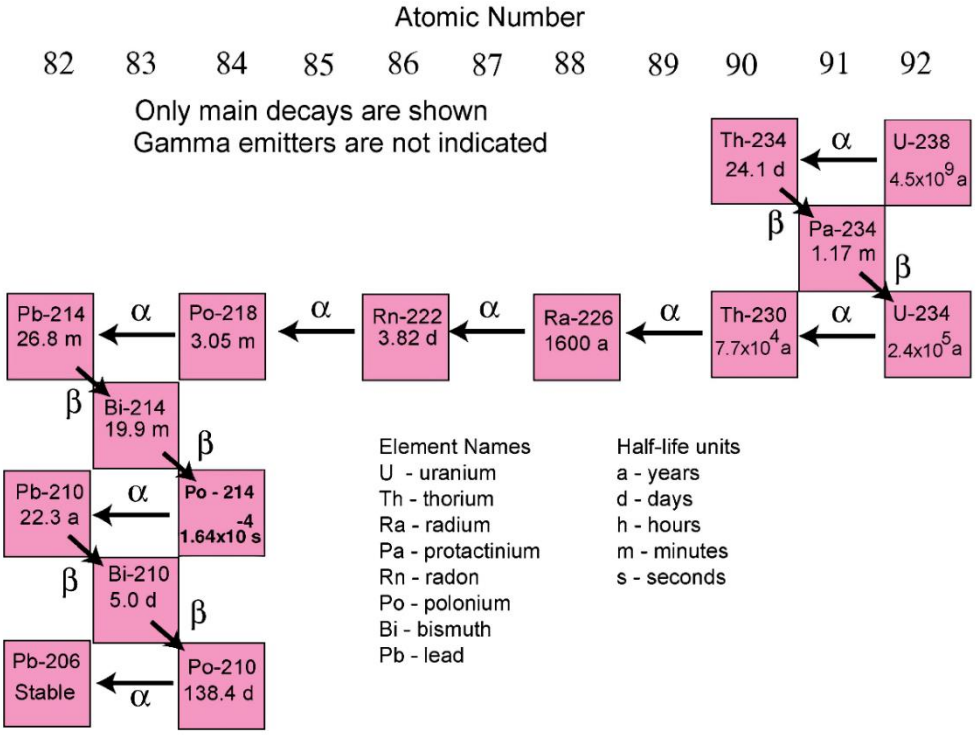

Figure 1-2 The uranium-238 decay chain (Source: U.S. Geological Survey (Duval et al., 2004)**)**

Figure 1-2 and Figure 1-3 show the decay chain of ^{238}U and ^{232}Th. The mean aggregate half-life of the daughter products of ^{222}Rn (^{218}Po, ^{214}Pb, ^{214}Bi, ^{214}Po) is 71.57 min while the corresponding aggregate mean-lives of the ^{220}Rn (^{216}Po, ^{212}Pb, ^{212}Bi, ^{212}Po) and ^{219}Rn (^{215}Po, ^{211}Pb, ^{211}Bi, ^{207}Tl) are 16.81 h and 1.03 h, respectively.

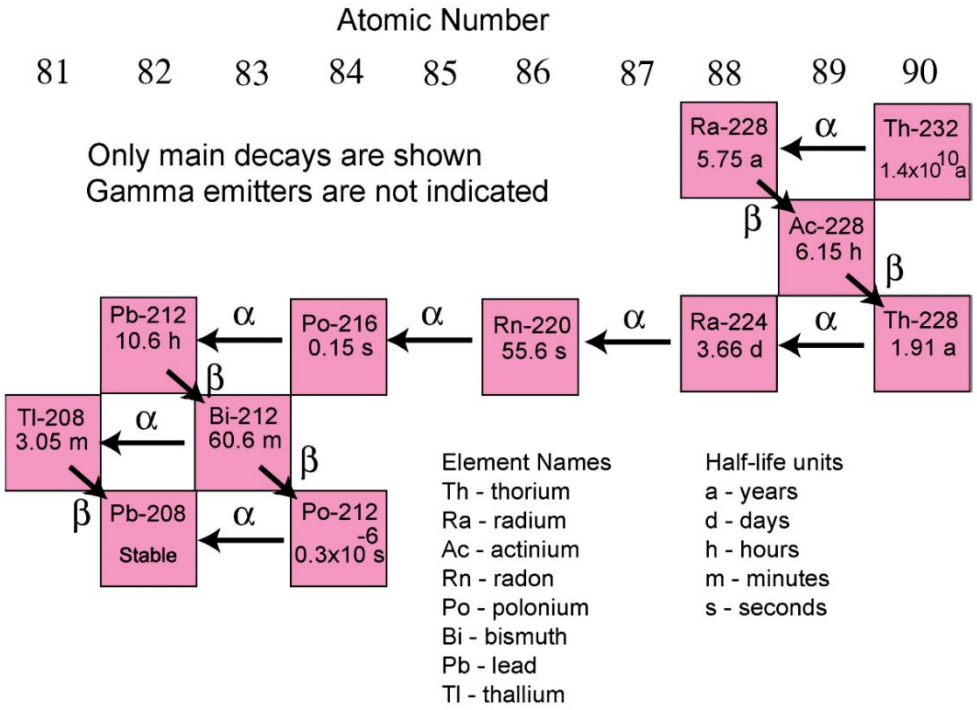

Figure 1-3 The thorium-232 decay chain (Source: U.S. Geological Survey (Duval et al., 2004)**)**

When radon or even thoron is inhaled, the gas may decay within the body, thereby giving rise directly to a radiation dose. However, the dosage of the decay products of radon and thoron are of much greater significance, in particular, those that emit alpha radiation. The emitted alpha rays can result in high local radiation doses at the peak of the bronchial tissues, which can finally lead to lung cancer (O'Connor et al., 2014).

Since all the isotopes of radon are radioactive, the radioactivity units are used to express the radon activities. The most used units in the literature are: Curie (denoted as Ci) is the activity of 1.00 g of ^{226}Ra and is equal to 37 billion disintegrations per second, dps (3.7×10^{10} or 2.22×10^{12} disintegrations per minute, dpm; thus, 1 pCi = 2.2 2 dpm. Becquerel (Bq), which is the SI unit of radioactivity and is equal to one atom decaying per second. The amount of natural radioactivity given off by radon and other decay products is very small and is commonly measured in trillionths of one Ci (10^{-12} or pico Curie) (Baskaran, 2016).

The concentration of radon significantly varies in different environments; the average outdoor radon level ranges between 5–15 Bq m^{-3}. However, radon concentrations are higher indoors, generally between 10 Bq m^{-3} to more than 10 000 Bq m^{-3} with the highest levels found in places like mines, caves and water treatment facilities (WHO, 2009). The air in the soil (i.e., soil gas radon) can be heavily loaded with radon depending on the type of rocks and the depth at which it is measured (usually measured 0.5–

1 m beneath the soil surface), There is no limit for radon activity in soil gas and it can even reach levels as high as 500 kBq m^{-3}(Kemski et al., 2001). The average concentration of radon in public water supplies derived from groundwater sources is about 20 Bq L^{-1}. Some wells have been identified with high concentrations, up to 400 times the average. Surface water, such as in lakes and streams, has the lowest concentrations, about one-tenth that of most wells (NRC, 1999).

1.2.2 Generation and Transportation from Source to Ground Level

Radon and thoron are formed by the alpha decay of their radium parents ^{226}Ra, ^{224}Ra. Therefore soils and rocks containing uranium-radium-bearing minerals are the primary sources of radon. Specific elements of accessory minerals include (for uranium) zircon, apatite, titanite, monazite, xenotime and allanite and also (for thorium) monazite and allanite (Kohn, 2003). Radon atoms located within a solid grain are unlikely to escape the mineral grain due to low diffusion coefficients in solids. However, it is widely recognized that radon escapes from a mineral grain as a result of its recoil when its parent, radium, undergoes radioactive decay (Baskaran, 2016). Then as shown in Figure 1-4, the mobilization of the formed radon atom takes place through three main processes: a) *Emanation*, radon atoms formed from the decay of radium escape from the grains (mainly because of recoil) into the interstitial space between the grains. b) *Transport*, diffusion and advective flow cause the movement of the emanated radon atoms through the soil profile to the ground surface. c) *Exhalation*, radon atoms that have been transported to the ground surface and then exhaled to the atmosphere (Ishimori et al., 2013).

The amount of radon generated in the soil grains and available for transport to the surface is given by the radon generation rate per unit volume of the soil material (Foley et al., 2020), G (Bq m^{-3} s^{-1}):

Equation 1-1 : $$G = \lambda_{Rn} E R \rho_b / \varepsilon$$

where λ_{Rn} is the radon decay constant (2.1×10^{-6} s^{-1}), E is the emanation coefficient, R is the mass activity of radium ^{226}Ra (Bq kg^{-1}), ρ_b is the soil bulk density (kg m^{-3}) and ε is the soil porosity.

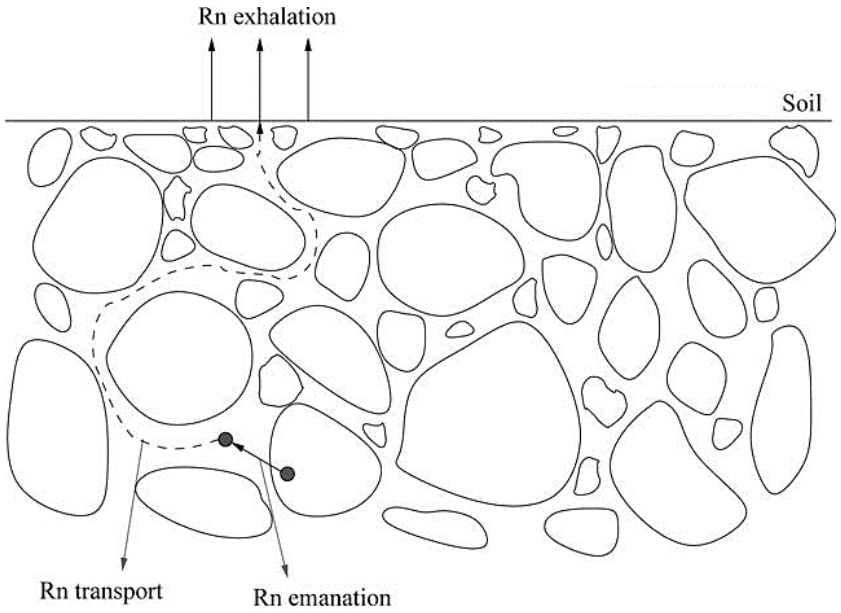

Figure 1-4 Schematic of mechanisms of radon released to the atmosphere (modified after (Ishimori et al., 2013)**).**

As can be understood from Equation 1-1, the rate of radon production increases with the emanation coefficient, the radium activity concentration and the bulk density. Emanation coefficient as one of the main processes that control the radon emanation rates from rocks/minerals/soils is defined as the fraction of the total number of radon atoms formed from the alpha decay of ^{226}Ra that can escape into the pore volume between the grains and become free to migrate (Ishimori et al., 2013). A typical value for the emanation coefficient of the soil is 0.2 (Nero et al., 1990). Factors that have substantial effects on the emanation coefficient include radium distribution within a grain, granulometric parameters of soil particles (e.g., shape, grain size), moisture content, mineralogy, temperature differences between air and soil and variations in atmospheric pressure (Baskaran, 2016).

The radon accumulated in pore spaces is transported to the surface by diffusion and advective flow, the diffusive transport of radon is affected by moisture, porosity and tortuosity. Fick's law of diffusion in terms of a diffusion coefficient can be used to formulate the diffusion coefficient (Equation 1-2 and Equation 1-3) (Ishimori et al., 2013). According to this law, radon flow density is linearly proportional to its concentration gradient under the assumption of a steady-state condition:

Equation 1-2 : $\varphi_d = -D_e \nabla C_{Rn}$

where φ_d is the diffusion flow density (Bq m^2 s^{-1}), D_e is the effective diffusion coefficient (m^2 s^{-1}) and C_{Rn} is the radon activity concentration (Bq m^{-3}). The negative sign arises

from the fact that radon diffuses from high to low concentrations. Consequently, the diffusion coefficient can be calculated as follows:

Equation 1-3 : $D_e = \varepsilon \tau D_M$

where τ is the tortuosity factor, which is typically less than unity in soils (e.g., 0.6 for tightly packed uniform spheres) and D_M is the molecular diffusion coefficient ($m^2\ s^{-1}$).

Although the dominant radon transport mechanism is diffusion, the advective flow may also be significant in some cases owing to surface cracks or holes, gas production, transport in water, or the presence of large voids (Ishimori et al., 2013). This type of radon transform mechanism is significantly influenced by air permeability of the soil, moisture and pressure gradient and Darcy's law can describe it in terms of air permeability, which strongly depends upon the pressure differential (Chauhan & Kumar, 2015; Nazaroff, 1992). Advective flow density φ_a can be obtained based on Darcy's law by calculation of the apparent velocity of fluid flow through the soil to the pressure gradient employing Equation 1-4 and Equation 1-5 :

Equation 1-4 : $$\vec{v} = -\frac{K_D}{\mu}\nabla P$$

Equation 1-5: $$\varphi_a = -\frac{C_{Rn}}{\varepsilon}\frac{K_D}{\mu}\nabla P$$

Where $\vec{v}$ is the superficial velocity vector ($m\ s^{-1}$), K_D is Darcy's permeability of the soil (m^2) that shows the ability of a fluid to transmit through the soil (porous material), P is the pressure (Pa) and μ is the dynamic viscosity of the gas-phase of the soil pores ($kg\ m^{-1}\ s^{-1}$).

Finally, the general term for calculation of soil radon transport, considering diffusion and advection mechanisms, radon production rate and the radioactive decay can be expressed by Equation 1-6 (Jiranek & Svoboda, 2007; Muñoz et al., 2017):

Equation 1-6: $$\frac{\partial C_{Rn}}{\partial t} = D_e \nabla^2 C_{Rn} + \frac{\nabla C_{Rn}}{\varepsilon}\frac{K_D}{\mu}\nabla P + G - \lambda_{Rn} C_{Rn}$$

1.2.3 Entry into Buildings and Contribution to Enhanced Indoor Radon Levels

Indoor radon concentration is affected by several parameters (Figure 1-5), all of which can vary from residence to residences, such as local geology, building design, meteorological parameters and living habits. However, the primary source of indoor

radon is the gas flux coming from soil and geology under the building foundations. Besides building and construction materials, the water supply and natural gas can all be considered as other sources of radon in the buildings (Bruno, 1983).

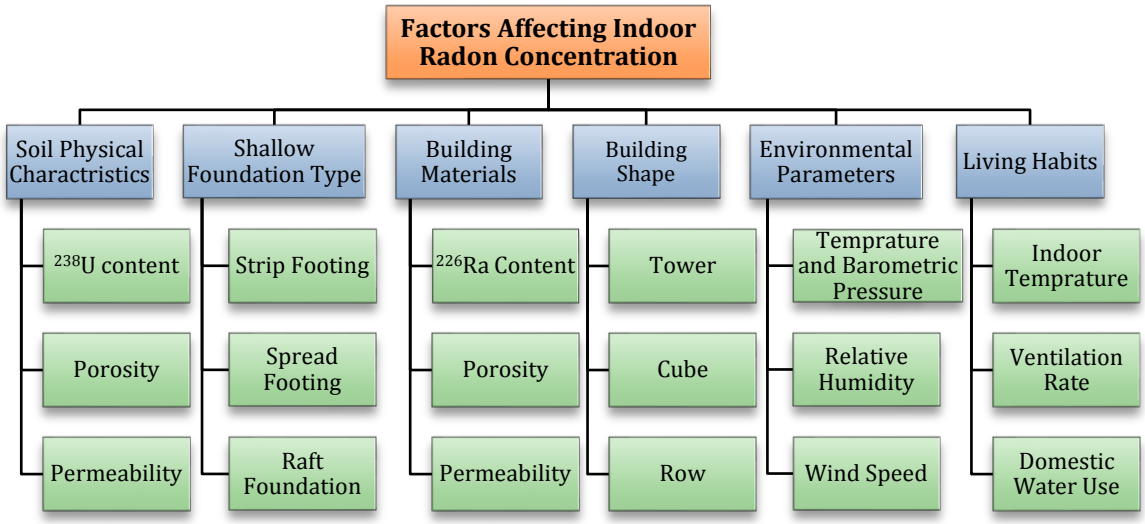

Figure 1-5 Summary of parameters that can affect indoor radon levels. Modified after (Ippolito & Remmeti, 2019)**.**

The radon released from the surface into the atmosphere (which is referred to as radon exhalation and is characterized by the exhalation flux density (Ishimori et al., 2013)), is transported to the indoor spaces through joints, gaps and other leakage routes existing in the foundation structures. The pressure difference (ordinarily negative) between external and internal air is known as the primary mechanism of radon transportation into the buildings. The main phenomena that can change the amount and rate of radon entry into the building are as follows (Ippolito & Remmeti, 2019)(see also Figure 1-6):

- The *Chimney effect*: As a result of a temperature difference between indoor and outdoor air, depressurization inside the buildings occurs and consequently, the air is sucked from the ground and outdoor.
- *Convection*: Difference in the exterior and interior pressure caused by wind, house heating, atmospheric pressure and mechanical ventilation brings radon into the dwelling. The shape of the building also affects the pressure drop and subsequently changes the indoor radon concentration. For example, in tall buildings (towers), enhanced radon levels can be observed at upper floors as a result of the chimney effect, however, for lower buildings, the primary source of indoor radon is through radon entry from the soil as a result of direct contact between soil and building foundations.

- *Soil Permeability*: This parameter controls the rate of radon entry. The presence of cracks and local joints in the soil might facilitate pathways and increase the speed of radon transformation to the ground level.
- *Metrological parameters*: events like rain or ice layers can facilitate radon entry to indoor spaces by providing a natural barrier (i.e., rainwater saturates the soil and prevents radon from being released into the atmosphere and conveys it to the foundation area)
- *Foundation type and presence of radon membrane*: the type of building foundation is significant to increase (e.g., Slab on-ground) and either prevent radon entry. Furthermore, the application of the radon barrier, a flexible, impermeable membrane that blocks radon can help to decrease radon entry into the building significantly.

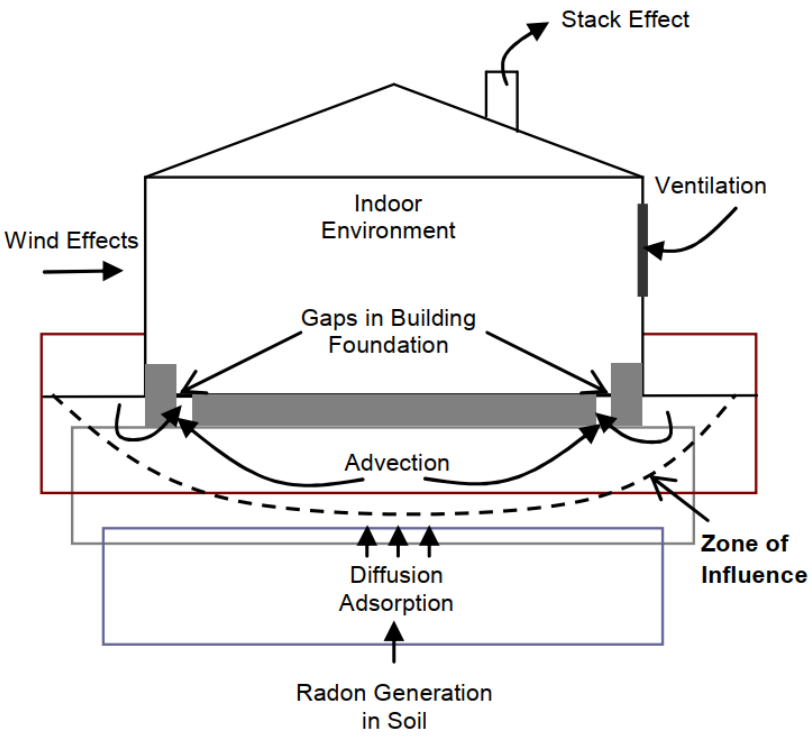

Figure 1-6 Processes affecting the concentration of indoor radon intrusion on site-scale (Kristensen, 2013)**.**

As mentioned above, the soil gas flux and radon exhalation from building materials are the primary sources of indoor radon. An indoor radon model can be defined based on theories suggested by Arvela et al., 1988 and Guiteras, 2008. This model takes into account several important factors. Equation 1-7 indicates the rate of change in indoor radon concentrations attributed to radon entry (i.e., entry from the soil via diffusive and advective flow and e diffusive flow caused by the difference in radon concentrations

between building material and the indoor space), radon exchange caused by ventilation, differences in indoor and outdoor radon levels and the decay of radon. Accordingly, the rate of change in radon concentrations in the soil and building materials can be calculated by Equation 1-8 and Equation 1-9, respectively (Whang, et al., 2018).

Equation 1-7: $$\frac{dC_i}{dt} = \{k_{d,s}(C_s - C_i) + k_a \Delta P_{s-i} C_S\} \frac{S_g}{V} + k_{d,bm}(C_{bm} - C_i) \frac{S_{bm}}{V} - \lambda v (C_i - C_o) - \lambda C_i$$

Equation 1-8: $$\frac{dC_s}{dt} = E_s S_g V - \{k_{d,s}(C_s - C_i) + k_a \Delta P_{s-i} C_s\} S_g V - \lambda C_s$$

Equation 1-9: $$\frac{dC_{bm}}{dt} = E_{bm} S_{bm} V - k_{d,bm}(C_{bm} - C_i) S_{bm} V - \lambda C_{bm}$$

where C_{bm} = radon concentrations in building materials (Bq m^{-3}), C_i = indoor radon concentrations (Bq m^{-3}), C_s = radon concentrations in the soil (Bq m^{-3}), C_o = radon concentrations in outdoor air (Bq m^{-3}), E_{bm} = effective radon exhalation rate of building materials (Bq m^{-2} hr^{-1}), E_s = effective radon exhalation rate of soil (Bq m^{-2} hr^{-1}), k_a = advection transfer coefficient of soil (m Pa^{-1} hr^{-1}), $k_{d,bm}$ = diffusion transfer coefficient of building materials (m hr^{-1}), $k_{d,s}$ = diffusion transfer coefficient of soil (m hr^{-1}), S_{bm} = indoor surface area of radon containing building materials (m^2), S_g = building area towards the ground (m^2), V = volume of the indoors (m^3), λ = radon decay constant (hr^{-1}), λ_v = ventilation rate (hr^{-1}) and ΔP_{s-i} = soil-indoor pressure difference (Pa).

By knowing the steady-state solution of the above system of differential equations, the estimated indoor radon concentrations can be written as follows:

Equation 1-10: $$C_i = \frac{E_s S_g V + E_{bm} S_{bm} V + \lambda_v C_o - \lambda (C_s + C_{bm})}{\lambda + \lambda_v}$$

As can be understood from Equation 1-10, one can estimate the indoor radon concentration by using the information on the radon release potential of the soil and radon emanation power of the building material used in the interior spaces. Another important parameter of the proposed model is the ventilation rate, which depends on many factors. However, a simple prediction of the ventilation rate using information about the frequency of opening windows in a room and meteorological factors, such as indoor-outdoor temperature difference and wind speed can be achieved by the following equation (Arvela et al., 1988; Park, Whang, et al., 2018):

Equation 1-11: $$\lambda_v = (f_t \mid T_i - T_o \mid + f_w u^2) N^p$$

where f_t, f_w = fitting parameters, T_i, T_o = indoor and outdoor temperatures, respectively (˚C), u = wind speed (m s^{-1}), N = the number of ventilations (dimensionless), p = fitting parameter (0 < p < 1- typically 0.5).

1.2.4 Radon in Public Buildings and Workplaces

Indoor radon measurements are generally associated with residential buildings. However, a typical person spends more than eight hours a day in their workplace, so that it is recognized as essential to monitor workers' exposure to radon to control their health risks (Brenner, 1994). In general, public buildings are also workplaces and in most cases, the measures for the protection of workers are likely to provide adequate protection for the public. Although it is believed that due to the presence of efficient mechanical ventilation systems in workplaces and public buildings, the radon concentration is lower than in houses (Bucci et al., 2011), all types of indoor workplace including factories, warehouses, offices, shops, universities, schools, hotels, nursing homes, residential care homes and health centers, theatres, building-material firms, monasteries, cathedrals, etc. can still have high radon levels. Underground workplaces such as basements, cellars, mines, galleries, caves, metro stations, underground car parks and utility industry service ducts can have significant levels of radon as can any above-ground workplaces, mainly in radon affected Areas (San Alduan et al., 2008). It should be taken into account that work activities (such as mineral extraction and processing, oil and gas production, metal recycling, or water treatment (Chen & Quayle, 2019)) together with the workplace characteristics, can also significantly affect radon concentration.

Due to differences in building characteristics and construction requirements/standards, radon levels in workplaces can differ significantly from the levels in residential homes. Therefore, the risk of radon-induced lung cancer may differ in those environments (Bucci et al., 2011). Health risks associated with radon/thoron exposure depends on the concertation of the solid decay products and is represented by the radon/thoron equilibrium equivalent concentration (EEC) which is estimated by using Equation 1-12 as follows (Chen, 2019):

Equation 1-12 : $$EEC\ \left(Radon \text{ or } Thoron\right) = F_{eq} \times C^{222}Rn \text{ or } C^{220}Rn$$

Where $C^{222}Rn$ and $C^{220}Rn$ are radon and thoron gas concentrations and F_{eq} is the equilibrium factor that describes the degree of disequilibrium between radon or thoron gas and its progeny. The characteristics of radon decay products differ significantly in different indoor environments. Many environmental factors, as well as human activities

and habits, affect the value of F_{eq}. Measured F_{eq} values vary widely from as low as 0.1 to as high as 0.8 for radon. Radon equilibrium factors in workplaces and public buildings can differ significantly from those of residential dwellings (Chen, 2019). The values of F_{eq} for thoron are relatively small compared to those for radon (e.g., 0.04 for indoors and 0.004 for outdoors) and therefore, the dose absorbed from radon decay products is higher than those for thoron (Ruzer & Harley, 2012).

1.3 Legislative Aspects of Radon

Protection against the dangers arising from exposure to ionizing radiation has become more prominent recently, following the 2013/59/EURATOM BSS Directive, which has been mandatory since the 6th of February 2018 within the member states of the European Union. This Directive established that the reference limit level for the concentration of radon gas activity in closed environments of new buildings, in buildings intended for education and in buildings that are open to the public must not exceed 300 Bq m^{-3} in all premises of the building in question as measured as an annual average concentration (EU, 2013). It is noteworthy that the past Italian regulation (Legislative Decree 230/95) – which has been replaced by the forthcoming transposition of the 2013/59/Euratom Directive, was dealing only with the protection from radon in workplaces (including schools). In particular, radon measurements were required in fully underground workplaces and other workplaces (with priority to those in the basement and ground floor) only in radon-prone areas declared by the Regions. Remedial actions were required if the measured radon level exceeded 500 Bq m^{-3} (value of the Italian action level) and if the annual effective dose for workers was higher than 3 mSv (Bochicchio et al., 2019).

For the natural radioactivity in building materials, two parameters can be considered, radon exhalation rates and gamma radiation level. However, building materials give the most significant contribution to the indoor gamma dose (UNSCEAR, 2008). In this regard, article 75 of the European Directive also states that the reference level for the indoor external exposure to gamma radiation from building materials is 1 mSv per year, in addition to the outdoor external exposure. Building materials as a radon source are dealt with in the Annex XVIII of this Directive, listing items to be considered in preparing the national action plan to address long-term risks from radon exposure. Annex VIII also expresses the activity concentration index I_γ (Equation 1-13) (EC, 2000), which depends on the activity concentrations of ^{226}Ra (C_{Ra}), ^{232}Th (C_{Th}) and ^{40}K (C_k). It is a conservative screening tool and for building materials of concern "the calculation of dose needs to take

into account other factors such as density, the thickness of the material as well as factors relating to the type of building and the intended use of the material (bulk or superficial) (Nuccetelli et al., 2017).

Equation 1-13: $$I_\gamma = \frac{C_{Ra}}{300^{Bqkg^{-1}}} + \frac{C_{Th}}{200^{Bqkg^{-1}}} + \frac{C_K}{3000^{Bqkg^{-1}}}$$

A good database of activity concentrations, radon emanations and radon exhalation rates of some of the building materials commonly used by European countries can be found in the report published by Istituto Superiore di Sanità, Rome, Italy (Nuccetelli et al., 2017).

Furthermore, the Ra_{eq} method is another widely used criteria for screening and evaluating construction materials which uses dose criteria of 1.5 mGy per year, which corresponds to roughly 1 mSv per year and, approximately, to 370 Bq kg^{-1} of ^{226}Ra, 260 Bq kg^{-1} of ^{232}Th and 4800 Bq kg^{-1} ^{40}K. In Equation 1-14, exposure to gamma radiation is controlled by limiting Ra_{eq} 370 Bq kg^{-1} (Beretka & Mathew, 1985).

Equation 1-14: $$Ra_{eq} = C_{226Ra} + 1.43C_{232Th} + 0.077C_{40K}$$

Surface and underground waters can also contribute to radon exposure from two different pathways: ingestion of water and inhalation (Noverques et al., 2020) Radon in water may also originate from the dissolution of airborne radon into the water and other higher radon bearing water in-flows in the catchment area (Jobbágy et al., 2017). According to Directive 2013/51/EURATOM, the European countries must set a threshold level that can range between 100 Bq L^{-1} and 1000 Bq L^{-1} (the reference level for 24 EU Member States, including Italy is 100 Bq L^{-1}) for radon in waters intended for human consumption. Remedial action without further consideration is justified in all EU countries when the concentration exceeds 1000 Bq L^{-1} (EU, 2013). It must be noted that mineral waters are still exempted from this Directive despite their regular/preferred consumption (Jobbágy et al., 2017).

1.4 Thesis Aims

This research work is focused on the preparation of a draft of a geogenic radon potential map to be used for the prediction of radon levels in public buildings and workplaces of the Sardinian region in line with the 2013/59/EURATOM BSS Directive. Since radon behavior in workplaces and domestic dwellings is not identical and the application of radon maps developed based on indoor radon data measured in dwellings may cause legal

implications in workplaces and public buildings, it was essential to prepare a map that does not depend on building characteristics and living habits (e.g., potential map).

To aim this at the first step, the most recent methodologies for geogenic radon potential mapping are reviewed and the available bibliographic information and previous measurement data are collected. Field and laboratory-based experiments are carried out to evaluate the suitability of geological information for the preparation of a geogenic radon risk map. After finding the most suitable data, different approaches are tried to develop a geogenic map that better estimates the radon risk in Sardinia. The model of geogenic radon should be tested through several in-situ and laboratory tests.

In addition to radon of geogenic origin, building and construction materials are also important sources of radon (and especially thoron). Therefore, the natural radioactivity and radon exhalation rates of Sardinian building material are investigated in parallel with the development of the GRP map of the Sardinian territory. Both the developed GRP map and the information on building material can be efficiently utilized to estimate the indoor radon levels not only in public buildings and workplaces but also for other types of buildings, including residential dwellings.

Furthermore, through a pilot field experiment, the methodology for accurate prediction of a geogenic radon potential model and estimation of uncertainty of prediction is examined. The introduced model can be utilized as a promising tool to estimate radon risk with high precision for the sites that the prerequisite data are available.

In addition to the investigation of radon health risk potential in Sardinia, the application of natural radioactivity as a tool for radiogenic assessments is discussed in the final section of the thesis.

More generally, the results of this research work can help to increase public (and political) awareness of radioactive environments and radon risks, provide a guide for targeting future measurement points and finally, estimation of the radon hazard of future construction sites.

1.5 Thesis Outline

Following the first chapter, which summarized the basics of radon and natural radioactivity together with the legislative aspects of radon, the second chapter introduces the methodologies for radioactivity detection (including radon activity in different environments), mathematical models and the instruments utilized for testing purposes.

The third chapter describes the approaches and methodologies for radon risk mapping adopted by different European countries. The advantages, disadvantages and limitations of those methods are mentioned in this chapter. The last section of chapter 3 discusses the radon mapping problem in Sardinia and reviews the available data that can be used to solve this problem.

In chapter 4, the correlation between different data classification methods (e.g. geology and soil type), with radon-related variables (radiometric surveys and geochemical data), the indoor radon concentration and radon and thoron exhalation rates are investigated in an area with complex geology and various soil types in South-Eastern Ireland. The goal of this study was to find out which classification method is better and which geogenic information can more appropriately represent the radon behavior of an area.

Chapter 5 includes two parts; the first part describes the procedure to develop the GRP map of the Sardinian region. Based on the methodologies discussed in chapter 3 and the results of the study carried out in chapter 4, two GRP maps had been produced. The first map is prepared in a similar method that is used for the development of the European Geogenic Radon map (i.e. using extrapolation radon-related data from German geotypes). However, the second map employs local geogenic information concerning geological boundaries to produce a Sardinian GRP map. The comparison of produced maps indicates that the second map was found to be more applicable than the first one. The second part of this chapter expresses the result of a laboratory experiment carried out in parallel with GRP mapping to investigate the contribution of building materials to the natural radioactivity and indoor radon levels.

Chapter 6 introduces the set of validation tests that were employed for the evaluation of the workability of the proposed GRP map. To aim examination of the GRP map, an experiment based on in-situ and laboratory tests in a radon priority area, a radon monitoring practice in an underground workspace (e.g., dam gallery), a model developed to predict indoor radon concentrations in public and workspace of a university in Sardinia by setting the predicted GRP levels and anthropogenic factors as the input variables, together with the comparison of predicted risk classes with available indoor radon for Sardinian post offices, were considered.

Chapter 7 states the procedure for the development of an accurate geospatial model to produce high-resolution GRP maps for any area where data on radon-related input variables is available. This study was based on the results of data processing and field tests carried out for a site in a granitic area of south-eastern Ireland.

Chapter 8 shows the application of radon and natural radioactivity monitoring as a quick and reliable tool for radiological characterization of a heavy mineral placer deposit in Southern Sardinia.

Finally, the general conclusions that are drawn from the work presented in Chapters 4 to 8 and future research opportunities are discussed in Chapter 9.

2 NATURAL RADIOACTIVITY DETECTION AND MEASUREMENTS OF RADON IN DIFFERENT ENVIRONMENTS

Summary

In this thesis work, in order to investigate natural radionuclide levels in rocks, soil and sediments, the gamma-ray detection based methods were adopted. The instruments, principals and models to estimate the radionuclide activity concentrations (i.e., ^{238}U, ^{226}Ra, ^{232}Th and ^{40}K) are expressed in this chapter. Further to natural radioactivity levels, it was necessary to predict the radon emanation and exhalation rates from different media. A set of laboratory and in-situ tests were considered for this purpose. The second part of this chapter introduces the methodologies to obtain radon release potentials.

2.1 Gamma Ray Methods for Radioelement Mapping

Gamma-ray spectrometry is a powerful tool for monitoring radiation in the environment. This technique is widely used for geological, geochemical and environmental mapping and mineral exploration. Many types of gamma-ray surveys can be used to estimate and assess the terrestrial radiation dose to the human population and to identify areas of potential natural radiation hazard. Spectrometers can even be mounted on aircraft or motor vehicles. Hand-held portable spectrometers for ground measurements and borehole spectrometers for down-hole measurements are available. Sea-bottom surveys are also possible and laboratory spectrometers can accurately measure rock and soil samples (Erdi-Krausz et al., 2003).

A Gamma spectrometer is used to identify radionuclides that emit gamma rays. While many naturally occurring elements have radioactive isotopes, only potassium and the uranium and thorium decay series, have radioisotopes that produce gamma rays of sufficient energy and intensity to be measured by gamma-ray spectrometry (Erdi-Krausz et al., 2003).

2.1.1 Laboratory Gamma-Ray Spectrometry

Spectroscopy of any kind deals with the analysis of spectrum, i.e., a variation of intensity with either wavelength or frequency or energy. In this research, a laboratory apparatus based on a NaI (Tl) gamma-ray spectrometer was utilized for the assessment of U, Th and K in rocks, soil, building material and also sediment samples (please refer to Gilmore, 2008 for basics of radioactivity and principles of gamma-ray spectrometry using NaI (Tl) detector). Generally, the high-energy resolution of the High-Purity Germanium (HPGe) gamma-ray detector is believed to be the best detector for unambiguous nuclide identification (Gilmore & Wiley, 2011). However, given that the radioisotopes to be tested in samples (series of Uranium and Thorium, ^{40} K) are known, it is convenient to use a tool with high efficiency and low energy resolution as the spectrometer to NaI (Tl) instead of an HPGe that would require longer acquisition times and much more complicated data processing.

Accordingly, the gamma-ray scintillation spectrometry system of the Nuclear Physics Laboratory of the University of Cagliari (Figure 2-1) was used for the determination of the activity of the concerning radioelements. The system consists of an EG & G-Ortec NaI (Tl) detector (3″ × 3″), connected to a multichannel analyzer PC board (1024 channels) equipped with a spectrum stabilizer for automatic gain shift compensation. The

sample and detector are enclosed within 6-10 cm of lead shielding to reduce the background radiation. A 5 mm thick brass plate is installed inside the lead shielding to minimize the effect of induced X-ray radiation in the lead shielding (Chiozzi et al., 2000). For the acquisition of gamma spectrums and visualization of data, the MAESTRO multichannel analyzer emulation software has been utilized.

Figure 2-1: NaI (Tl) gamma spectrometer of the nuclear physics laboratory of the University of Cagliari.

The determination of activity concentrations in samples comprises the preparation of the sample based on standard guidelines, the measurement and the calculation of activity concentration from the measurement results and finally, calculation of the uncertainty of the radioelement detection (Friedmann, Nuccetelli, et al., 2017).

The samples had to be prepared in a pulverized homogeneous form with a mass of 200-1000 g (Erdi-Krausz et al., 2003). The samples to be analyzed had the same shape as the reference samples and similar mass and volume; this allows us to hypothesize that the detection efficiency is similar for all the samples. The reference samples are samples with known activity concentration. The IAEA geological reference materials for laboratory gamma-ray spectrometry analysis (RGU-1 a U+Ra geological reference material with 400 ppm U and 392 ppm eU and RGTh-1 a Th geological reference material with 800 ppm Th (IAEA, 1987) together with high-pure KNO_3 salt) were used as the reference material.

To measure the radio element activities of each sample, at first, the spectrum of each sample analyzed turns out to be the weighted sum of the three reference spectra (U, Th and ^{40}K) plus the background spectrum. The weight of each spectrum of the three references depends on the mass (and hence the activity) of the radioisotope present in the

test sample. The procedure starts with comparing the reference spectra and the spectrum of the sample and then the algorithm identifies the weights of the three isotopes present in the sample under analysis. Then mathematical calculations based on the Maximum Likelihood (ML) technique in Microsoft Excel software is used to calculate both the weights and the standard deviations. The ML method of estimating the activities is derived from the condition of the maximum of the likelihood function or its logarithm. The logarithm of the likelihood function for the Poisson distribution of counts in the spectrum channels is as follows (Jánossy, 1965; Muravsky et al., 1998):

Equation 2-1: $$\ln L = \sum_{i=1}^{N}\left(-T\sum_{K=1}^{M} A_k f_k(i) + S(i)\ln\left(T\sum_{K=1}^{M} A_k f_k(i)\right) - \ln(s(i)!)\right)$$

where S(i) is the experimental spectrum of a mixture of radioactive nuclides, i the channel number, N the number of channels, T the spectrum accumulation time, M the number of spectral components, $f_k(i)$ for k = 1,2,. . ., M-1 the spectrum of the k^{th} nuclide, normalized to unit activity and unit time, $f_M(i)$ the spectrum of a background, normalized to unit time, A_k the unknown activity of the kth nuclide, A_M the unknown relative intensity of a background.

The estimates of A_k are determined by the solution of the following system of the M equations deriving from the condition of the maximum of Equation 2-1 (Jánossy, 1965).

Equation 2-2: $$\sum_{i=1}^{N}\left[\frac{S(i)\,f_j(i)}{\sum_{k=1}^{M} A_k f_k(i)} - T f_j(i)\right] = 0, \quad j=1,2,...,M$$

The system of Equation 2-2 may be solved by the iteration method. In every q^{th} iteration (q = 0, 1, 2. . .), one solves the set of the linear equations:

Equation 2-3: $$\sum_{k=1}^{M} A_k T \sum_{i=1}^{N} \frac{f_k(i)\,f_j(i)}{D_q(i)} = \sum_{i=1}^{N} \frac{S(i)\,f_j(i)}{D_q(i)},$$

Where $D_q(i) = \begin{cases} \sum_{k=1}^{M} A_k^{(q-1)} f_k(i) & \text{if } q > 0 \\ S(i)+1 & \text{if } q=0 \end{cases}$ and $A_k^{(q-1)}$ are the estimates of the activities obtained in q-1 iteration. Given the obtained estimates, $\hat{A}_{kj}^{(N)}$ the total relative error of the detection can be calculated by (Jánossy, 1965; Muravsky et al., 1998):

Equation 2-4: $$\sigma_k^{(N)} = \frac{1}{A_k}\sqrt{\frac{1}{P}\sum_{J=1}^{P}\left(\hat{A}_{kj}^{(N)} - A_k\right)^2}$$

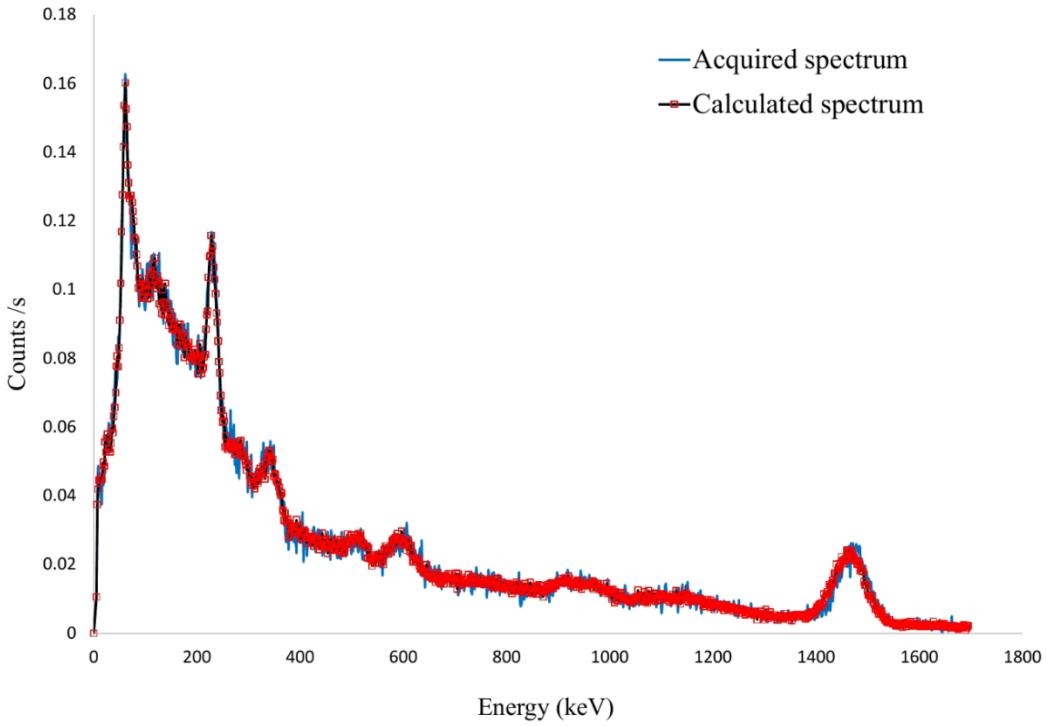

Figure 2-2: Comparison of the acquired spectrum with the spectrum which is calculated based on the optimal linear combination of the three base spectra and background correction for a sample

The verification of the correspondence between the experimental data and theoretical values can be carried out by performing the linear and plotting combination of the three spectra plus the background spectrum. Figure 2-2 shows an appropriately good correspondence of the weighed spectrum and also the experimental spectrum acquired.

2.1.2 Portable Gamma-Ray Spectrometry for In-situ Measurements

In situ gamma spectroscopy is a quick and low-cost technique to determine the concentration of natural and artificial radionuclides in soil, rocks and building materials. Portable gamma-ray spectrometers used for natural radionuclide mapping, monitor energy windows centered on the 1461 keV (^{40}K), 1765 keV (^{214}Bi) and 2615 keV (^{208}Tl) photopeaks for the estimation of K, equivalent U (eU) and equivalent Th (eTh) concentrations, respectively (Erdi-Krausz et al., 2003).

Ratios between radioelement concentrations (Th/U, Th/K and U/K) are often used to reduce the effect of terrain geometry on the concentration estimates (Erdi-Krausz et al., 2003). Anomalous ratios are often indicative of mineralization and rock alteration. The ground level total gamma dose exposure rate, E (nGy h^{-1}) can also be calculated from the apparent concentrations of K (%), eU (ppm) and eTh (ppm) using the expression (Grasty, 1991):

Equation 2-5: $E = 8.69 \times (0.505\ K\ +\ 0.653\ eU\ +\ 0.287\ eTh\ )$

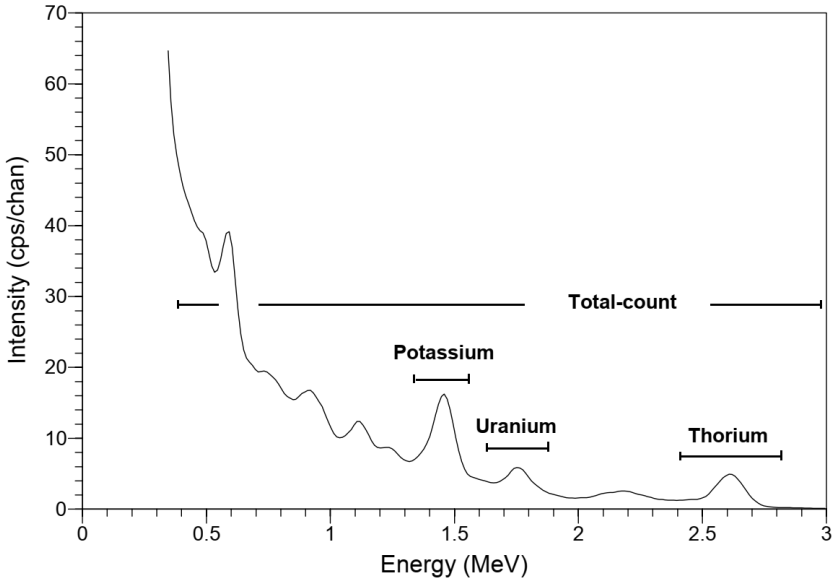

Figure 2-3: Typical gamma-ray spectrum showing the positions of the conventional energy windows. (taken from (Erdi-Krausz, Matolin, Minty, Nicolet, et al., 2003)

In this study, a calibrated RS-230 portable gamma-ray spectrometer (1024 channels) that includes a large (103 cm^3) BGO (Bismuth Germanate Oxide) detector together with a GT40S gamma-ray spectrometer with 104cm^3 BGO detector were used for the in-situ estimations of K, U and Th radioelement concentrations. Moreover, the GT-40 includes the ability to implement a local background reading for isolating counts from a particular sample. This function can be enhanced by fitting the Pb collimator which makes the system ideal for laboratory use.

Field measurements with portable gamma-ray spectrometers can be carried out in either static or dynamic mode. In static mode, the radioactivity is measured at discrete points. In dynamic mode, the instrument is transported over fixed distances during measurement and the accumulated counts reflect the average radioactivity of the traverse sector (Erdi-Krausz et al., 2003). The instruments store the georeferenced data in the spectrometer´s memory. Then the data can be utilized in GIS techniques to localize zones of radioelement enrichment or depletion.

Figure 2-4: Application of RS-230 (left) and GT-40S (right) spectrometers for field surveying of naturally occurring radioactive elements

2.1.3 Airborne Gamma-Ray Spectrometry

Airborne gamma spectrometry system has extensive applications in mineral exploration, inform land-use planning and provides environmental radioactivity monitoring baseline data (Hodgson & Young, 2016l). Moreover, the combined mapping of uranium along with other geological data can be modeled to help provide an indicator of the likely emission of radon gas (Appleton et al., 2011).

A gamma-ray spectrometry instrument mounted on an aircraft measures the real-time natural radiation of potassium, thorium and uranium emitted from surface rocks and soil at one-second intervals. The aircraft (see Figure 2-5) flies along with a network of pre-planned parallel lines, typically at a nominal height of between 30 and 500 m above ground level. Variations in the principal physical properties of soil/rocks, such as magnetic field, electrical conductivity and gamma radiation beneath the flight path can be automatically recorded at appropriate intervals (for gamma-ray surveys). As can be seen in Table 2-1, the radioelement contents can be obtained as a result of the gamma-ray surveys with a 256-channel gamma detector (e.g., Exploranium GR-820) covering 0.3–3 MeV energy window that measures gamma-ray counts in the 6 to 60-meter intervals. The position of the aircraft, together with height above ground and sea level, are simultaneously recorded (Hodgson & Young, 2016).

Figure 2-5 De Havilland Twin Otter survey aircraft. The wingtips contain the electromagnetic transmitter and receiver coils and one magnetometer sensor (taken from (Hodgson & Young, 2016)**).**

The obtained digital data will be corrected with a range of corrections and standardization, including removing aircraft, cosmic and radon background; application of stripping corrections derived from calibration data and application of height attenuation corrections (Appleton et al., 2008). Radon background correction due to the effects of the climatic factors such as rainfall, temperature and humidity, atmospheric and hydrological changes and seasonal changes, geological factors such as altitude, mineral types could also help to improve the accuracy of measurement and avoid false alarms (Zeng et al., 2019). After compensation for non-terrestrial effects, the processed data on natural radiation emitted primarily from isotopes of potassium (K), equivalent thorium (e Th, estimated from ^{208}Tl) and equivalent uranium (eU, estimated from ^{214}Bi) coming from the top 30 cm of the soils and rocks together with air absorbed dose rates can be transported to GIS environments to be able to distinguish between the radioactive characteristics of a different material (i.e., bedrock geologies and soils).

Table 2-1 Spectral energy ranges of the airborne radiometric data (Appleton et al., 2008)**.**

Window	Nuclide	Energy range (MeV)
Thorium (eTh)	^{208}Tl (2.61 MeV)	2.41-2.81
Uranium (eU)	^{214}Bi (1.76 MeV)	1.66-1.86
Potassium (%K)	^{40}K (1.46 MeV)	1.37-1.57

2.2 Radon Monitoring in the Environment

This section expresses the techniques and the methods used for measuring radon gas in the environment, including indoor spaces, soil, water, rocks and building materials. It is crucial to measure radon in different environments as exposure to enhanced levels of

radon present in an indoor environment, water and soils surrounding a human dwelling may increase the risk of lung cancer. There is a wide range of techniques for the detection and quantification of radon however, only the essential information on methods that have been used in this research are discussed here in detail., for further information, please refer to (Baskaran, 2016; Elzain, 2017; Friedmann, Nuccetelli, et al., 2017).

Generally, radon measurement techniques are categorized into two categories: a) based on test duration, which includes short-term (from a few days to 1 month) and long-term (up to one year) measurement periods. Long term tests are the most representative measurements of the actual exposure of radon gas in any environment. At the same time, short term tests are mainly employed for screening surveys to identify buildings with high radon concentrations and also to investigate the geographical variations. The second category is based on the way that radon is being measured; it can be either active or passive (Elzain, 2017).

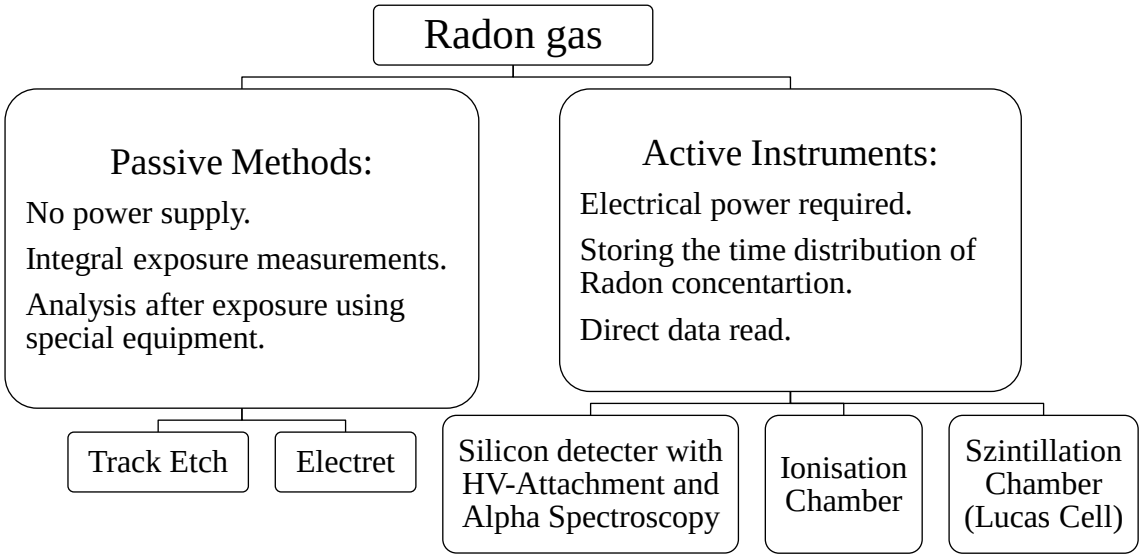

Figure 2-6: Methods and Instruments to measure radon (modified after http://www.SARAD.de/)

If an instrument detects the radon and or radon decay products that sample radon based on the natural diffusion without any power supply, the method is called the passive testing technique. This method includes two types of detectors i) Detectors with a real-time response (typically scintillators and semiconductors) and ii) detectors with no real-time response (e.g., track-etched detectors, activated charcoal and electrets). In the active radon testing techniques, the gas is measured by forced sampling through the use of a power supply (pumps) (Elzain, 2017). In this research, the CR-39s, the solid-state nuclear track detector (SSNTD) together with four active radon monitors (i.e., Radon detector

RM-2 and RADEX MR107 (Ion chamber), MR1 (ZnS (Ag) scintillation cell) and DURRIDGE RAD7 (Solid-state alpha detector) were utilized for the detection of radon in different environments. The radon detection principles of the mentioned radon monitors and the CR-39 test kits are as follows (Friedmann, Nuccetelli, et al., 2017; ISO 11665-1, 2012):

1. Ionization chamber: When traveling through the air, each alpha particle creates several tens of thousands of ion pairs, which, under some experimental conditions, produces an ionization current. Although very low, this current may be measured using an ionization chamber that gives the activity concentration of radon and its decay products. When the sampling is performed through a filtering medium, only radon diffuses into the ionization chamber and the signal is proportional to the radon activity concentration.
2. ZnS(Ag) scintillation (silver-activated zinc sulfide): Some electrons in scintillating media, such as ZnS(Ag), have the particular feature of emitting light photons by returning to their ground state when they are excited by an alpha particle. These light photons can be detected using a photomultiplier. The principle adopted for scintillation cells, such as Lucas cells, is the same.
3. Alpha spectrometry (based on the semiconductor detector): A semiconductor detector (made of silicon) converts the energy from an incident alpha particle into electric charges. These are converted into pulses with amplitudes proportional to the energy of the alpha particles emitted by the radon or thoron decay products. The progeny is concentrated either near the front of the detector in case of sampling on a filter or are precipitated directly onto the surface of the detector due to the electric field created specially in the measuring chamber.
4. Solid-state nuclear track detectors (SSNTD): An alpha particle triggers ionization as it passes through some polymer nuclear detectors (such as cellulose nitrate). Ion recombination is not complete after the particle has passed through. Appropriate etching acts as a developing agent. The detector then shows the tracks as etching holes or cones, in quantity proportional to the number of alpha particles that have passed through the detector.

The precision/accuracy of radon measurements using the following instruments depends on the applications.

2.2.1 Radon in the Indoor Air

As mentioned before, the radon concentration in the indoor air of buildings can vary significantly due to the combined effects of (i) a considerable variation of radon exhalation fluxes from its sources, regarding both the exhalation from soil underlying the building (which is generally the primary source of indoor radon) and the exhalation fluxes of building materials; (ii) a significant variation of building characteristics affecting radon entry and ventilation (Ishimori et al., 2013). Furthermore, radon varies daily and even seasonally, therefore to decrease the radon concentration variability, annual averages of radon (i.e., an average over a total period of 12 consecutive months) are considered to decide whether a dwelling has indoor radon levels or not. In the case of public buildings and workplaces, long term (3 to12 months but 12 months is optimal) measurements are recommended to obtain the annual averages. Seasonal correction factors are also needed in the case the measurement period is less than one year. To provide a representative radon estimate for such buildings which are different from houses as they usually contain many rooms, the measurements should be made in the lowest-level occupied rooms of the building, preferably tested at the same time. A room subdivided by partitions can also be treated as one room. A radon measurement should be made in each room occupied in a basement or if no basement exists, on the ground floor, or the floor with the lowest-level occupied rooms. For larger rooms, further detectors per room might be needed (Health Canada, 2008).

The SSNTDs are commonly used to obtain the annual averages of indoor radon concentrations. For the calculation of the radon activity measured by these detectors, the track density should be determined and then converted into activity concentration C_{Rn} (Bq m^{-3}) using Equation 2-6 (A. Elzain, 2016; Park, Lee, et al., 2018). The seasonal correction factor can also be applied if needed.

Equation 2-6: $$C_{Rn} = \frac{\rho_{Rn}}{K_{Rn} T} \quad \text{and} \quad C_{Rn-year} = C_{j,k}^{\frac{f_j + \cdots + f_{j+k-1}}{k}}$$

where ρ_{Rn} is the track density (tracks per cm^2), K_{Rn} is the calibration constant, which must be previously determined in tracks cm^{-2} h^{-1} per (Bq m^{-3}) and t is the exposure time. $C_{j,k}$ denotes the measured indoor radon concentration starting in j month during the k months.

Furthermore, short-term measurement of duration less than three months (more typically two to7 days) with "Closed-building" conditions can be utilized where a more rapid

indication of the radon concentration may be required or to perform follow-up test where the highest concentrations are found, especially when the results exceed the reference levels (Health Canada, 2008). We used CR-39 test kits for long-term radon measurements in workplaces of a university. Besides, the RADEX MR107 and MR1 continuous radon monitors were employed to carry out short-term radon follow-up tests inside the gallery of a dam for which enhanced radon levels were previously measured.

2.2.2 Radon in Soil and Building Material

Gas flux from the soil and the exhalation from building and construction material are the main contributors to indoor radon concentrations and they can be estimated through laboratory or field testing of gas exhalation rates of soil/rock samples. In-situ measurements can detect radon release from the soil profile. This type of testing is a site-specific individual technique that enables us to propose an optimal preventive strategy corresponding to local conditions. However, sometimes the laboratory tests are preferred since in-situ determinations of ^{222}Rn and ^{220}Rn fluxes from the ground are long and affected by significant uncertainties due to changing physical conditions such as soil moisture, temperature and pressure gradients (Lucchetti et al., 2019). Based on the facilities available, we employed both in-situ and laboratory tests radon exhalation from the soils.

2.2.2.1 Laboratory Testing of Radon and Thoron Flux

We developed two radon gas analyzer set-ups to measure the radon/thoron surface exhalation rates based on the "Close-chamber method" (passive accumulation of radon in a closed container), which is the most common technique for radon/thoron measurements. It is based on the principle of radon accumulation in a closed container (usually of cylinder shape, with a diameter of 0.1–0.5 m and a volume of 1–10 L), which is mounted on the surface of the soil or the building material (Friedmann, Nuccetelli, et al., 2017; Ishimori et al., 2013). The RADEX MR107 and DURRIDGE RAD7 radon monitors were employed for the continuous measurement (1-hour cycles) of ^{222}Rn concentrations accumulated inside the chamber. The DURRIDGE RAD7 also had the advantage of measuring both ^{222}Rn and ^{220}Rn simultaneously. Based on the data recorded by the instruments, the growth model of activity concentration of ^{222}Rn and ^{220} Rn (only for the chamber containing DURRIDGE RAD7) inside the accumulation chamber vs. time can be developed.

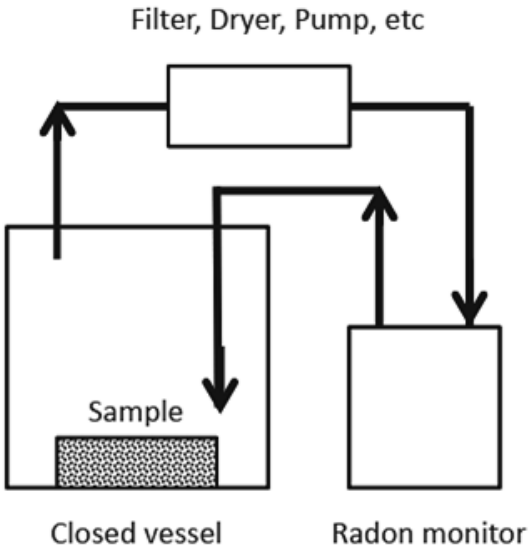

Figure 2-7: Scheme of a measurement setup based on the Close-chamber method. (Ishimori et al., 2013)

Finally, based on the geometry and the type of the sample and also the specifications of the instruments, two similar approaches can be utilized for the estimation of exhalation rates. First, the radon and thoron exhalation rates (E_{222Rn}, Bq m^{-2} h^{-1} and E_{220Rn}, Bq $m^{-2}h^{-1}$) can be simply estimated by finding the slope of growth curves of ^{222}Rn and ^{220}Rn using linear regressions and solving the Equation 2-7 and Equation 2-8, respectively (Lucchetti et al., 2019).

Equation 2-7: $$E_{222\,Rn} = \frac{(m + \lambda_{222} C_0)V}{S}$$

Equation 2-8: $$E_{220\,Rn} = \frac{\lambda_{220} V_0}{S} \frac{C_m}{e^{-\lambda_{220}(V_1/Q)}}$$

where λ_{222} and λ_{220} are ^{222}Rn and ^{220}Rn decay constants (h^{-1}), C_0 is the initial radon concentration (Bq m^{-3}), V is the free total volume of the analytical system (m^3), S is the surface of the sample, V_0 and V_1 (m^{-3}) are the free volume of the accumulation chamber and the volume between the outflow of the accumulation chamber and the inflow of the radon monitor, respectively. Q (L h^{-1}) is the flow rate in the system.

The second approach, as expressed in Equation 2-9, the ^{222}Rn exhalation rate can be estimated by finding the steady-state radon activity (C_m) and λ_e (effective radon decay constant accounting for the radon decay constant, the leak rate of the system and the so-called "back diffusion") using nonlinear least-squares fitting (Tan & Xiao, 2011) with the two-dimensional diffusion theory (Equation 2-10) (Ishimori et al., 2013; Sahoo & Mayya, 2010).

Equation 2-9: $$C(t) = C_0 e^{-t\lambda_e} + C_m(1 - e^{-t\lambda_e})$$

Equation 2-10: $$E_{^{222}Rn} = \frac{\lambda_{eff} C_m V}{S}$$

2.2.2.2 In-situ soil gas radon testing

In situ measurements of radon gas and the gas permeability are essential for the estimation of radon risk at specific sites. The most popular method in the in-situ category is the soil radon depth profiling method. Radon concentration from an infinite column of soil (Figure 2-8) as a function of distance z can be modeled using Equation 2-11 (Fleischer & Mogro-Campero, 1978):

Equation 2-11: $$C_z = C_\infty (1 - e^{z/l_s})$$

Where $l_s = \sqrt{D/\lambda}$, λ is the decay constant, D is the diffusion constant and C_∞ is the concentration at infinite depth. The soil gas radon concentration increases up to a certain depth (~ $3l_s$) and after that, the concentration saturates.

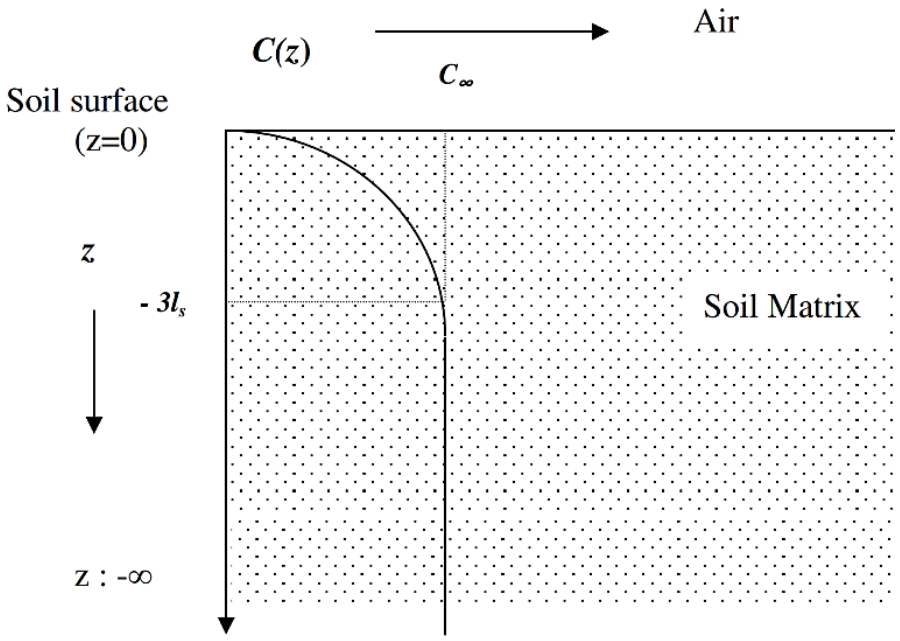

Figure 2-8: Schematic diagram of radon gas vs. soil depth (taken from (Park, Lee, et al., 2018)**).**

Soil gas radon concentrations at different depths can be measured by sampling radon gas through a hollow rod and detecting of activity of the sampled air. As can be seen in Figure 2-9 using hollow steel rods and a plastic large-volume syringe it can be possible to sample the soil air and then by transferring the air into the RM-2 radon detector, the activity of radon in each sample can be measured (Neznal et al., 2004).

Figure 2-9: Instruments for sampling the soli air and in-situ detection of soil gas radon.

2.2.3 Radon in Water

Continuous monitoring of radioactivity in drinking water, mineral and thermal waters are necessary for radiation protection purpose and also to discriminate between ground and surface water that is important because underground water that often travels through rocks might contain radium, which in the process of disintegration releases radon into water (Cosma et al., 2008; CRAERD, 1999). Measuring the concentration of radon activity in groundwater can also help to identify different cracks as well as geothermal sources that lie deep beneath the earth's surface (Durrani et al., 1997).

A simple way to measure radon in water is to use unique accessories that are connected to the typical continuous radon monitors. The setup includes a calibrated radon detector, which indirectly determines radon levels by measuring the concentration of the radon degassed from the water sample. In this study, the ACQUAKIT accessory connected in a closed circuit with an MR1 scintillation cell equipped with an air bubbling tool was utilized to measure the radon activity of water samples sampled on-site in glass bottles (Cardellini, 2017). A specific time delay of 15 minutes was considered after sampling to eliminate the thoron effect.

Figure 2-10: Setup for radon in water measurements using MR1 radon detector and ACQUAKIT accessory (Cardellini, 2017)

2.3 An Outlook of Chapter 3

For the creation of a radon potential map, the first step is to treat the measured and available radon-related data as input variables to a radon categorization model. In the next chapter, the most common radon mapping methods and the data required for that will be expressed. Then the available radon-related data in Sardinia will be reviewed and the possible approaches for producing a radon potential map of Sardinia based on geogenic information will be discussed.

3 RADON MAPPING METHODOLOGIES

Summary

The adverse health effects of radon and thoron pollutants are well-known to the scientific society. To protect the public from the health implications of radon in Europe, the Directive 2013/59/EURATOM requires the member state countries to coordinate measures in the frame of national action plans to identify areas where enhanced radon concentrations might occur. According to this Directive, European countries have regulated protocols to prepare potential radon maps to aim mitigation or prevention of indoor radon ingress in buildings. There are two main approaches to produce radon potential maps: a) based on the spatial distribution of indoor radon concentrations and b) estimation of geogenic radon potential based on geological factors that control indoor radon levels. There are also direct and indirect models to create GRP maps (i.e., susceptibility maps). Nowadays, the second approach has found greater interest since the first approach has significant limitations, which will be mentioned in the following chapter. Moreover, the critical point of a GRP map is that it indicates the potential of the source of indoor radon; therefore, the resulting map is independent of building type and it can be used to estimate radon risk in both residential dwellings and also public buildings and workplaces.

This chapter reviews the most efficient radon mapping methodologies employed by different countries, focusing more on the geogenic potential mapping approach. Finally, the goal of this section is to introduce the most suitable methods to produce a GRP map for Sardinia, having considered the data available in local and European bibliographic references.

3.1 Concept of Geogenic Radon Mapping

Indoor radon concentration can vary even in neighborhood houses as radon activity is a complicated function of both natural and anthropogenic factors (Figure 3-1). Natural or so-called geogenic factors mainly depend on geology, soil properties and hydrology (Bossew et al., 2020). However, anthropogenic factors are generally related to metrological factors, living habits and the construction characteristics of a building, including building materials. It is believed that in most cases, the geogenic variables control the indoor radon levels (Bossew et al., 2013). A map produced based on geogenic information (or the main predictors of indoor radon) quantifies the amount of radon that is delivered to the earth's surface (Bossew et al., 2013). The benefit of such maps is that they can have meaning for very larger areas rather than just inhabited ones, they can be used for future construction sites, targeting measurement points, land planning purposes (Ciotoli et al., 2017; Kropat et al., 2017) and more importantly, these maps are produced based on information that is available for free in most cases. Therefore, the mapping procedure is quicker and cost-effective (Bossew, 2015).

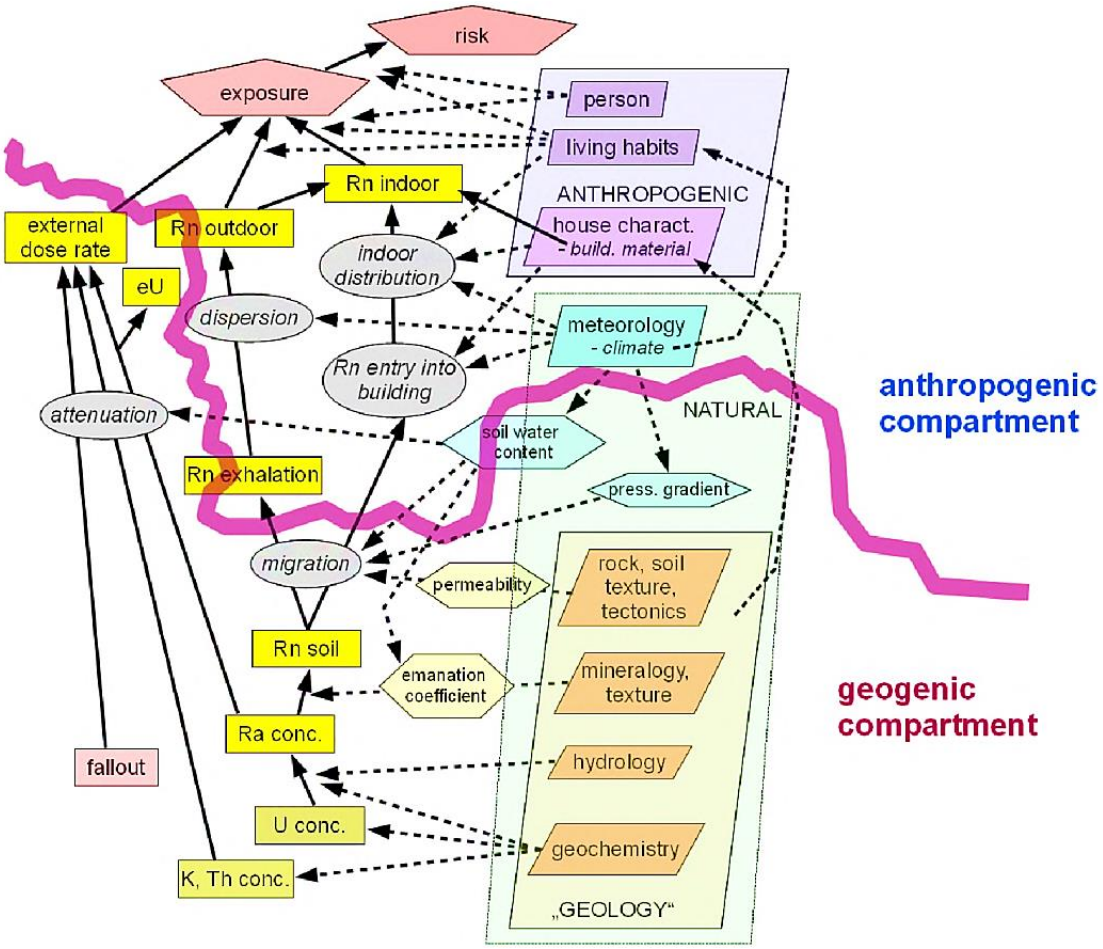

Figure 3-1: Network of natural and anthropogenic radon-related factors which can affect indoor radon levels- Taken from (Bossew et al., 2013)

A further limitation of maps produced based on solely indoor radon (frequently residential radon) is that when it comes to being used for bigger buildings like the public and workplace, it can be conservative and cause legal implications. On the other hand, the main advantage of indoor radon maps is that radon is directly measured at the exposure point (Elío et al., 2017).

There are several ways to define the geogenic radon potential. However, the most common methods are a) a physics-driven approach in which a quantity reflects the indoor radon potential for dwelling with the specific non-geogenic condition (standard house condition). An example of this approach is called "Neznal RP" (Barnet, 2008), which was introduced by Neznal and is based on soil gas radon concentration and also the gas permeability of the Soil. b) The second approach is based on multivariate cross-tabulation between input quantities. In this method, which is easier to work with higher dimensional spaces of input quantities, the scores are assigned to the classes (frequently regarding radon source and radon transport potential) of input quantities (Gruber et al., 2013). The resulting radon potential obtained by the second approach is expressed in categorical-ordinal quantity (e.g., low to high).

Recently, multivariate regression techniques (e.g., ordinary least square regression, logistic regression and geographically weighted regression) are used by researchers to estimate geogenic radon potential (Ciotoli et al., 2017). In this method, accurate predictions of GRP are modeled by using a spatial regression in which a target value (either soil-gas radon or indoor radon activity concentrations) is considered as the response variable and several proxy variables, derived from geological, topographic and geochemical data are set as the explanatory input parameters.

The data required for developing radon potential maps can be obtained directly through field or laboratory tests and also radiometric surveys. Indirect data can also be used where this information is not available (Ielsch et al., 2010). In other words, if measurements of these quantities are not available, one may look for other data, which allows predicting, if only roughly, whether the region may be Rn prone (Bossew, 2015). Accordingly, the geology can serve as the main predictor to predict the mentioned information wherein similar formations occur (Bossew, 2015). An important question remains in this regard that "Can the behavior of the different geological units as investigated in an area be extrapolated to similar geological units in other parts of the country or even to other countries?" (Friedmann, Baumgartner, et al., 2017) For any possible answer to this question, some critical issues should be considered as follows;

- In general, the rock material is very inhomogeneous, even on a small scale of several tens of meters. Therefore a statistical approach is necessary to characterize the parameters that will be used to quantify the radon potential (Barnet, 2008).
- Special care is needed when searching for similar geologies as they are occasionally classified under alternative systems (by different countries), and they do not have identical geological properties. In this case, a harmonized geology map (e.g., the one geology project) can serve as a link to find similar geologies (Gruber et al., 2013).
- From the lithological point of view, even the rocks classified identically may have different compositions of the accessory phases, which may have very different radionuclide contents (i.e., uranium). Rocks can hold uranium enrichments according to the geodynamic, stratigraphic, environmental and geochemical features, climatic conditions and mainly for the sedimentary rocks, the composition of the source areas, which feed the sedimentary basins. Thus, it can be deduced that the different geological evolutions linked to the paleogeography of the geological regions do not allow to completely export the measurements carried out in other geological regions without carrying out the measurements for the evaluation of the contents of the Rn producing elements.

3.2 Proxy Data to be used for Geogenic Radon Mapping

The data (both qualitative and quantitative) that can be used to produce a geogenic radon map can be categorized into two groups, a) parameters related to radon source (Table 3-1) and b) factors that are indicators of radon mobility and transportation from source to ground level (Table 3-2). Additionally, climate conditions and soil physical properties can affect radon diffusion and, consequently, radon exhalation rates from the soil surface (Table 3-3) (Zeng et al., 2019). Considering the contribution of these parameters while mapping geogenic radon potential, would increase the accuracy and the prediction ability of a GRP map.

Table 3-1: Data used for geogenic radon mapping-Indicators of radon source.

	Data Sets	**Description**
Radon source Indicator	Soil Gas Radon	Including in-situ and laboratory measurement data on radon and thoron levels
	Geochemical data	e.g., Soil and stream sediment K_2O, U, Th, Zr, Y, CaO, SiO_2, Al_2O_3, MgO and Fe_2O_3 contents
	Airborne radiometric	i.e., eU, eTh, K and total gamma counts.
	Gamma Spectrometry	Radioelement activity concentrations obtained from in-situ and laboratory tests
	Ambient gamma dose rate	e.g., data obtained from SSNTD LR-115 detectors
	Geology/Lithology/soil type	Sometimes regrouped even based on indoor radon concentrations
	Other	Altitude, Electromagnetic Field, Magnetic Anomaly, etc.

Table 3-2 Data used for geogenic radon mapping-factors that contribute to radon mobility.

	Data Sets	**Description**
Radon mobility Indicator	Porosity and permeability	It can be measured directly or estimated in a categorical form (i.e., low to high).
	Faults	In the form of calculated fault density, applying a buffer around the fault and measuring the distance from the fault.
	Secondary permeability	Karst features, underground mines (shafts, galleries), caves, main mineral and thermal groundwater sources.
	Carrier gas concentrations	e.g., CO_2, CH_4, etc.

Table 3-3. Additional parameters that can affect geogenic radon potential.

	Data Sets	**Description**
parameter	Topsoil physical properties	Moisture, grain size distribution, fine fraction, density, saturation rate, temperature.
	Hydroclimate data	Rainfall rate, wind speed, barometric pressures, outdoor temperature, humidity.

Among the above-mentioned parameters, the soil gas radon and Uranium contents, together with the permeability of the soil, are the most influential variables and have more extensive applications for geogenic radon mapping purposes (Ielsch et al., 2010; Kropat et al., 2017).

3.3 European Experiences of Radon Mapping

In this section, a summary of methodologies and data used for the development of geogenic radon maps in some European countries will be presented. In 2001 (Kemski et al., 2001) presented one of the very first geogenic maps for Germany. They used a distance-weighted interpolation of the site-specific values of radon concentration in soil gas and in situ gas permeability of soils to estimate the geogenic radon potential. In the report of "radon in the Czech environment," Barnet, 2008 described the Czech methodology for the production of radon potential maps based on measurements of radon in soil gas and determination of the soil permeability. As part of the research to prepare the GRP maps of both Germany and Czech, radon characteristics of different geological formations were categorized. In 2009, Scheib et al., published a research work presenting the methodology of using main geological features and geochemical data to produce the GRP map of Scotland based on spatial variation in radon potential to be delineated both within and between geological groupings. In 2010, Ielsch et al. published a research paper in which the first geogenic radon potential map of France was created based on a classification of the geological units according to their uranium content. The effect of additional parameters that control the preferential pathways of radon through the ground and which can increase the radon levels in soils was also considered in that GRP map. Through a research project in Hungary (Szabó et al., 2014), the spatial pattern of soil gas radon concentration, soil permeability, GRP and also the relationship between geological formations and these parameters were studied. As a result, a geogenic radon map was developed. In 2017, as a result of detailed research, a radon potential map was generated for the Oslo area by combining indoor radon measurements with airborne gamma-ray spectrometer survey data (Smethurst et al., 2017a). In the same year, research published by Sainz Fernández et al., 2017 that was expressing the Spanish approach to producing a geogenic map using terrestrial gamma dose rate data together with other criteria regarding the surface of Spain, population, the permeability of rocks, uranium and radium content in soils. Recently, the generated GRP maps are mostly prepared based on Geospatial Regression models such as; ordinary least square regression (e.g., GRP of the municipality of Celleno from a volcanic area of central Italy (Giustini et al., 2019)), logistic regression (e.g., GRP map of Ireland (Elío et al., 2017) and Switzerland (Kropat et al., 2017)) and geographically weighted regression (e.g., the geogenic radon potential map of the Lazio region of Italy (Ciotoli et al., 2017)). The recent techniques provide a more accurate prediction of geogenic radon potentials and can be considered as a

promising tool to create high-resolution GRP maps. It is also possible to simulate the indoor radon concentration using a soil-indoor transfer factor defined for a 'Standard dwelling (i.e., a dwelling with well-defined construction properties) (Giustini et al., 2019)

Furthermore, as part of the European Atlas of Natural Radiation (EANR) project, the Joint Research Centre (JRC) of the European Commission is currently developing a map of the European Geogenic Radon Map (EGRM). In this project, which is still ongoing, the correlation between radon-related data (e.g., soil gas radon measured at German geotypes) is used to extrapolate radon characteristics for similar geologies occurring all over Europe (Szűcs et al., 2018). Figure 3-2 shows the trial version of EGRM.

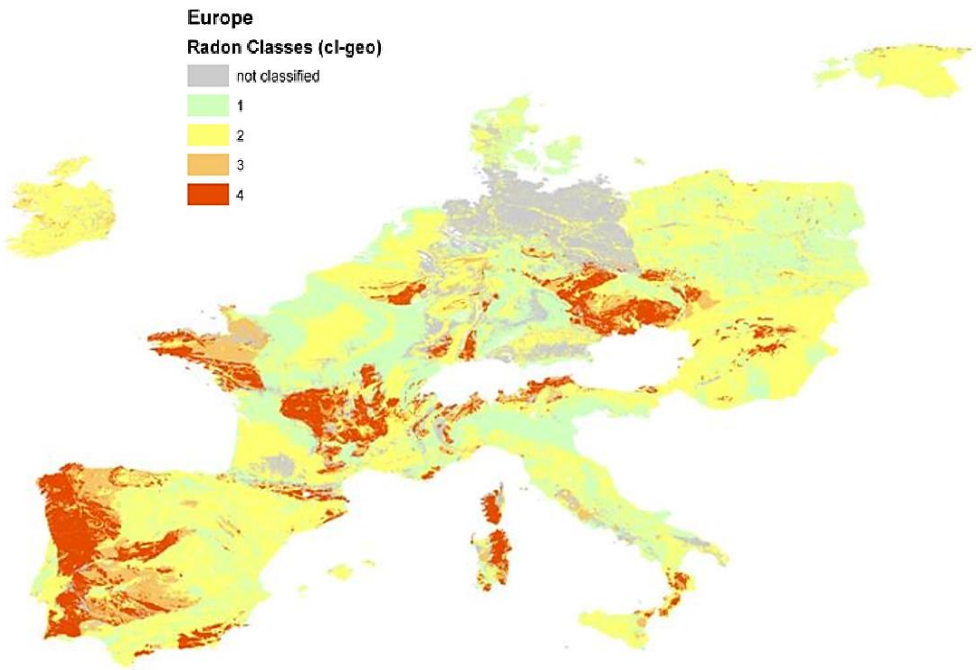

Figure 3-2: Trial version of EGRM generated based on data calibrated using German geotypes- Taken from (Bossew et al., 2013)

3.4 Radon mapping problem in Sardinia

In previous sections, the methodologies and data useful for geogenic radon mapping were introduced. In this section, the availability of data (inclusively local geogenic data) suitable for the generation of a radon potential map independent from active anthropogenic variables, will be evaluated. Among the geogenic actors that can be indicative of radon source, soil gas radon data can be ideally used for the production of geogenic radon maps (Kropat et al., 2017); however, currently, no data are available related to soil radon gas concentration in Sardinia. Literature data on Uranium concentration in the rocks (as one of the most used variables in GRP mapping) of Sardinia are scarce and the few available data is obtained from 279 samples analyzed in the laboratory aimed at determining the concentration of the leading natural radioisotopes

(i.e., U, Ra, Th, K) (ARPAS, 2016). The samples are generally collected from the lithological typologies mainly present in the south of Sardinia. All the samples were placed inside12 geo-lithological classes and mainly within the rocks of the Palaeozoic metamorphic complex (with a total number of 192 samples). Besides, the Granitoid Complex is well represented with a total of 33 samples and there were also 35 samples for the whole soil sediment classes. In the Plio-Pleistocene and Oligo-Miocene volcanic units, 12 samples were taken (ARPAS, 2016). The other available data include the concentration of geochemical elements in stream sediments (De Vivo et al., 1997) and some additional data provided by treating petrographic or environmental studies.

There are also a few data from more recent work focused on the radioactivity of rocks measured by gamma spectrometer methods in the Variscan Basement of North-eastern Sardinia (Xhixha et al., 2016)(Figure 3-3). In general, Igneous rocks of north Sardinia are characterized by eU (equivalent Uranium) concentrations generally higher than the average upper continental crust abundance (2.7 µg g-1). Some Ordovician sedimentary formations containing eU up to 45 µg g-1 and eTh up to 480 µg g-1 associated with heavy minerals occur in the placer deposits in the Sarrabus area (South-East Sardinia).

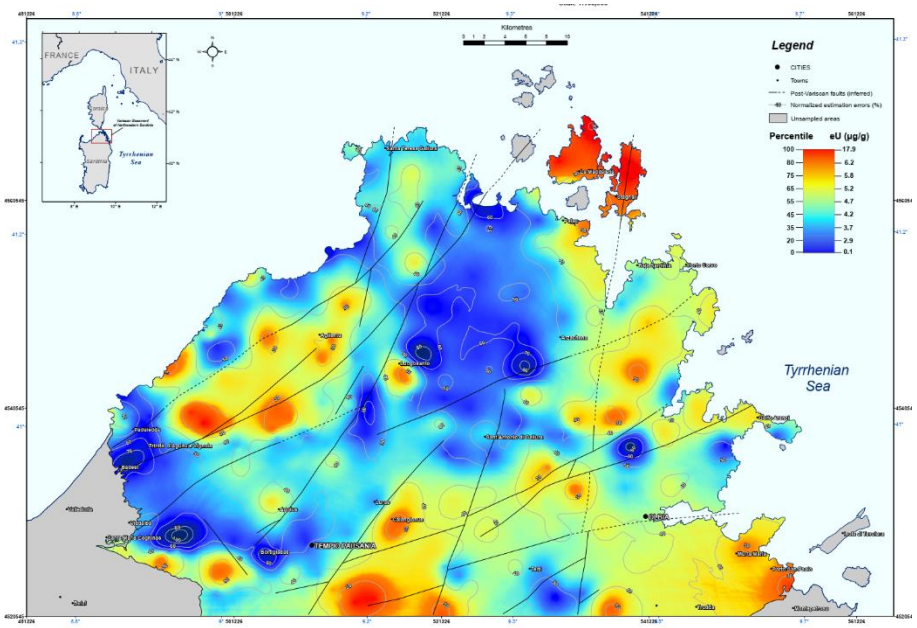

Figure 3-3: The equivalent Uranium (eU) map of Variscan Basement of North-eastern Sardinia- Extrapolated from (Xhixha et al., 2016)

In the case of factors that can affect radon transportation by providing pathways for radon to reach the ground level, the spatial distribution of permeability and fault density (Kropat et al., 2017) can be efficiently used to map the GRP of Sardinia. Data on these two variables together with information on other increasing parameters (e.g., Karst features, underground mines (shafts, galleries), caves, main mineral and thermal groundwater

sources) are available at the local database of Sardinia called "Sardegna Geoportale"- http://webgis2.regione.sardegna.it/download/

Considering the nature of the data available on Sardinian literature, a draft of a geogenic radon potential map can be prepared based on the definition of a multivariate cross-tabulation matrix of radon source and radon mobility classes. To categorize these classes, a statistical approach (mean values) could be considered to define the GRP classes for different polygons. The polygons can contain either geological boundaries or soil type variations. Both base maps (Figure 3-4 and Figure 3-5) are available at the 1:250,000 scale in bibliographic sources.

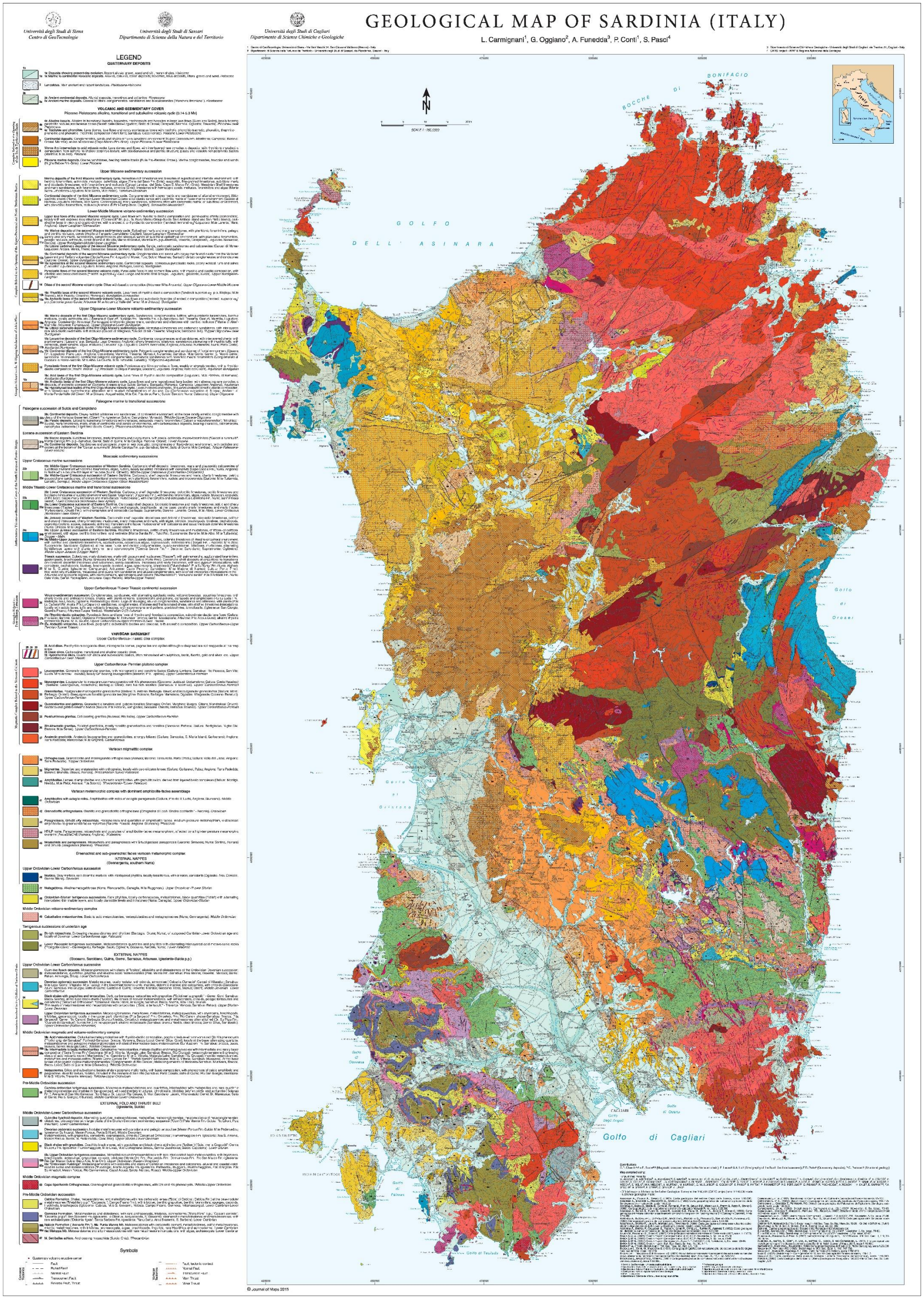

Figure 3-4: The geological map of Sardinia at 1:250,000 scale- (Carmignani et al., 2016)

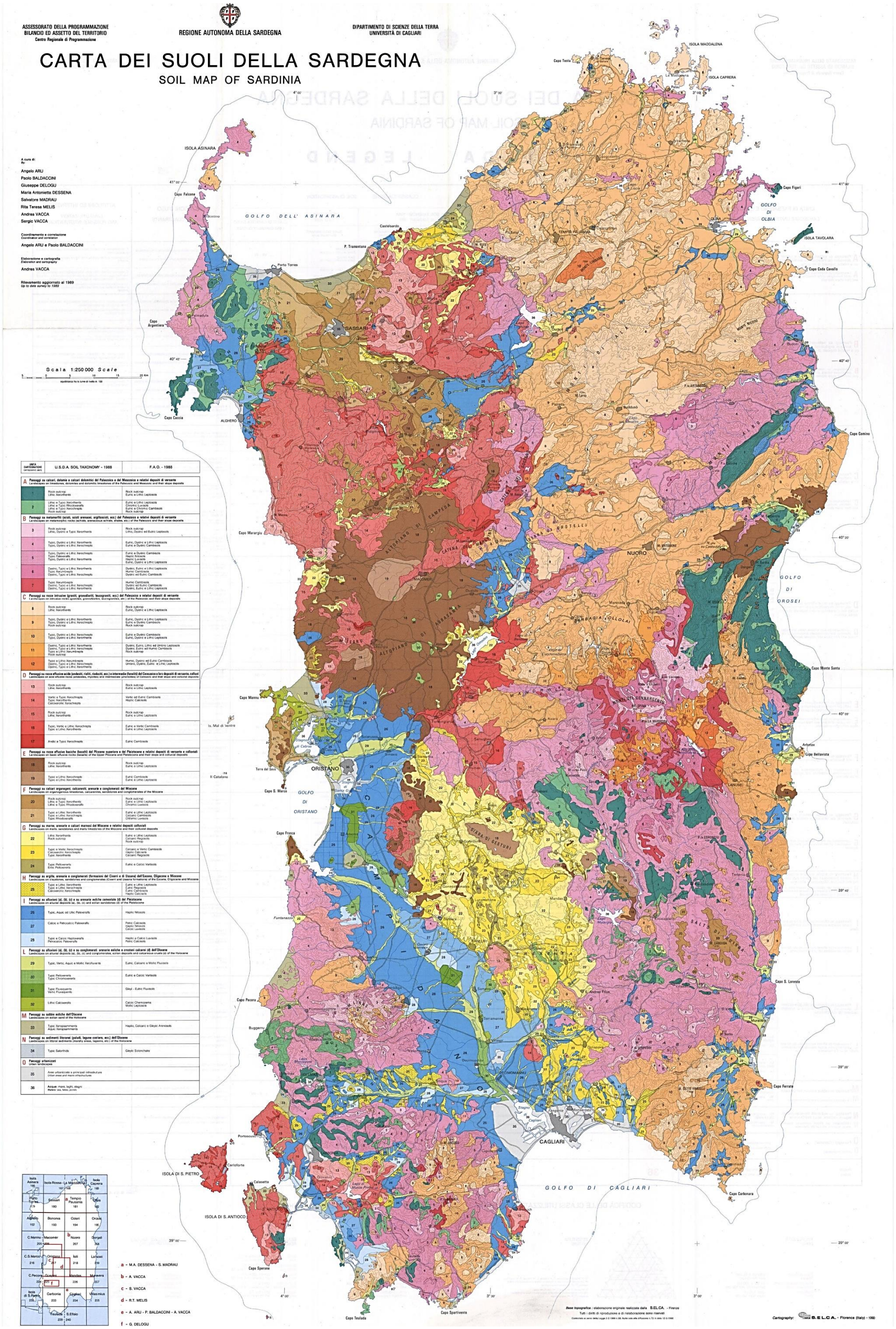

Figure 3-5: The soil map of Sardinia at 1:250,000 scale- (Aru et al., 1990)

An outlook of Chapter 4

As discussed in this chapter, limited sets of geogenic information are available for the Sardinian region. In the next chapter, through a detailed investigation, the suitability of similar datasets to be used for the characterization of radon (and thoron) behaviors of different rock and soil types will be investigated. This investigation has been carried out in an area where sufficient geogenic data was available. The study area was located in south-eastern Ireland, where complex geology and soil type variations were observed. The occurrence of different geologies and soil types allowed us to distinguish between the release potential of different geological units and soil types. This investigation was in cooperation with the School of Natural Science, Trinity College Dublin, and the Geological Survey of Ireland.

The results of the next chapter can help with GRP mapping in Sardinia by leading to understanding firstly: which geogenic data can better represent radon release potential / indoor radon levels? And secondly, which polygon boundary (geo units or soil variation) would better classify radon behaviors of different units?

4 INVESTIGATION OF CORRELATION BETWEEN INDOOR RADON AND GEOGENIC RADON SURROGATES CLASSIFIED BASED ON GEOLOGICAL BOUNDARIES / SOIL-TYPE VARIATIONS

Summary

This chapter includes a detailed investigation to study the natural radioactivity levels and radon/thoron exhalation rates of an area in south-eastern Ireland where it is supposed to be a radon priority area because of its background geopedological conditions. To aim this, firstly, available data on indoor radon, airborne radiometric and stream sediment geochemistry were collected and a set of soil samples were taken from the study area. The collected samples were introduced to laboratory testing of radon and thoron exhalation rates. While sampling, the ambient dose rates were also measured at 1m above the ground level using a handheld radio dosimeter. Collected and measured data were classified based on geological combinations and soil type variations. The main goals of this chapter include: a) to find out which input data is more correlated with radon and thoron release potentials, b) to understand which polygon (geology or soil type) better classifies radon/thoron potentials and c) to develop radon and thoron release potential maps of the area under exam.

4.1 Geological Setting and Soils of the Study Area

The study area is located about 130 km SW of Dublin, in south-eastern Ireland; it can be found in County Kilkenny on the border with County Carlow. It includes the towns of Graignamanagh, Thomastown and Muine bheag.

In environmental radioactivity studies, both geology and soils play an essential role in determining the characteristics of a region. The underlying geology has a significant influence on landform and the bedrock provides the parent material from which soils are created. The nature of the rock helps to determine the nature and chemistry of the soil formed (Pettit, 1996; Missimer et al., 2019).

The geological setting of the study area is underlain by extremely various strata, principally of Lower Palaeozoic, Devonian and Carboniferous age, with extensive and spatially variable, overlying subsoil deposits. According to the GSI (https://www.gsi.ie/en-ie/data-and-maps/Pages/Bedrock.aspx) and the 1:100,000 bedrock geology map (Figure 4-1), the study area comprises 12 geological formations. The Lower Palaeozoic strata outcrop at the eastern and south-eastern part of the area in which the primary deposits comprise metasedimentary (phyllites and schists of the Maulin Formation) and volcanic rocks (Caledonian Leinster Granite). Devonian sandstones and conglomerates are overlying an offshoot of the Caledonian Leinster Granite, which intrudes Ordovician sediments. The Lower Carboniferous sandstones and shales comprise a series of sandstones, siltstones and mudstones in the southwestern part of the study area. The Sub-Waulsortian Limestones, namely the Ballymartin and Ballysteen Formations, conformably overlie the Lower Carboniferous Sandstones and Shales. These two formations mainly comprise bioclastic limestones (Tedd et al., 2011).

Soils in any area are the result of the interaction of various factors, such as parent material, climate, vegetation and human action. The soil classification map (Figure 4-2) (http://gis.teagasc.ie/soils/map.php) identifies ten soil associations within the study area. The parent material of soils in the study area consists of a mantle of glacial drift with a considerable variation in geological composition, physical constitution and thickness. The dominant soil type is Grey Brown Podzolic, which is deep and has a medium-heavy texture. They are well-drained soils derived from calcareous drift composed mainly of limestone with some coal shales and sandstone. Lighter, shallower soils are found on the

shores of the rivers located within the area (e.g., Barrow river), derived from alluvial deposits, i.e., coarse-textured gravels and sands (CAAS, 2003).

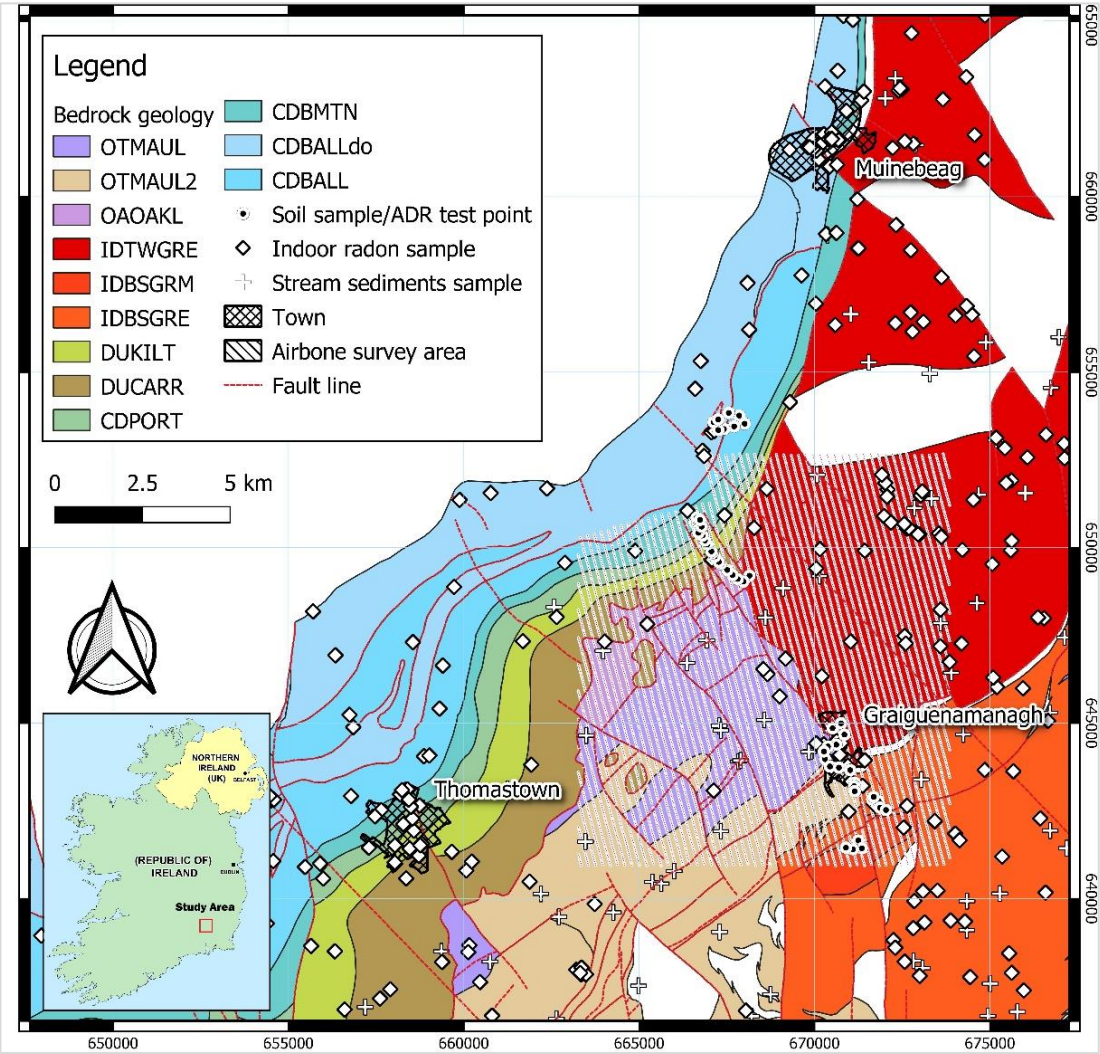

Figure 4-1: Bedrock geology (at 1:100,000 scale- Irish Transverse Mercator (ITM)) of the study area with location of the sampling and airborne survey sites; OTMAUL (dark blue-grey slate, phyllite & schist), OTMAUL2 (Dark grey semi-pelitic, psammitic schist), OAOAKL (Green, red-purple, buff slate, siltstone), IDTWGRE (Pale, fine to coarse-grained granite- Tullow type Equigranular Granite), IDBSGRM (Granite with microcline phenocryst), IDBSGRE (Pale, fine to coarse-grained granite- Blackstairs type, Equigranular Granite) DUKILT (Yellow & red sandstone & green mudstones), DUCARR (Red, brown conglomerate & sandstone), CDPORT (Sandstone, shale & thin limestone), CDBMTN (Limestone & dark-grey calcareous shale), CDBALLdo (Dolomitized dark-grey muddy limestone), CDBALL (Dark muddy limestone, shale). Base map obtained from https://www.gsi.ie/en-ie/data-and-maps/Pages/Bedrock.aspx

Previous studies have shown that some soils and rocks (e.g., acid intrusive rocks like granites, shales, psammites, semipelites and meta-limestones) may have higher levels of naturally occurring radon (Appleton et al., 2008; Drolet et al., 2013). As it was discussed in previous paragraphs, outcrops of some of these geologies can be found in the study

area. Moreover, traces of autunite (Ca $(UO_2)2(PO_4)2·10–12H_2O$), an uranium-bearing mineral has been observed during geological explorations in Ordovician sediments within the area. According to these, it was necessary to evaluate natural radioactivity levels and radon release potentials of the area under the exam.

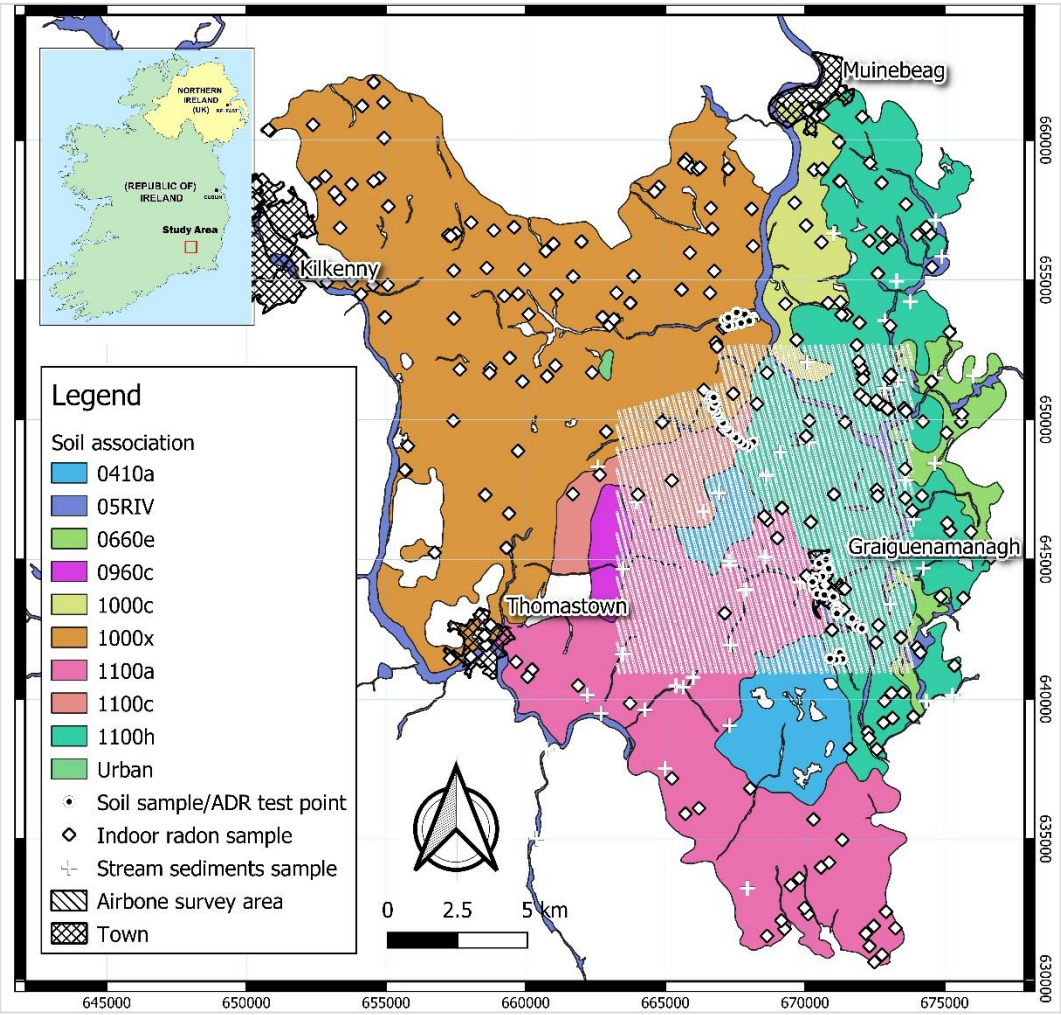

Figure 4-2: Soils map (at 1:250,000 scale- Irish Transverse Mercator (ITM)) of the study area with location of the sampling and airborne survey sites; 0410a (Peat over lithoskeletal acid igneous rock), 05RIV (River alluvium), 0660e (Coarse loamy drift with igneous and metamorphic stones), 0960c (Fine loamy over mudstone, shale or slate bedrock), 1000c (Fine loamy drift with limestones), 1000x (Fine loamy drift with limestones and substrate of siliceous stones), 1100a (Fine loamy drift with siliceous stones), 1100c (Coarse loamy drift with siliceous stones), 1100h (Coarse loamy drift with igneous and metamorphic stones). Base map obtained from http://gis.teagasc.ie/soils/map.php

4.2 Materials and Methods

In this section to characterize different rock and soil types from the radon point of view, at the first step, the vectorized version of bedrock geology map and soil associations were utilized in GIS software and the statistics of radon-related quantities like indoor radon

concentration, radiometric data, soil geochemistry, ambient dose rates and radon exhalation rate were calculated for different bedrock geologies and soil types. In the second step, statistical relationships were evaluated using Pearson's correlation matrix.

4.2.1 Indoor Radon Data

In the process of mapping indoor radon risk, an important step is to define geological units well-correlated with indoor radon concentration (Tondeur et al., 2014). As a part of the Irish national survey of indoor radon, the EPA, Environmental Protection Agency of Ireland has collected indoor radon measurement data measured over a minimum three month measurement period using passive alpha track detectors (CR-39) (Burke et al., 2010; Hodgson et al., 2014). A total number of 2886 geo-referenced indoor radon data was available for the study area. Elevated levels of indoor radon (i.e., higher than the Irish national reference level, 200 Bq m^{-3}) were observed in the study area (Elío et al., 2017). The geometric mean values of indoor concentrations (GM) for bedrock geologies and soil types are reported in Table 4-1and Table 4-2.

4.2.2 Airborne Radiometric Survey

According to the Tellus project, the geological survey of Ireland is in charge of two types of surveying a) airborne geophysical survey and b) ground-based geochemical surveying of soil, stream water and stream sediment. The airborne radiometric survey is carried out by using a low-flying aircraft (flying at 60 m in rural areas and 240 m in urban areas). The data are recorded by a 256-channel gamma spectrometer (Exploranium GR820) covering 0.3–3 MeV(Hodgson and Young, 2016). They are integrated over flying distances of about 50m. Potassium (^{40}K), equivalent uranium (eU, estimated from ^{214}Bi) and equivalent thorium (eTh, estimated from ^{208}Tl) are measured as a result of the surveys and finally, the recorded values were subjected to the corrections (cosmic radiation, height attenuation, etc.). Then the corrected values which had the unit of count per seconds (cps) were converted to part per million-ppm (^{238}U and ^{232}Th), percent (^{40}K) and nano Gray per hour, nGy h^{-1} (total count) using the standard conversion rate, suggested by Geosoft® (Barberes et al., 2015). Some countries have employed radiometric data for producing geogenic radon potential maps (Appleton et al., 2008). As noticed before, a statistical approach was also employed for studying the radon release behavior of different rocks and soils. Table 4-1 and Table 4-2 show the mean values of radioelement concentrations and air absorbed dose rates (ADR_{air}) for different geological combinations

and soil types, respectively. The classifications were based on about 9400 airborne survey data points.

4.2.3 Geochemistry of Stream Sediment Samples

Stream sediment and topsoil geochemistry can also be useful for radon mapping purposes; however, topsoil geochemical data is preferable as this type of data can better represent radon characteristics of the overlaying environment (Ferreira et al., 2018). Stream sediment data, grouped by bedrock superficial geology classifications, was investigated to estimate radon potential in Scotland (Scheib et al., 2009) and it was found that indoor radon correlates most strongly with U, followed by Rb, K, Y, La and Zr in stream sediments. According to the Tellus project, the GSI has collected soil and stream samples at a density of approximately one sample per 4 km^2. Through multi-element laboratory analyses using X-ray fluorescence spectroscopy (XRF), geochemical data were provided for 55 elements (Young et al., 2016). Presently, there is no available data on topsoil geochemistry for the study area; however, in total, about 500 point data on stream sediment geochemistry is available for different bedrock geologies of the area under examination. As shown in Table 4-3 and Table 4-4, the average soil K_2O, U, Th, Zr, Y, CaO, SiO_2, Al_2O_3, MgO and Fe_2O_3 were calculated for each geological formation and soil category.

4.2.4 Ambient Dose Rate (ADR) Mapping and $^{222}Rn/^{220}Rn$ Exhalation Rates

In-situ soil gas radon measurements performed in various lithological types can give the first radon characterization of an area. This approach is considered to be the most appropriate to estimate the geogenic radon potential (Barnet, 2008; Kropat et al., 2017). However, laboratory testing of exhalation rate is sometimes preferred since in-situ determinations of radon fluxes from the ground are long and affected by large uncertainties, due to changing physical conditions such as soil moisture, temperature and pressure gradients (Lucchetti et al., 2019).

Integration of laboratory radon and thoron exhalation data with ground gamma radiation mapping has been successfully utilized to study the source of natural radiation and characterize radon release potential of a volcanic area near Rome (Lucchetti et al., 2019). A similar approach has been adopted in this section to estimate the radon release potential of different rock and soil types, whereby 45 soil samples were taken from 50 cm below

the surface using an auger sampler. The ambient gamma dose rate (μSv h-1) at 1m above the ground level was also measured at the same sampling point by using a handheld radio dosimeter. The recorded values were georeferenced and introduced to GIS software. The samples were then oven-dried and sieved to minus 2 mm. About 500 gr of each sample was introduced to a 7- liter sealed accumulation chamber connected to a RAD7 radon monitor (Durridge Company Inc.) (Figure 4-3). A small fan was also mounted inside the chamber to increase the air circulation rate. ^{222}Rn and ^{220}Rn activities of each sample were measured at 1-hour cycles for about 36 hours. The measurement time depended on the alignment of ^{222}Rn data points and the time required to reach the equilibrium of ^{220}Rn concentration.

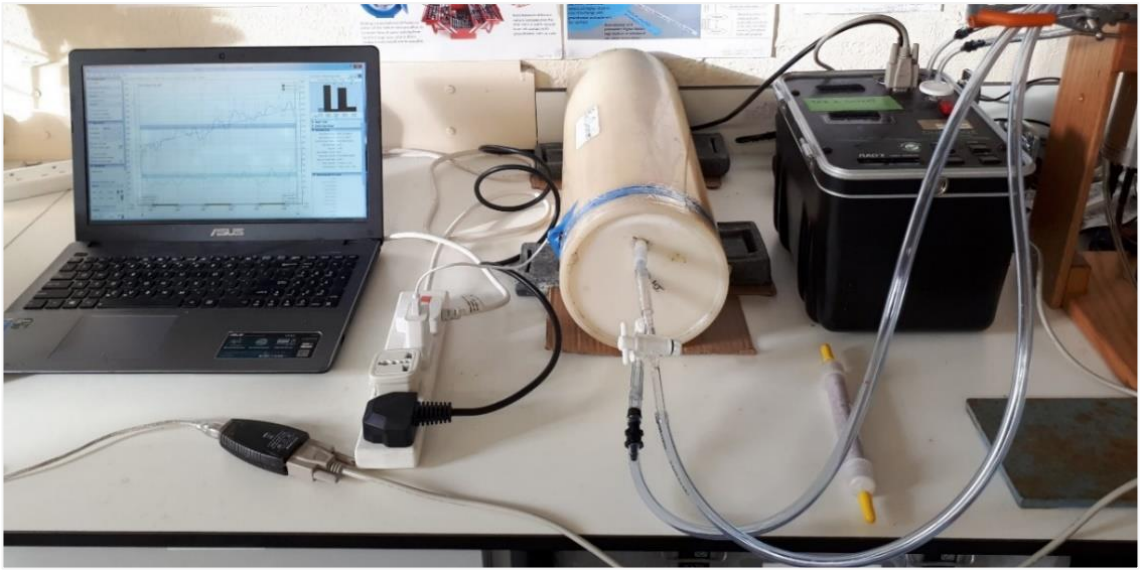

Figure 4-3: Experimental set up for ^{222}Rn/^{220}Rn exhalation rates

Table 4-1: Summary of indoor radon, airborne radiometric, gamma dose and radon exhalation rates statistics for bedrock geologies. Numbers specified with * represent only the value of a single measurement. Please refer to Figure 4-1 for the description of bedrock codes.

Geology	**Indoor radon**		**Airborne radiometric data**					**Ambient dose and radon exhalation rates**			
Bedrock code	Number	GM_{Rn} (Bq m^{-3})	Number	K_{air} (%)	eTh (mg kg^{-1})	eU (mg kg^{-1})	ADR_{air} (nGy h^{-1})	Number	ADR (μSv h^{-1})	Ex ^{222}Rn (Bq m^{-2} h^{-1})	Ex ^{220}Rn (Bq m^{-2} h^{-1})
CDBALL	1348	50.32	127	2.33	13.47	5.16	108.73	3	0.14	0.91	1520.94
CDBALLdo	132	72.06	48	2.26	13.74	4.63	106.38	3	0.17	1.12	1459.66
CDBMTN	118	56.61	293	2.55	13.53	5.04	112.29	3	0.16	1.18	1907.97
CDPORT	27	69.64	149	3.38	15.18	4.88	130.35	3	0.22	0.91	1796.68
DUCARR	101	69.44	471	4.04	12.10	4.42	133.39	4	0.19	0.91	2037.72
DUKILT	158	75.69	214	3.52	13.74	4.56	128.32	3	0.17	1.02	2016.31
IDBSGRE	46	188.07	765	4.87	12.92	5.31	153.97	6	0.20	0.94	745.68
IDBSGRM	2	366.48	177	5.15	18.25	6.17	178.43	3	0.21	1.52	1430.27
IDTWGRE	312	116.89	3220	4.83	11.43	5.10	147.37	4	0.18	1.10	1313.37
OAOAKL	226	118.84	468	4.60	16.09	5.79	160.33	3	0.22	1.29	2187.31
OTMAUL	387	71.45	2302	4.24	16.40	4.85	148.54	4	0.18	0.61	1301.50
OTMAUL2	29	120.49	1140	4.07	15.74	4.82	143.59	6	0.18	0.82	789.21

Table 4-2: Summary of indoor radon, airborne radiometric, gamma dose and radon exhalation rates statistics for soil types. Numbers with specified * represent only the value of a single measurement. Please refer to Figure 4-2 for the description of soil associations.

Soil type	**Indoor radon**		**Airborne radiometric data**					**Ambient dose and radon exhalation rates**			
Association	Number	GMRn (Bq m^{-3})	Number	K_{air} (%)	eTh (mg kg^{-1})	eU (mg kg^{-1})	ADR_{air} (nGy h^{-1})	Number	ADR (μSv h^{-1})	E_{222Rn} (Bq m^{-2} h^{-1})	E_{220Rn} (Bq m^{-2} h^{-1})
0410a	1*	729.00	719	4.43	16.22	4.73	152.05	0	-	-	-
05RVI	0	-	400	3.67	10.68	4.89	125.74	5	0.19	0.75	895.54
0660e	5	296.40	141	5.48	12.99	5.80	165.41	0	-	-	-
0960c	4	131.28	120	3.81	11.76	3.90	126.16	0	-	-	-
1000c	13	104.86	129	4.63	11.75	4.46	140.02	0	-	-	-
1000x	95	99.39	691	2.77	14.03	5.02	117.23	15	0.17	1.03	1740.31
1100a	36	193.85	2673	4.13	15.89	4.85	145.22	3	0.18	0.71	1648.11
1100c	4	104.86	892	4.42	14.94	5.20	151.12	6	0.21	1.07	2138.02
1100h	76	304.32	3636	4.92	12.28	5.21	151.93	13	0.20	1.15	1108.96
Urban	16	318.88	89	3.90	11.19	4.37	126.43	3	0.17	0.79	706.34

Table 4-3: Summary of soil geochemistry for grouped bedrock geologies. Numbers specified with * represent only the value of a single measurement. Please refer to Figure 4-1 for the description of bedrock codes.

Geology	Stream Sediment Geochemical Data										
Bedrock	Number	MgO	Al_2O_3	SiO_2	K_2O	CaO	Fe_2O_3	Y	Zr	Th	U
		(%)						(mg kg^{-1})			
CDBALL	53	1.55	9.26	46.55	1.44	4.90	4.81	21.21	303.16	6.73	3.54
CDBALLdo	2	1.60	10.30	59.20	1.90	2.65	4.33	20.45	815.00	8.45	2.60
CDBMTN	5	1.22	10.52	59.10	2.29	1.61	4.01	22.84	489.86	8.40	2.74
CDPORT	1*	1.40	16.30	60.60	4.14	0.42	5.03	36.40	339.40	10.20	4.20
DUCARR	11	1.22	12.95	60.05	3.66	0.82	4.83	32.06	488.30	9.65	3.85
DUKILT	6	1.25	13.45	59.90	3.16	0.90	5.27	31.43	484.85	9.50	3.15
IDBSGRE	35	0.70	14.41	55.64	3.71	0.77	2.69	21.45	212.45	17.37	40.10
IDBSGRM	0	-	-	-	-	-	-	-	-	-	-
IDTWGRE	117	1.15	10.86	54.52	2.49	4.23	2.77	22.99	352.31	16.01	11.96
OAOAKL	104	1.51	17.91	57.84	2.89	0.45	6.73	30.66	266.38	10.57	2.89
OTMAUL	152	1.54	16.36	53.27	2.87	0.78	6.64	32.98	284.32	10.79	3.07
OTMAUL2	23	1.37	15.18	56.07	3.25	0.57	5.73	32.00	327.55	9.52	4.28

Table 4-4: Summary of soil geochemistry for grouped soil associations. Numbers with specified * represent only the value of a single measurement. Please refer to Figure 4-2 for the description of soil associations.

Soil type	Stream Sediment Geochemical Data										
Association	Number	MgO	Al_2O_3	SiO_2	K_2O	CaO	Fe_2O_3	Y	Zr	Th	U
		(%)						(mg kg^{-1})			
0410a	1*	1.70	18.60	59.30	3.37	0.32	5.95	38.20	255.00	8.80	2.80
05RVI	29	1.40	14.44	54.68	3.03	2.08	4.77	29.24	276.73	11.55	8.26
0660e	2	0.70	13.90	55.30	3.73	1.25	2.23	26.10	292.15	33.40	39.05
0960c	0	-	-	-	-	-	-	-	-	-	-
1000c	3	2.20	8.67	55.17	2.22	5.17	1.63	18.37	386.90	8.53	5.77
1000x	1*	1.40	16.30	60.60	4.14	0.42	5.03	36.40	339.40	10.20	4.20
1100a	10	1.81	15.61	54.66	3.01	1.44	5.51	34.08	265.63	8.31	3.32
1100c	1*	1.90	21.20	56.00	3.77	0.18	6.72	39.80	204.80	8.60	3.40
1100h	8	1.35	13.55	52.94	2.99	2.02	3.91	26.49	266.73	12.69	14.91
Urban	0	-	-	-	-	-	-	-	-	-	-

Considering the Equation 4-1 and Equation 4-2 (Lucchetti et al., 2019) ^{222}Rn ($E^{222}Rn$, Bq m^{-2} h^{-1}) and ^{220}Rn ($E_{220}Rn$, Bq $m^{-2}h^{-1}$) exhalation rates were calculated by extrapolating the slope of the growth curve (m) (Bq $m^{-3}h^{-1}$) and the equilibrium ^{220}Rn concentration (C_m) (Bq m^{-3}), respectively. Figure 4-4 shows an example of $^{222}Rn/^{220}Rn$ concentrations as a function of time and the derived exhalation rates.

Equation 4-1: $$E_{^{222}Rn} = \frac{(m + \lambda_{222}.C_0).V}{S}$$

Equation 4-2: $$E_{^{220}Rn} = \frac{\lambda_{220}.V_0}{S} \frac{C_m}{e^{-\lambda_{220}.(V_1/Q)}}$$

where λ_{222} and λ_{220} are ^{222}Rn and ^{220}Rn decay constants (h^{-1}), C_0 is the initial radon concentration (Bq m^{-3}), V is the free total volume of the analytical system (m^3), S is the surface of the sample, V_0 and V_1 (m^{-3}) are the free volume of the accumulation chamber and the volume between the outflow of the accumulation chamber and the inflow of the radon monitor, respectively. Q (39 L h^{-1}) is the flow rate in the system. The mean values of the mapped dose rates and calculated $^{222}Rn/^{220}Rn$ exhalation rates for geological bedrocks and soils of the study are reported in Table 4-1 and Table 4-2, respectively.

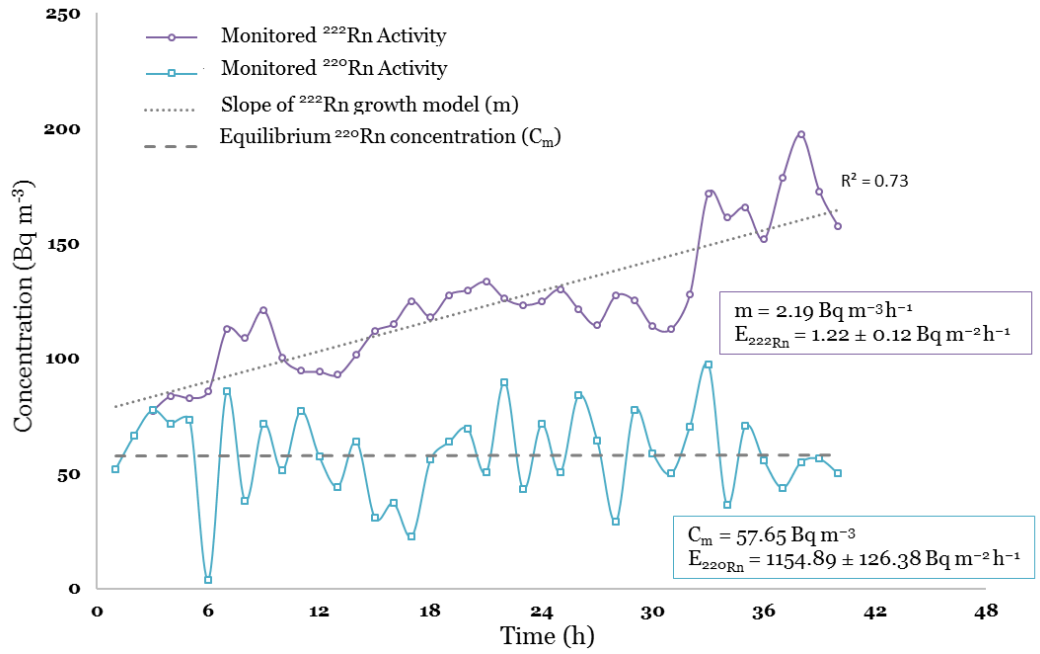

Figure 4-4: $^{222}Rn/^{220}Rn$ concentrations as a function of time inside the accumulation chamber and calculated radon and thoron exhalation rates from the surface of a soil sample.

4.3 Results and discussion

4.3.1 Grouping Based on Geological Bedrock contacts

As it can be understood from Table 4-1, the highest values of geometric mean indoor radon (366.48 Bq m^{-3}) and mean values of air potassium (5.15%), equivalent uranium and thorium (6.17 and 18.47 mg kg^{-1}, respectively), annual effective dose rates (178.43 nGy h-1) and radon exhalation rates (1.52 Bq m^{-2} h^{-1}) were found in granites with microcline phenocryst (geocode: IDBSGRM). Granites are typically known as the geo units associated with higher radionuclide concentration (Örgün et al., 2005), however, there are significant variations of natural radioactivity levels in different granite types. The variations are mainly due to the different levels of accessory minerals such as orthite or

allanite, monazite, zircon, appetite and sphene concentrated in granitic rocks (Valković, 2000). Other affecting parameters include hydrogeological processes causing U solution and precipitation, geological phenomena such as faults, hydrothermal alterations and weathering conditions (Tzortzis & Tsertos, 2004). In this study, two other types of granite (i.e., pale and fine to coarse-grained equigranular granites of Tullow and Blackstairs type (geocode: IDBSGRE and IDTWGRE, respectively)) were studied. Although these two units have lower levels of radon-related values (i.e. indoor radon, eU and U) compared to granites with microcline phenocryst, on average, their radon exhalation rates were higher than other lithological types. Moreover, the green red-purple buff slates and siltstones of Oakland's formation show the second highest values among most of the radon-related values. This can be explained by the fact that some types of sedimentary rocks (e.g., phosphates, reworked igneous, or magmatic clastic rocks (Drolet et al., 2013)) may contain organic matter and silt-clay size mineral grains which have large openings in their crystal structures. Therefore the big positive ions (cations) of potassium, uranium and thorium can fit well into them (Hurley, 2009). The mean values of airborne radioelement concentrations are higher than the world averages of 45 Bq kg^{-1} (11.08 mg kg^{-1}) for ^{232}Th, 33 Bq kg^{-1} (2.67 mg kg^{-1}) for ^{238}U and 412 Bq kg^{-1} (1.32 %) for ^{40}K (Erdi-Krausz, Matolin, Minty, & Nicolet, 2003; UNSCEAR, 2008). The mean value of calculated air absorbed dose rates is about 2~3 times the reported population-weighted mean value of 58 nGy h^{-1} for the regular area (UNSCEAR, 2008).

Table 4-3 shows the mean values stream sediment data, grouped by bedrock superficial geology, which was investigated to find their relation to radon-related variables. Among the elements analyzed, U and Th are considered the most important ones as they are mostly used in studies related to the assessment of radon potential. As it was anticipated, the highest values correspond to the pale and fine to coarse-grained equigranular granites of the Tullow and Blackstairs type. This again strongly indicates the influence of a granitic environment on radionuclide concentrations. There was no available stream sediment data for the granites with microcline phenocryst. A simple comparison between U and Th from stream sediments values with eU and eTh shows that for most of the lithological types, the values obtained for stream sediments are lower. This can be due to the mobilization of radionuclide through the water. The deduction is more evident in U than Th as Thorium is more stable and will not readily dissolve in a solution and

transported by water during the weathering process; however, U forms soluble salts, which can be transported in the river water (Schön, 2015). On average K_2O values are less than K_{air} activity concentration. This can be explained by the adsorption of the ^{40}K in water (Appleton et al., 2008).

Table 4-5 expresses correlations of indoor radon, airborne radiometric, geochemical data and gamma dose and radon exhalation rates for geological combinations. It indicates that the indoor radon is most strongly related to eU, U. There is also a good correlation between radon exhalation rates, indoor radon levels and eU. There is also a close correlation between the broad distributions on the radiometric and the air absorbed dose rates. This correlation is more robust for K_{air}. The average ambient dose rates recorded by handheld radiometer are also in a good correlation with air absorbed dose rates. This means that handheld radiometers can give a fast evaluation of gamma dose rate levels in an area. However, the values obtained by handheld radiometer are higher. This can be justified by the fact that no corrections were applied to the recorded gamma values by the handheld radiometer and therefore, background and cosmic radiation may probably have influenced the measured ADR values.

In the case of stream sediment geochemical data, positive correlations were found between U and Th and also between K_2O, Al_2O_3 and Y. The negative functional correlations are obtained for U and Th with MgO and also K_2O with CaO. It is worth noting that there is almost no correlation between thoron exhalation rates, Th, eTh, using the categorization of data based on geological combinations Grouping Based on Soil Type Variations.

As can be seen in Table 4-2, it was not possible to efficiently differentiate between radon-related parameters (i.e., GMRn, eU, E222Rn and U) of different soil types. Table 4-6 expresses Pearson's correlation matrix of indoor radon, airborne radiometric, geochemical data, gamma dose and radon exhalation rates categorized based on soil variations. Comparing the correlation coefficients represented in this table and also Table 4-5, it can be understood that although there are functional correlations between radon exhalation rate with eU and also eU with U in the soil classification system, the bedrock geology borders are better classifiers comparing to the soil variations.

On the other hand, using the grouping system based on soil variations, significant positive correlations were found between thoron exhalation rates and eTh and also Th with eTh.

Higher correlation coefficients for radon in geological grouping systems and the presence of good correlation for thoron related values in soil classification system can be explained by differences in ^{222}Rn and ^{220}Rn's half-lives. In other words, radon has a longer half-life and, therefore, can go through longer distances or even originate from deeper sources; in this case, lithology is the better representative of radon behavior. However, as thoron decays quickly, the measured thoron in the ground level should originate from shallow soil; therefore, in this case, soil type variation better classifies thoron behaviors. Similar to the classification system based on geological combinations, positive correlation coefficients between U and Th and also K_2O with Al_2O_3 and Y were also found in the soil type grouping method.

4.3.2 Estimation of Annual Effective Dose Rate and Radon Release Potential based on Airborne Radiometric

In previous sections, good correlations between mean eU and radon exhalation rates (based geological combination system) and also eTh with thoron exhalation rates (based on soil type grouping) were achieved. Moreover, as mentioned before, the airborne radiometric data is available in a high resolution (50m × 50m) for most of the territory of Ireland. In this section, the precision and workability of radiometric data in the estimation of radon/thoron exhalation rates at the sampling points have been evaluated. To aim this, at the first step, the linear fit between the estimated radioelement activity concentrations (i.e., eU and eTh) and radon/thoron exhalation rates were obtained. As can be seen in Figure 4-5 significant correlation between the estimated eU and radon exhalation rate (R^2 = 0.55) and also the estimated eTh and thoron exhalation rates (R^2 = 0.55) were found.

In the second step, based on the obtained relationships (Equation 4-3 and Equation 4-4), the radon and thoron exhalation rates were calculated for the area of airborne surveys. Figure 4-6 and Figure 4-7 show the individual distributions of radon and thoron exhalation rates, respectively.

Equation 4-3: $$E_{^{222}Rn} = 0.17 \cdot eU + 0.20$$

Equation 4-4: $$E_{^{220}Rn} = 162.63 \cdot eTh - 679.60$$

Table 4-5: Pearson's correlation matrix of indoor radon, airborne radiometric, geochemical data, gamma dose and radon exhalation rates categorized based on geological combinations.

	GM_{Rn}	E_{222Rn}	eU	U	E_{220Rn}	eTh	Th	K_{air}	K_2O	MgO	Al_2O_3	SiO_2	CaO	Fe_2O_3	Y	Zr	ADR_{air}	ADR
GM_{Rn}	1.00																	
E_{222Rn}	**0.62**	1.00																
eU	**0.77**	**0.69**	1.00															
U	**0.84**	-0.05	0.32	1.00														
E_{220Rn}	-0.32	0.31	-0.08	-0.59	1.00													
eTh	0.53	0.25	0.56	-0.35	-0.05	1.00												
Th	**0.83**	0.01	0.32	**0.82**	-0.48	-0.33	1.00											
K_{air}	**0.67**	0.19	0.50	0.50	-0.28	0.27	**0.79**	1.00										
K_2O	0.40	-0.27	-0.14	0.32	-0.03	0.15	0.40	0.58	1.00									
MgO	**-0.69**	-0.05	-0.09	**-0.85**	0.34	0.54	**-0.76**	-0.51	-0.47	1.00								
Al_2O_3	0.36	-0.22	0.28	0.06	0.03	**0.72**	0.21	**0.61**	**0.70**	0.02	1.00							
SiO_2	0.00	0.34	-0.33	-0.12	0.42	0.01	0.01	0.05	0.56	-0.16	0.30	1.00						
CaO	-0.25	0.16	0.07	-0.06	-0.11	-0.54	-0.07	-0.37	**-0.79**	0.17	**-0.81**	**-0.65**	1.00					
Fe_2O_3	-0.35	-0.24	0.03	**-0.64**	0.35	**0.84**	-0.56	-0.02	0.07	**0.70**	**0.60**	0.02	-0.44	1.00				
Y	-0.16	-0.39	-0.24	-0.39	0.30	0.56	-0.17	0.31	**0.69**	0.24	**0.76**	0.40	**-0.70**	**0.68**	1.00			
Zr	-0.47	0.31	**-0.60**	-0.40	0.27	-0.26	-0.43	**-0.62**	-0.34	0.31	-0.51	0.45	0.16	-0.13	-0.26	1.00		
ADR_{air}	**0.78**	0.32	**0.67**	0.42	-0.24	0.53	**0.69**	**0.95**	0.56	-0.36	**0.75**	0.03	-0.46	0.18	0.39	**-0.69**	1.00	
ADR	0.46	0.26	0.39	0.20	0.12	0.44	0.41	**0.67**	**0.80**	-0.19	**0.84**	0.57	**-0.73**	0.23	**0.61**	-0.32	**0.71**	1.00

Table 4-6: Pearson's correlation matrix of indoor radon, airborne radiometric, geochemical data, gamma dose and radon exhalation rates categorized based on soil variations

	GM_{Rn}	E_{222Rn}	eU	U	E_{220Rn}	eTh	Th	K_{air}	K_2O	MgO	Al_2O_3	SiO_2	CaO	Fe_2O_3	Y	Zr	ADR_{air}	ADR
GM_{Rn}	1.00																	
E_{222Rn}	-0.20	1.00																
eU	0.08	**0.73**	1.00															
U	0.05	0.40	**0.82**	1.00														
E_{220Rn}	**-0.93**	0.39	**0.62**	**-0.74**	1.00													
eTh	0.08	**0.73**	1.00	**0.82**	**0.62**	1.00												
Th	0.07	0.34	**0.83**	**0.98**	**-0.82**	**0.83**	1.00											
K_{air}	0.29	0.26	0.45	**0.64**	-0.06	0.45	0.56	1.00										
K_2O	0.02	0.44	**0.61**	0.18	**0.69**	0.61	0.30	-0.30	1.00									
MgO	-0.18	-0.20	**-0.84**	**-0.83**	**0.75**	**-0.84**	**-0.85**	-0.22	-0.52	1.00								
Al_2O_3	0.25	0.24	0.23	-0.28	**0.88**	0.23	-0.19	-0.23	**0.71**	-0.01	1.00							
SiO_2	0.24	0.14	-0.17	-0.32	0.50	-0.17	-0.18	-0.58	0.59	0.04	0.42	1.00						
CaO	-0.31	-0.35	-0.47	0.02	**-0.93**	-0.47	-0.09	0.24	**-0.88**	0.37	**-0.91**	-0.48	1.00					
Fe_2O_3	0.20	-0.10	-0.10	**-0.60**	**0.84**	-0.10	-0.53	-0.46	0.47	0.23	**0.90**	0.35	**-0.76**	1.00				
Y	0.24	0.06	0.08	-0.43	**0.94**	0.08	-0.32	-0.44	**0.70**	0.05	**0.96**	0.57	**-0.90**	**0.94**	1.00			
Zr	-0.32	-0.08	-0.36	0.05	-0.30	-0.36	0.04	-0.18	-0.38	0.11	**-0.81**	0.15	**0.70**	**-0.74**	**-0.67**	1.00		
ADR_{air}	0.39	0.35	**0.63**	0.56	0.34	**0.63**	0.52	**0.91**	-0.05	-0.23	0.10	-0.39	-0.09	-0.17	-0.10	-0.42	1.00	
ADR	-0.13	0.52	**0.72**	0.37	0.30	**0.72**	0.18	**0.67**	-0.22	0.24	0.37	-0.58	0.06	0.21	-0.08	**-0.84**	**0.71**	1.00

Furthermore, to estimate the radiation risk to the public, the annual effective dose rate (AEDR) in mSv y^{-1} was calculated from the air absorbed dose rate (ADR_{air}, nGy h^{-1}) using Equation 4-5 and the map of the distribution of annual effective dose rates was produced for the survey area as shown in Figure 4-8. The annual effective dose for some areas exceeded the recommended level of 1mSv y^{-1} for the general public by ICRP, 2007.

Equation 4-5: $$AEDR = ADR_{air} \times 8760 \times 1.0 \times 0.7 \times 10^{-6}$$

Where the factor of 8760 represents the number of hours (h) in a year of 365 days and the occupancy unit of 0.7 was used for the conversion coefficient from the absorbed dose in the air to the effective dose received by adults. The coefficient of 10^{-6} was used for nGy to Sv conversion for a unitary indoor-outdoor exposure.

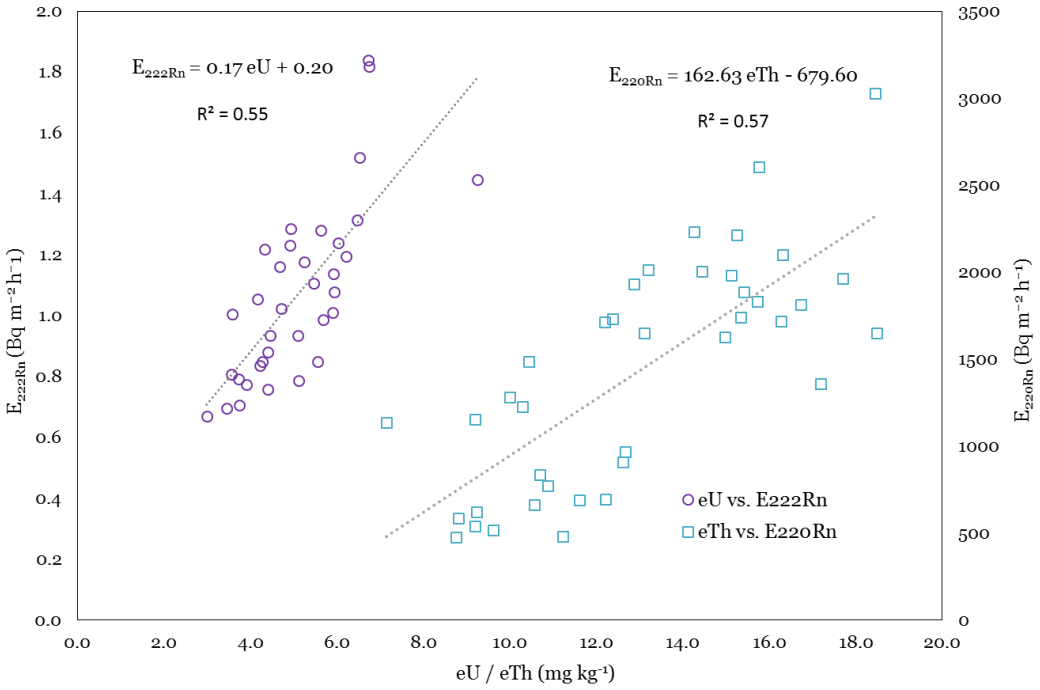

Figure 4-5: $^{222}Rn/^{220}Rn$ exhalation rates plotted against Tellus airborne eU and eTh

As can be understood from Figure 4-6, variations in radon exhalation rates even within an individual geological unit can be seen. However, the highest values of exhalation rates occurred in granites with microcline phenocryst (IDBSGRM) and green, red-purple, buff slate, siltstone of Oakland's formation (OAOAKL). In the case of the thoron exhalation rate, the estimated values are higher for IDBSGRM, OTMAUL (dark blue-grey slate, phyllite & schist), OTMAUL2 (Dark grey semi-pelitic, psammitic schist) and OAOAKL formations.

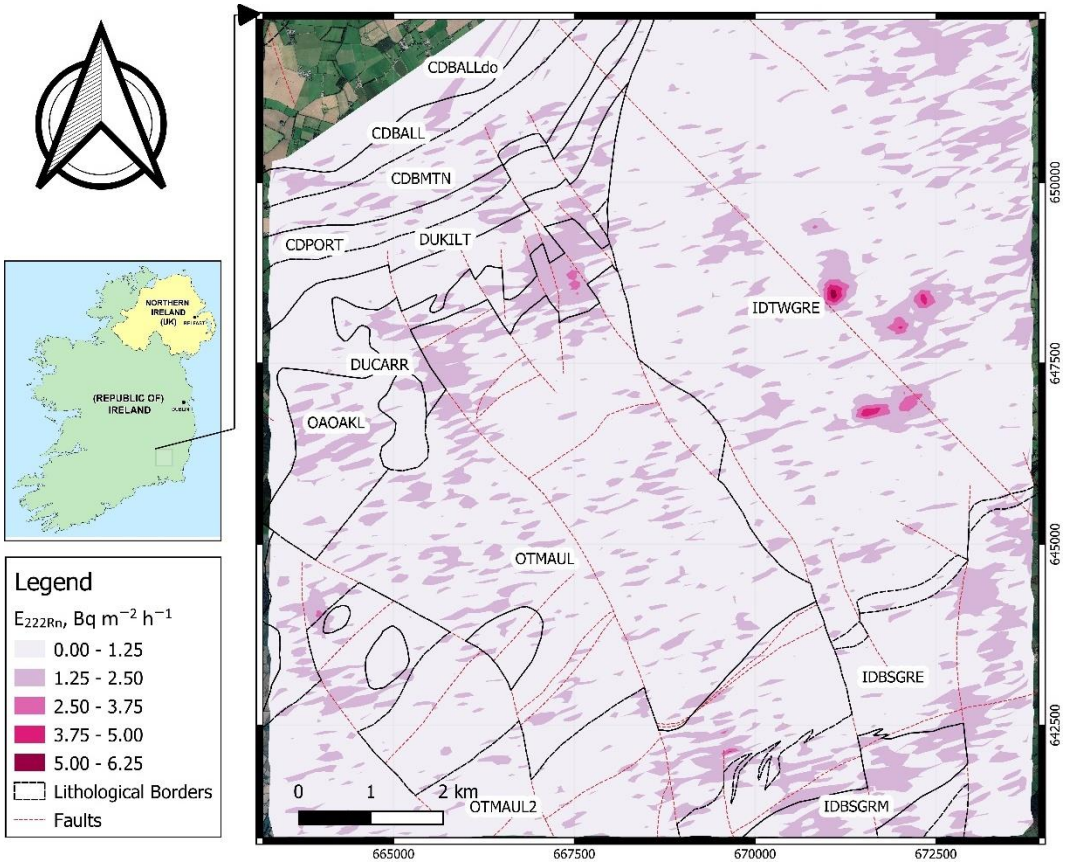

Figure 4-6: Distribution map of ^{222}Rn exhalation rates over geological contacts

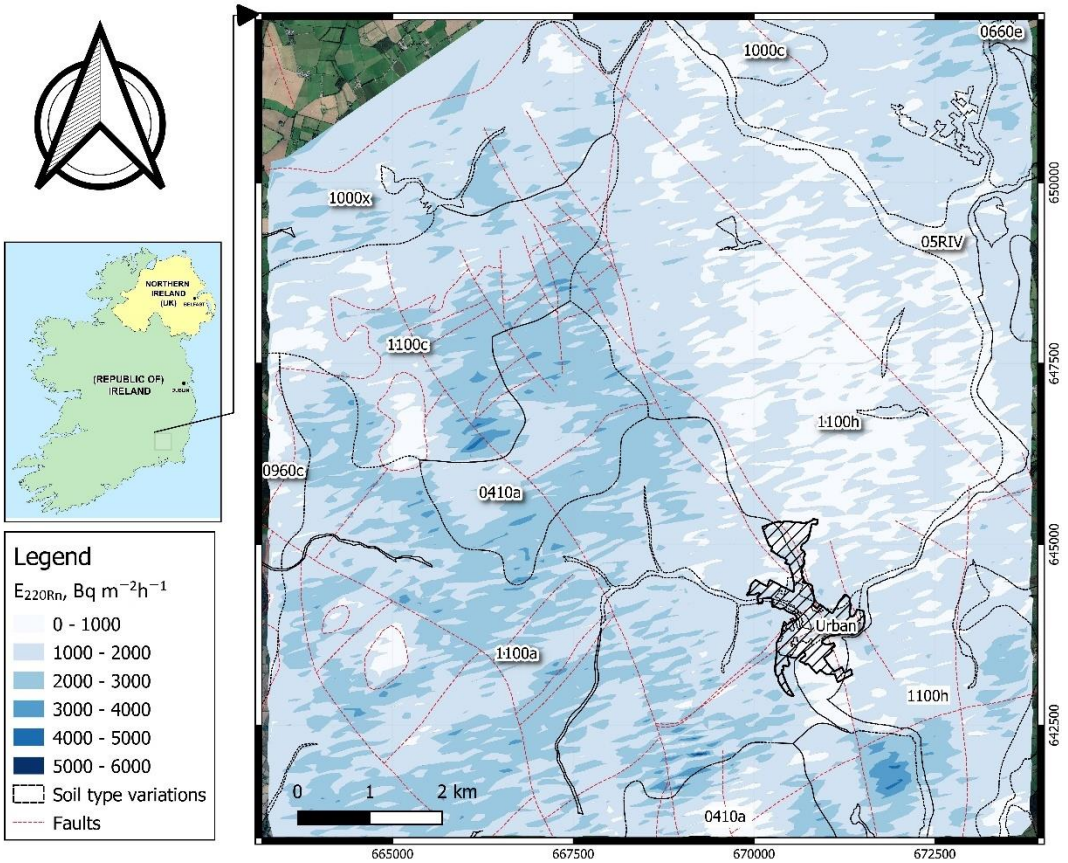

Figure 4-7: Distribution map of ^{220}Rn exhalation rates over soil type boundaries

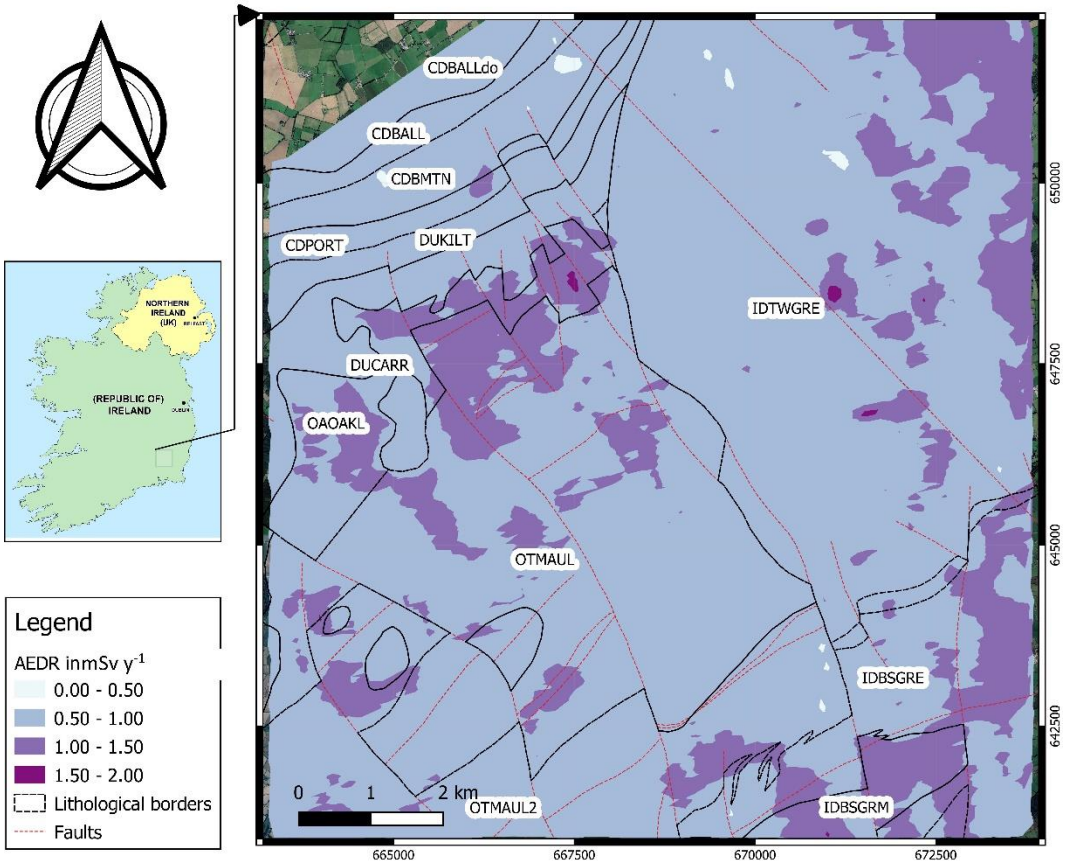

Figure 4-8: Map of estimated annual effective dose rates.

An interesting point in these two maps is that in a relatively small area, complex geology occurred and this caused different radon exhalation rates. The variations are more evident near the geological contacts. Figure 4-7 shows the distribution map of thoron exhalation rates. In that map, the overlapped layer shows the soil variations. As can be understood from this map and also in Table 4-2, the highest thoron exhalation rates are observed in soil associations of 0410a (peat over lithoskeletal acid igneous rock) and also fine to coarse loamy drift with siliceous stones (1100a and 1100c). The thoron exhalation rates in river alluviums (05RIV) are very low compared with other soil types.

The effect of tectonics is also apparent in both maps; higher values in radon/thoron exhalation rates can be found near some of the major faults. Thus, zones influenced by tectonics can be considered as areas with high-risk potentials. However, one should notice that the type of material filling the faults can also influence the radon exhalation from tectonic structures (Barnet, 2008).

The epidemiological effects of radon exposure in Ireland have been well studied and its correlation to annual numbers of lung cancer cases was estimated (approximately 270–

280≈ 12% of the annual lung cancer incidence) (Elío et al., 2018). Nevertheless, the missing point is that few studies estimate the dose coefficients for thoron and its decay products. Although thoron has a short half-life and may decay almost completely in indoor air, significant concentrations of its decay products remain. It is estimated that exposure to air-containing thoron decay products at a concentration of 1 Bq m^{-3} gives rise to an average annual dose of approximately 750 µSv (O'Connor et al., 2014). Therefore, considering the relatively high thoron exhalation rates found in this study, it would be necessary to take into account the possible adverse health effects of thoron exposure in the definition of priority areas. Thoron effect might be more significant for the houses where the floors and walls are made of earth.

An outlook of chapter 5

As one of the main results of this chapter, the average uranium contents classified based on geological borders were found to be representative of the radon release potential for different rock types. In the next chapter, by calculation of mean values of uranium content for different geological units, a GRP map will be developed for the Sardinian region. Available local data discussed in the last section of chapter 3 will be employed for this purpose.

The joint research center of the European Commission is also working on the preparation of the geogenic radon potential map of Europe (EGRM project) based on the geological similarities and radon-related parameters measured in Germany. We will firstly reproduce a map similar to EGRM using data on activity concentration of radon-related variables (i.e., Soil gas radon and uranium contents) that are measured in Germany and Czech. It is noteworthy that the One-Geology map of Europe was considered as the link for searching the geological similarities. Then we will compare it with the map produced based on local data.

5 ADDRESSING GEOGENIC RADON SOURCES IN SARDINIA

Summary

In this chapter, the primary sources of indoor radon in Sardinia, including geogenic radon and radon released from building material, will be investigated. Geogenic radon is mapped based on data on local radon-related variables obtained from bibliographic sources. Additionally, a map similar to the trial version of EGRM was produced. Each map has its benefits and applications, but the map developed based on local geogenic has fewer limitations, higher resolution and it considers the specific geologic evolutions of Sardinia. Therefore, it is more reliable and better represents the geogenic radon release potential of the Sardinian territory. The developed GRP map of Sardinia represents radon risk in categorical format. As for any draft of a GRP model, it will be examined later, however in general, the result of the tests to be discussed in the next chapter, show that the developed GRP map is a useful tool to predict geogenic radon in workplaces and public buildings and even residential dwellings of Sardinia.

Furthermore, the radon exhalation rates and the natural radioactivity of eighteen dimension stones mostly used in Sardinia and widely exported worldwide have been estimated employing laboratory tests on the samples to be tested, which include twelve granitoids, four pyroclastic rocks and two basalts.

As expressed in chapter one, one can approximate the indoor radon concentration of an individual building having information on the geogenic radon potential and simulating the radon exhalation rate from building materials used in interior design. Both of these parameters are discussed in detail in this chapter.

5.1 A Rough Estimation of Geogenic Radon by Extrapolation of Radon-related Data from German and Czech Geotypes

As mentioned before, the radon potential of an area can be necessarily quantified based on two main approaches; the first is defined by a physics-driven process to quantify the input data, which contributes to potential indoor radon. The second one is based on multivariate cross-tabulation of input variables, which finally results in a categorical-ordinal quantity (Gruber et al., 2013). According to the second method, an estimated class of radon potential for an area is a result of the summation of scores assigned to two sets of input parameters; a) the presence of the radon source and b) the persistence of conditions that favor migration from the source to indoor spaces. In this section, a method was developed to build a rough geogenic radon potential map for the study area regarding the set of input parameters, as mentioned earlier. To do this, five GIS layers were created based on the available geological maps, geochemical data and mechanical properties of soil and rocks. For each layer, a grid, including 313 cells, was created. Open source QGIS software (https://qgis.org/en/site/) was used for the geographic display of the map layers and to process relevant numerical data. As shown in Figure 5-1, the methodology for indirect estimation of the GRP map of Sardinia includes two main stages; (1) the creation of primary GIS layers, (2) the categorization of the risk-based on cross-tabulation of input data using radon ranking matrix. In order to prepare the primary GIS layers, the following data has been taken into account (See also Figure 5-1);

- Surface Lithology and Geological Age maps (1:1M) of Sardinia: http://portalesgi.isprambiente.it/lista-servizi-wms/Geological%20Maps, Germany: https://produktcenter.bgr.de/terraCatalog/Start.do and Czech: http://www.geology.cz/extranet-eng/maps/online/download-services
- Soil gas radon data of 39,684 measurement points in Germany: https://www.imis.bfs.de/geoportal/#map
- Complex radon information of 15,093 municipal authorities in Czech, including soil gas radon measurement data: https://mapy.geology.cz/radon/
- Soil Uranium concentrations (a grid of 10km × 10km cells) obtained from Joint Research Centre of European Commission, Radioactivity Environmental Monitoring Group: https://remon.jrc.ec.europa.eu/About/Atlas-of-Natural-Radiation/Uranium-in-soil/Uranium-concentration-in-soil-
- Soil Permeability map of Sardinia with 500 m resolution extrapolated from Joint Research Centre of European Commission, Radioactivity Environmental Monitoring Group: https://remon.jrc.ec.europa.eu/About/Atlas-of-Natural-Radiation/Soil-permeability/Soil-permeability-

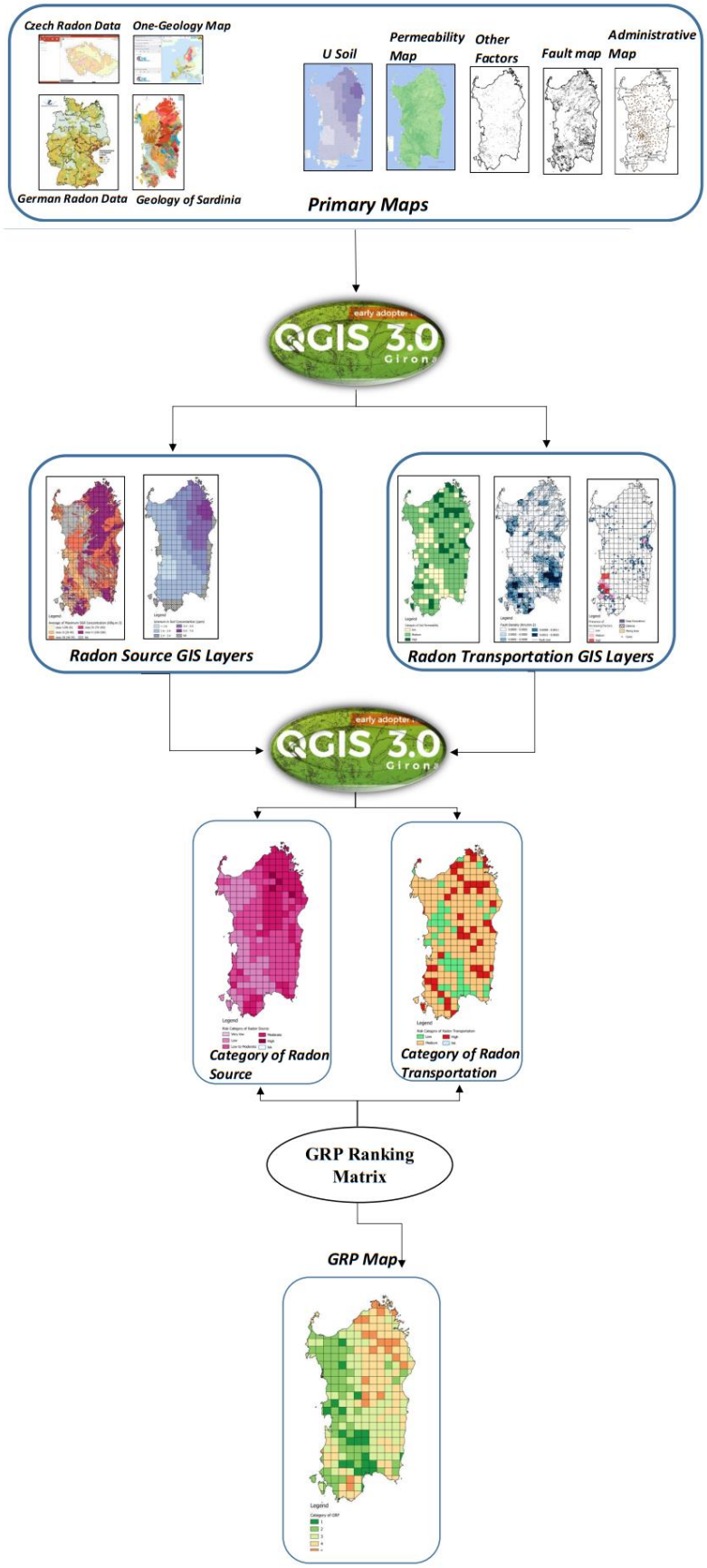

Figure 5-1: Methodology flow chart for a rough estimation of geogenic radon by extrapolation of data from German and Czech geotypes

Furthermore, the shapefile of the following layers were downloaded for the study area from Sardinian Geo-portal service; (http://webgis2.regione.sardegna.it);

- Map of the major faults (1:50,000).
- Map of mines, deep excavations, galleries and tunnels located within the regional territory (1:50,000).

5.1.1 Grouping of Geological Units Based on Soil Gas Radon Data

The main contributor to the occurrence of elevated levels of indoor radon is the local geology (P. Bossew, 2015) and in order to categorize the potential of expected radon release from different geological units, the parameters like soil gas radon measurements, indoor radon (IRC) statistics and also uranium content of superficial deposits and bedrock have been utilized in many studies (Appleton & Miles, 2010; Cinelli et al., 2017; Friedmann, Baumgartner, et al., 2017; Ielsch et al., 2010; Kropat et al., 2015; Szabó et al., 2014). Because the soil gas radon (SGR) data are independent of anthropogenic factors and there is also a strong relationship between the geology and soil gas radon concentrations (Guida et al., 2013), results of SGR measurements can be used as a proper predictor to estimate the GRP of an area (Kropat et al., 2017).

Ideally, the results of direct measurements (i.e., SGR, IRC, uranium content, etc.) are used for the preparation of a GRP map. However, if the measurements of these quantities are not available, one may look for other data, which allows for predicting rough estimations of the radon potential of an area until the better data are attainable (Bossew, 2015). Given the relationship between geology and radon-related quantities (e.g., soil gas radon), it can be possible to use geological similarities as a cheap predictor of radon release potential of similar or equally classified geological units. It is noteworthy to say that in the territory of Czech and Germany, a systematic soil gas radon testing was carried out and the relevant data are available on web-GIS databases mentioned in the previous section. Therefore, one can find a rough estimation of radon release potential for the areas where there are geological similarities with Czech and Germany. An example of this application is the "characterization of particular rock types in Austria based on SGR data measured in Germany and the Czech (Barnet, 2008).

It should also be noted that rock material is very inhomogeneous even on a small scale of several tens of meters and therefore, a statistical approach should be utilized for the characterization of similar units (Barnet, 2008). Further to this, when looking for

geological similarities on an international scale, the incompatibility of different national classification schemes may cause inconsistency (Gruber et al., 2013). To avoid this problem, adopting a harmonized scheme (e.g., European OneGeology project) can be useful (Gruber et al., 2013). In this chapter, to categorize the radon release potential of Sardinian geo units, at the first level, based on the OneGeology project, the possible geological similarities of Sardinia, Germany and the Czech were investigated. Although geological similarities of Sardinia could be better investigated even in other parts of Europe, at the moment, systematic data on soil gas radon measurements are mostly available for Czech and Germany.

5.1.2 Geological Similarities between Sardinia, Germany and Czech

Sardinian geology is like a fascinating puzzle (Carmignani et al., 2016), which includes rocks of all the periods belonging to Phanerozoic Eras (Carmignani et al., 2016). Sardinia is a part of the Southern branch of the European Variscan chain. A complete section of this chain is exposed in the territory of this island, including a Permo-Carboniferous batholith emplacement (Carmignani et al., 2016) and a metamorphic basement (consist of a Foreland zone in the SW, a Nappe zone in the central part and, finally, an Inner zone exposed in the northern sector of the island) (Cocco et al., 2018 and references therein). When Sardinia was still part of southern Europe, a Permian to Oligocene sedimentary succession was deposited. Widespread deposition of carbonate platforms occurred during the Mesozoic opening of the Tethys Ocean. During the Paleogene, clastic deposition prevailed in a transitional environment and small outcrops of Lower Eocene limestones record a marine deposition. Depositions of Sardinian rifts have also occurred during an Upper Oligocene to Upper Miocene volcano-sedimentary succession. Subsequently, due to an eastward drifting and counterclockwise rotation, the Sardinian-Corsican plate blocked away from Europe during the Aquintanian-Burdigalian. During the Tortonian and Messinian, carbonate-mixed siliciclastic deposition occurred in shallow marine and transitional environments and finally, the Campidano region developed in southern Sardinia during the middle Pliocene -Early Pleistocene (Carmignani et al., 2016 and references therein).

As mentioned earlier, Sardinia is a part of the Variscan chain, which extends from Portugal, Ireland and England in the west and continues through Spain and France to Germany and the Czech (Barceló et al., 2006). In the territory of the Czech, the most

substantial part of geology consists of the bohemian massif, one of the large fragments of Variscan orogeny (Grygar, 2016). Furthermore, in the territory of Germany, the Variscan belt strikes away from southwest to northeast, such as the Rhenish Slate Mountains. Moreover, to this, evidence of the presence of microfossils both in Western Germany and South Western Sardinia state the existence of a similar geological condition for both regions during the Early Cambrian (Elicki & Wotte, 2003).

Some examples of geological similarities were stated in the previous paragraph, but in order to have a comprehensive view of all possible similarities, it was necessary to utilize a harmonized geological map. For this purpose, the maps of Geological Age and Lithology from the OneGeology project of Europe (Figure 5-2 and Figure 5-3) were used. It can be understood from these maps that the geological similarities between Sardinia, Czech and Germany can mostly be investigated during the development of Variscan orogeny (Permian- Carboniferous) and also during the sedimentological evolution in Cambrian.

In this research, to investigate similarities, two variables were considered; "geological age" and "superficial lithology." Then a criterion was defined to search for similarities in which the units having the same lithology and geological age are defined as similar ones. To be able to recognize the similarities automatically, the Geological Age and Lithology map of the OneGeology project were processed and analyzed using the QGIS software as follows; the vector files of both maps were merged and a unified map of geological age-lithology was created. Then, the units having the same values of both geological age and superficial lithology were considered as similar units. After finding the similar units, a point layer consisted of soil gas measurement data, measured in the territory of Czech and Germany was added. Finally, using the geostatistical tools and based on the thresholds defined by Kemski et al., (1998) and the German Federal Office of Radiation Protection for classification of radon activity in soil air (20, 40, 70, 100 and 250 KBq m^{-3} for soil gas radon concentration), the classes of radon potential were determined for the Sardinian geo units that were considered as similar ones (Table 5-1and Figure 5-4). The similarity was only found in 78.24 percent of the Sardinian geo units.

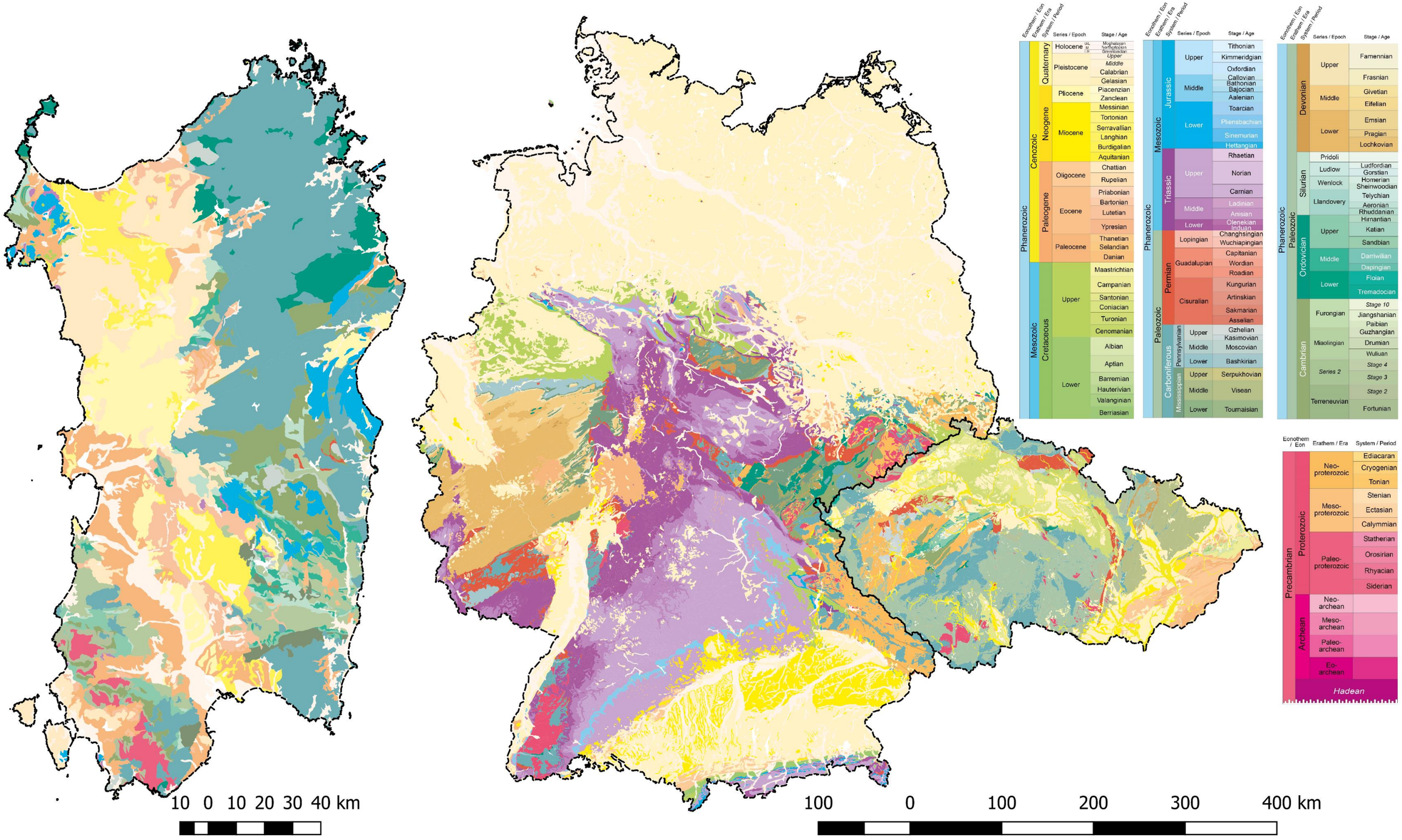

Figure 5-2: The Geological Age map (1:1M) of the OneGeology project of Europe for the territory of Czech, Germany and Sardinia. Note: different scales were utilized for the geological map of Sardinia and Czech-Germany

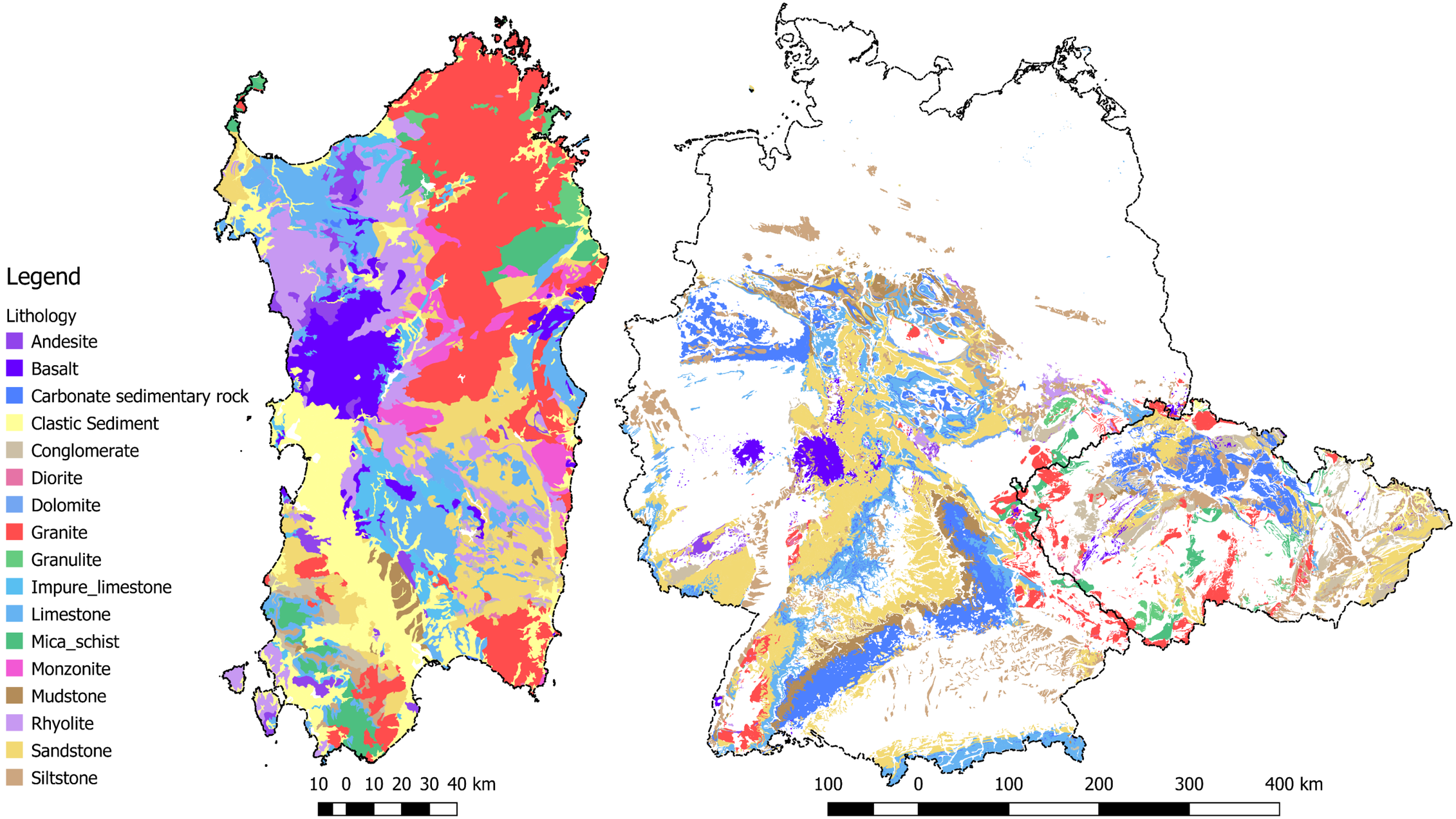

Figure 5-3: The Lithological similarities of Czech, Germany and Sardinia, according to the Lithology map (1:1M) of the OneGeology project of Europe. Note: different scales were utilized for the lithology map of Sardinia and Czech-Germany.

Table 5-1: Calculated values of average Soil gas radon (SGR), measured in Germany (SGR-GR) and Czech (SGR-CZ) and the classes of predicted radon release potential of units.

Unified units according to One-Geology project	% Area	Mean SGR-CZ KBq m^{-3}	Mean SGR-GR KBq m^{-3}	Category of Radon Release Potential
Holocene Clastic Sediment	8.23	-	39.86	II
Pleistocene Clastic Sediment	8.08	39.35	24.66	II
Pliocene Mudstone	0.79	-	-	NA
Pliocene Basalt	6.5	47.5	-	III
Pliocene rhyolite	0.36	-	-	NA
Messinian Impure Limestone	0.09	-	-	NA
Langhian Carbonate Sedimentary Rock	0.12	-	-	NA
Burdigalian Limestone	5.78	-	-	NA
Chattian Rhyolite	8.31	-	-	NA
Chattian Andesite	2.46	-	-	NA
Lutetian Impure Limestone	3.91	-	85.94	IV
Eocene Sandstone	0.78	18.3	-	I
Paleocene Mudstone	0.12	-	-	NA
Late Cretaceous Limestone	0.18	-	54.95	III
Jurassic Limestone	3.56	58.7	42.44	III
Middle Triassic Dolostone	0.23	-	62.04	III
Permian Andesite	0.08	-	69.01	III
Pennsylvanian conglomerate	0.2	58.37	59.3	III
Pennsylvanian Rhyolite	0.81	-	93.93	IV
Mississippian Sandstone	0.98	55.8	65.27	III
Carboniferous Conglomerate	~ 0	58.7	-	III
Carboniferous Granite	23.68	118.41	114.61	V
Carboniferous Monzonite	3.42	-	107.88	V
Carboniferous Diorite	0.05	56.2	83.1	IV
Silurian Limestone	0.32			NA
Silurian Sandstone	1.49	58.7	-	III
Late Ordovician conglomerate	1.54	58.73	-	III
Middle Ordovician Rhyolite	1.78	-	-	NA
Ordovician Mica Schist	2.39	53.02	-	III
Ordovician Granulite	1.23	44.82	-	III
Cambrian Sandstone	4.72	56.43	-	III
Cambrian Limestone	1	-	-	NA
Cambrian Siltstone	0.64	-	-	NA
Cambrian Mica Schist	1.46	-	125.93	V

NA: No measurement data were available

It is noteworthy that the adopted measurement policies in the Czech and Germany were not identical. In Germany at each measurement site, the maximum radon value and the arithmetic mean of soil permeability obtained from three boreholes were used to categorize the radon potential (Kemski et al., 1996). However, in Czech, the averages of maximum radon activities in the geological base (1:500,000) were reported. Therefore, in order to avoid incomparability due to different measurement approaches, for radon data acquired from the German database, the averages of all SGR values measured within the area of an individual geological unit were first calculated and then utilized.

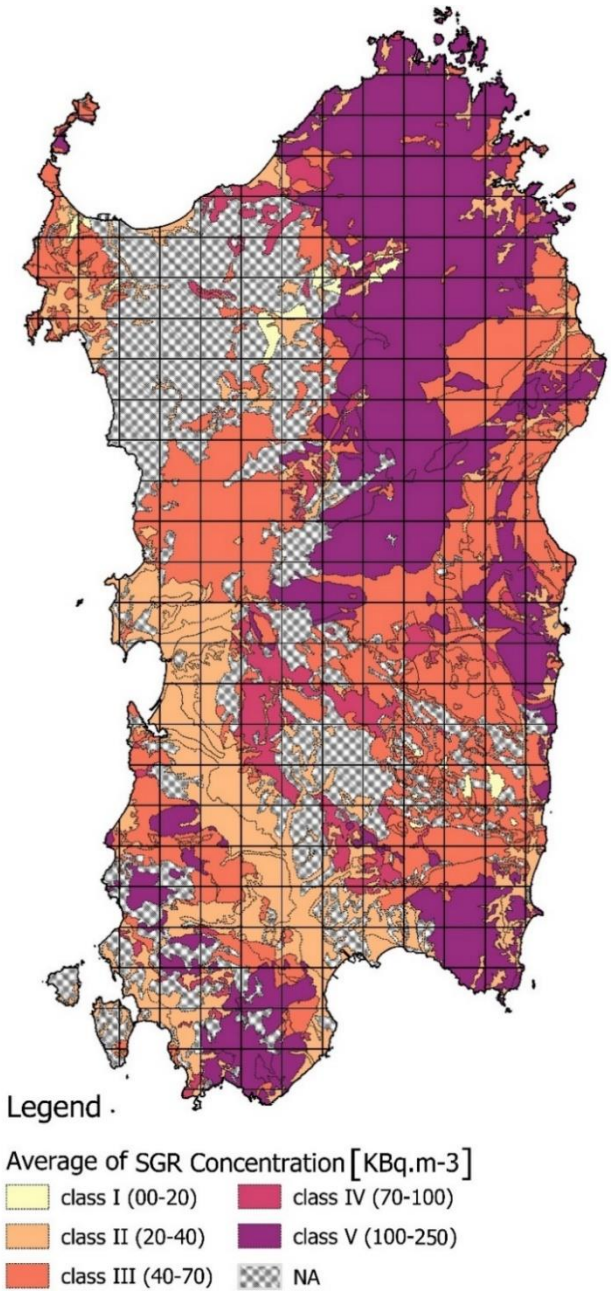

Figure 5-4: Hypothetical distribution of average SGR and the classes of predicted radon release potential for different geological units of the Sardinian region

Figure 5-5 shows the statistics of attributed values of measured SGR concentrations that were used as a predictor for the categorization of generalized geological units. Variations, even within an individual geo unit, can be seen. However, there are distinct differences in soil gas radon activity of different lithology - geological ages. For example, considerably higher values of SGR occur in Cambrian mica schists and Carboniferous granites in comparison with Eocene sandstone and Pleistocene clastic sediments.

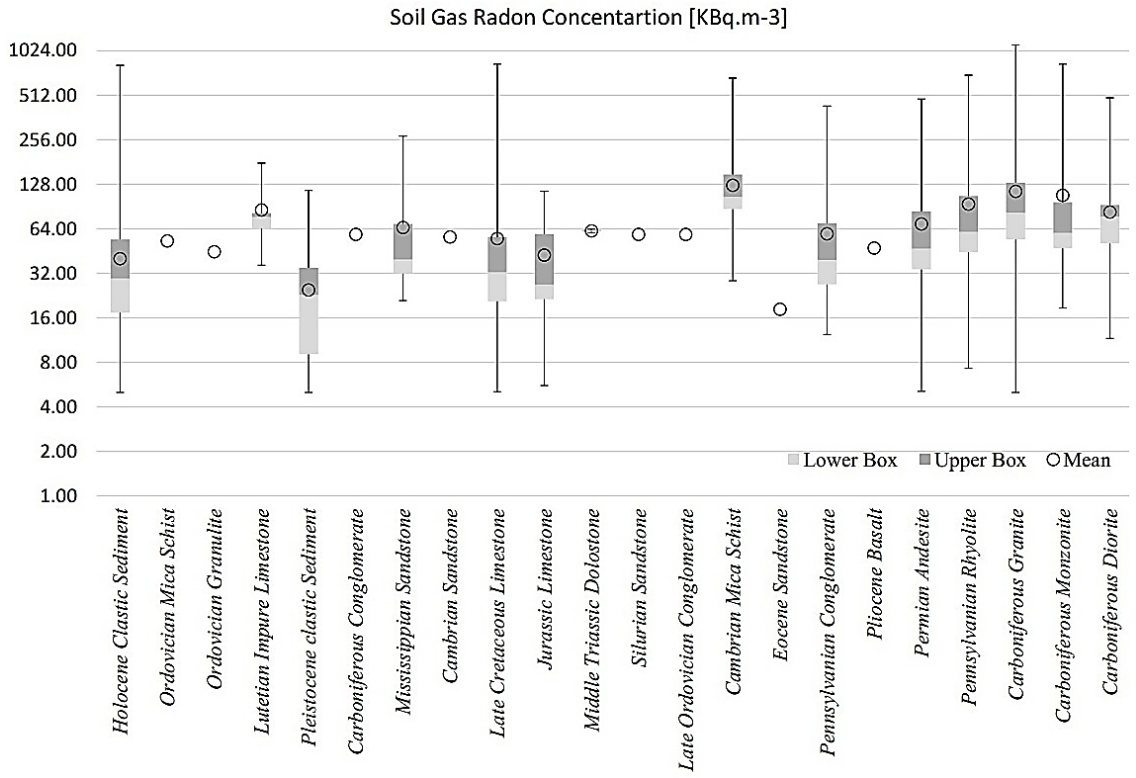

Figure 5-5: Box and Whisker plot, displaying the maximum, median, minimum, 1st and 3rd quartile of the soil gas radon data measured in Czech and Germany

5.1.3 Uranium in Soil Data

^{222}Rn is a product of the ^{238}U decay chain (Kemski et al., 1996) and therefore information on the uranium geochemistry can serve as an essential contributor to estimate the geogenic radon potential (Cinelli et al., 2017). In the previous section, by classification of the units based on SGR values, 78.24 percent of the area was categorized. In order to cover the remainder of the area, the map of uranium concentration in soil displaying the geometric mean value of uranium content over a 10km × 10km grid cell was also utilized. This map is published by the JRC-REM group based on the data from topsoil samples. The map was first converted into a vector format to be able to assign the uranium values to each cell of the grid, as shown in Figure 5-6.

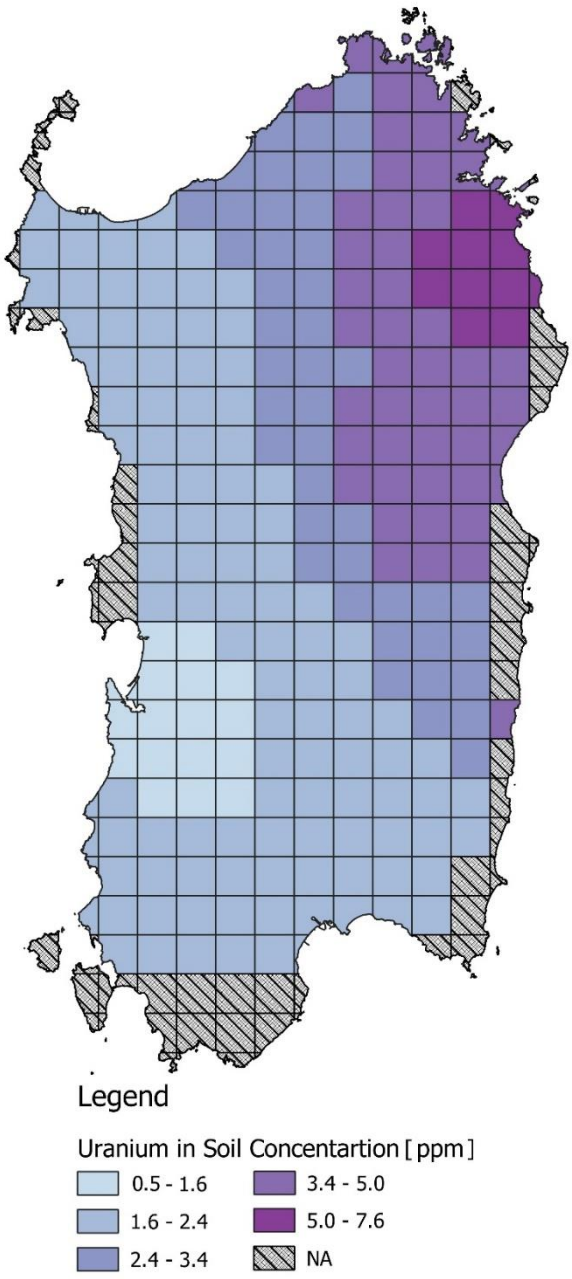

Figure 5-6: Map of Uranium in soil distribution presenting the geometric mean of uranium concentration [ppm] over a 10 × km 10 km grid cell. Raw data were derived from the map of uranium in soil published by the JRC-REM group

5.1.4 Soil Permeability

The effect of soil permeability, fault density and other factors such as the mine areas, groundwater wells, caves, shafts and galleries on increasing radon exhalation from the earth were also included in studies related to geogenic radon mapping (Cinelli et al., 2017; Kropat et al., 2017; Licour et al., 2017). The variables mentioned above can facilitate the transportation of radon from source to indoor spaces (Ielsch et al., 2010).

A rough estimation of soil permeability can be derived from a hydrogeological map (Ciotoli et al., 2017) or using the weight percentage of fine fraction (<63 mm), according to the Czech approach (Neznal et al., 2004).

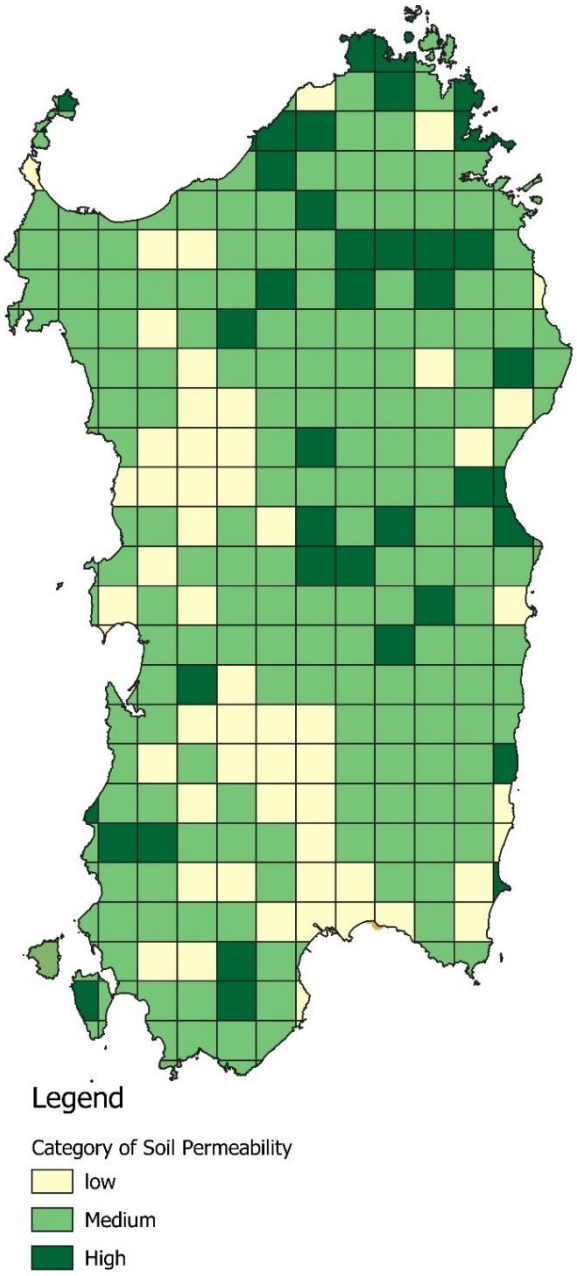

Figure 5-7: Map of topsoil permeability. For each cell, the most prevalent permeability class was assigned. Derived from the map of soil fine fraction (resolution 500m) published by the JRC-REM group, vectorized using GIS software and finally, permeability ranges reclassified based on the Czech approach.

In the case of the second method, soils with the weight percentage of fine fraction < 15 % are categorized as high permeable soils, in the range 15-65 % as medium permeable and in the case of the fine fraction above 65 % as low permeable ones. To approximate

the percentage of fine fraction from the contents of clay, silt, sand and course material, Equation 5-1 was used (Neznal et al., 2004):

Equation 5-1:
$$\%\ \text{Fine Fraction} = \frac{Silt_{LUCAS} + Clay_{LUCAS} + (0.05 \times Sand_{LUCAS})}{Silt_{LUCAS} + Clay_{LUCAS} + Sand_{LUCAS} + Coarse_{LUCAS}}$$

Topsoil physical properties of Europe with a resolution of 500 meters were mapped as a result of the LUCAS project (Tóth et al., 2013) and are available on the JRC-REM database. The Sardinian soil fine fraction map was extrapolated from that database and then, using the Czech approach, permeability classes (i.e., low, medium and high) were assigned to each cell, considering the most prevalent permeability class (Figure 5-7).

5.1.5 Fault Density and Other Effective Factors

The presence of faults can facilitate radon migration from deeper basements (Bigi et al., 2014). Not only the presence of faults but also the type of the material filling the faults can as well influence the radon exhalation from tectonic structures (e.g., the presence of clayey minerals can decrease the radon release) (Barnet, 2008).

Barnet, 2008 reported that enhanced radon concentration must be expected on the tectonic zones, where the presence of outlier concentrations is a frequent phenomenon. Thus the areas influenced by tectonics must be considered as radon-prone areas. To consider the effect of faults as a proxy of secondary permeability, the map of main faults for the Sardinian region was used and subsequently, the density of fault lines was calculated by dividing the total length of fault lines by the area of each grid cell as shown in Figure 5-8 a).

Parameters such as mine areas, caves, deep excavations, groundwater wells, shafts and galleries can provide pathways for transportation of radon to the ground level. The effects of such parameters on a GRP map can be considered locally by applying an increasing step along or around these features (Ielsch et al., 2010).

However, to include the effect of increasing factors in our case in which a grid cell is used, approximate limits were set. The cells that the number of the caves and density of the total area of other increasing factors inside it was significant; an increasing step was applied (see Table 5-2). We used the maps (1:50,000) of caves, mining areas, galleries and deep excavations that were extrapolated from Sardinian Geo-portal. Most of these factors can be found in the Sulcis-Iglesiente district, where the majority of Sardinian

abandoned mines are located. As shown in Figure 5-8 b, the cells of the grid are categorized into low, medium and high classes based on how much being affected by the presence of increasing factors.

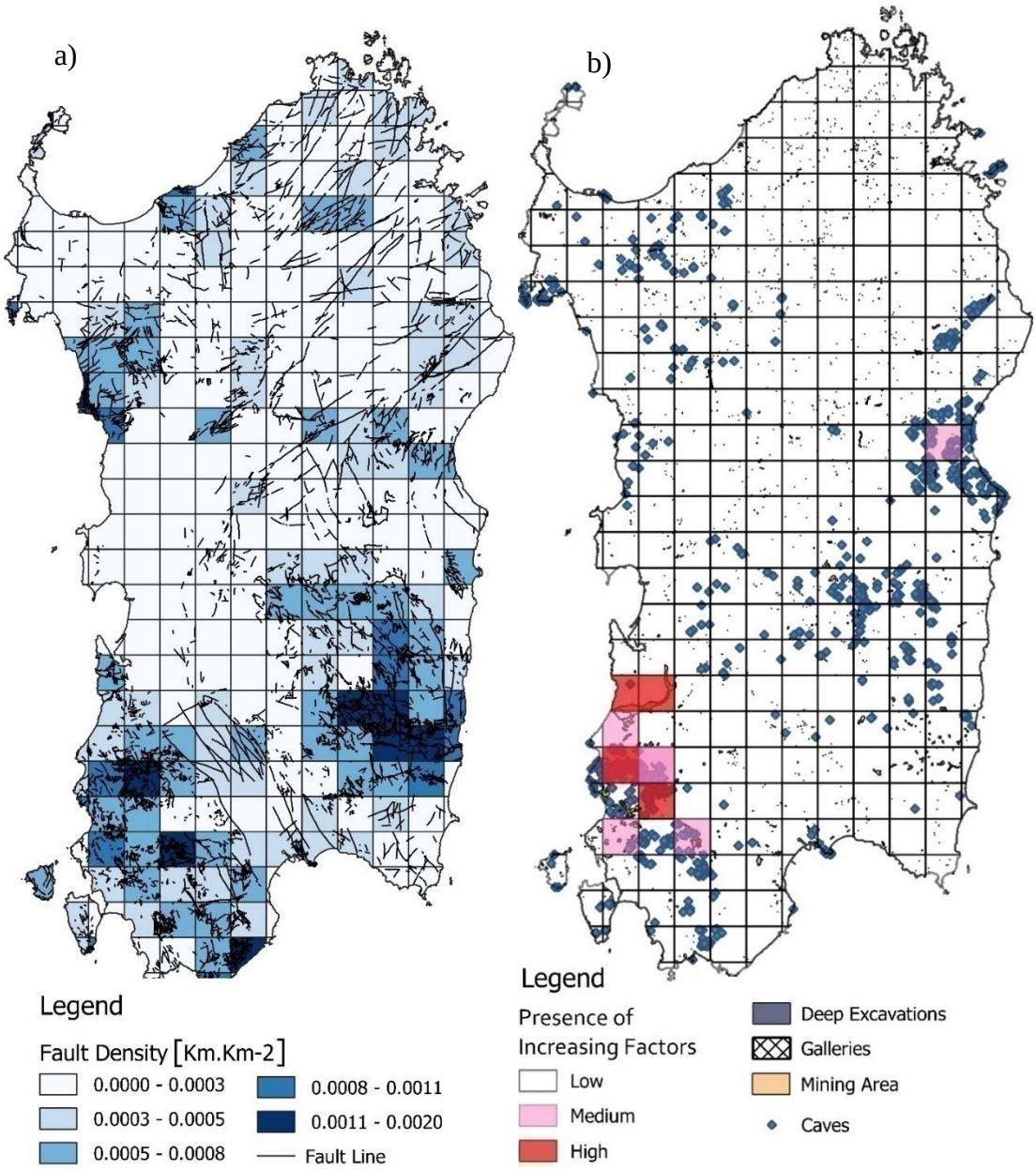

Figure 5-8: a) Map of fault lines and density of fault lines calculated for each cell of the Sardinian grid. b). **Probability of the presence of radon increasing factors, including mine areas, caves, deep excavations and galleries. Base maps are extrapolated from the Sardinian geo-portal service.**

5.1.6 Production of the GRP Map Based on Cross Tabulation of Input Variables

Table 5-2 shows the GRP ranking matrix, which is used to predict the category of GRP for the Sardinian grid cell. According to this matrix, for an individual cell, two terms were allocated. Each term includes categorical classes and the worst condition from these

classes is considered as the determinant factor of the relevant term. As a predictor of the category of the term "the presence of radon source," classes of the mean soil gas radon measured at different geo units together with uranium in soil contents were used. In the case of categorization of the term "feasibility of radon transportation," soil permeability, fault density and presence of other increasing factors were taken into account.

The approximate thresholds used in this matrix are similar to limits used in literature (Ielsch et al., 2010; Kemski et al., 2001; Winkler et al., 2001). Based on the proposed thresholds, numerical values were assigned for each class of the mentioned terms, where the term presence of radon source is given higher weight (Kemski et al., 1996). The output of this matrix is a map with a GRP category between 1 and 6. The higher the category class of a cell, the more risk from radon is anticipated.

Table 5-2: GRP ranking matrix

Category of Geogenic Radon Potential		***Category of Radon Source***	**Very low**	**Low**	**Low to Moderate**	**Moderate to High**	**High**
			U_C [1] ≤ 0.5	$0.5 < U_C \leq 2.4$	$2.4 < U_C \leq 5.0$	$5.0 < U_C \leq 7.6$	$U_C > 7.6$
			Mean-SGR[2] ≤ 20	$0.5 <$ *Mean-SGR* ≤ 40	$40 <$ *Mean-SGR* ≤ 100	$100 <$ *Mean-SGR* ≤ 250	*Mean-SGR* > 250
Category of Radon Transportation		Score	-	***1***	***2***	***3***	-
Low	*SP* [3] *= Low*	***0***	**1**	**1**	**2**	**3**	**6**
	FD [4] ≤ 0.0005						
Medium	*SP = Medium*	***1***	**2**	**2**	**3**	**4**	
	$0.0005 <$ *FD* < 0.0011						
	$+N_{Cells}$ *with increasing factor category = Medium*						
High	*SP = High*	***2***	**3**	**3**	**4**	**5**	
	$FD \geq 0.0011$						
	$+N_{Cells}$ *with increasing factor category =High*						

5.1.7 The draft of the Sardinian GRP grid

Figure 5-9 shows the GRP map of the Sardinian region. Cells with the highest GRP category can be found mostly in the North-Eastern and Eastern parts of Sardinia. A

possible reason for that could be the presence of Variscan Batholiths (mainly; Monzo-sienogranites, Leuco monzogranites and Sienogranites (Xhixha et al., 2014) however, some Ordovician sedimentary formations containing relatively high uranium concentration can be found in SE Sardinia and might be considered as potential areas for elevated radon concentrations. The map produced here does not seem to be able to meet the needs for higher precision, although it can be used for having a general understanding of radon in Sardinia on the European scale, for prediction of radon on a local scale, a more fundamental approach must be adopted.

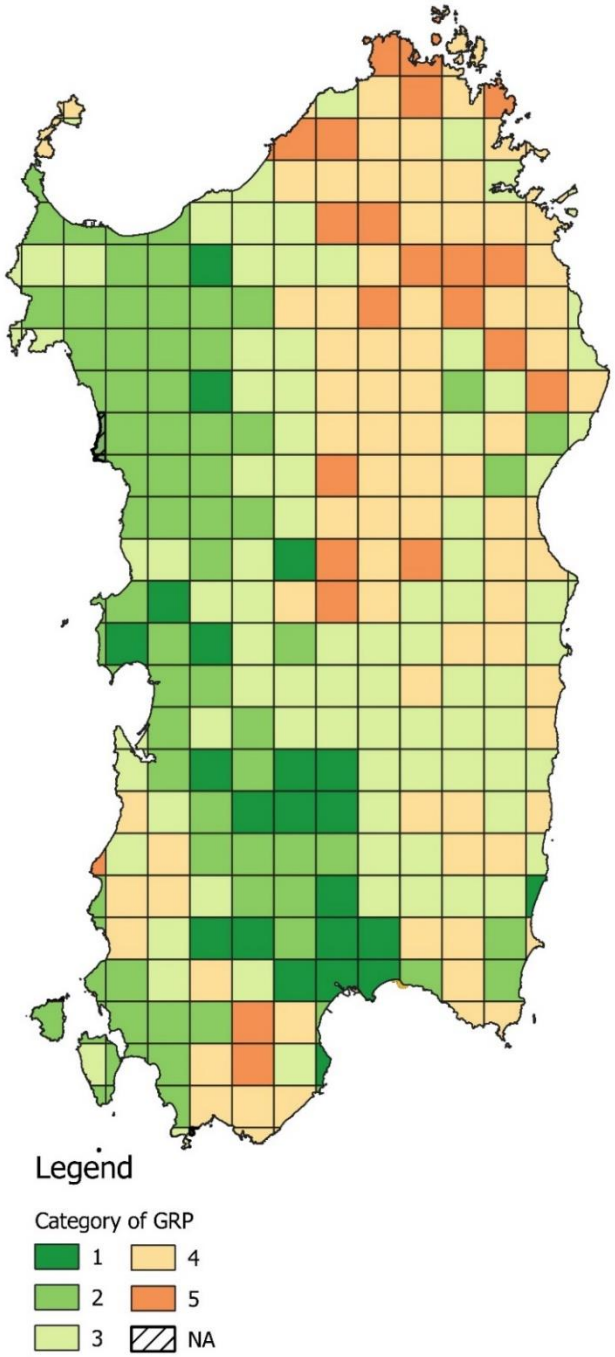

Figure 5-9: Category of the predicted GRPs for Sardinia

5.1.8 Discussion

The goal of this section was to represent a fast and approximate method to predict the GRP category of Sardinia by using an approach similar to that used for EGRM. A map was produced using the multivariate cross-tabulation of input variables, which mainly consisted of two sets of parameters; the presence of radon source and the presence of factors that can facilitate radon mobility. Grouping the radon release potential of geological units and uranium content were used as variables to determine the category of the presence of radon source.

Due to the lack of measurement data in Sardinia, the results of soil gas radon tests measured in Germany and Czech were utilized for grouping geological units based on the evaluation of geological similarities.

It should be noted that the evaluation of geological similarities is very complicated, which makes this approach indeterminate. In general, incomparability due to the different geological scheme, along with the evaluation of the similarities over a relatively small-scale map (1:1M) can be considered as the primary sources of bias.

Despite these limitations, investigation of similarities to extrapolate radon release potential to similar geological units was already used by some authors and a few examples of this application are present in literature. However, prediction of the geogenic radon risk from studies in similar geo units relative far away is a new practice; therefore, further real-time testing is needed to validate the usability of this method.

The GRP model of Sardinia proposed here can be used as a rough estimation of the geogenic radon risk map of Sardinia, which can be updated once enhanced measurement data are available.

5.2 GRP mapping in Sardinia Using Local Data on Radon-related Variables

In the first part of this chapter, a 10km size grid of geogenic radon potential map was produced. This map is useful for administrative decision making on the European scale and even national scale. It can help to have an approximate overlook of the situation of Sardinia regarding the potential of geogenic radon release; however, it is not decent enough for evaluation of risk on a regional and zonal scale. For this purpose, a map with a higher resolution is necessarily needed. To aim the production of a more powerful geogenic radon map, the utilization of direct local data would be helpful. Furthermore, to

increase the resolution and precision of the proposed GRP map, a larger scale geological map (1:250K instead of 1:1M) could be considered.

As previously mentioned, the geological borders can better distinguish between the radon behaviors of different rock types, therefore increasing the accuracy of the map, especially for the zones where the borders of geological units meet. This time…we avoided using grids and instead, the statistics of the radon-related input variable were calculated for geological polygons. We created the shape of the polygons of Sardinian geological units based on the recently published geological map of Sardinia (Carmignani et al., 2016). Also, rock units having a similar property of radon release potential were regrouped (see Figure 5-10)

The most reliable data currently available for Sardinia, which can be efficiently used for GRP production fulfilling above mentioned requirements is the mean uranium content of rock types (U). The mean value of available uranium data was calculated for the polygons of the geological map mentioned in the previous paragraph. Table 5-3, together with Figure 5-11 shows the calculated mean values and the map of mean uranium contents of rocks assigned to each Sardinian geo unit. The attributed U values are classified in ordinal classes, according to Ielsch et al., 2010.

In 2019, when the grid of the Sardinian GRP was already prepared, the geological survey of Sardinia published the map of rock permeability (1:25K) (ARPAS, 2019) (Figure 5-12. We used both maps of mean uranium contents and the new permeability map of rocks to develop a GRP map of Sardinia with higher resolution. Similar to the previous GRP map, a cross-tabulation matrix (Table 5-4) was used to categorize the GRP of Sardinian geo units. As a result of this matrix, a GRP map was developed, which expresses the geogenic radon release potential in ordered classes (very low to very high). As can be seen in Figure 5-13, this map can be considered as a powerful tool that can predict radon potentials even on the municipal scale. The GRP of three major municipalities of Sardinia (Cagliari, Olbia and Sassari) are also shown in this Figure. According to the GRP map, higher radon potential is predicted for Olbia compared with Cagliari and Sassari.

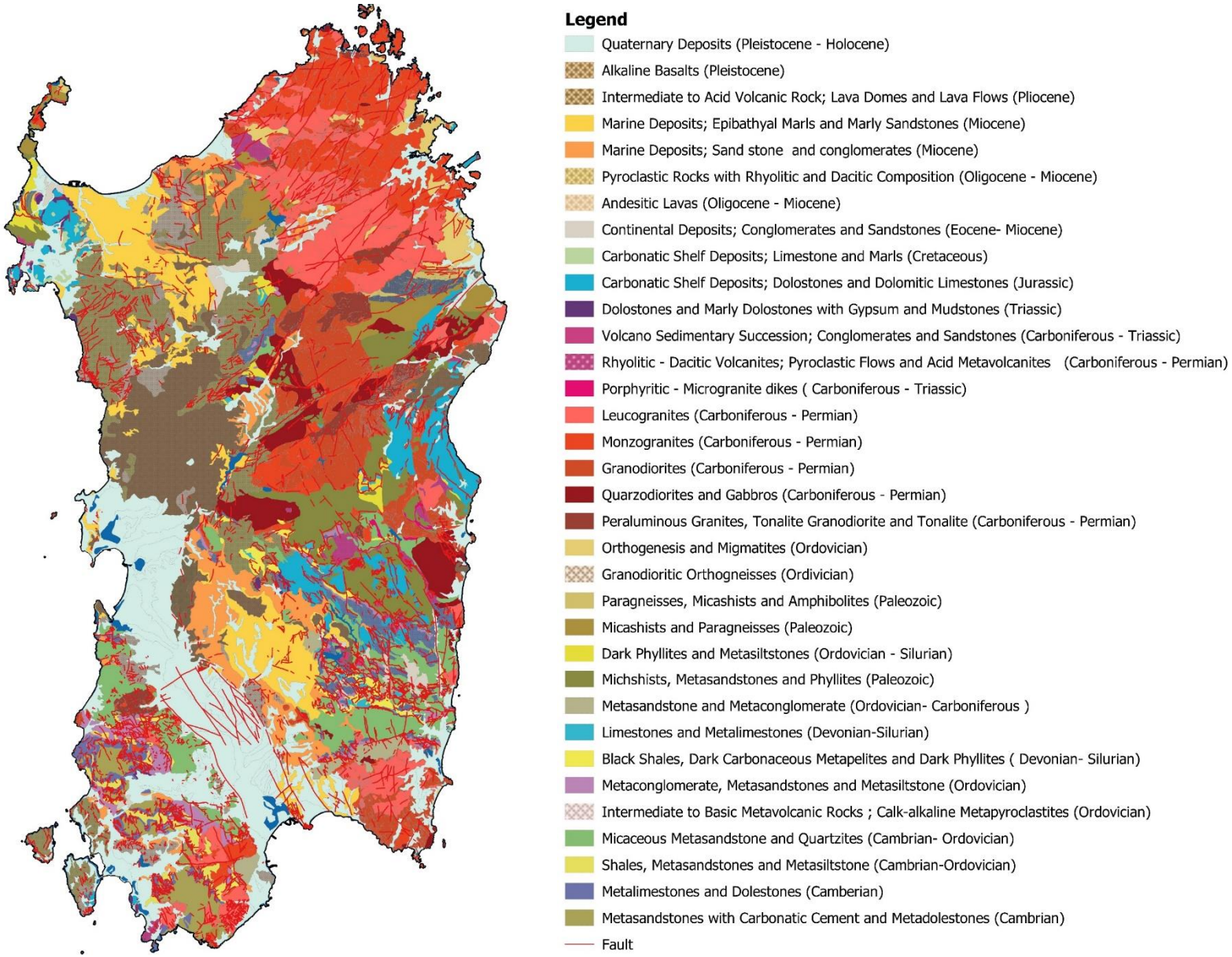

Figure 5-10: The map of Sardinian geo units, including the major fault lines. Modified after (Carmignani et al., 2016)

Table 5-3: Mean uranium contents of Sardinian geo units

Categories of lithology	**Description based on the geological map** (Carmignani et al., 2016)	**Uranium data**		
		Mean / [Range] (ppm)	**Reference**	**Category ***
Quaternary Deposits	Quaternary Deposits (Pleistocene - Holocene)	1.30	ARPAS, 2016	2
Marine Carbonatic Sediments	Marine Deposits; Epibathyal marls and marly sandstones (Miocene)	0.97	ARPAS, 2016	1
Marine and Continental Clastic Sediments	Marine Deposits; Sandstone and conglomerates (Miocene)	1.6	ARPAS, 2016	2
	Continental Deposits; Conglomerates and Sandstones (Eocene- Miocene)			
Carbonatic Shelf Deposits	Carbonatic Shelf Deposits; limestone and marls (Cretaceous)	0.97	ARPAS, 2016	1
	Carbonatic Shelf Deposits; Dolostones and dolomitic Limestones (Jurassic)			
	Dolostones and marly dolostones with gypsum and mudstones (Triassic)			
Meta Carbonatic rocks	Limestones and Metalimestones Devonian-Silurian	0.5± 0.6	Bezzon et al., 2010	1
	Metasandstones with carbonatic cement and Meta dolostones (Cambrian)			
	Metalimestones and dolostones (Cambrian)			
Black Shale and Dark phyllites	Black shales, dark carbonaceous metapelites and dark phyllites (Devonian- Silurian)	[4.5- 50]	Fello et al., 2006	5
Meta Clastic Rocks	Shales, Metasandstones and Metasiltstones (Cambrian-Ordovician)	2.5± 1.1	Bezzon et al., 2010	3
	Dark Phyllites and Metasiltstones (Ordovician - Silurian)			
	Metasandstones and Meta conglomerates (Ordovician- carboniferous)			
	Micaceous metasandstones and quarzites (Cambrian- Ordovician)			
	Metaconglomerates, meta sand stones and Metasiltstones (Ordovician)			
Micashists, Metasandstone	Micashists, meta sandstones and phyllites (Paleozoic)	2.59	ARPAS, 2016	3
Volcano Sedimentary Succession	Volcano Sedimentary succession; Conglomerates and Sandstones (Carboniferous - Triassic)	-	ARPAS, 2016	NA
Intermediate to Acid Volcanic Rock	Intermediate to acidic Volcanic rock; Lava domes and lava flows (Pliocene)	3.8	ARPAS, 2016	3
Alkaline Basalts	Alkaline Basalts (Pleistocene)	1.05	ARPAS, 2016	2
Pyroclastic Rocks with Rhyolitic and Dacitic Composition	Pyroclastic rocks with Rhyolitic and dacitic composition (Oligocene - Miocene)	0.97	ARPAS, 2016	1
	Andesitic Lavas (Oligocene - Miocene)			
Porphyritic - Micro granite dikes	Porphyritic - microgranite dikes (Carboniferous - Triassic)	[4-30.9] 10	Ielsch et al., 2010	5
Rhyolitic - Dacitic Vulcanites	Rhyolitic - dacitic vulcanites; Pyroclastic flows and Acid Metavolcanites (Carboniferous - Permian)	[4-10] 7.62	Ielsch et al., 2010	4
Intermediate to Basic Metavolcanic Rock	Intermediate to basic Metavolcanites rock; calc-alkaline metapyroclastites (Ordovician)	3.40	ARPAS, 2016	3
Leucogranites	Leucogranites (carboniferous - Permian)	4.24	Xhixha et al., 2014	4
Monzogranites	Monzogranites (carboniferous - Permian)	4.85	Xhixha et al., 2014	4
Granodiorites	Granodiorites (carboniferous - Permian)	2.97	Xhixha et al., 2014	3
Tonalitic granodiorites and Tonalite	Peralluminous Granites, Tonalitic granodiorites and tonalite (carboniferous - Permian)	1.93	Xhixha et al., 2014	2
Quarzodiorites and Gabbros	Quarzodiorites and Gabbros (carboniferous - Permian)	1.28	Xhixha et al., 2014	2
Micashists, Paragneisses and Amphibolites	Paragneisses, Micashists and Amphibolites (Paleozoic)	2.59	ARPAS, 2016	3
Granodioritic Orthogneisses	Granodioritic Orthogneisses (Ordovician)	4.40	Xhixha et al., 2014	4
Orthogenesis and Migmatites	orthogenesis and migmatites (Ordovician)	4.55	Xhixha et al., 2014	4

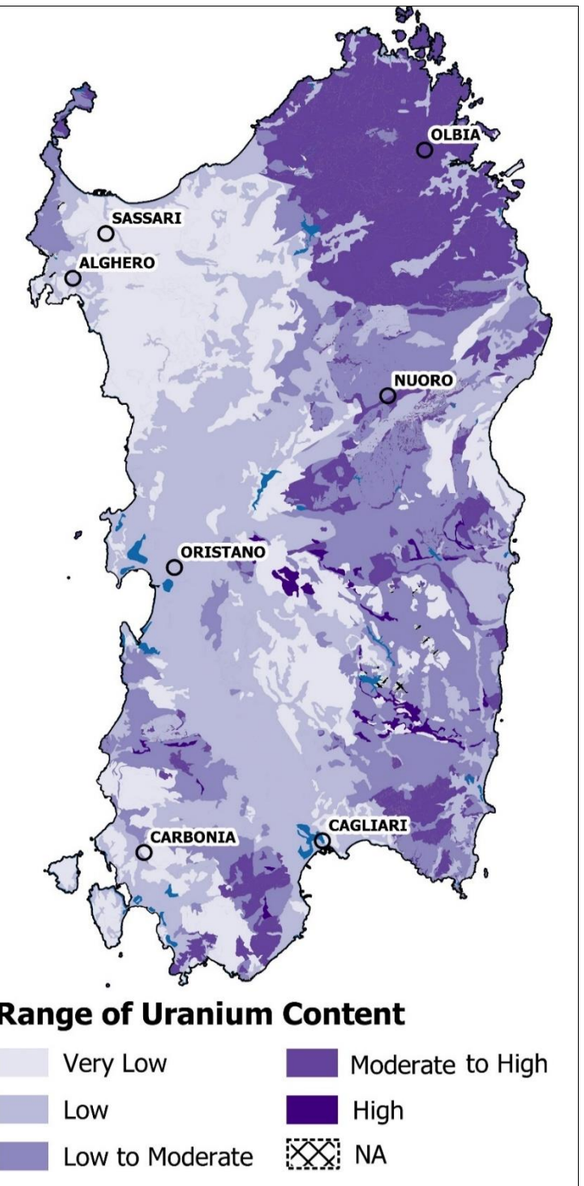

Figure 5-11: Map of the hypothetical distribution of mean uranium in Sardinian rocks.

***Categorization according to** (Ielsch et al., 2010)

1 Very Low: $U_{mean} \leq 1$ ppm
2 Low : $1 < U_{mean} \leq 2$ ppm
3 Low to Moderate: $2 < U_{mean} \leq 4$ ppm
4 Moderate to High: $4 < U_{mean} \leq 8$ ppm
5 High : $U_{mean} > 8$ ppm

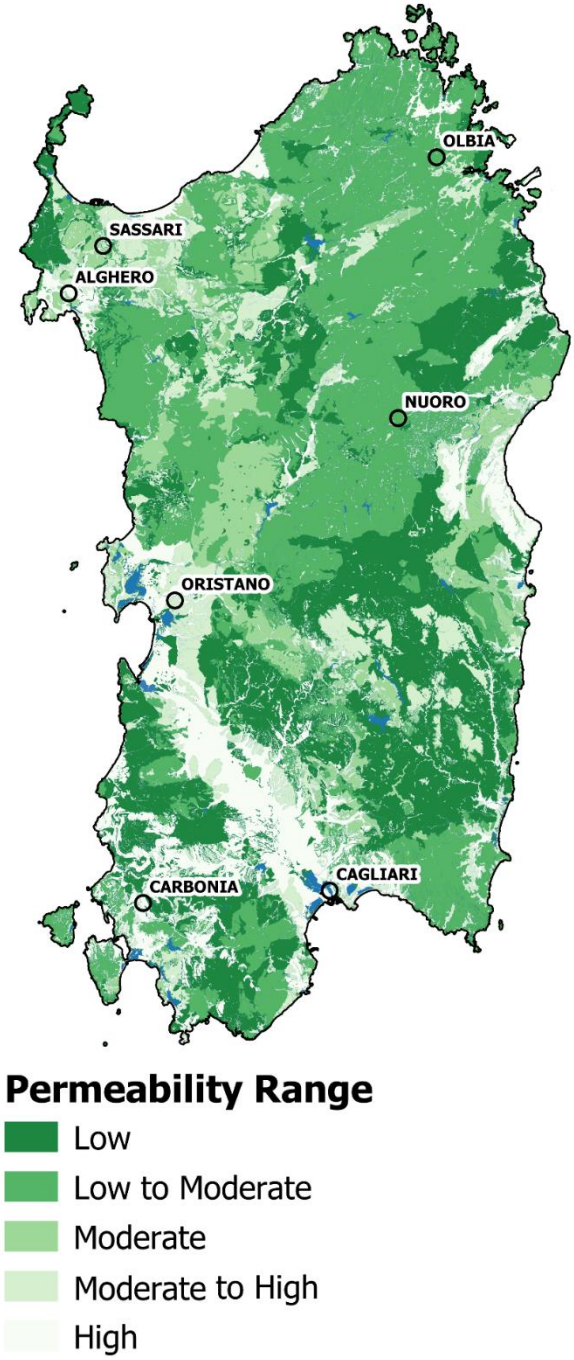

Figure 5-12: Permeability map of Sardinia's substrates (ARPAS, 2019)**.**

Table 5-4: The GRP categorization matrix

GRP Categorization Matrix		***Radon Source Potential***				
		Very Low	*Low*	*Low to Moderate*	*Moderate to High*	*High*
Radon Transport Potential	*Low*	Very Low		Low	Low to Moderate	Moderate to High
	Low to Moderate					
	Moderate	Very Low	Low	Low to Moderate	Moderate to High	High
	Moderate to High	Low	Low to Moderate	Moderate to High	High	Very High
	High					

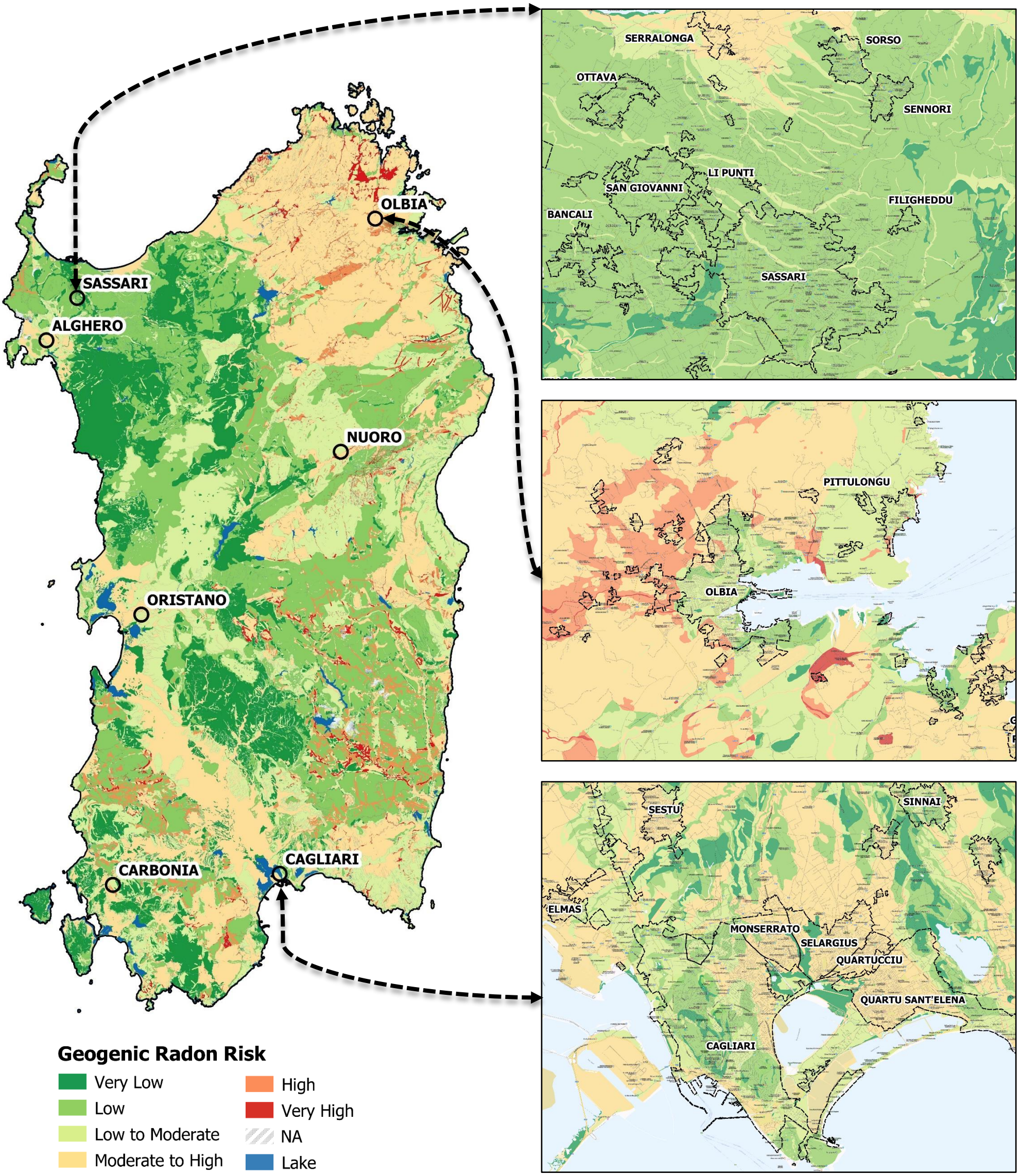

Figure 5-13: Geogenic radon potential (GRP) map of Sardinia together with predicted GRP maps of the three most important Sardinian municipalities.

5.3 Comparison of GRP Map Produced Based on Extrapolation from Similar Geologies with the GRP Obtained from Local Geogenic Information

As shown in Figure 5-14, a simple comparison of both GRP maps reveals that there is a good agreement for the majority of the areas; however, for some minor areas, there is considerable conflict in the prediction of geogenic radon potentials. It also expresses that although extrapolation of radon data from relatively distant geo units (i.e., Germany and Czech) can be a quick and cheap way to get a rough overview of radon potential in Sardinia, misleading results can be achieved for areas where the geology has experienced local evolutions like alteration, uranium mineralization and enrichment in heavy minerals in various sedimentary facies of shallow-marine placer deposits. In other words, correlating similar geologies would be very complicated while considering the specific geological events that might occur in the area where the data is being extrapolated. Therefore, for such areas extrapolating radon behavior of geological units relative far away should be preceded by carrying out further tests for the evaluation of the contents of the Rn producing elements.

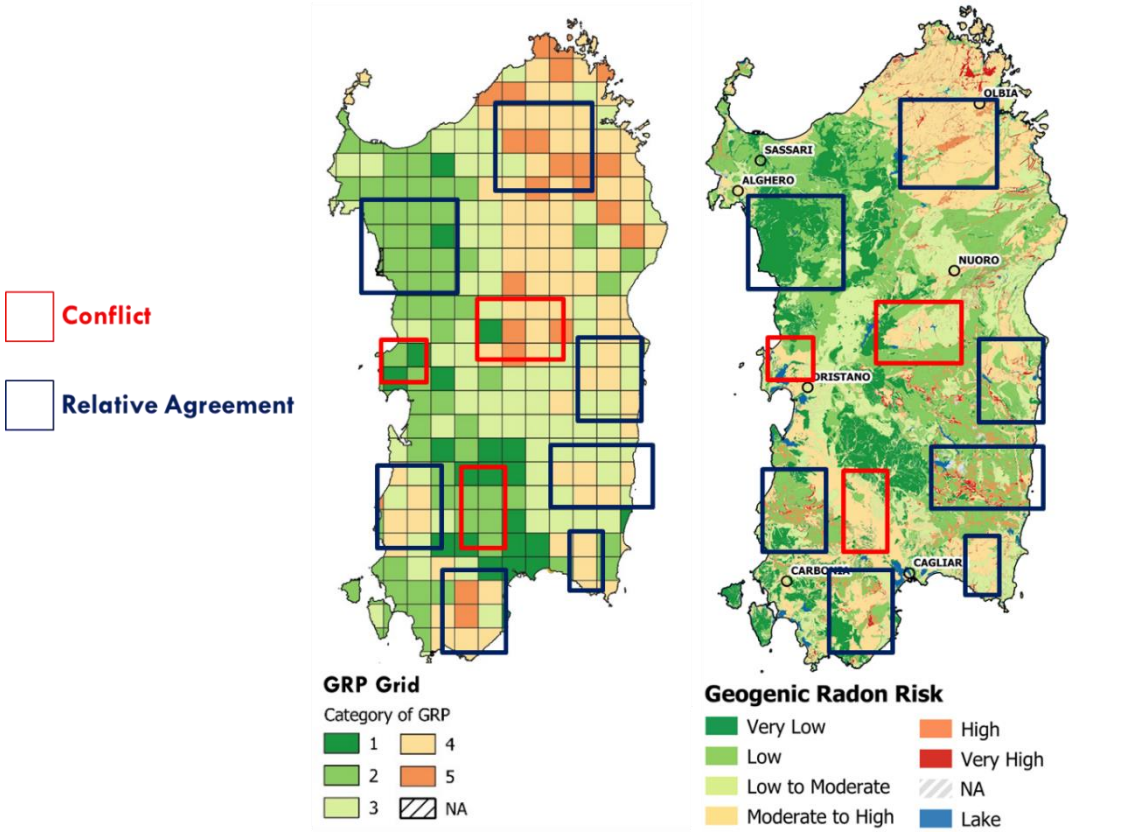

Figure 5-14: Comparison of GRP maps created based on extrapolation of radon data from German and Czech geotypes (left) and local geogenic data available for Sardinia (right).

5.4 Natural Radioactivity and Radon Exhalation Rate of Sardinian Dimension Stones

Due to the ever-growing public concern about radon risk arising from building materials, the radon exhalation rates and the natural radioactivity of eighteen dimension stones mostly used in Sardinia and widely exported worldwide have been estimated by means of laboratory tests. Some of the quarrying companies that operate within the Sardinian territory provided the samples to be tested, which include twelve granitoids, four pyroclastic rocks and two basalts. The Activity Concentration Index (I_γ), the External Radiation Hazard Index (H_{ex}) and the Radium equivalent activity (Ra_{eq}) were calculated for each rock sample under investigation, based on the estimated values of ^{222}Rn exhalation rate and ^{226}Ra, ^{232}Th and ^{40}K radioactivity concentration.

Although measurements of U/Ra activity can provide useful information about radon release potential, the exhalation of Radon (^{222}Rn) from a given rock surface is strongly influenced by the petrographic and petro-physical characteristics of the rock itself (i.e., micro-fissures, grain size, arrangement, alteration degree and contact surfaces between constituents) (Amaral et al., 2012). Therefore, real-time measurements of ^{222}Rn exhalation rates need to be performed in order to estimate the actual risk associated with a given natural stone (Chen et al., 2010). Those measurements must be performed on samples in the form of blocks or slabs, as grounding the rock increases the specific surface and decreases the grain size, thus producing an overestimation of the radon exhalation rate and consequently a false alarm about the actual risk associated with the material under investigation (Pereira et al., 2013).

This section discusses the results of the experimental tests carried out on eighteen Sardinian dimension stones, which were aimed at estimating their natural radioactivity and the potential for radon emission. All samples considered in the study were provided by quarrying companies that operate in Sardinia and include twelve granites (Rosa Beta to Grigio Majore), two basalts (Basalto Rosso Vino and Basalto Sardo) and four pyroclastic rocks (Pietra di Serrenti to Porfido Rosso di Arbatax). Three criteria were taken into account for the selection of the rocks to be investigated: i) to be commonly available in the market; ii) to belong to those categories of rocks that are believed to pose a higher risk, according to the results of former studies (Al-Azmi et al., 2018), (Chen et

al., 2010), (Stoulos et al., 2003); iii) to be representative of different geological settings related to different commonly widespread geodynamic environments.

It is worth highlighting as the use of the natural stones under investigation is testified since prehistoric age by many examples of engineering and architectural works, both in private dwellings and public buildings, throughout the Sardinian territory. Entire villages in Sardinia were built with boulders of natural stones provided by the quarries operating nearby. Nowadays, the use of the same natural stones, which have been recently categorized as Global Natural Heritage Stone Resources (GHSE) (Careddu & Grillo, 2015), (Nicola Careddu & Grillo, 2019), has become essential for the restoration of those historical constructions, while many touristic locations along the coastline have been recently built with the same stones to recall the Sardinian heritage resources. The wide use of the construction material under investigation, which is not strictly related to ornamental purposes, highlights the relevance of the risk evaluation hereby discussed.

5.4.1 Materials and Methods

5.4.1.1 Geological and Petrographic Characteristics of the Tested Samples

The most important dimension stones extracted in Sardinia are granites, limestone, basalt and pyroclastic stones (generally marketed as trachyte, without distinction). Granites and limestones are mainly quarried in central-eastern and north-eastern Sardinia, while the extraction sites of basalts and pyroclastic rocks are widespread in a large portion of central-western Sardinia (Careddu et al., 2018).

In Sardinia, outcropping rocks give evidence of global geological events that occurred over periods dating back from Cambrian to Quaternary. Rocks belonging to the Palaeozoic Era cover about half of the island's surface (13,000 out of 24,000 km^2) (Carmignani et al., 2016).

Granites constitute the calc-alkaline plutonic complex, extended for about 6,000 km^2 (Ghezzo & Orsini, 1982). This outcrop is a sequence of Corsican- Sardinian batholite, which is closely related to the evolution of the south European Variscan belt (Paquette et al., 2003). The Sardinian batholite consists mainly of monzogranites (65%) and, subordinately, leucogranites, tonalites and granodiorites (34%). Gabbroic masses are scarce and crop out mainly in the south of Sardinia (Puccini et al., 2014). Zircon is probably the main ^{238}U and ^{232}Th bearing mineral in the less evolved granites (such as Rosa Beta and Grigio Malaga), while Y-bearing phases, such as allanite and xenotime,

become progressively more important during the evolution of magmas (Puccini et al., 2014). Pyroclastic rocks and basalts are linked to the geodynamic evolution of the Mediterranean area, which led to intense volcanism coeval or alternated to the deposition of marine and continental sediments of the transgressive and regressive phases that occurred between the Middle Eocene and the Miocene. The formers are related to two main geological events: the west-dipping subduction of the Adria plate, which gave a calc-alkaline volcanic cycle in the Oligocene–Miocene represented by prevailing andesitic suites and the opening of the Algero-Provençal and North Tyrrhenian basins associated with volcanism from calc-alkaline to peralkaline, with prevailing riodacitic suites. The basalts are related to the extensional tectonics that affected in the Pliocene, the south-Tyrrhenian area following the opening of the S-Tyrrhenian Basin. Continental and (rare) marine deposits were covered and partially interlayered with interpolate basaltic lava flows, alkaline, transitional and sub-alkaline volcanic cycle (Carmignani et al., 2016).

Table 5-5: Main features and exploiting quarries of tested samples

Rock type	**Commercial name**	**Petrographic name***	**Main quarries exploiting the dimension stone**
Granitoid rock (G)	Rosa Beta Acceso	Monzogranite	Aggius, Arzachena, Luogostano, Luras, Sant Antonio di Gallura, Tempio P.
	Rosa Beta (β)	Biotite Monzogranite	
	Giallo San Giacomo	Biotitic leucogranite-equigranular	Luogostano, Olbia, Sant Antonio di Gallura
	Rosa Ferula	Leucogranite- equigranular	Orosei
	Grigio Malaga	Tonalitic granodiorite	Buddusò
	Grigio Sardo Sarrabus	Leucogranite	Castiadas
	Granito di Villasimius	Monzogranodiorite	Villasimius
	Rosa Limbara	Monzogranite-non-equigranular	Aggius, Calangianus, Luras, Sant Antonio di Gallura (Priatu)
	Rosa Gamma	Leucogranite	Luras
	Bianco Sardo	Leuco-monzogranite	Buddusò
	Grigio Majore	Monzogranite-equigranular	Villagrande Strisaili, Tortoli
	Porfido Rosso di Arbatax	Porphyry granite	Arbatax
Pyroclastic rock (PR)	Trachite di Ozieri	Ignimbrite	Ozieri
	Pietra di Serrenti	Dacite and Ryodacite	Serrenti
	Trachite Verde di Fordongianus	Dacite and Ryodacite	Fordongianus
	Trachite di Bosa	Dacite and Ryodacite	Bosa
Basalt (B)	Sardinian basalt	Basalt	Bauladu, Mogoro, Paulilatino, Sardara
	Basalto Rosso Vino	Basalt	Paulilatino

*petrographic classification from (N. Careddu & Grillo, 2015; Nicola Careddu & Grillo, 2019; Primavori, 2011; Puccini et al., 2014)

Figure 5-15: Sardinian dimension stones tested for radon emission (Careddu & Grillo, 2015)

The experimental tests discussed in this study were carried out on the eighteen dimension stones represented in Figure 5-15, which belong to different geodynamic settings. The granitic samples represent a Palaeozoic crust formed in a collisional orogen; the calc-alkaline pyroclastic rocks were emplaced in a continental volcanic arc related to Cenozoic

subduction and finally, basaltic lava flows emplaced in an anorogenic setting. Table 5-5 summarizes the main features and the provenance of each investigated rock sample (Careddu & Grillo, 2015), (Careddu and Grillo 2019), (Puccini et al., 2014), (Primavori, 2011).

A simplified geological map of Sardinia with the location of the main quarries that exploit the dimension stones under investigation is reported in Figure 5-16. The main geochemical features of the tested rocks are reported in (Primavori, 2011). The activity concentration of radionuclides in those rocks varies from about 10 Bq kg^{-1} of ^{226}Ra in basalts to 1180 Bq kg^{-1} of ^{40}K in granites. Table 5-6 reports the mean values and the standard deviation of the activity concentration of ^{226}Ra, ^{232}Th, ^{40}K determined for the same lithotypes tested in this study (Carrera et al., 1997; Primavori, 2011; Puccini et al., 2014).

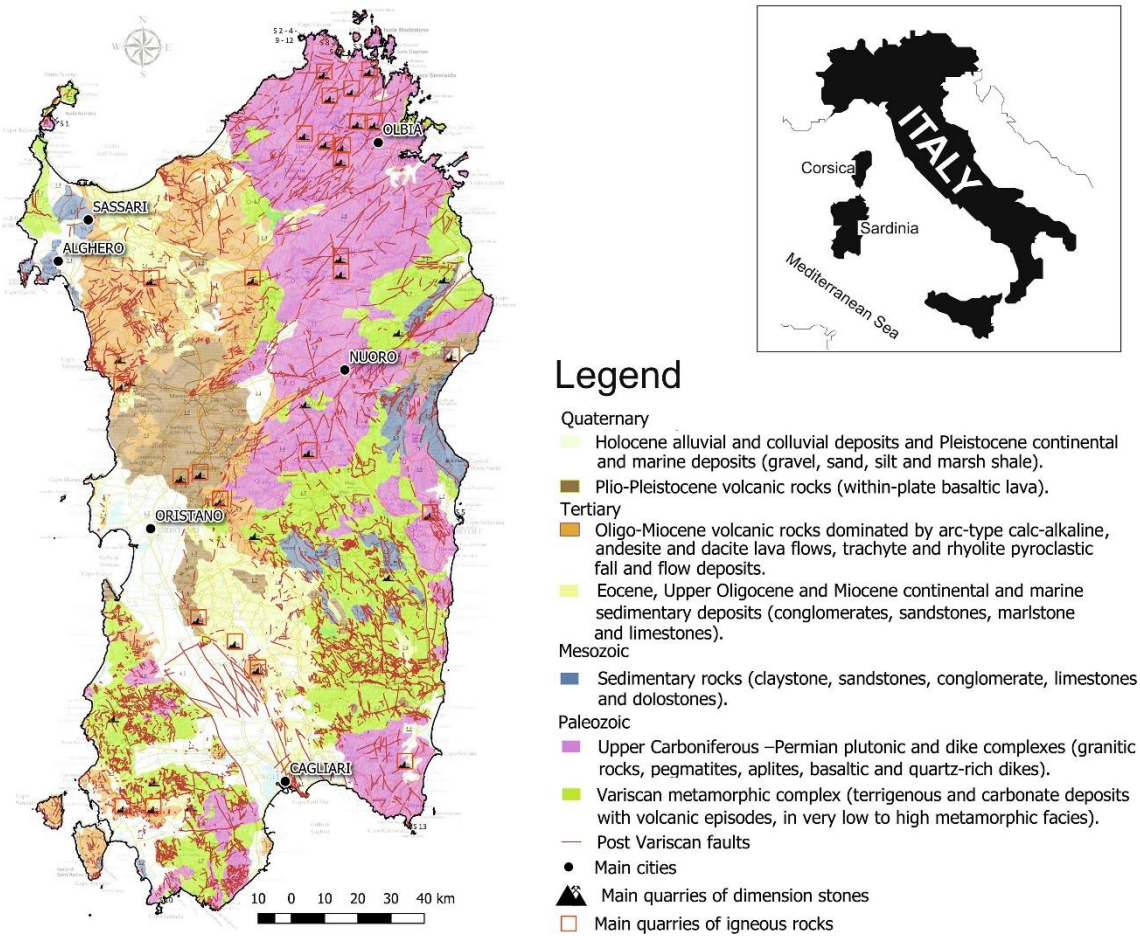

Figure 5-16: Simplified geological map of Sardinia with main quarries of dimension stones, (after (Careddu & Grillo, 2015)**, modified)**

Table 5-6: Mean values and standard deviation of activity concentration of ^{226}Ra, ^{232}Th, ^{40}K published in the literature for the same lithotypes tested in this study.

Rock Type	n. of data	Radionuclide Concentration (Bq kg^{-1})			Refs.
		^{226}Ra ± σ	^{232}Th ± σ	^{40}K ± σ	
Granites	10	41 ± 17	53 ± 22	1068 ± 137	(Carrera et al., 1997)
Granites	17	47 ± 32	66 ± 33	1013 ± 215	(Primavori, 2011)
Granites	7	–	69 ± 29	1177 ± 400	(Puccini et al., 2014)
Trachytes	7	31 ± 5	42 ± 4	1038 ± 252	(Primavori, 2011)
Basalts	6	10 ± 3	14 ± 4	442 ± 100	(Primavori, 2011)

5.4.2 Measurement of Radon Exhalation Rates

Direct measurements of radon exhalation rates were performed on rock slabs about 3-4 cm thick, with sides between 9 and 21 cm and total emitting surface from 490 to 2100 cm^2. The volume and porosity were estimated for all samples, according to ISRM (Franklin, 1979). Each sample was first polished and then enclosed in a 10.4-liter closed chamber, together with a real-time radon-monitoring instrument (Radex MR-107), which measures the radon activity growth over time (Chen et al., 2010), (Leonardi et al., 2018), (Zhang et al., 2012). According to Leonardi et al., 2018, the dynamic method was applied in order to overcome problems of chamber leakages since the chamber was not perfectly airtight. Radon concentration, temperature and relative humidity inside the chamber were registered each hour, for an overall test duration of about 120 h. The radon activity concentration inside the sealed chamber is described by the two-dimensional diffusion theory (Sahoo and Mayya 2010). Considering both the back diffusion and the radon leakage, the following formula is used to express the variability of the radon concentration over time:

$$\textbf{Equation 5-2: } C(t) = C_0 e^{-t\lambda_e} + C_m(1 - e^{-t\lambda_e})$$

where λe is the effective radon decay constant (h^{-1}), which accounts for the radon decay, the leak rate of the system and the back diffusion; C_0 and C_m are the radon activity concentration (Bq m^{-3}) at time = 0 and its maximum value respectively (Leonardi et al., 2018). As shown in Figure 5-17 for Rosa Limbara, the activity growth was modeled for all samples by using the nonlinear least-squares fitting of the experimental data with Equation 5-2 (Sahoo and Mayya 2010), (Kemmer & Keller, 2010), (Tan & Xiao, 2011). The resulting parameters λ_e and C_m allowed the calculation of the exhalation rate (E_{Rn}), according to Equation 5-3 (Ishimori et al., 2013):

$$\textbf{Equation 5-3: } E_{^{222}Rn} = \frac{\lambda_{eff} C_m V}{S}$$

where V_{eff} is the effective volume of the calibration container (m^3) and S is the sample's total surface area (m^2) (Leonardi et al., 2018). The radon exhalation rates were determined for all samples under the exam, according to the procedure above described.

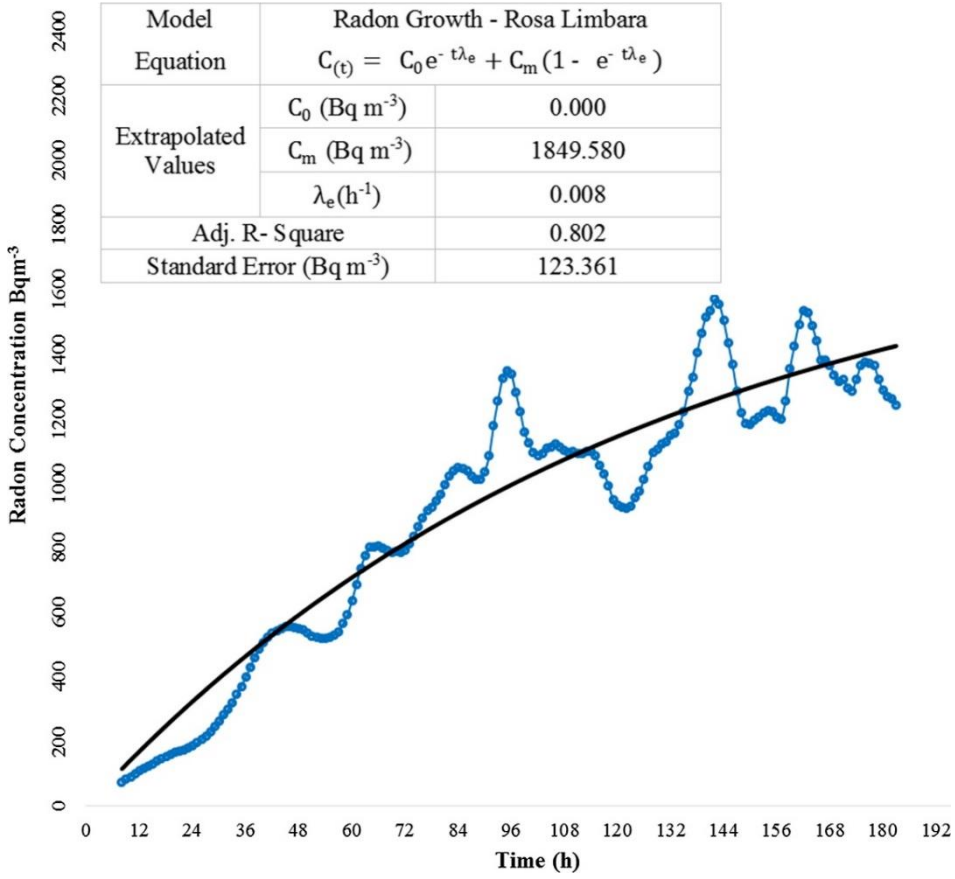

Figure 5-17: Radon activity concentration vs. time (Rosa Limbara).

5.4.3 Measurement of Radionuclide Activity Concentrations

In order to perform the measurements of radionuclide activity concentration, a small part of each sample was crushed and grounded to a fine powder to obtain the same grain size, shape and similar mass and volume as the reference samples, providing similar detection efficiency. About 100 gr (accuracy ± 0.01 g) of the powdered sample, with grain size less than 1 mm, were separated and oven-dried. The 100 gr sub-samples were placed inside cylindrical polyethylene containers, sealed and left undisturbed for four weeks, in order to reach the radioactive equilibrium between radon and its progenies. The activity concentrations of ^{226}Ra, ^{232}Th and ^{40}K were analyzed utilizing gamma-ray spectrometry performed with a 1024 channels NaI (Tl) scintillation detector (3 × 3 in.), which was protected from background radiation with a lead shield. The acquisition of the spectra was carried out using the Ortec MAESTRO software. Radioactive sources of ^{137}Cs and

^{60}Co were used for energy calibration. The activity of each reference radioactive source was known, making the efficiency calibration dispensable. The energy resolution was calculated to be 10.36%, regarding the full width of the peak at half of the maximum count level of 661 keV photopeak for the ^{137}Cs source. Three reference samples of Uranium, Thorium and Potassium were prepared using IAEA (International Atomic Energy Agency) sources and a Potassium salt of acknowledged chemical composition. The spectrum of each analyzed sample was obtained as the weighted sum of the three spectra ^{226}Ra, ^{232}Th and ^{40}K, plus the background spectrum, the weight of each spectrum depending on the mass (i.e., the activity) of the radioisotope in the sample under analysis. The specific activity of samples was estimated according to the maximum likelihood algorithm (Ashrafi & Jahanbakhsh, 2019). The variance reduction technique was applied to calculate both the weights and the standard deviations. The correspondence between experimental data and theoretical values was verified by performing and graphing the linear combination of the three appropriately weighted spectra. The correspondence between calculated and experimental spectra was excellent in all cases; an example is given in Figure 5-18 for Rosa Limbara. By using the ^{238}U and ^{226}Ra mass ratio ($U_{natural}$: ^{226}Ra = 1: 3.376 × 10^{-7}) (Erdi-Krausz et al., 2003), the specific activity of ^{226}Ra was also determined.

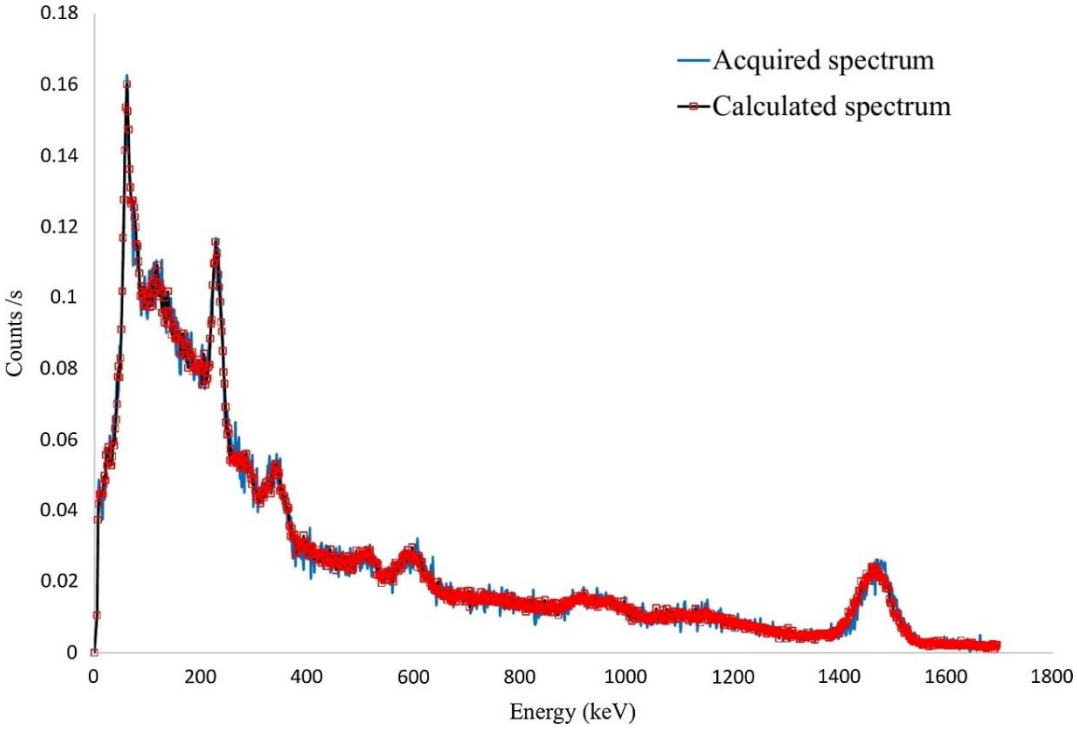

Figure 5-18: Comparison of calculated and experimental spectra for Rosa Limbara.

5.4.4 Exposure Indexes

The contribution of building materials to radon exposure can be expressed either as whole-body exposure to gamma radiation or an internal dose of inhaled radon (Pereira et al., 2013). To evaluate the exposure to gamma radiation, which mainly originates from the presence of primordial radionuclides (i.e. ^{226}Ra, ^{232}Th and ^{40}K) in the material under investigation, three indexes are commonly used: the activity concentration index (I_γ) (EC, 2000), the external radiation hazard (H_{ex}) (Beretka & Mathew, 1985) and the Radium equivalent activity (Ra_{eq}) (Ashrafi & Jahanbakhsh, 2019). Equation 5-4 to Equation 5-6 describe the three indexes:

Equation 5-4: $$I_\gamma = \frac{C_{Ra}}{300^{Bqkg^{-1}}} + \frac{C_{Th}}{200^{Bqkg^{-1}}} + \frac{C_K}{3000^{Bqkg^{-1}}}$$

Equation 5-5: $$H_{ex} = \frac{C_{Ra}}{370^{Bqkg^{-1}}} + \frac{C_{Th}}{359^{Bqkg^{-1}}} + \frac{C_K}{4810^{Bqkg^{-1}}}$$

Equation 5-6: $$Ra_{eq} = C_{226Ra} + 1.43C_{232Th} + 0.077C_{40K}$$

where C_{Ra}, $C_{Th\ and}$ C_K are the activity concentrations of ^{226}Ra, ^{232}Th and ^{40}K, respectively. The building materials should be restricted in their use if their activity concentration index I_γ is higher than 1, which corresponds to an effective annual dose exceeding 1 mSv (EC, 2000). However, the limitation only applies to the hypothesis of the massive use of the indicted material (i.e., construction of structural walls and/or interior coating of confining surfaces). The H_{ex} index must be less than the unity for the radiation hazard to be negligible (Krieger, 1981) and Ra_{eq} should not exceed the value of 370 Bq kg^{-1} for the material to be used for newly built dwellings and public buildings (UNSCEAR, 2000).

5.4.5 Results and Discussion

5.4.5.1 Measurements Results and Risk Indexes

Table 5-7 summarizes the test results and the radiological indexes, together with the porosity of each sample. As regards radon exhalation rates, the detected levels were found between the minimum detectable value and a maximum value of 0.92 ± 0.05 Bq m^{-2}h^{-1} (Pietra di Serrenti); the average value was 0.48 ± 0.29 (SD). The lowest exhalation rates were estimated for basalts. Although granites gave evidence of wide variability in the results, higher mean values were generally found for granites compared to other rock types. Among granites, with some exceptions, higher mean exhalation rates were detected

for Leucogranites compared to Monzogranites. The results are comparable to those reported by several authors for rocks of the same commercial type or same geological environment (Carrera et al., 1997), (Al-Jarallah, 2001), (Hassan et al., 2011), (Pereira et al., 2012).

Table 5-7: Radon exhalation rates, radionuclide contents and radiological indexes.

Sample name	Porosity	Rn exhalation rate ± SE*	Radionuclide Concentration (Bq kg^{-1})			I_γ	H_{ex}	Ra_{eq}
		(Bq m^{-2}h^{-1})	^{226}Ra ± σ*	^{232}Th ± σ*	^{40}K ± σ*			(Bq kg^{-1})
Rosa Beta Acceso	0.9	0.33 ± 0.06	46 ± 2	45 ± 1	762 ± 53	0.63	0.46	169
Rosa Beta (β)	0.8	0.108 ± 0.009	26 ± 2	55 ± 2	1049 ± 57	0.71	0.5	186
Giallo San Giacomo	1.3	0.39 ± 0.02	80 ± 2	73 ± 1	1057 ± 48	0.98	0.72	265
Rosa Ferula	1.1	0.33 ± 0.03	33 ± 2	82 ± 1	1376 ± 53	0.98	0.69	257
Grigio Malaga	0.9	0.22 ± 0.06	18 ± 2	53 ± 1	709 ± 47	0.56	0.4	149
Grigio Sardo Sarrabus	0.8	0.91 ± 0.09	35 ± 2	74 ± 1	945 ± 51	0.8	0.58	214
Granito di Villasimius	1.0	0.1713 ± 0.0008	23 ± 2	36 ± 1	813 ± 48	0.53	0.37	137
Rosa Limbara	1.7	0.85 ± 0.06	25 ± 2	61 ± 1	956 ± 57	0.71	0.5	186
Rosa Gamma	0.8	0.31 ± 0.06	31 ± 2	62 ± 1	1045 ± 54	0.76	0.54	200
Bianco Sardo	1.2	0.59 ± 0.02	28 ± 2	97 ± 1	1078 ± 55	0.94	0.68	251
Grigio Majore	0.8	0.68 ± 0.06	47 ± 2	86 ± 1	1206 ± 54	0.99	0.71	264
Porfido Rosso di Arbatax	2.3	0.91 ± 0.09	29 ± 2	68 ± 1	1140 ± 52	0.82	0.58	214
Trachite di Ozieri	24.2	0.29 ± 0.04	8 ± 2	12 ± 1	238 ± 54	0.17	0.12	43
Pietra di Serrenti	12.9	0.92 ± 0.05	35 ± 3	41 ± 2	1778 ± 72	0.92	0.63	231
Trachite verde di Fordongianus	34.0	0.26 ± 0.01	33 ± 3	42 ± 2	1826 ± 59	0.93	0.63	234
Trachite di Bosa	12.2	0.34 ± 0.05	20 ± 2	32 ± 2	1436 ± 58	0.71	0.48	177
Sardinian basalt	5.7	ND*	8 ± 2	9 ± 1	345 ± 50	0.19	0.13	48
Basalto Rosso Vino	7.5	ND*	3 ± 2	4 ± 1	308 ± 49	0.13	0.09	33

SE*: Standard Error of the Estimated Value, σ*: Associated Uncertainty (1σ), ND*: Not Detectable.

The activity concentration of ^{226}Ra, ^{232}Th and ^{40}K was found to be consistent with the literature data reported in Table 5-6 and, specifically, in the range from 3 to 80 Bq kg^{-1} (mean value 29) for ^{226}Ra, from 4 to 97 Bq kg^{-1} (mean value 52) for ^{232}Th and from 238 to 1826 Bq kg^{-1} (mean value 1004) for ^{40}K, in. The mean radionuclide concentration of ^{226}Ra and ^{232}Th resulted respectively lower and slightly above the mean reference value of 50 Bq kg^{-1} (both for ^{226}Ra and ^{232}Th) (UNSCEAR, 2000). The mean activity concentration for ^{40}K resulted in twice the mean reference value of 500 Bq kg^{-1} (UNSCEAR, 2000), which may be correlated to high contents of potassium feldspar minerals in the tested samples (Primavori, 2011).

In order to assess the radiation hazard with reference to both the whole-body exposure and to radon intake (inhalation and ingestion), the radiological parameters Iɤ, Hex and Ra_{eq} were calculated (Table 5-7): I_γ varied between 0.13 and 0.99, H_{ex} between 0.09 and 0.72 and Ra_{eq} was in the range 33–265 Bq kg^{-1}. None of those indexes exceeded the reference limits. The results were found in agreement with previous studies (Puccini et al., 2014), (Carrera et al., 1997), (Ashrafi & Jahanbakhsh, 2019).

Figure 5-19 shows the contribution to the I_γ index of the radioactivity content for Potassium, Thorium and Radium. The limit of 1, beyond which the building materials should be restricted in their use, is also reported. The lower value of I_γ was observed in Basalts and Trachite di Ozieri, while the highest value was in Grigio Majore, Giallo San Giacomo e Rosa Ferula. The major contribution to radioactivity in trachyte and basalts comes from Potassium. In most granites, Thorium and Potassium contribute to about 50% each.

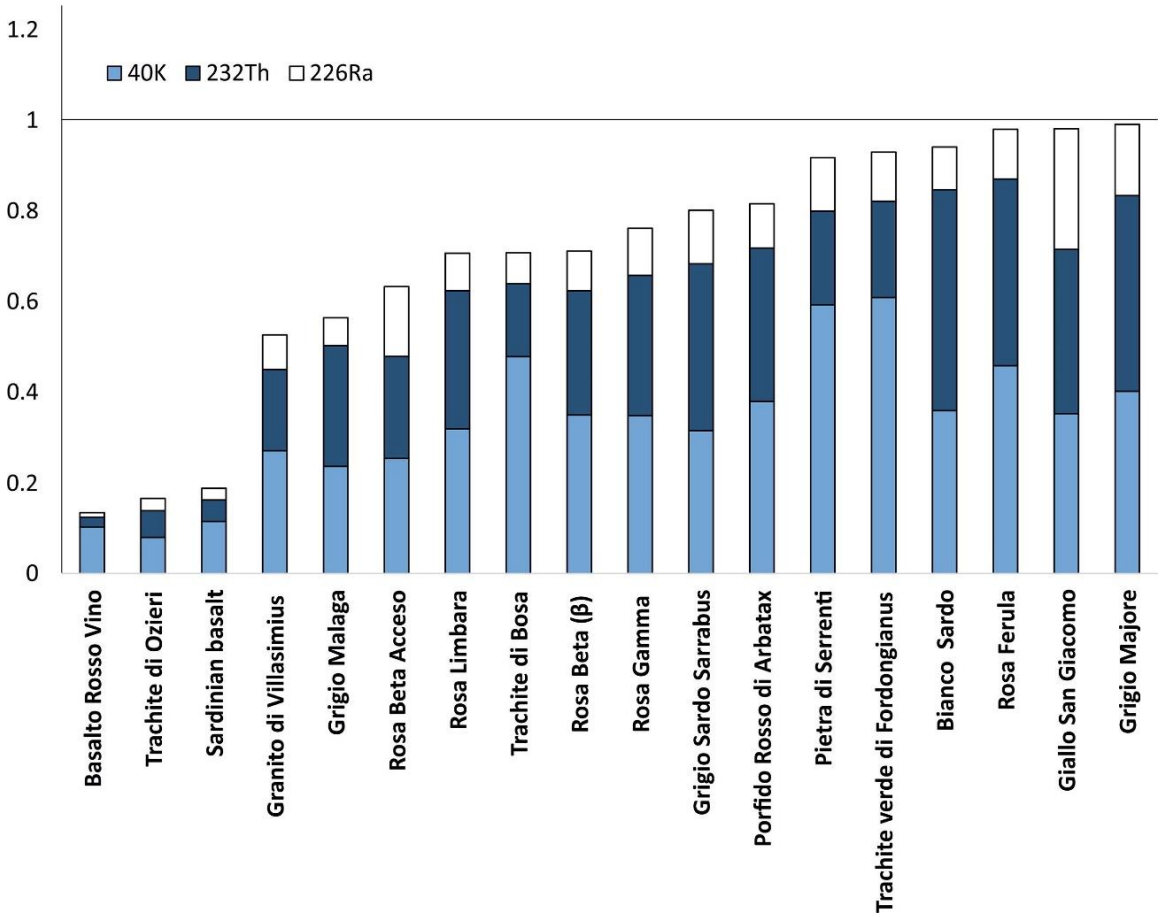

Figure 5-19: Contribution to the Iγ index calculated for each sample of ^{40}K, ^{232}Th and ^{226}Ra.

5.4.5.2 Correlation between Radium Content and Radon Exhalation Rate

Uranium/Radium levels in a given rock depend on its genetic nature, evolution degree and mineralogical composition (Amaral et al., 2012). The sample with the highest Ra activity concentration was Giallo San Giacomo (Leucogranite), even though the radon exhalation rate was not the highest compared to other samples. This can be explained by taking into account the textural features, fractures and weathering state of the rock (Pereira et al., 2013), (Pereira et al., 2012), (Cuccuru et al., 2012), which determine the possibility for radon atoms to escape from the surface of the Ra-bearing minerals or remain trapped within the rock. In fact, when a ^{226}Ra atom decays a Rn atom is formed together with an alpha particle (Amaral et al., 2012). The radon atom is ejected from the crystal or molecular lattice in the opposite direction to the surface. Based on the recoil energy and its direction, only a fraction of radon atoms escapes from the rock structure (Baskaran, 2016). The presence of microfractures and porous media in the rock structure can facilitate radon escape and increase the probability of reaching outside environments (Amaral et al., 2012), (Cuccuru et al., 2012).

In the case of rock samples Rosa Limbara, Grigio Sardo Sarrabus, Pietra di Serrenti and Porfido Rosso di Arbatax, although the activity concentration of Ra was found not to be significantly high compared to the other samples, high radon exhalation rates were observed (see also Figure 5-20). That might depend on the radium distribution within the mineral grains, the texture and size of the grains, the grain's permeability (Hassan et al., 2011) and the sample porosity. For example, the Pietra di Serrenti has an activity concentration of ^{226}Ra similar to Rosa Gamma, but the texture of Pietra di Serrenti is porfiric while that of Rosa Gamma is equigranular and holocrystalline, with larger crystals; moreover, the Pietra di Serrenti is hydrothermally altered and its porosity is about 16 times that of Rosa Gamma. In some samples, a large proportion of Uranium/Radium elements could not be confined to accessory minerals, as a result of the alteration processes that affected the rock (Pereira et al., 2012), so that the daughter nuclides (Rn) can easily getaway.

In accordance to other studies (Hassan et al., 2011), (Pereira et al., 2012), a poor correlation was found between radon exhalation rate and radium content, as the actual exhalation rate remains strongly influenced by the rock’s physical characteristics (e.g., texture, density, porosity, alteration, etc.) (Carrera et al., 1997), (Pereira et al., 2012), (Sarrou & Pashalidis, 2017). Some authors found a better correlation (Al-Jarallah, 2001),

but for exhalation rate lower than 2 Bq $m^{-2}h^{-1,}$ the relationship Ra/Rn becomes more dispersed and the correlation definitely lower.

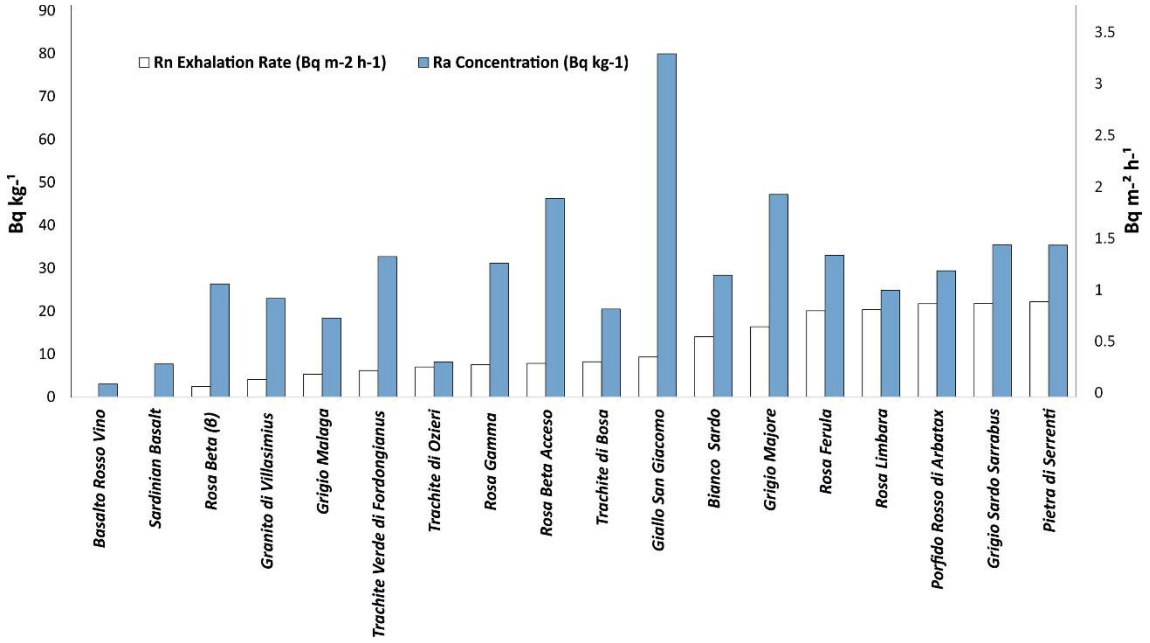

Figure 5-20: Radon exhalation rate and radium concentration for each stone sample.

5.4.5.3 Contribution of Building Materials to Indoor Radon Concentration

With the necessary schematic assumptions and based on the results of the radon exhalation test, it is possible to calculate the contribution to indoor radon accumulation of a given stone, hypothetically used to confine a defined volume.

The indoor radon concentration originated from the confining walls can be easily estimated as follows (Vukanac et al., 2016):

Equation 5-7: $C_{Rn} = E_{Rn}A_r / V_r\lambda_v$

where Ar is the area of the wall surface; V_r is the volume of the confined space and v is the room ventilation rate. The Ratio of A_r/V_r is 1.6, considering a standard room of 4 × 5 × 2.8 m^3, while the ventilation rate is assumed to be between 0.2 and 2 h^{-1} (Vukanac et al., 2016). In this study, the highest calculated value of E_{Rn} was about 0.92 Bq $m^{-2}h^{-1}$ for Pietra di Serrenti. Considering the lowest air ventilation rate (λ_v = 0.2), the estimated indoor radon concentration would be about 7.36 Bq m^{-3} (Table 5-8), thus considerably lower than the recommended level established by EC Directive 2013/59/Euratom (300 Bq m^{-3}).

Table 5-8: Estimated steady-state radon concentration (Bq m^{-3}) due to radon exhalation from the rocks with the highest calculated radon exhalation rate.

Sample name	Test duration	Recorded radon concentrations			Estimated Rn exhalation rate	Air exchange rate	Estimated indoor radon concentration
	(h)	(Bq m^{-3})			(Bq $m^{-2}h^{-1}$)	(h^{-1})	(Bq m^{-3})
Pietra di Serrenti	100 h	Min	Max	Average	0.92	0.2	7.36
		36	840	429			

An outlook of Chapter 6

In this chapter, the main sources of radon in Sardinia, including geogenic variables and building material, were investigated. As a result of this chapter, an initial version of a predictive GRP map (Figure 5-13) was produced. In the next chapter, through three experiments and additional available data for indoor radon measured at workplaces (i.e., some post offices of Sardinia), we will examine the workability of the proposed GRP model.

6 EVALUATION OF THE WORKABILITY OF THE GRP MAP OF SARDINIA

Summary

Any model for the prediction of geogenic radon potential needs to be examined in order to test the predictive power of the proposed map. This could be carried out through the comparison of test results conducted at the pilot test sites and the predicted risk category at the same location. Here in this chapter, at first, the available indoor radon data measured at Sardinian post offices will be compared with the predicted GRP levels at the same measurement point. Indoor radon concentration (IRC) not only depended on GRP levels but also can be significantly affected by anthropogenic factors like building material, ventilation rates, etc. Therefore, to understand the influence of other effective factors, a model is developed for the prediction of indoor radon concentration in workspaces of a university in Sardinia in the next section, which considers both predicted GRPs and the effect of anthropogenic factors as the input parameters of the model for IRC estimation. As mentioned before, the number of available indoor radon data for the Sardinian region was not enough to cover the whole Sardinian territory. Therefore alternative method was adopted to evaluate the GRP by investigating the radon release potential and natural radioactivity levels in non-residential areas. For this purpose, an area where the predicted GRP is supposed to be very high was selected.

Besides, the indoor radon levels in the gallery of a Sardinian dam were evaluated and the process of radon transfer from origin to the closed space of the dam was studied. The results of the validation tests confirm that the predicted model could be a promising tool to indicate the geogenic radon potentials of Sardinia.

6.1 From Geogenic radon potential toward indoor Radon in Public Buildings and Workplaces

6.1.1 Comparison of Predicted GRPs with Measured Indoor Radon Levels in Italian Post-offices of Sardinia

In February 2019, the radon project that ARPAS carried out over the years 2017-2018 on behalf of the Sardinia-ASSL (Cagliari Health Protection Company) was terminated. However, as we didn't have access to the georeferenced radon data of ARPAS radon survey, we looked for other available data. In this regard, the activity concentration of indoor radon measured at Italian post offices of Sardinia was acquired from the E-laboRad database (http://www.e-laborad.it/).

To be able to evaluate the correlation between the predicted GRP classes with the statistics of measured radon values, at first, the georeferenced data was downloaded. Then using the "Join attributes by location (Summary)" tool in QGIS software, the statistics of this data were calculated according to the classes of predicted GRPs.

Generally, geometric mean values of indoor radon are utilized to distinguish between radon characteristics. Similarly, as can be seen in **Error! Not a valid bookmark self-reference.** and only for calculated GMs of indoor radon, a good correlation with GRP can be observed. As was anticipated, the correlation is not robust (R^2=0.52). This is since radon is a complicated function of numerous parameters that can significantly affect radon concentration. However, as mentioned before and can be either seen in this section, the most influential parameter is GRP.

One can reach a better correlation if he or she considers the effect of further effective parameters. Currently, information on anthropogenic factors regarding the sampled post offices is not available therefore in order to be able to build a model that not only considers GRP classes but also depends on the anthropogenic parameters, a comprehensive radon survey was carried in workplaces of the engineering department and at the student canteen of the University of Cagliari. As will be discussed in the next section, the result of this survey was used for the development of a model for the prediction of indoor radon concentration.

Table 6-1: Statistics of measured indoor radon values in Italian post offices of Sardinia within the GRP polygons

Predicted GRP	Very Low	Low	Low to Moderate	Moderate to High	High	Very High
Mean	38.0	144.1	63.7	199.9	90.4	NA
Max	115.0	1010.0	2617.0	2357.0	183.0	
Min	17.0	2.0	8.0	7.0	18.0	
Median	36.0	55.0	30.0	40.0	83.5	
Geo-mean	33.7	63.8	37.5	60.2	77.6	
Number of Observed Data	13	107	137	61	14	0

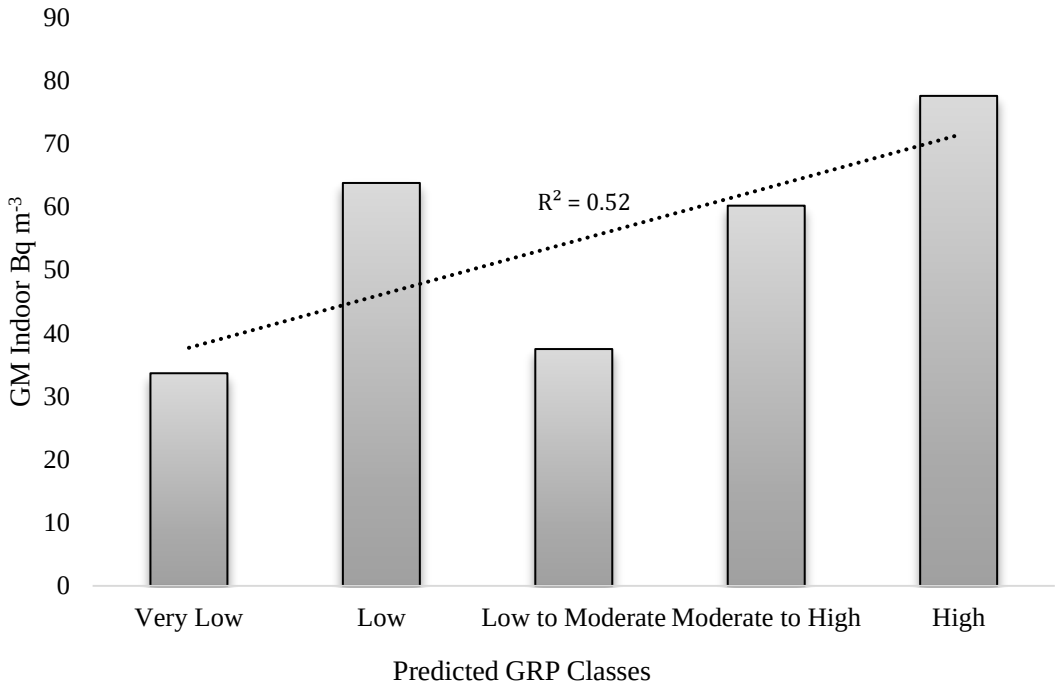

Figure 6-1: The geometric mean indoor radon concentrations in Italian post offices of Sardinia according to the predicted GRP classes.

6.1.2 Prediction of Indoor Radon Concentrations in Work Spaces of University of Cagliari by Running an ANCOVA Model based on Radon-related Variables

Through a radon testing survey and according to the EPA radon testing guidelines, Solid State Nuclear Track Detectors (CR-39) were placed in different environments, mostly in the ground and underground levels (Figure 6-2). The ambient gamma dose rates were measured simultaneously in the center of the room at one meter above the ground by using the handheld radiometer MKC-01CA1M. The gamma dose rate measurements were prolonged until the instrument's statistic error decreased to 5 percent.

The exposure period of the CR-39 detectors was about ten months, from March 2018 to January 2019. Before starting the test, the GRP category at the sampling point (Figure 5-13) were extrapolated. A questionnaire was prepared for each detector stating the testing information, type of building material, number of inhabitants, the time spent there and the ventilation rate of the room under exam (see Table 6-2). CR-39s were collected in January 2019 and they were etched for four hours in a 6.25 N NaOH solution with a constant temperature of 90 °C. The detectors were then removed and washed with distilled water. Using an optical microscope attached to a digital video camera, the alpha tracks were scanned. Based on the counted number of alpha tracks and using the calibration factor and taking into account the seasonal correction factors, the annual average concentration of radon and the standard deviation were calculated for each detector, as reported in Table 6-2.

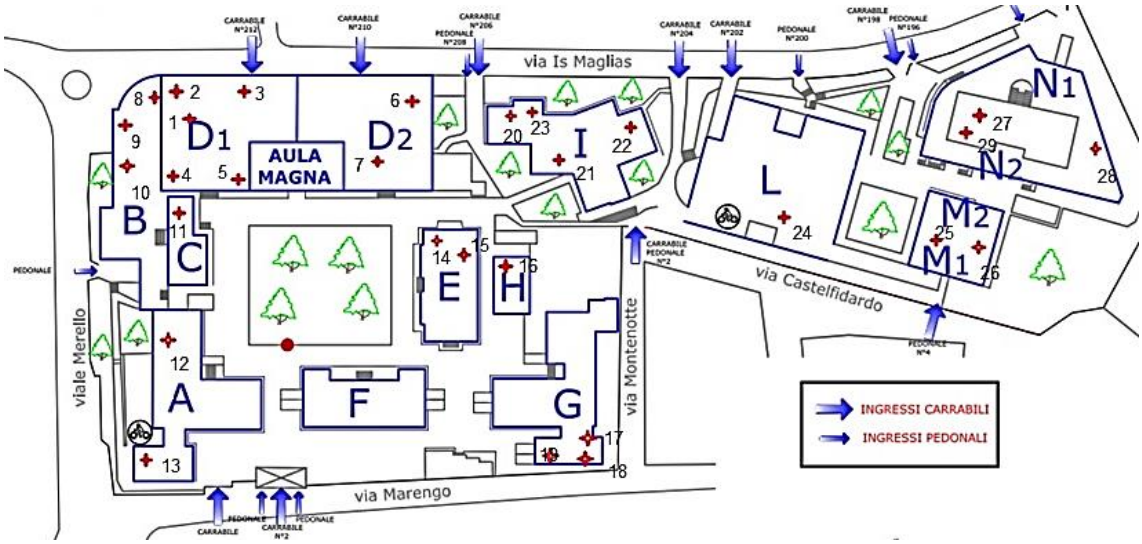

Figure 6-2: Location of CR 39 detectors used for assessment of radon levels in different rooms of engineering faculty, university of Cagliari. The base map is taken from www.unica.it

Furthermore, the Annual Effective Dose (AED) expressed in mSv y^{-1} was calculated according to the UNSCEAR model with Equation 6-1 (UNSCEAR, 2000):

Equation 6-1: $$AED = C_{Rn} \times F \times D \times u \times t$$

where C_{Rn} is the radon concentration (Bq m^{-3}), F is the equilibrium factor between radon and progenies (0.4 for buildings), D is the dose conversion factor (1.43 Sv J^{-1} h^{-1} m^{-3}), u is the unit factor (5.56×10^{-9} $J.m^{-3}$ Bq^{-1} m^3) and t is the exposure time (hour) in a year. The total time spent in a week was recorded for each room, so the periods in Table 6-2 were multiplied by 52 and then used for calculation of AED.

Table 6-2: Details of measured indoor radon concentrations, gamma dose rates, calculated annual effective dose and the sampled GRP classes according to Figure 5-13.

Detector Code	Building Code	Description of Testing Environment	Average C_{Rn} of Building (Bq/m^3)	C_{Rn} (Bq/m^3)	Standard Deviation	Ambient Gamma Dose Rate (µSv/hour)	Type of Building Material	Ventilation Rate (low, medium, high)	Floor	Total time spent in a week (hours)	Calculated Effective Dose (mSv y-1ear)	Sampled GRP Class
1	D	*Laboratory*	48.83	47	±15	0.17	Painted Cement/Ceramic Tiles	low	-1	15	0.117	very low
2		*Workshop*		27	±11	0.18	Cement	High	-1	15	0.067	very low
3		*Storage room*		89	±35	0.21	Painted Cement/Ceramic Tiles	low	-1	2	0.029	very low
4		*Classroom*		27	±8	0.21	Painted cement /Brick/Linoleum	Medium	G	8	0.036	very low
5		*Study room*		25	±12	0.19	Painted cement /Brick/Linoleum	High	G	20	0.083	very low
6		*Laboratory*		78	±20	0.31	Painted Cement/Ceramic Tiles	Medium	-1	15	0.193	very low
7		*Classroom*			NA	0.19	Painted cement /Brick/Linoleum	Medium	G	NA	NA	very low
8	B	*Copy room/Corridor*	116.33	123	±20	0.28	Bricks/Cement/Ceramic Tiles	Medium	-1	3	0.061	very low
9		*Classroom*		108	±28	0.25	Bricks/Cement/Ceramic Tiles	Medium	-1	12	0.214	very low
10		*Classroom*		118	±37	0.27	Bricks/Cement/Ceramic Tiles	Medium	-1	8	0.156	very low
11	C	*Classroom*	NA		NA	0.21	Painted Cement/Ceramic Tiles	Medium	G	NA	NA	very low
12	A	*Storage room*	129	68	±20	0.2	Cement/ Ceramic Tiles	low	G	10	0.112	very low
13		*Workshop*		190	±27	0.19	Cement	High	-1	20	0.628	low
14	E	*Corridor*	88.5	52	±18	0.24	Painted cement/Ceramic Tiles	Medium	G	30	0.258	very low
15		*Corridor*		125	±31	0.19	Painted cement/Ceramic Tiles	low	G	25	0.517	low to moderate
16	H	*Secretary office*	42	42	±9	0.19	Painted Cement/Ceramic Tiles	Medium	G	40	0.278	very low
17	G	*Corridor*	73.33	42	±16	0.2	Ceramic Tiles	Medium	G	16	0.111	very low
18		*Corridor*		121	±20	0.23	Painted Cement/Ceramic Tiles	Medium	-1	16	0.32	low to moderate
19		*Corridor*		57	±19	0.15	Painted Cement/Ceramic Tiles	High	-1	16	0.151	low
20	I	*Classroom*	61	49	±10	0.24	Painted cement/Ceramic Tiles	Medium	G	5	0.041	very low
21		*Student office*			NA	0.18	Painted cement/Ceramic Tiles	low	G	35	NA	very low
22		*Classroom*		73	±12	0.18	Painted cement/Ceramic Tiles	Medium	G	8	0.097	very low
23		*Classroom*		61	±19	0.23	Painted cement/Ceramic Tiles	Medium	G	6	0.061	very low
24	L	*Storage room in car parking*	291	291	±62	0.27	Cement	low	-1	1	0.048	low to moderate
25	M	*Storage room*	45		NA	0.18	Cement	low	G	NA	NA	low to moderate
26		*Laboratory*		45	±14	0.24	Ceramic Tiles	High	G	35	0.26	low
27	N	*Library*	39.67	51	±21	0.16	Painted Cement/Linoleum	Medium	1	25	0.211	low
28		*Basement storage*		27	±9	0.11	Cement	High	G	1	0.004	very low
29		*Computer room*		41	±12	0.17	Painted Cement/Linoleum	Medium	1	20	0.136	low
30	*Mensa Via Trentino*		15.5	12	±7	0.24	Painted Cement/Ceramic Tiles	High	G	12	0.024	very low
31				19	±8	0.24	Painted Cement/Ceramic Tiles	High	G	12	0.038	very low

6.1.2.1 ANCOVA Model Setting

An ANCOVA (analysis of covariance) is a model that holds both qualitative and quantitative independent variables. This model, which is similar to multivariate linear regression models, was employed to predict the indoor radon concentration at different workplaces of the Engineering department. To set a regression model, the explanatory variables and the response variable/s should be determined at the first level. In this study, the annual average of indoor radon (C_{Rn}) measured at different rooms was set as the response variable. Accordingly, the predicted GRP, the measured ambient gamma dose, ventilation rate, store level and the type of construction material were considered as the main predictors (also see Table 6-2). Among these predictors, the ambient dose rate is the only quantitative factor and the other parameters are qualitative variables (i.e., categorical variable). Table 6-3 shows the Summary statistics of qualitative input data, noticing that the predominant GRP of the study area is at a very low level. The measured indoor radon values can also confirm this (i.e., most IRCs are around 50 Bq m^{-3}).

Table 6-3: Summary statistics (Qualitative data)

Variable	Categories	Counts	%
Type of Building Material	Bricks/Cement/Ceramic Tiles	3	11.11
	Cement	4	14.81
	Cement/ Ceramic Tiles	1	3.70
	Ceramic Tiles	2	7.41
	Painted Cement/Ceramic Tiles	8	29.63
	Painted Cement/Linoleum	2	7.41
	Painted cement /Brick/Linoleum	2	7.41
	Painted cement/Ceramic Tiles	5	18.52
Ventilation Rate	High	8	29.63
	Medium	14	51.85
	low	5	18.52
Floor	-1	11	40.74
	1	2	7.41
	Ground	14	51.85
Predicted GRP Class	low	5	18.52
	Low to moderate	3	11.11
	very low	19	70.37

Before conducting the analysis, the multicollinearity of the input variables was assessed by using the Variance Inflation Factors (VIF) test. This test is an elementary test to assess multicollinearity in a regression model. The VIF identifies the correlation between independent variables and the strength of that correlation. In other words, it determines which predictor variable in a multiple regression model can be linearly predicted from the others with a substantial degree of accuracy. The goal was to avoid using data that fail

the multicollinearity test (i.e., VIF >7.5). As can be seen in Table 6-4, multicollinearity did not occur for any of the explanatory variables.

Table 6-4: Multicollinearity statistics

Input variable	**Ambient Gamma Dose Rate (µSv/hour)**	**Building Material-Bricks/Cement/Ceramic Tiles**	**Building Material-Cement**	**Building Material-Cement/ Ceramic Tiles**	**Building Material-Ceramic Tiles**	**Building Material-Painted Cement/Ceramic Tiles**	**Building Material-Painted Cement/Linoleum**	**Building Material-Painted cement /Brick/Linoleum**	**Building Material-Painted cement/Ceramic Tiles**	**Ventilation Rate -High**	**Ventilation Rate -Medium**	**Ventilation Rate -low**	**Floor: -1**	**Floor: 1**	**Floor: Ground**	**GRP-low**	**GRP-low to moderate**	**GRP-very low**
Tolerance	0.56	0.58	0.61	0.70	0.72	0.87	0.00	0.89	0.60	0.30	0.44	0.47	0.22	0.00	0.21	0.27	0.64	0.50
VIF	1.77	1.73	1.65	1.44	1.39	1.15	-	1.13	1.67	3.33	2.25	2.11	4.57	-	4.72	3.77	1.57	1.98

6.1.2.2 Model Running

The ANCOVA regression model was fitted by using the XLSTAT add-in of the Microsoft Excel software (Addinsoft, 2019). Equation 6-2 shows the achieved model and the values of coefficients of the relevant predictors. According to this formula, by using the predicted GRP classes and information on anthropogenic factors, one can estimate the indoor radon concentration (with an acceptable precision) in other work environments of the University of Cagliari as well as any residential and public building in Sardinia (assuming that the required input information is given). Table 6-5 shows the standardized coefficients of input variables of the indoor radon prediction model. According to this table, the higher the value, the greater influence of the concerning parameters is anticipated. Negative values are also representative of a negative correlation between indoor radon and the parameters under study. As can be seen in that table, except for the floor level, the remainder of the input variable has a considerable effect on indoor radon variations. Among the effective parameters, the ventilation rate and the predicted GRP class have the most considerable influence comparing to the other variables.

Equation 6-2: C_{Rn} (Bq m^{-3}) = -11.58+451.19 × **Ambient Gamma Dose Rate (µSv/hour)**+52.79 × ***Type of Building Material-Bricks/Cement/Ceramic Tiles**+96.39 × **Type of Building Material-Cement**-10.65 × **Type of Building Material-Cement/ Ceramic Tiles**-28.62 × **Type of Building Material-Ceramic Tiles**+5.09 × **Type of Building Material-Painted Cement/Ceramic Tiles**-79.77 × **Type of Building Material-Painted Cement/Linoleum**+11.95 × **Type of Building Material-Painted cement /Brick/Linoleum**-94.03 × **Ventilation Rate-High**-35.18 × **Ventilation Rate-Medium**-10.00 × **Floor:-1**+98.09 × **GRP-low**+71.376 × **GRP-low to moderate**

Table 6-5: Standardized coefficients of input variables of the indoor radon prediction model

Source	Value	Standard error	t	Pr > |t|
Ambient Gamma Dose Rate (µSv/hour)	0.335	0.115	2.923	**0.012**
Type of Building Material-Bricks/Cement/Ceramic Tiles	0.281	0.161	1.746	0.104
Type of Building Material-Cement	0.581	0.181	3.215	**0.007**
Type of Building Material-Cement/ Ceramic Tiles	-0.034	0.107	-0.318	0.755
Type of Building Material-Ceramic Tiles	-0.127	0.108	-1.178	0.260
Type of Building Material-Painted Cement/Ceramic Tiles	0.039	0.174	0.227	0.824
Type of Building Material-Painted Cement/Linoleum	-0.354	0.150	-2.368	**0.034**
Type of Building Material-Painted cement /Brick/Linoleum	0.053	0.108	0.492	0.631
Type of Building Material-Painted cement/Ceramic Tiles	0.000	0.000		
Ventilation Rate (low, medium, high)-High	-0.728	0.199	-3.660	**0.003**
Ventilation Rate (low, medium, high)-Medium	-0.298	0.163	-1.825	0.091
Ventilation Rate (low, medium, high)-low	0.000	0.000		
Floor--1	-0.083	0.184	-0.453	0.658
Floor-1	0.000	0.000		
Floor-Ground	0.000	0.000		
GRP-low	0.646	0.167	3.865	**0.002**
GRP-low to moderate	0.381	0.108	3.529	**0.004**
GRP-very low	0.000	0.000		

* Bold numbers show statistical significance

The calculated adjusted value R^2 (0.82) of the model shows that the proposed model can explain 82 percent of the variations in indoor radon by consideration of the defined predictors. The statistics of analysis regarding the goodness of fit model are stated in Table 6-6. In general, the obtained values show that the model was able to predict the indoor radon concentrations successfully. Figure 6-3, which shows the correlation between the measured and predicted indoor concentrations, confirms this hypothesis.

Table 6-6: Goodness of fit statistics

Observations	27
Sum of weights	27
DF	13.000
R^2	**0.904**
Adjusted R^2	**0.807**
MSE	696.162
RMSE	26.385
MAPE	32.956
DW	2.605
Cp	14.000
AIC	184.997
SBC	203.138
PC	0.304
Press	61935.292
Q^2	0.340

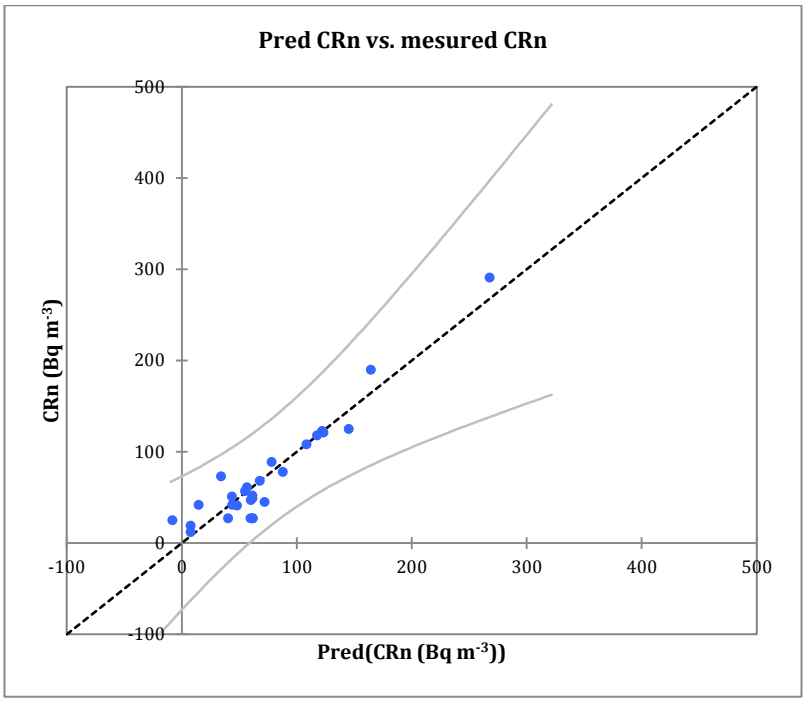

Figure 6-3: Correlation between measured and predicted indoor concentrations

6.1.2.3 Sensitivity Analysis

Table 6-7 shows the results of the analysis of the variance and the Fisher's F test. Given the fact that the probability corresponding to the F value is lower than 0.0001, it means that one would be taking a lower than 0.01% risk in assuming that the null hypothesis (no effect of the two explanatory variables) is wrong. Therefore, it can be concluded with confidence that the predictor variables do bring a significant amount of information.

Table 6-7: Analysis of variance

Source	DF	Sum of squares	Mean squares	F	$P_r > F$
Model	13	84772.196	6520.938	9.367	**0.000**
Error	13	9050.100	696.162		
Corrected Total	26	93822.296			

* Bold number show statistical significance

Furthermore, to find out if the explanatory variables provide the same amount of information, the type I Sum of Squares (SS) and Type III SS were analyzed. The Type I SS analysis results (Table 6-8) is constructed by adding variables in the model one by one and by evaluating the impact of each on the model sum of squares (Model SS). In consequence, in Type I SS, the order in which the variables are selected will influence the results. The lower the F probability corresponding to a given variable, the stronger the impact of the variable on the model as it is before the variable is added to it. As can be

seen in this table, any individual input parameter would bring sufficient information to the model, once the others have been added.

Table 6-8: Type I Sum of Squares analysis

Source	DF	Sum of squares	Mean squares	F	$P_r > F$
Ambient Gamma Dose Rate (μSv/hour)	1	12166.063	12166.063	17.476	**0.001**
Type of Building Material	7	30624.468	4374.924	6.284	**0.002**
Ventilation Rate (low, medium, high)	2	19222.030	9611.015	13.806	**0.001**
Floor	1	3305.963	3305.963	4.749	**0.048**
GRP	2	19453.673	9726.836	13.972	**0.001**

* Bold numbers show statistical significance

Table 6-9: Type III Sum of Squares analysis

Source	DF	Sum of squares	Mean squares	F	$P_r > F$
Ambient Gamma Dose Rate (μSv/hour)	1	5948.477	5948.477	8.545	**0.012**
Type of Building Material	6	19584.809	3264.135	4.689	**0.009**
Ventilation Rate (low, medium, high)	2	9522.745	4761.372	6.839	**0.009**
Floor	1	142.720	142.720	0.205	0.658
GRP	2	19453.673	9726.836	13.972	**0.001**

* Bold numbers show statistical significance

Finally, the type III SS analysis is computed by removing one variable of the model at a time to evaluate its impact on the quality of the model. This means that the order in which the variables are selected will not have any effect on the values in the Type III SS. The Type III SS is generally the best method to use to interpret results when an interaction is part of the model. The lower the F probability corresponding to a given variable, the stronger the impact of the variable on the model. It that be concluded from Table 6-9 that the Floor level brings the least information to the model.

6.1.2.4 Evaluation of the Influence of Anthropogenic Factors on Indoor Radon Activity

The type of building material of interior space was found to be effective in variations of indoor radon concentration. As shown in Figure 6-4, painting the cement or the use of Linoleum for the roof would act as an obstacle for radon exhalation and entry to indoor spaces. On the other hand use of bricks would slightly increase indoor radon activity; this can be since clays as one of the main components of bricks may contain uranium-bearing minerals and thus radon could be released from its surface.

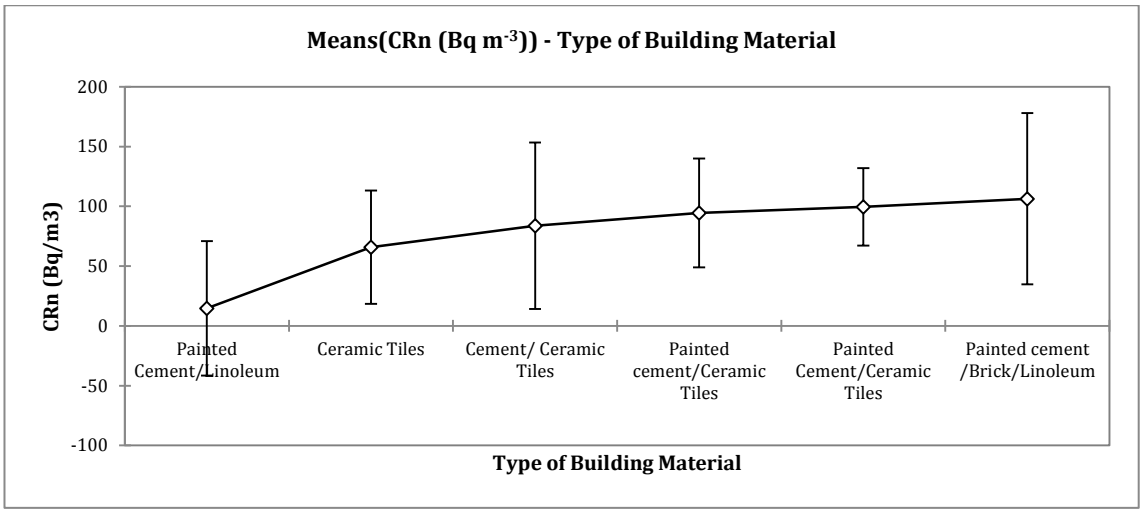

Figure 6-4: Relationship between the type of Building material and indoor radon activities.

In addition to the type of building material, the ventilation rate was found to be a significant parameter controlling the indoor radon levels. Therefore the use of ventilators, HVAC systems and even taking benefit of natural ventilation would be helpful to reduce enhanced radon levels. The first measure that can be adopted to lower radon is to increase the rate of air exchange, for the case that radon levels are very high, application of Radon Barriers or sub-floor depressurization (radon sump) could be recommended to protect inhabitants from adverse health effects of Radon. Figure 6-5 shows the relationship between radon levels and ventilation rates.

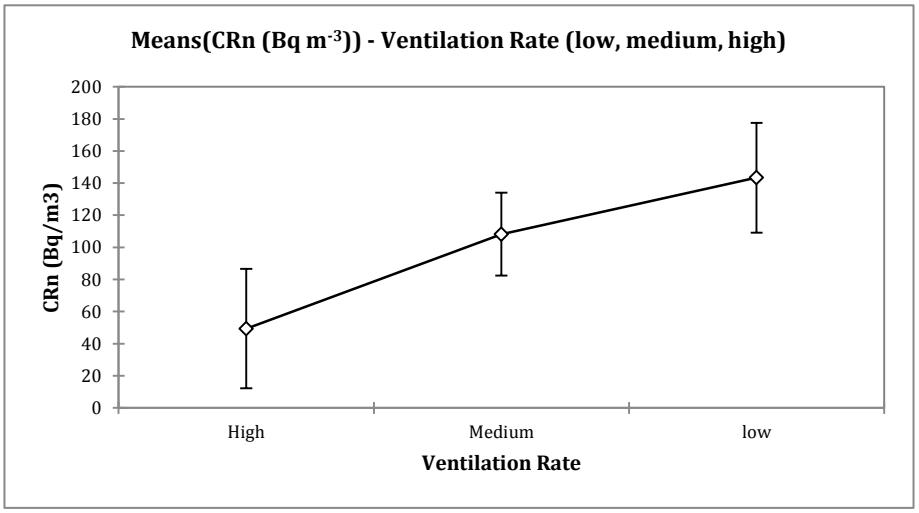

Figure 6-5 Ventilation rate vs. Indoor radon concentrations

Radon is about six times heavier than the air and therefore it usually accumulates at the lower part of the building. Further to this, the major part of radon in buildings is supposed to be exhaled from the surface of the soil underlying the foundation, therefore higher

radon levels are anticipated for lower stores of the building, especially if the ground floor is in direct contact with the soil. Nevertheless, the indoor radon concentrations were not found to vary significantly by a change in the floor level (Figure 6-6). The level of building stores measured in the study was -1, ground floor and 1st floor and maybe if there were also samples available for higher levels (i.e., 2nd, 3r and 4th floor), it could be possible to see the anticipated trend.

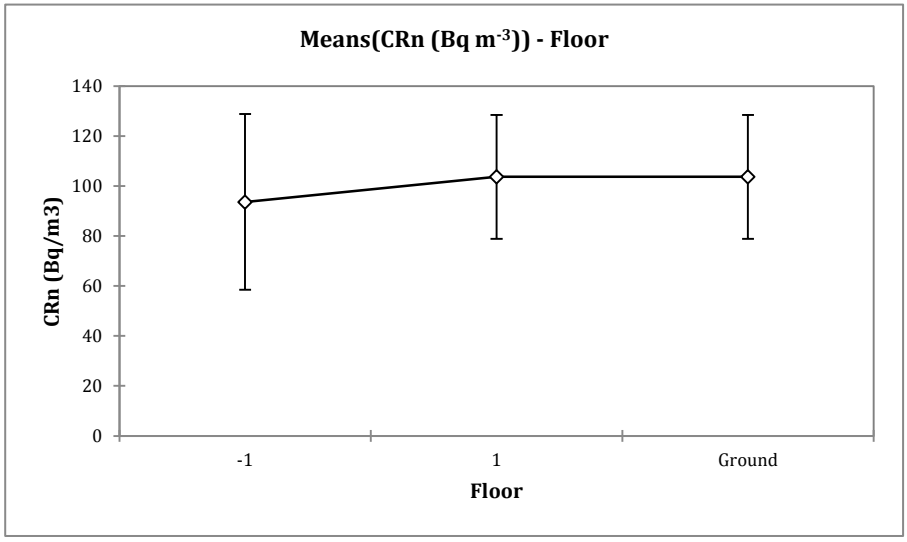

Figure 6-6 Variation in indoor radon levels by changing floor levels.

6.2 Assessment of Natural Radioactivity and Radon Release Potential of Silurian Black Shales of Villasalto District, SE Sardinia, Italy

In the previous section, the proposed model, which was based on predicted GRP classes together with the information on anthropogenic factors, provided sufficient information to predict the indoor radon concentrations. However, because the indoor radon data is not available for all the areas, an alternative method should be considered to examine the prediction power of the proposed GRP map for the zones where there is no available indoor radon, or even the area to be examined is a future construction site.

In this section, an area in southeastern Sardinia located at Silurian black shales is selected as the pilot test site. As seen in Figure 6-7, the predicted GRP for sampling sites is at a high to a very high level.

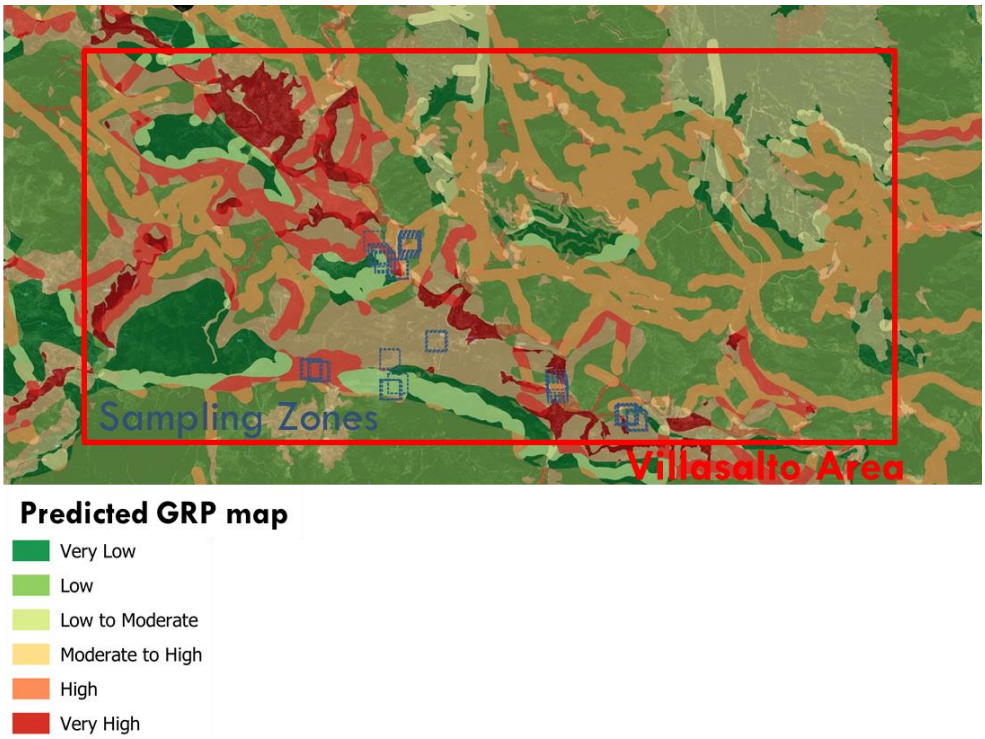

Figure 6-7: Predicated GRP map of the Villasalto district

6.2.1 Black Shale and Radon Emanation Potential

Radon producing radionuclides are widely spread in the earth's environment and strongly correlated with the geological context. Hence, defining geological units well correlated with indoor radon has gained increasing interest and attention in the process of mapping radon risk research literature in the last years (Appleton and Miles, 2010; Tondeur et al., 2014). On average Earth's Crust contains 2.5 ppm of uranium However, higher concentrations of radioactive elements are more common in certain types of rocks such as granites (Dentoni et al., 2020) and black shale (Harrell, 1991; Ketris and Yudovich, 2009) among others. The "black shales" are sedimentary rocks containing organic carbon anomalously enriched in ^{238}U, ^{235}U, ^{40}K and ^{232}Th and other trace elements comparing to less organic-rich grey shales, sandstone, or limestone (Ketris and Yudovich, 2009; Perry and Team, 2011). The major source of the enriched uranium in black shales was the seawater and the quantity of uranium deposited is related to the amount of the uranium content of the seawater. There are different interpretations of the ways that uranium deposited in black shales and muds from the sea, however the indirect or direct responsible of the processes that lead to the concentration of uranium in shales is organic matter (Swanson, 1961) which is also the major cause of the dark color in black shales. This is since ^{238}U and ^{235}U preferentially bond to organic matter that dies and settles to the bottom of the sea/ocean. (Adams and Weaver, 1958). As black shales contain more

organic matter and clays than other shales or sedimentary rocks they are generally more radioactive than other shales (Schmoker, 1981).

Enrichment of uranium in black shales can be a result of a two-phase process: a) either by deposition in anoxic environments (Swanson, 1961)(deep water as well as shallower environments (Baucon et al., 2020)) in which uranium is immobilized and concentrated or even b) as a result of the occurrence of subsequent metamorphic alterations that leads to remobilization and re-concentration of uranium. The most extensive black shale deposits are the product of this two-phase event (Föllmi, 2012) which can be observed in many Palaeozoic and Mesozoic strata around the world. In Europe, the Estonian graptolite argillites and Swedish Alum shale are good examples of deposition of uranium as a result of oceanic anoxic events (Soesoo and Hade, 2014). As another example, due to the waxing and waning of Gondwanan ice sheets and subsequent eustatic fluctuations, the cyclic deposition of paleosols, coals, limestones, gray shales occurred (Heckel, 2008). The same phenomena led to the deposition of black shale in the Late Pennsylvanian Midcontinent Sea, a large epeiric sea that covered an extensive area in the United States (Algeo and Heckel, 2008).

In general, due to high levels of metal enrichment in black shales and association with climactic events their occurrences are well studied and documented worldwide. Here we study the radon exhalation potential and natural radioactivity of bioturbated black shales from the Genna Muxerru Formation (Silurian) near Villasalto, a district in the south-east of Sardinia (Italy). Wherever black shales are lying on or near the surface, they represent an important source for radon exhalation (Soesoo and Hade, 2014), therefore a concern arises for this area regarding the protection of the public against the risks of natural radiations. Furthermore, based on the result of a previous study in the area under exam, Cidu et al., 2014 stated that bioturbated black shales may be commoner than traditionally expected. They also reported rather high contamination in soils by trace elements (Sb) which might express that other trace elements like uranium may be present in the area. This report together with the background environmental information on black shale justified that further tests might be necessary for the study area. For this purpose, testing of activity concentration of ^{226}Ra, ^{232}Th and ^{40}K and the production rate of ^{222}Rn (P_{RN}) were considered. Seventeen specimens of highly deformed Silurian black shales were collected from six selected sites (test-sites) within Villasalto district. Laboratory and in-situ gamma-ray spectrometry techniques were employed to determine the natural

radioactivity of the rocks under investigation. As regard radon gas, the concentration growth inside a sealed chamber was modeled to enable the calculation of the radon emanation coefficient (E) for each rock sample, which mainly depends on the ^{226}Ra distribution within the rock, on the rock particles size, moisture content and mineralogy (Ishimori et al., 2013). The correlation between the main influencing variables and the radon emanation coefficient was investigated employing Pearson's matrix, a measure of association between ordered pairs of continuous measurements from two groups (Pearson, 1895). Furthermore, the main radiological hazard indexes (radium equivalent activity Ra_{eq}, the outdoor gamma-ray dose rate and the annual effective dose) were estimated for the test sites under investigation.

The results of this study give an overlook of the natural radiation of Silurian black shales which can be also found in the other parts of the island (both in the eastern part of Sulcis-Iglesiente (southwestern Sardinia) and in the Sarrabus-Gerrei (south-eastern Sardinia)). Because very few studies about natural radioactivity have been carried out in the Villasalto district, the results hereby discussed may represent a valuable contribution for the production of an accurate geogenic radon map which can help to target the further test points and could represent a first step for the development of more in-depth analysis of natural radioactivity of the whole area.

In addition to radioprotection aspects of black shales, they are of interest commercially, they contain organic material that sometimes breaks down to form natural gas or oil. They can be also considered as a possible source of uranium (Soesoo and Hade, 2014). Furthermore, shales (in general) can be crushed and mixed with water to produce clays that can use to build a variety of objects (e.g. valuable raw material for tile, brick and pottery (Ries, 1922)). They can be also used to manufacture some types of cement and construction materials (Frías-Rojas et al., 2017). There are pieces of evidence that when shales were used as construction material, they became a primary source of indoor radon (Baskaran, 2016). As an example, high activities of ^{226}Ra (parent element of radon) were recorded in concretes in which the alum shale (a variety of shale or clay-slate used to produce a particular type of light concrete) was included in the mixture (WHO, 2009).

6.2.2 Geological Description of the Study Area

The geology of the study area consists of low-grade metamorphic rocks belonging to the allochthonous units set in place during the Hercynian orogenesis (Carmignani et al.,

1986). The outcropping succession consists of Cambrian to Lower Ordovician siliciclastic deposits, mainly micaceous metasandstones and quartzite, followed by metavolcanic rocks (Middle Ordovician), black shale and quartzite (Silurian to Lower Devonian), Devonian metalimestones and Lower Carboniferous deposits of the Culm type (Cidu et al., 2014). The most complete and best known Silurian succession of southeastern Sardinia is exposed in the Gerrei tectonic Unit. The Silurian sequence starts with Rhuddanian-lowermost Gorstian black graptolitic shales (Lower Graptolitic Shales), followed by a lower Gorstianend Pridoli nodular calcareous unit (Ockerkalk). Graptolitic shales (Upper Graptolitic Shales) document the Lower Devonian (Corradini and Ferretti, 2009). For detailed information regarding the Silurian graptolites and black shales of south eastern Sardinia, we refer to the set of reports called" The Silurian of Sardinia" published by the Italian Paleontological Society (http://paleoitalia.org/).

The area under exam comprises the abandoned mine Su Suergiu and the villages of Villasalto and Armungia. Figure 6-8 shows the modified and simplified version of the geological map of the Villasalto area together with the location of sampling points and the test sites. Wherever the outcrops and the veins of black shales were present, a test site was defined. The samples (soil/rock) were collected from freshly broken surfaces. Figure 6-9 shows the Silurian black shales of the Suergiu and surroundings in Sardinia (Italy). Initial assessments suggested that the rocks have undergone severe metamorphism. The veins of quartzite can be observed between the deformed rocks.

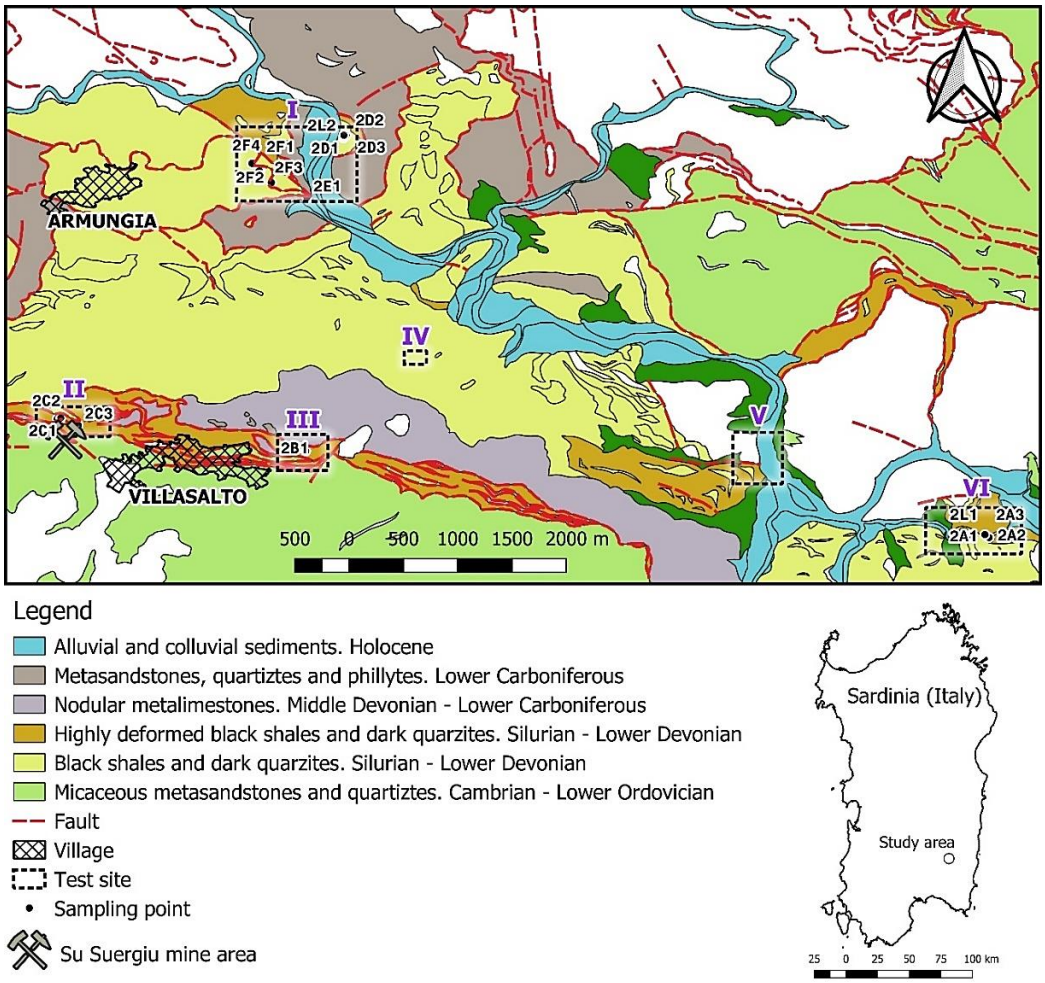

Figure 6-8: Study area and sampling points overlapping a modified geological map of Villasalto district (Cidu et al., 2014; RAS, 2013).

Figure 6-9: Deformed black shale and quartzite veins (Su Suergiu and surroundings in Sardinia (Italy)

6.2.3 Preparation and Characterization of Rock samples

Seventeen rock specimens of about 2-3 kg each were collected from the surface of the highly deformed Silurian black shales formation within the study area (special care was taken to avoid weathered rocks). The specimens were packed into polyethylene bags, tagged and transported to the laboratory, where each specimen was manually crushed by using a mortar and pestle, homogenized (less than 1 mm grain size) and oven-dried for 12 h at 110 ˚C. Two set of samples of about 100 gr were separated from the original specimens. The 17 samples from the first set were hermetically sealed in 125 ml polycarbonate cylindrical containers (with diameter 9 cm and height 2 cm) and left undisturbed for a minimum of four weeks, to reach the radioactive equilibrium before carrying out the gamma-ray spectrometry. The other 17 samples from the second set were placed in the same type of container but this time, the top caps were left open to enable the exhalation of radon from the sample surface during the test inside a sealed chamber. Table 6-10 reports the sample's apparent density (γ_d), which was estimated before the laboratory tests and the particle size distribution determined after the tests.

Table 6-10: Particle size distribution of the tested samples.

Code*	γ_d	**Particle Size Distribution %**					
	$Kg.cm^{-3}$	**0.5 - 1** (mm)	**0.25 - 0.5** (mm)	**0.125 - 0.25** (mm)	**0.063 - 0.125** (mm)	**0.038 - 0.063** (mm)	**< 0.038** (mm)
#2A1	1.39	45.81	21.47	14.62	12.37	5.52	0.20
#2A2	1.36	49.91	21.18	13.53	10.35	4.38	0.65
#2A3	1.36	58.79	21.21	7.14	3.82	7.04	2.01
#2B1	1.30	55.19	14.38	11.55	10.27	7.24	1.37
#2C1	1.19	45.52	22.36	16.26	10.44	4.33	1.08
#2C2	1.32	51.55	20.44	13.06	8.97	4.79	1.20
#2C3	1.60	44.17	18.69	13.90	11.58	10.75	0.91
#2D1	1.43	52.45	20.47	9.73	5.92	8.71	2.71
#2D2	1.56	55.41	19.85	11.74	8.78	4.05	0.17
#2D3	1.43	54.57	19.12	11.57	9.98	4.57	0.19
#2E1	1.36	51.85	20.88	13.19	10.29	3.10	0.70
#2F1	1.34	49.26	19.33	12.78	13.38	5.05	0.20
#2F2	1.34	53.65	20.62	12.51	8.81	4.00	0.40
#2F3	1.28	5.58	23.72	43.74	24.66	2.19	0.10
#2F4	1.50	56.17	20.33	11.71	8.17	3.45	0.18
#2L1	1.37	70.78	14.86	7.03	3.01	3.82	0.50
#2L2	1.44	14.51	10.97	21.73	42.39	10.12	0.28

* The First digit represents the project code, the alphabet shows the attribute code for the site and the last digit shows the sample number taken from the same site

6.2.4 Measurement of Radionuclide Activity Concentration

The radioactivity concentrations of ^{226}Ra, ^{232}Th and ^{40}K were estimated through gamma-ray spectrometry technique, with a 1024-channels NaI (Tl) scintillation detector (3 × 3 inches). Radioactive sources of ^{60}Co and ^{137}Cs were used for energy calibration. The IAEA uranium and thorium references (RGU1 and RGTh1) and high pure potassium nitrate (KNO_3) salt were employed to calibrate the spectrometer. To measure the radio element activities of each sample, at first, the spectrum of each analyzed sample turned out to be the weighted sum of the three reference spectra (U, Th and ^{40}K) plus the background spectrum. The weight of each spectrum of the three references depends on the mass (and hence the activity) of the radioisotope present in the test sample. The procedure starts with comparing the reference spectra and the spectrum of the sample and then the algorithm identifies the weights of the three isotopes present in the sample under analysis. Then mathematical calculations based on the Maximum Likelihood technique in Microsoft Excel software were used to calculate both the weights and the standard deviations. As an example, Figure 6 10 shows the comparisons between the built and the acquired spectrum for sample *#2A2*. If the mass activity of the reference materials and their base spectra are known, the specific activity of the three main radioisotopes in a given sample is obtained as an optimal solution of the problem (i.e.: distinction of the three radioisotopes contribution plus background).

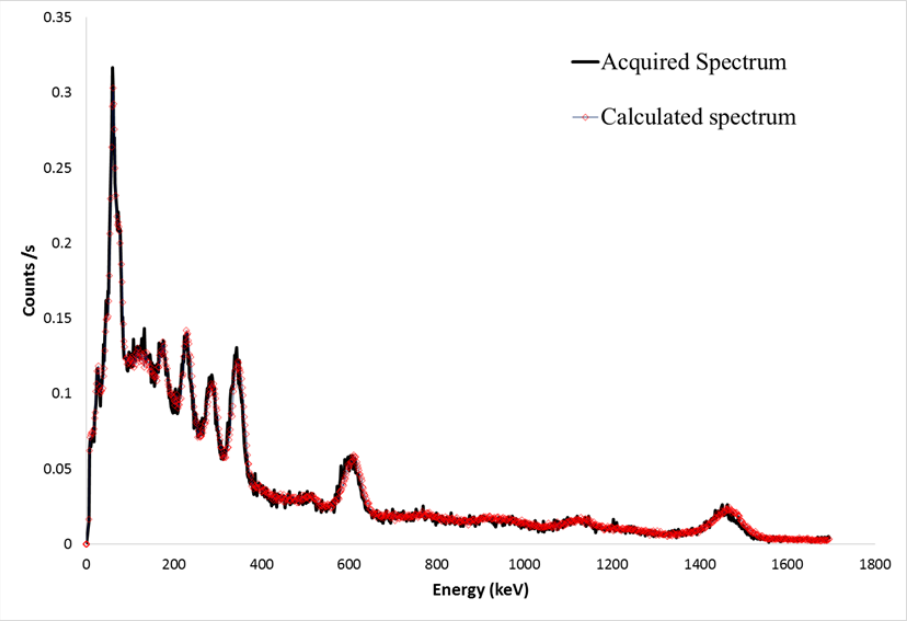

Figure 6-10: Acquired spectrum for sample #2A2 and the calculated spectrum (red)

The ^{238}U, ^{232}Th and ^{40}K activity concentrations were estimated using the method above described. The ^{226}Ra concentration was calculated as the equivalent equilibrium concentration of ^{238}U using the ^{238}U - ^{226}Ra mass ratio 1: 3.376×10^{-7} (Erdi-Krausz et al., 2003)

6.2.5 Estimation of Radon Emanation Coefficient and Radon Production Rate

One of the most commonly used techniques for monitoring the radon activity of a given material is the *enclosed sample method*, where the real-time concentration of Rn gas is measured inside a sealed chamber containing both the sample under investigation and the radon monitoring system (Leonardi et al., 2018). In this study, a pressure-resistant vacuum glass container of 6.2 L effective volume was used as an accumulation chamber (Figure 6-11). The Radon activity concentration, the temperature and the relative humidity were simultaneously measured for each sample with a monitoring instrument Radex MR-107, for 72 h (at least) at 1 h-time interval (sampling time). A vacuum pump was used to maintain the system airtightness. The real-time activity concentration C (t) produced by each sample was stored, graphed and elaborated afterward. The activity concentration growth C(t) was modeled according to Sahoo and Mayya, 2010, with the two-dimensional diffusion theory expressed by Equation 6-3;

Equation 6-3: $$C(t) = C_0 e^{-t\lambda_e} + C_m(1-e^{-t\lambda_e})$$

where λ_e is the effective radon decay constant (h^{-1}), accounting for the radon decay, the leak rate and the *back diffusion*, C_0 and C_m is the radon activity concentration (Bq m^{-3}) respectively at t= 0 and t= ∞ (i.e.: c(t) maximum value) (Leonardi et al., 2018).

The values of λ_e and C_m were extrapolated using the nonlinear least-squares fitting of the experimental data with Eq.1 (see Figure 6-12) (Kemmer and Keller, 2010; Tan and Xiao, 2011)The *radon emanation coefficient* (E) was then calculated according to Equation 6-4 (Ishimori et al., 2013):

Equation 6-4: $$E = \frac{V_{eff} C_m}{A_{Ra} W}$$

where W is the sample weight (kg) and A_R is the mass activity of ^{226Ra} in the sample (Bq kg-1).

The *radon production rate* P_{Rn} (Bq m^{-3} h^{-1}) was also estimated according to Equation 6-5 (Ishimori et al., 2013; A. Pereira et al., 2017)

Equation 6-5: $P_{Rn} = \lambda_e E A_{Ra} \gamma_d$

where ɣd is the estimated apparent density reported in Table 6-10.

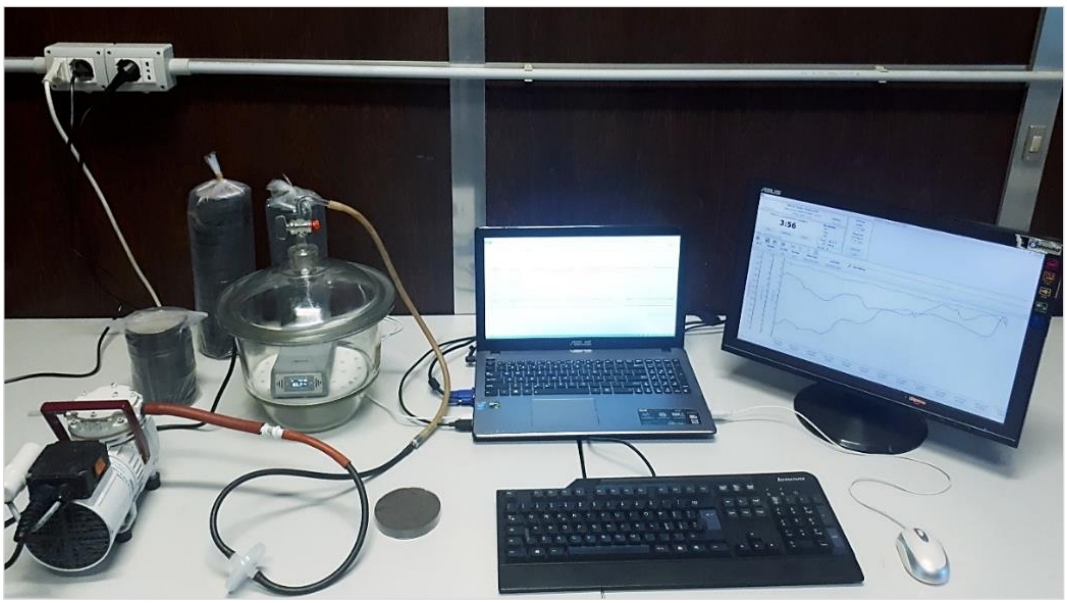

Figure 6-11: Experimental setup for radon exhalation rate measurement including the accumulation chamber, samples and the Quarta-RAD software.

Model	Radon Growth - #2A2	
Equation	$C_{(t)} = C_0 e^{-t\lambda_e} + C_m(1 - e^{-t\lambda_e})$	
Extrapolated Values	C_0	4.30E-07
	C_m	575.19
	λ_e	1.11E-02
Adj. R-Square	0.88	
Standard Error (Bq/m³)	19.93	

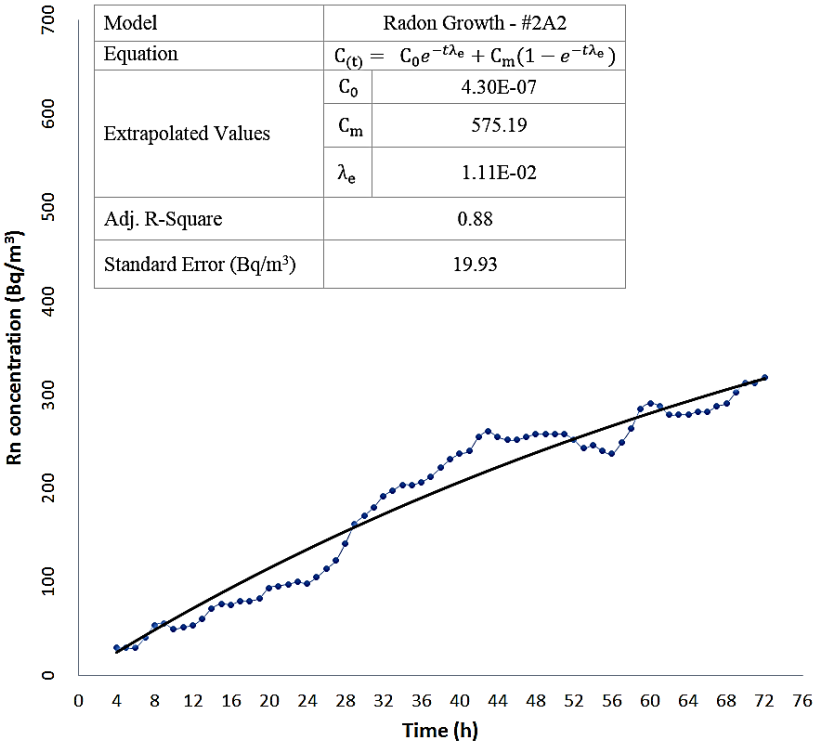

Figure 6-12: Radon activity growth inside the sealed chamber and nonlinear least-squares fit of measured radon activity with Equation 6-3.

6.2.6 In-situ Gamma-ray Spectrometry

To map the distribution of natural radioactivity within the study area, U (ppm), Th (ppm) and K (%) contents were measured with an RS-230 BGO (Bismuth Germanate Oxide) Super–Spec portable radiation detector. A total number of 986 readings were taken at the six test sites shown in Figure 6-8. The goal was to scan the outcrops of black shales present in the pathways of each test site. The radiometric data was elaborated and then graphically displayed on satellite maps.

6.2.7 Results and Discussion

6.2.7.1 Results of Laboratory Tests

The results of the experimental test performed on the 17 specimens of Silurian black shales are reported in Table 6-11. The activity concentration (Bq kg^{-1}) of the terrestrial radionuclides was found between 103.32 and 384.51 for ^{226}Ra, between 23.84 and 63.62 for ^{232}Th and between 216.70 and 1450.13 for ^{40}K, with mean values of 256.32 ± 87, 44.16 ± 9.47 and 856.28 ± 392.41 respectively.

Table 6-11: Statistics for radionuclide concentration and radon characteristics of the tested samples.

Code	Radionuclide Concentration (Bq kg^{-1})			D	C_m ± SE*	E	P_{Rn}
	A_{Ra} ± σ*	A_{Th} ± σ	A_K ± σ	(nGy h^{-1})	(Bq m^{-3})		(Bq m-3 h^{-1})
#2A1	258.36 ± 3.22	41.17 ± 2.48	487.93 ± 90.12	164.57	553.36 ± 16.33	0.13	983.22
#2A2	286.70 ± 3.60	53.67 ± 2.76	820.20 ± 100.67	199.08	575.19 ± 19.93	0.12	1887.38
#2A3	313.98 ± 3.86	39.68 ± 2.96	534.65 ± 107.95	191.32	946.31 ± 34.65	0.18	1681.40
#2B1	200.78 ± 3.46	44.41 ± 2.66	1188.57 ± 96.91	169.15	262.45 ± 16.58	0.08	1372.34
#2C1	103.32 ± 2.85	47.83 ± 2.19	1292.58 ± 79.63	130.52	215.10 ± 25.06	0.14	1124.76
#2C2	136.56 ± 2.77	56.57 ± 2.13	1148.48 ± 77.58	145.15	239.21 ± 35.35	0.11	1245.11
#2C3	151.73 ± 2.80	37.39 ± 2.15	846.71 ± 78.46	127.99	307.51 ± 30.30	0.10	1607.99
#2D1	238.81 ± 3.47	63.62 ± 2.66	1420.12 ± 96.97	207.98	874.33 ± 23.05	0.21	1553.49
#2D2	162.44 ± 2.77	46.03 ± 2.13	1394.35 ± 77.64	160.99	266.18 ± 23.25	0.09	1401.23
#2D3	290.98 ± 3.36	43.18 ± 2.58	965.75 ± 93.97	200.79	284.25 ± 20.49	0.06	1486.37
#2E1	277.33 ± 4.19	49.27 ± 3.22	1450.13 ± 117.24	218.36	621.31 ± 30.64	0.14	1103.94
#2F1	331.24 ± 4.87	34.50 ± 3.74	490.52 ± 136.23	194.33	444.66 ± 27.16	0.08	790.08
#2F2	384.51 ± 4.33	32.63 ± 3.33	516.92 ± 121.10	218.91	822.13 ± 34.92	0.13	859.79
#2F3	382.36 ± 5.29	50.61 ± 4.07	623.91 ± 148.13	233.23	430.64 ± 10.55	0.07	765.16
#2F4	180.48 ± 2.53	23.84 ± 1.94	578.35 ± 70.75	121.89	204.62 ± 11.36	0.06	1073.51
#2L1	321.75 ± 3.86	40.87 ± 2.97	580.97 ± 108.02	197.56	595.25 ± 30.05	0.11	1057.63
#2L2	336.08 ± 3.92	45.52 ± 3.02	216.70 ± 109.82	191.80	717.64 ± 22.37	0.12	1275.10

SE: Standard Error of the Estimated Value, σ*: Associated Uncertainty (1σ).*

Except for ^{232}Th, the calculated mean values were found significantly higher than the worldwide average activity reported by (UNSCEAR, 2008): 32 Bq kg^{-1} (^{226}Ra), 45 Bq kg^{-1} (^{232}Th) and 412 Bq kg^{-1} (^{40}K). However, it should be notified that the measured values of radionuclide concentrations are consistent with those reported for the black shale of

the other parts of the world (Ketris and Yudovich, 2009). The elevated concentration of uranium and low activity of thorium in measured samples can be explained by the behavior of these radioisotopes in the environment. High uranium concentration for black shales was anticipated. However, weathering and alteration processes can also lead to an increase of ^{226} Ra concentration. Because, considering the relative solubility over long periods, ^{226}Ra has a greater chance to be transported from the host rocks and to be deposited as loess, silt placers and tertiary soil (East, 2014; Perry and Team, 2011; Thu et al., 2019). Unlike ^{226}Ra, the ^{232}Th is very stable, it does not dissolve in a solution and cannot be transported by water during weathering processes (Jürgen & Schön, 2015). This can be the reason for the relatively high ^{226}Ra concentration and low thorium contents recorded for most of the tested samples. The radionuclide activity levels obtained in this research are similar to the results of a previous study on uranium, thorium and potassium content measurements, which had been carried out for black Shales of the Bazhenov formation located at the west Siberian marine basin (Zanin et al., 2016)

6.2.7.2 Results of Field Tests

The results of the gamma-ray spectrometry carried out at the six test sites displayed in Figure 6-8 are reported in Table 6-12. Appropriate conversion factors were used to homogenize the unit of measure (1 ppm corresponds to 12.35 Bq kg^{-1} for ^{238}U and 4.06 Bq kg^{-1} for ^{232}Th; 1% of ^{40}K is 313 Bq kg^{-1}) (Erdi-Krausz et al., 2003). According to this table, the mean activity concentration of ^{232}Th (11.52 ± 3.84 ppm or 46.77 ± 15.59 Bq kg^{-1}) and ^{40}K (2.98 ± 1.1 % or 932.74 ± 344.3 Bq kg$^{-1)}$ measured in-situ are similar to the values obtained from laboratory gamma-ray spectrometry.

Table 6-12: Descriptive statistics for the distribution of natural radionuclides and the attributed dose rates in the test sites.

Site Code	N.readings	U (Bq kg^{-1})		Range		Th (Bq kg^{-1})		Range		K (Bq kg^{-1})		Range		Dose Rate (nSv h^{-1})		Range	
		Mean	± SD	min	max	Mean	± SD	min	max	Mean	± SD	min	max	Mean	± SD	min	max
I	485	203.40	157.09	2.47	684.19	48.35	18.31	36.54	112.46	957.78	322.39	187.80	2097.10	195.56	93.05	32.70	483.70
II	125	102.75	40.76	38.29	211.19	39.87	8.57	16.65	62.12	701.12	184.67	406.90	1126.80	122.26	31.99	68.90	191.40
III	31	97.57	39.03	50.64	174.14	47.91	10.47	34.10	68.21	892.05	115.81	563.40	1064.20	135.49	16.83	110.00	165.10
IV	18	52.36	20.75	28.41	114.86	63.99	12.75	25.58	82.01	1032.90	84.51	782.50	1126.80	131.5	11.72	109.40	155.10
V	120	78.42	34.21	22.23	191.43	47.10	14.94	15.02	84.45	1230.09	541.49	469.50	2535.30	141.93	36.67	74.20	218.10
VI	207	158.70	76.57	35.82	344.57	48.64	9.46	24.36	73.49	851.36	156.50	532.10	1283.30	164.05	40.13	77.60	260.40
Total	986	160.06	127.58	2.47	684.19	46.77	15.59	10.96	112.46	932.74	344.30	187.80	2535.30	169.97	75.58	32.70	483.70

Figure 6-13 shows the distribution map of uranium concentrations in the studied test-sites. The maximum value of recorded uranium is 55.4 ppm (684.19 Bq kg^{-1}). Figure 6-14 and Figure 6-15 show the thorium and potassium distribution maps.

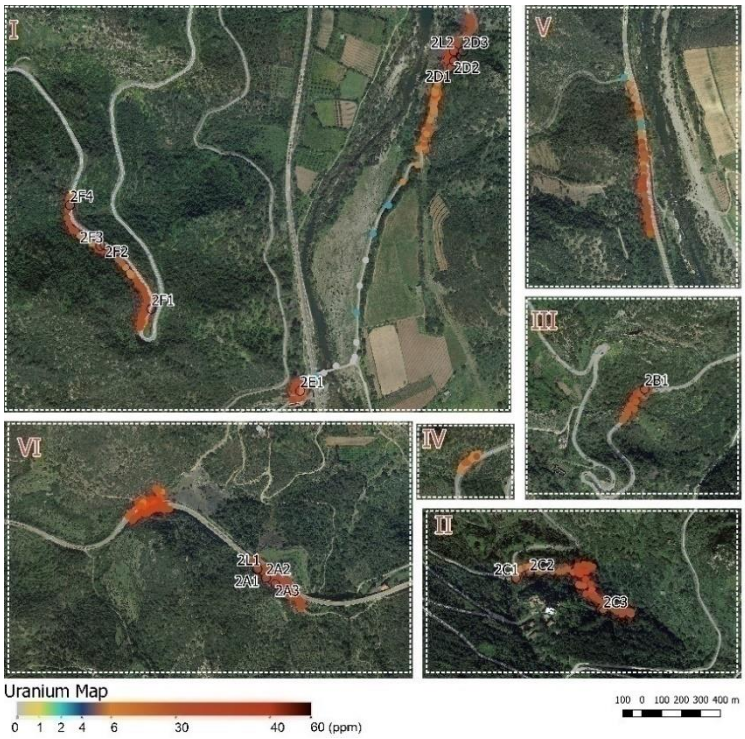

Figure 6-13: Activity concentration of U (ppm) in the test sites (see also Figure 6-8)

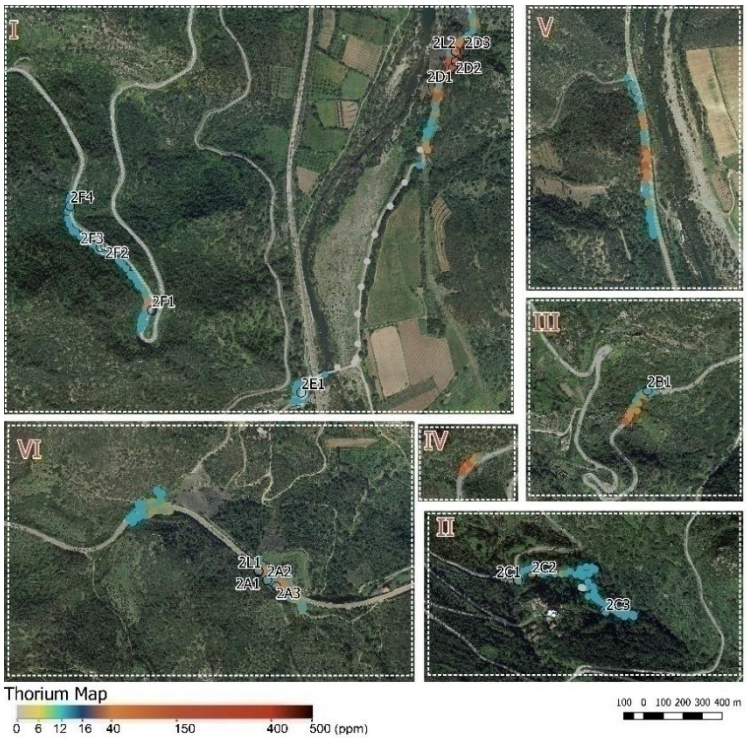

Figure 6-14: Activity concentration of Th (ppm) in the test sites (see also Figure 6-8)

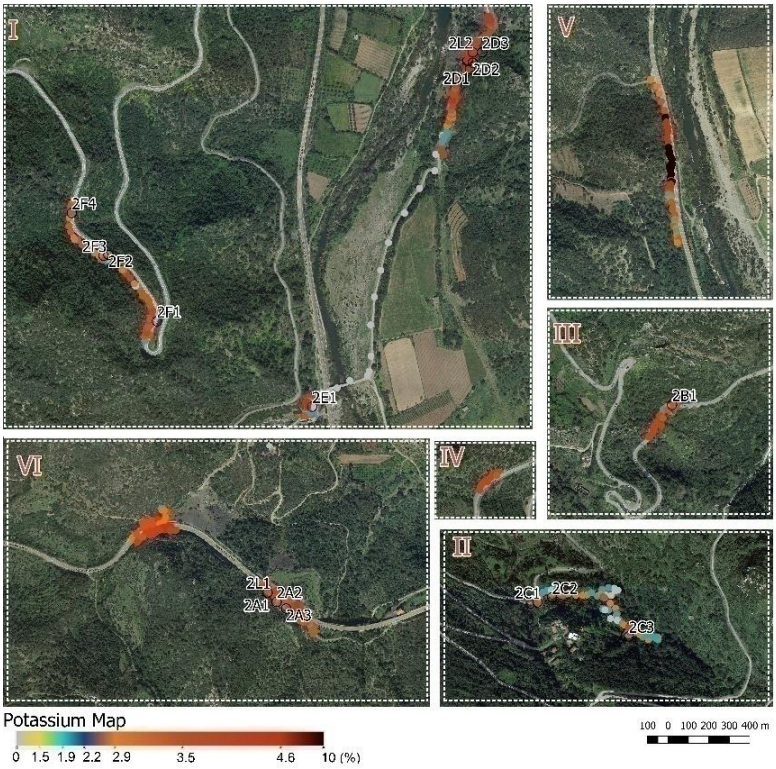

Figure 6-15: Activity concentration of K (%) in the test sites (see also Figure 6-8)

The Th/U ratio indicates the relative depletion or enrichment of radioisotopes. The expected Th/U ratio for the normal continental crust is about 4. Alteration, weathering, or other metasomatic activities can change this ratio (Örgün et al., 2005). As shown in Figure 6-16, Th/U values are much lower than 4, which indicates that the area under exam has been significantly affected by alteration phenomena.

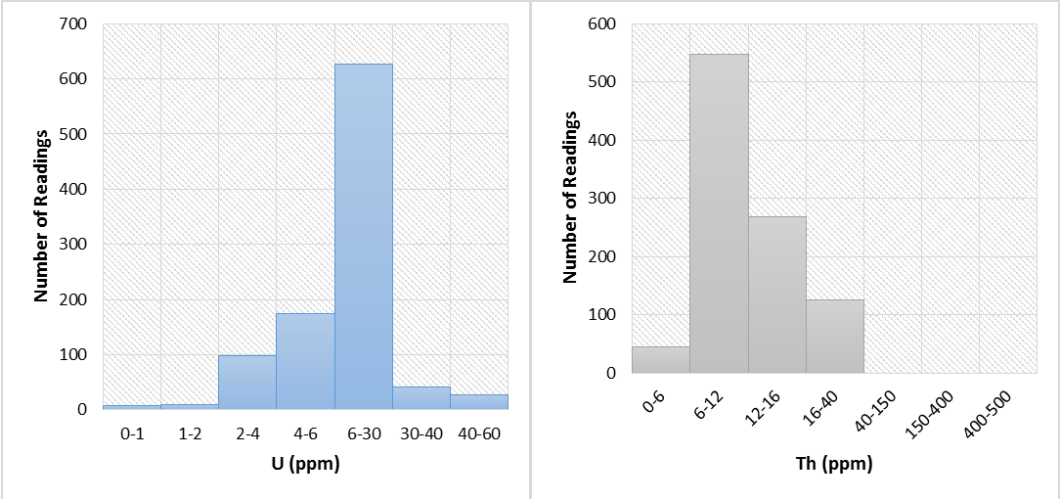

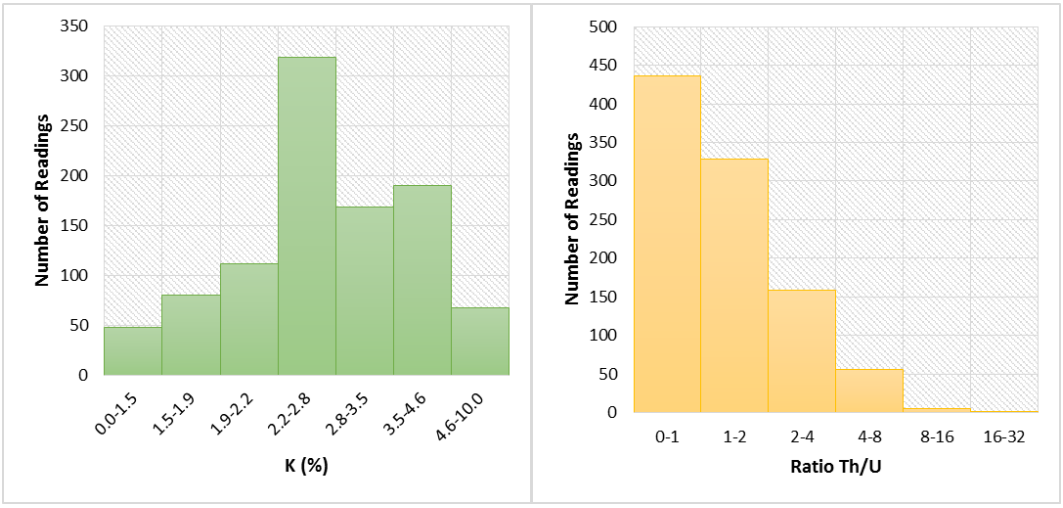

Figure 6-16: Histogram of measured radionuclide concentrations and the Th/U ratios.

6.2.8 Radiation hazard parameters

Knowing the activity concentration of terrestrial radionuclides (^{226}Ra, ^{232}Th and ^{40}K), it is possible to estimate the radiological indexes to be used for the assessment of public exposure to natural radiation. The most commonly used hazard parameters are: the Radium equivalent activity Ra_{eq} (Bq kg^{-1}), the outdoor gamma-ray dose rate D (nGy h^{-1}) and the annual effective dose E (mSv y^{-1}).

The above-mentioned indexes can be calculated according to Equation 6-6 - Equation 6-8 (UNSCEAR, 2008):

Equation 6-6: $$Ra_{eq} = C_{226Ra} + 1.43C_{232Th} + 0.077C_{40K}$$

Equation 6-7: $$D(\text{nGy h}^{-1}) = 0.462C_{226Ra} + 0.462C_{232Th} + 0.0417C_{40K}$$

Equation 6-8: $$D(\text{mSy y}^{-1}) = D(\text{nGy h}^{-1}) \times 8760 \times 0.7 \times 10^{-6}$$

Where, C_{Ra}, C_{Th} and C_K are the activity concentrations of radionuclides ^{226}Ra, ^{232}Th and ^{40}K (Bq kg^{-1}) respectively and O_f is the occupation factor, which is the fraction of the year hypothetically spent outdoors ((UNSCEAR, 2008 suggested value is 0.2).

Table 6-13 reports the values of the radiation hazard parameters calculated based on the results of the laboratory and in-situ gamma-ray spectrometry tests hereby discussed. The mean values of Ra_{eq} were found always below the reference level of 370 Bq kg^{-1} (Beretka and Mathew, 1985), which corresponds to an external effective dose of 1.5 mGy (1 mSv y^{-1}). The mean values of the calculated dose rate are about 3 times the reported population-weighted mean value of 58 nGy h^{-1} for a regular area (UNSCEAR, 2000). The

mean annual effective dose values are within the worldwide ranges (0.01–0.43 mSv y^{-1}) (UNSCEAR, 2008).

Table 6-13: Estimated values of the radiation hazard indexes calculated base on the results of laboratory and in-situ gamma-ray spectrometry.

	Ra_{eq} (Bq kg^{-1})		D (nSv h^{-1})		E (mSv y^{-1})	
	Mean ± SD	**Range**	**Mean ± SD**	**Range**	**Mean ± SD**	**Range**
Laboratory test	327.22 ± 87.74	177.85 - 466.13	180.80 ± 34.12	121.89 - 233.23	0.22 ± 0.04	0.15 - 0.29
Field test	299.07 ± 138.62	53.86 - 883.18	169.97 ± 75.58	32.70 - 483.70	0.21 ± 0.09	0.04 - 0.59

6.2.9 Emanation and exhalation of radon

Radon release from a source to the air is governed by three main processes: the emanation of radon from radium-bearing grains, the accumulation of radon atoms in pore spaces, the transport of radon from porous media to the surface and the subsequent exhalation from the soil surface to the atmosphere (Ishimori et al., 2013). The emanation of radon depends on the ^{226}Ra distribution within the rock, the rock's particle size, its moisture content and mineralogy (Ishimori et al., 2013). To study the role of factors that might affect *radon emanation coefficient* (E), a Pearson correlation matrix (Table 6-14) was built in Excel and the relationships between E, the steady-state activity concentration of radon (C_m) and the contents of thorium and potassium (Table 6-11) were evaluated. A significant positive correlation was found between C_m and E (0.74). A relatively good correlation was also found between the radium content and E (0.65).

Thu et al., 2019 reported that radon emanation is not dependent on the radium content of the soil sample. Because radium has been found to adsorb onto oxidized Fe phases (East, 2014) which makes radium more concentrated on the surface of the soil grains. Black shales are formed in low oxygen environments and therefore the concentration of radium on grain surfaces does not often occur. This fact may explain the reason for the lack of correlation (0.02) between Ra and the radon emanation factor (see Table 6-14).

Table 6-14: Correlation matrix between radon concentration, emanation coefficient and radionuclide concentrations of the tested samples.

Variables	Radon concentration	Emanation coefficient	^{226}Ra	^{232}Th	^{40}K
Radon concentration	1.00				
Emanation coefficient	**0.74**	1.00			
^{226}Ra content	**0.65**	**0.02**	1.00		
^{232}Th content	-	-	**-0.13**	1.00	
^{40}K content	-	-	**-0.61**	**0.57**	1.00

The correlation coefficients obtained for the emanation factor, the radon and ^{226}Ra concentration in this study are similar to values reported by Thu et al., 2019. Moreover, a medium positive correlation was found between ^{40}K and ^{232}Th contents, however the correlation coefficient of ^{226}Ra vs. ^{232}Th and ^{226}Ra vs. ^{40}K were found to be -0.13 and -0.61, respectively. The significant inverse correlation between uranium and potassium (-0.61) can be explained by noticing that a positive correlation between U concentration in black shales and organic carbon and also a negative correlation between K and organic carbon exist (Zanin et al., 2016).

The content of small particles in a rock/soil sample (i.e. silty-clay size) can make differences in the radon emanation coefficient (Sakoda et al., 2010; Thu et al., 2019). Therefore, the correlation between E (Table 6-11) and the particle size intervals (Table 6-10) of the tested samples have been evaluated using Pearson's correlation matrix (Table 6-15). A reasonably good correlation (0.77) was found between the radon emanation coefficient and soil content with a size of less than 0.038 mm (clay size). This is also consistent with the results of the study by Thu et al., 2019.

Using the extrapolated values of C_m and the effective decay constant (λ_e), the radon emanation factor (E) and the radon production rate (P_{Rn}) were calculated (see also Table 6-11). The highest and lowest values of P_{Rn} are 1887.38 and 765.16 Bq m^{-3} h^{-1} respectively. While the mean value is about 1250 Bq m^{-3} h^{-1}. Figure 6-17shows the distribution of the calculated radon production rates.

Table 6-15: Correlation matrix between radon concentration, emanation coefficient and radionuclide concentrations of the tested samples.

Variables		**Emanation coefficient**	**Particle Size (mm)**					
			[0.5 - 1]	[0.25 - 0.5]	[0.125-0.25]	[0.063-0.125]	[0.038 - 0.063]	[< 0.038]
Emanation coefficient		1.00						
Particle Size (mm)	*[0.5 - 1]*	**0.14**	1.00					
	[0.25 - 0.5]	**0.14**	0.00	1.00				
	[0.125-0.25]	**-0.29**	-0.91	0.22	1.00			
	[0.063-0.125]	**-0.19**	-0.87	-0.42	0.65	1.00		
	[0.038 - 0.063]	**0.36**	-0.14	-0.52	-0.20	0.29	1.00	
	[< 0.038]	**0.77**	0.27	0.07	-0.36	-0.37	0.46	1.00

According to a study by Pereira et al., 2017, the arithmetic mean values of the radon production rate for two sets of borehole samples, collected from Hercynian granites of the northern and central part of Portugal, were about 88 and 382 Bq m^{-3} h^{-1}. Furthermore, the radon production rate of three surface samples collected from the same unit but with different degrees of alteration was found to be 403, 598 and 653 Bq m^{-3} h^{-1} (considering an increasing order for the degree of alteration).

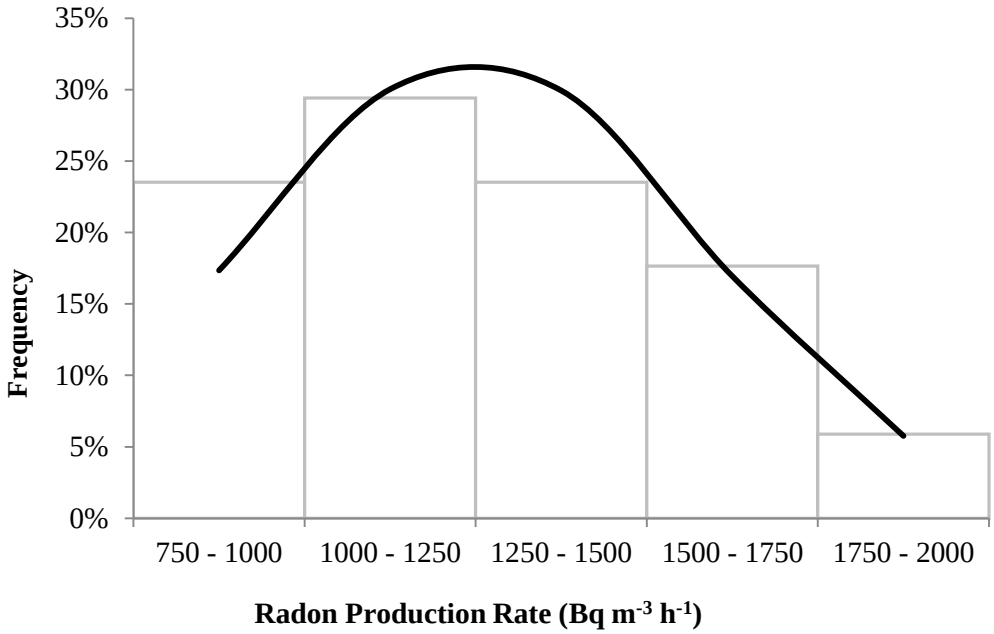

Figure 6-17: Distribution of the radon production rates (Bq m^{-3} h^{-1}) obtained from the analysis of 17 black shale samples.

A simple comparison between the values of radon production rates reported in that research and the estimated radon production rates in this study reveals that the radon production rate of black shales, especially those with higher alteration degrees, can be even considerably higher (about 2~3 times) than the granite formations, which are generally believed to have enhanced geogenic radon potential.

Furthermore, there is another way to have a better overview of the geogenic radon potential levels of black shales of the study area. The soil gas radon (C_{SGR}) can be modeled based on the radon production rate of soils (P_{Rn}) using the following formula (G Cinelli et al., 2015):

Equation 6-9: $$\mathbf{C_{SGR}\left(-\infty\right) = P_{Rn} / \lambda_{Rn}}$$

Unit of C_{SGR} is (KBq m^{-3}), P_{Rn} is (Bq m^{-3} h^{-1}) and for the decay constant of ^{222}Rn, λ_{Rn} is equal to 0.0076 h^{-1}. For our study, the highest and lowest values of P_{Rn} are 1887.38 and 765.16 Bq m^{-3} h^{-1} respectively. While the mean value is about 1250 Bq m^{-3} h^{-1}. So according to the above formula the Min, Average and Max estimated soil gas radon concentrations would be 101, 164 and 248 KBq m^{-3}, respectively.

According to the Neznal categorization indexes (Neznal et al., 2004) (Figure 6-18), even for the minimum estimated soil gas radon and considering the lowest permeability the radon index category would be in the high category.

Radon index (RI) category	Soil gas radon concentration ($kBq.m^{-3}$)		
Low	$c_A < 30$	$c_A < 20$	$c_A < 10$
Medium	$30 \leq c_A < 100$	$20 \leq c_A < 70$	$10 \leq c_A < 30$
High	$c_A \geq 100$	$c_A \geq 70$	$c_A \geq 30$
	low	*medium*	*high*
	permeability		

Figure 6-18: Radon index assessment according to the Neznal method (Neznal et al., 2004)

Moreover, Neznal has also formulated the above-mentioned index as follows (Neznal et al., 2004):

$$\textbf{Equation 6-10: } RP = \left(C_{SGR} - 1 \right) / \left(- \log k - 10 \right).$$

It enables the determination of RI as low, medium, or high (if RP < 10, then RI is low; if $10 \leq RP < 35$, then RI is medium; if $35 \leq RP$, then RI is high). K (m^2) is the permeability of the soil. The low category includes: $10^{-14} \leq K \leq 4*10^{-13}$

So based on even the lowest permeability value ($K= 10^{-14}$) the average RI would be 40.75 which is located in the high-risk zone. The comparison of the results of radon production rate measurements of a similar experiment together with categorized levels of the modeled soil radon express that the black shales of the Villasalto area might represent high geogenic radon potential which is in agreement with the predicted level of GRP by the proposed geogenic radon map of Sardinia Figure 5-13.

6.3 Evaluation of levels of Occupational Exposure to Radon in the Gallery of Medau Zirimilis Dam, Sardinia Italy

The last experiment to examine the prediction power of the GRP map is a comprehensive radon survey in Medau Zirimilis Dam. According to Figure 5-13, the predicted GRP varies between very low to moderate levels. However, some veins of high GRP can be seen within the dam area (Figure 6-19). As can be seen in the map below, the structure of the dam itself has been built on the bedrocks, which might have elevated radon release potential.

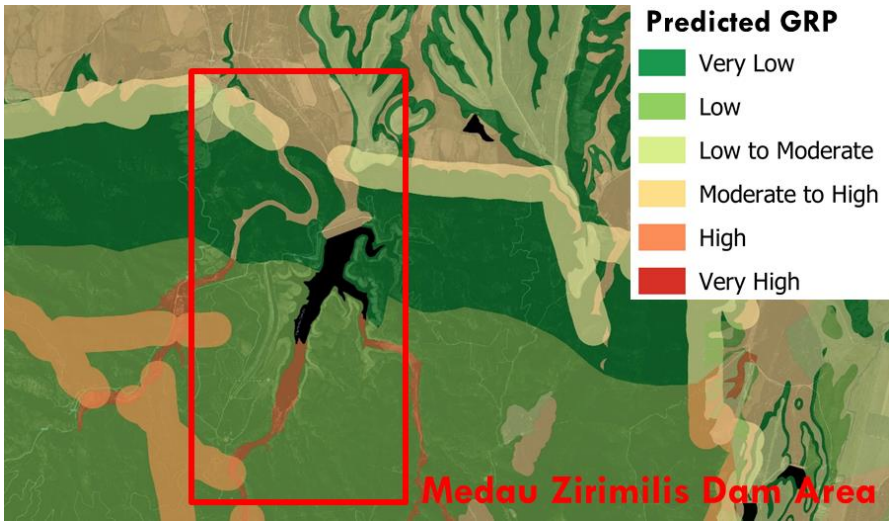

Figure 6-19: Predicted GRP levels for Zirimilis Dam Area according to Figure 5-13

Records of occurrence of elevated indoor radon concentrations were observed in this dam during the preliminary analysis of radon levels using an active radon monitor. This highlighted particular conditions that required further investigations and, therefore, to identify the source of radon and to understand how radon is transferred from the source to the indoor space of the dam gallery, a set of in-situ and laboratory tests were considered for this pilot study area. The measurement results were analyzed and the rate of radon production from the solid sediments collected from the drainage system of the dam was estimated. Finally, possible remediation solutions for the protection of life and health of the employees were introduced.

6.3.1 Site Description

The Medau Zirimilis Dam is an embankment dam which is located on the Casteddu River in the southwest of Sardinia. The dam was constructed for irrigation purposes and the supply of drinking water. The materials for the construction of the dam were taken from the pediments and terrace levels. The dam was completed in 1991 with a capacity of 19

Hm^3, longitude of 480 m and a maximum height of 151 m asl, reaching 44 m from the lower part of the reservoir (Anchuela et al., 2018). As shown in Figure 6-20, the dam is located in the transition area where the Palaeozoic basement is related to the Hercynian orogenic evolution outcrops. The Palaeozoic basement consists of an originally sedimentary succession (Lower Cambrian to Early Carboniferous) that was deformed during the Carboniferous period under the low metamorphic to anchizonal setting (Baiocchi et al., 2015; Carmignani et al., 1982). The Arburese Unit outcropping at the dam site consists of the Arenarie di San Vito Formation (Middle Cambrian to Lower Ordovician), which is several hundred meters thick and is composed of decimetric to metric alternations between micaceous metasandstones, quartzites and metasiltstones. Clastic, poorly cemented sediments, from gravels to sands and silts, of the Upper Pleistocene to the Holocene overlay the metamorphic basement (Baiocchi et al., 2015; D'Angelo et al., 2013).

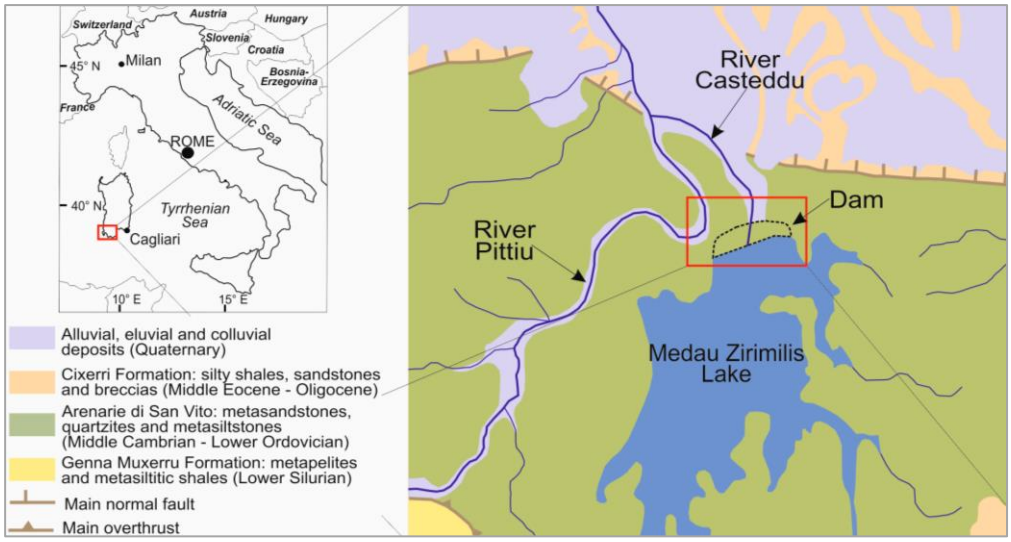

Figure 6-20: Simplified map of the main geological features and the location of Medau Zirimilis Dam (Baiocchi et al., 2015).

The structural framework is mainly linked to the Hercynian Orogeny and Pliocene tectonic events. The Hercynian tectonics favored the thrust of the Arburese Unit over the Upper Ordovician to Lower Carboniferous succession and its deformation in large scale folding with axes of folds E–W and N–S oriented. The Pliocene tectonics shallow modified the structural setting through typical fault systems E–W and N–S to NNW–SSE oriented (Baiocchi et al., 2015; Barca et al., 1982; Carmignani et al., 2001). In the case of hydrogeological properties of the Palaeozoic basement, it is known that the metamorphic rocks form a low-permeability aquifer where groundwater circulation occurs in the fissured zones close to the surface (on average, the first tens of meters). In

the most heavily fractured zones (i.e., near the faults), the groundwater flow is more active and can occur at a greater depth (Baiocchi et al., 2015).

6.3.2 Methodology

During the preliminary inspections, outgassing and dispersion of the radon dissolved in the water (or more accurately, the radon coming from sediments), which was flowing through the drainage system, was recognized as the most probable scenario for the occurrence of enhanced radon concentrations. To verify this hypothesis, sediment samples from three different parts of the drainage canal of the gallery (see Figure 6-21) together with a water sample were collected. Then, the indoor radon concentration was monitored in the center of the gallery (redpoint on Figure 6-21.c) using two continuous radon monitors (CRMs) (MR1 plus and Radex MR-107). The collected sediments were mixed and then oven-dried for 24 hours at 110 ◦C, sieved (mesh size finer than 200 microns) and eventually, introduced to radon exhalation rate testing. The natural radionuclide concentrations of the homogenized sediment sample were also measured by using the gamma-ray spectrometry technique. Besides, the radon in the water concentration of the sample taken from the drainage system of the dam was determined. Based on the result of the mentioned tests, the steady-state radon concentration, radon emanation factor and radon production rate of the sediment sample were calculated and compared with levels of radon dissolved in the water sample.

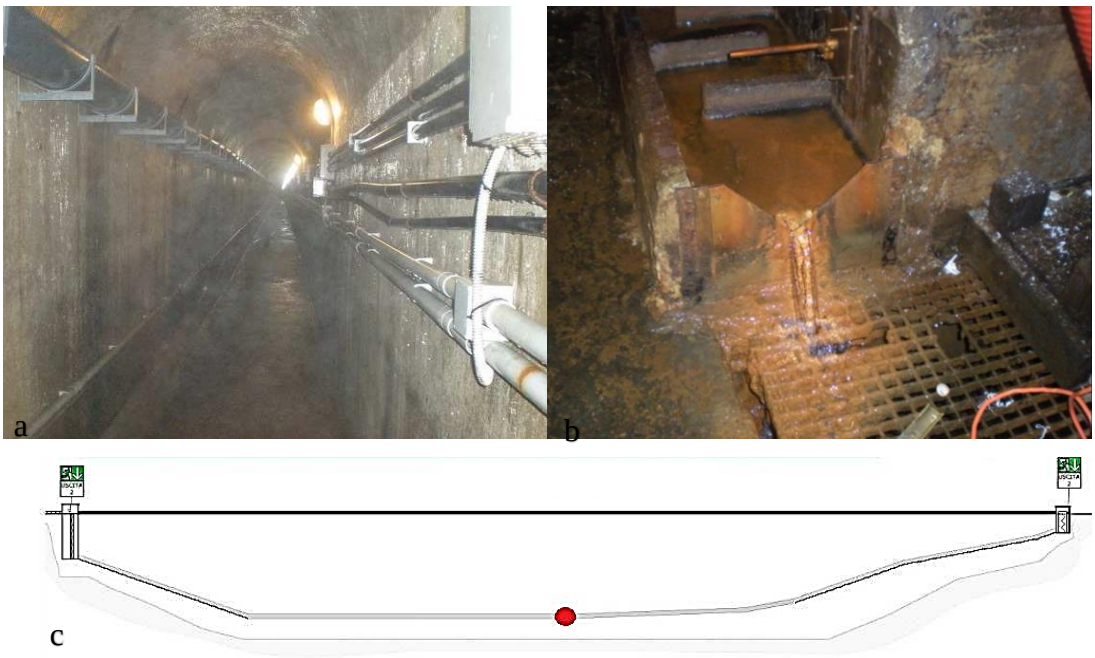

Figure 6-21: The gallery of Medau Zirimilis Dam, b): the drainage canal of the dam gallery containing considerable consents of sediments and c): section plan of the dam, the radon measurement point is also specified.

6.3.3 The Radon Production Rate of Sediments

The experimental set-up to measure the radon exhalation rate from the surface of the sediment sample makes use of a Radex MR-107, which is an active radon monitor that was placed inside an accumulation chamber consisting of a pressure-resistant vacuum glass chamber. In the first step, the soil sample was weighted and put inside a plastic container with a known volume. Then, as shown in Figure 6-11, while the sample was placed inside the system, the chamber was efficiently closed to keep the airtightness.

The activity concentration of radon inside the chamber was measured hourly for about 120 hours. The radon growth model released from the surface of the sediment sample can be modeled using the two-dimensional diffusion theory (Sahoo & Mayya, 2010), according to Equation 6-11:

Equation 6-11: $$C(t) = C_0 e^{-t\lambda_e} + C_m(1 - e^{-t\lambda_e})$$

Where λ_e is the effective radon decay constant (h^{-1}), accounting for the radon decay constant, the leak rate of the system and the so-called ‘‘back diffusion”, C_0 and Cm are the radon activity concentration (Bq m^{-3}) in the closed chamber at time = 0 and its maximum value, respectively (Leonardi et al., 2018). The values of λ_e and Cm for each sample were extrapolated using nonlinear least-squares fitting of the experimental data with Equation 6-11 (Tan & Xiao, 2011)(Kemmer & Keller, 2010). The radon emanation coefficient (E) was calculated from the following equation (Ishimori et al., 2013):

Equation 6-12: $$E = \frac{V_{eff} C_m}{A_{Ra} W}$$

Where W is the weight of the sample (kg) and A_{Ra} is the ^{226}Ra mass activity (Bq kg^{-1}) of the test sample. From the abovementioned parameters and considering the γ_d as the apparent density of the sample, the radon production rate P_{Rn} (Bq m^{-3} h^{-1}), was also estimated using the following equation (Ishimori et al., 2013)(Pereira et al., 2017):

Equation 6-13: $$P_{Rn} = \lambda_e E A_{Ra} \gamma_d$$

6.3.4 Determination of the Radionuclide Concentrations in Sediment Samples

The radionuclide (i.e., ^{226}Ra, ^{232}Th and ^{40}K) activity concentrations were measured using the Ortec NaI (Tl) detector (3 × 3 inches) placed in the laboratory of nuclear physics of the University of Cagliari (Figure 2-1). The homogenized sediment sample (with a weight of approximately 32g) was filled in a plastic beaker, sealed carefully and left undisturbed for about four weeks to reach equilibrium in the ^{238}U chain before measurement. IAEA

reference source of RGU1 and RGTh1, together with a high pure potassium nitrate salt, was used for calibration of the system. Energy calibration of the detector was carried out using disc sources of ^{60}Co and ^{137}Cs. The spectrum was processed by MAESTRO multichannel analyzer emulation software. The effect of the background was also evaluated while estimating the activity concentration of radionuclides.

6.3.5 Radon in Water Measurement

To measure the concentration of radon in water, the MR1 plus radon monitor was connected to the H2O-Kit accessory, which was provided by the manufacturer (Figure 2-10). A glass vessel of 300 ml of active water sampled from the drainage canal of the dam gallery was set up in a closed air loop with the MR1 plus. By operation of the instrument's pump, the sample was aerated via a bubbler and the radon that was in the water throughout the loop was distributed. Then the radon gas was introduced into the Lucas cell. A filter was also used to remove humidity from the air entering the Lucas cell.

6.3.6 Results

As a follow-up test, the indoor radon level in the gallery of the Medau Zirimilis dam was monitored for 72 hours using two continuous radon monitors. Due to the loss of the electric power supply during the test operation, the MR1 plus was turned off. Because of this, only the values recorded by Radex MR-107 are presented in this section (see Figure 6-22). The results show a mean indoor concentration of radon of about 683 ± 516 Bq m^{-3} with minimum and maximum values of 30 and 1998 Bq m-3, respectively (Figure 6-22: Results of indoor radon concentration monitoring inside the dam gallery are presented in Table 6-16. To identify the source of indoor radon, sediment samples together with a water sample were collected. The sediments were introduced to the gamma-ray spectrometry and radon exhalation rate tests. The results of measurements are shown in Figure 6-23 and Figure 6-24. A significantly high ^{226}Ra concentration (226.27 ± 7.07 Bq kg^{-1}) was found in the sediment sample. However, the concentration of ^{232}Th (37.25 ± 5.43 Bq kg^{-1}) and ^{40}K (210.45 ± 197.82 Bq kg^{-1}) were relatively low. This can be justified by the behavior of these radioisotopes in the environment. When the water passes through the bedrocks hosting uranium-bearing minerals (the shales from Genna Muxerra formation can be an example for this study- see also Figure 6-20), ^{226}Ra from the host rocks can be easily dissolved in water due to its relative solubility and transported through the aquifer. While ^{232}Th is very stable, it will not dissolve in a solution (Schon et

al., 2015) and cannot be transported by water. The low concentration of ^{40}K can also be related to the low concentration of this element in the host rock.

To measure the radon production rate, the technique of radon accumulation inside a closed chamber was employed. Using the nonlinear least-square fitting of Equation 6-11 on the measured data, the steady-state radon concentration was predicted to be 3652.16 ± 159.65 Bq m^{-3} and then utilizing Equation 6-12 and Equation 6-13, the radon emanation factor and the radon production rate of the sediment sample were calculated (Table 6-17). A considerably high value of radon production rate was obtained (4969.21 Bq m^{-3} h^{-1}). This can be explained by the presence of high ^{226}Ra content and also tiny particle size (less than 200 microns) of the sediments that increase the emanation of radon and subsequently leads to higher radon production rates.

Table 6-16: Summary of radon in the air and radon in water test results

Measurement type	Testing time (hour)	Statistic of radon concentrations (Bq m^{-3})			
		Mean ± SD	Median	Min	Max
Radon in the air	72	683 ± 516	554	30	1998
Radon in the water	146	4760 ± 3879	3968	203	17268

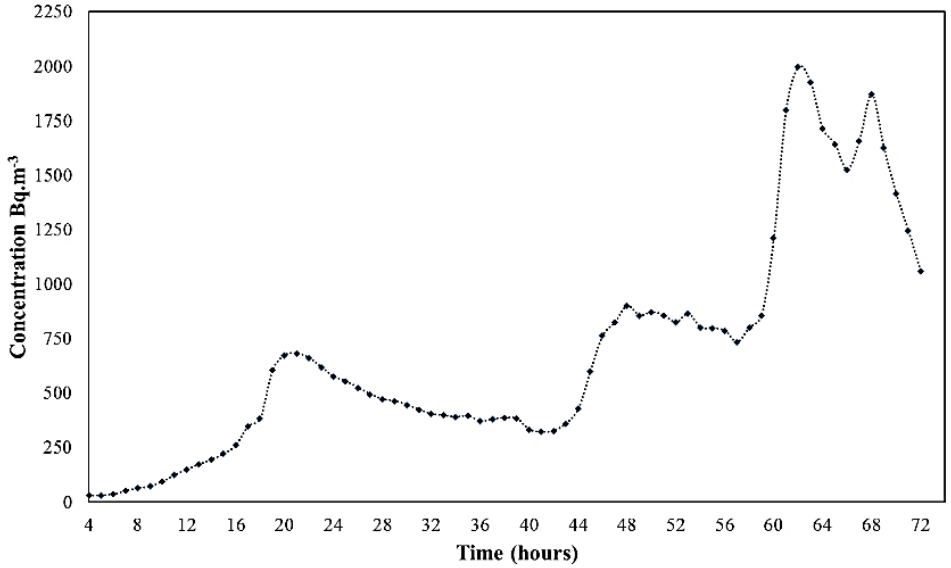

Figure 6-22: Results of indoor radon concentration monitoring inside the dam gallery

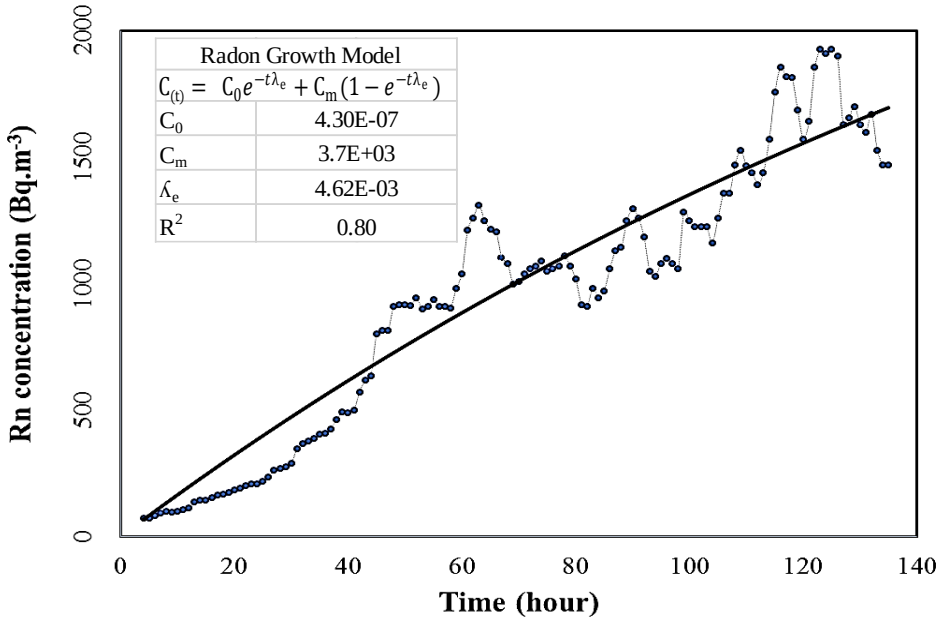

Figure 6-23: Monitored radon activity concentrations released from sediment sample and the fitted radon growth model, based on the results of radon exhalation rate testing.

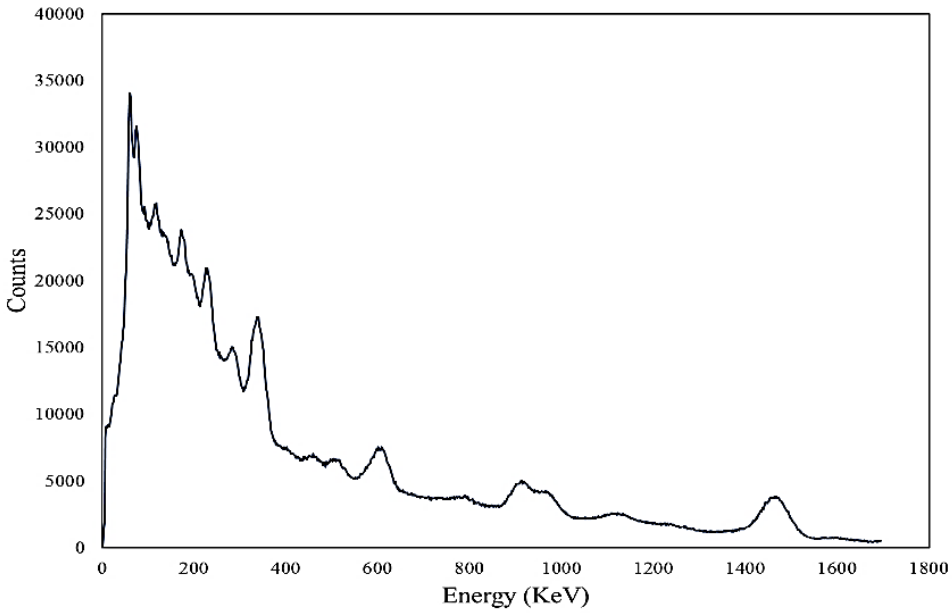

Figure 6-24: Gamma spectrum of the sediment sample obtained by NaI (Tl) detector.

The radon activity concentration of the water sample containing 300 ml of active water was measured for about 140 hours, according to the Lucas cell method. As presented in Table 6-16, the mean concentration over the measurement period is about 4.96 KBq m^{-3} that ranges between 0.2 to 17.2 KBq m^{-3}. Figure 6-25 shows the recorded values of radon in water concentrations in which high variations can be seen. The reason for this is the presence of the non-equilibrium state between radon and its progeny.

6.3.7 Radon Transportation Scenario

In surface waters like lakes and rivers, the radon concentrations are generally very low values in the range. This is since radon can readily escape from the water surface and subsequently be diluted in the free air (Yalcin et al., 2011). In the case of the outgassing of radon in underground spaces (ex. waterworks), the radon released from water accumulates in indoor spaces and contributes to high concentrations. It is believed that the same phenomenon occurs in the gallery of Medau Zirimilis Dam. The radon originating from uranium-bearing minerals of the bedrock is transported through the aquifer and penetrates to the gallery through the cracks and joints on the structure. While the drainage system of the dam is collecting the water, a part of this radon escapes to the indoor air due to the aeration process. Finally, Due to the lack of proper ventilation, the released radon accumulates inside the gallery in concentrations that may exceed the reference levels.

Table 6-17: Natural radionuclide activity concentrations and estimated values of radon emanation factor and radon production rates of the solid sediment.

Radionuclide activity concentrations		
Ra ± σ (Bq kg^{-1})	**Th ± σ (Bq kg^{-1})**	**K ± σ (Bq kg^{-1})**
226.27 ± 7.07	37.25 ± 5.43	210.45 ± 197.82
Radon exhalation rate testing		
Extrapolated steady-state activity ± standard error (Bq m^{-3})	**Radon emanation factor**	**Radon production rate (Bq m^{-3} h^{-1})**
3652.16 ± 159.65	3.17	4969.21

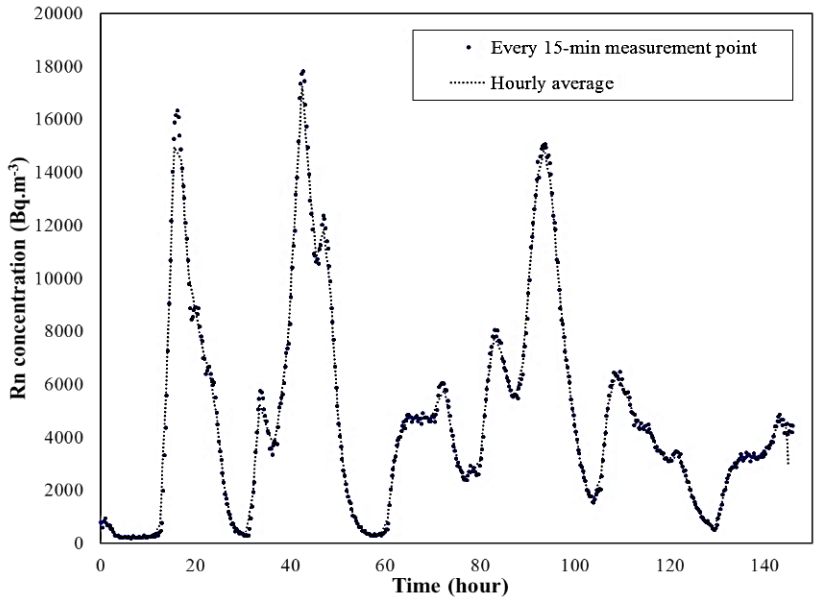

Figure 6-25: Monitored radon in water concentrations, the water sampled from the drainage system.

An outlook of Chapter 7

In this chapter, the prediction power of the GRP map was tested through three experiments plus a comparison of available indoor radon data with GRP categories. In general, it was found that the estimated GRP categories are in agreement with real-time measurement test results. Thus the developed map would help better to understand the geogenic radon potential of an area to be examined. However, the methodology used for the development of this map was a comparative approach. In other words, if one needs an accurate prediction of radon for smaller sites (i.e., better resolution) or even for future construction sites (e.g., for a new hospital building), the proposed map would not be able to give sufficient precision. Therefore in the next chapter, the methodology for the production of accurate radon maps will be introduced. This technique is based on the development of geostatistical models to predict geogenic radon risk.

7 APPLICATION OF GEOSPATIAL MODELS FOR ACCURATE GRP PREDICTIONS

Summary

A detailed survey for the accurate geogenic radon potential (GRP) prediction was carried out by performing geostatistical analysis on radon-related variables to evaluate the exposure of people to natural radiation in a radon-prone area near Graiguenamanagh town (County Kilkenny) in south-eastern Ireland. The geological setting of the study area mainly includes an offshoot of the Leinster granite. To model radon release potential at different points, an Ordinary Least Squared (OLS) regression model was developed in which soil gas radon (SGR) concentration measured in-situ using a Radon RM-2 detector was considered as the response value. Proxy variables such as radionuclide concentrations obtained from airborne radiometric surveys, soil gas permeability, distance from major faults and Digital Terrain Model were used as the main predictors. All data processed in Geographic Information Systems (GIS) using geospatial analysis and geostatistics. The proposed model was validated through diagnostic tests. Empirical Bayesian kriging (EBK), a geostatistical interpolator, was used to produce the map of the spatial distribution of predicted GRP values and to estimate the prediction uncertainty. The EBK was also used for a cross-validation procedure between the predicted SGR values and those measured. This model could be successfully used to estimate the GRPs of other areas where data on the mentioned radon-related proxy values are available.

In Ireland, the Environmental Protection Agency (EPA) had produced a 10km grid cell size radon map based on results of indoor radon surveys in approximately 11,000 homes (http://www.epa.ie/radiation/radonmap/). The map was later improved by a combination of indoor radon measurements and relevant geological information (Elío et al., 2017). In the latest map, logistic regression was used to predict the probability of having an indoor radon concentration above the Irish national reference level (i.e., 200 Bq m^{-3}). Furthermore, the Geological Survey of Ireland is working with the EPA to predict natural sources of radon in rocks, soils and waters based on Tellus airborne geophysical data and soil geochemistry data. In this chapter, the goal is to develop a geostatistical model to predict the geogenic radon potential for a granite area in south-eastern Ireland. To aim this, airborne radioelement concentrations (i.e., eU and eTh), air absorbed dose rate, distance from the major fault, soil permeability and the digital train model were considered as proxy variables (i.e., predictors). Soil-gas radon concentration was taken into account as the response value. Then an Ordinary least squared (OLS) regression model was developed and the significance of each proxy variable to support the proposed model together with the validity of the model was evaluated. The method introduced here can be robust and utilized to develop geogenic radon potential maps with a high spatial resolution for the other parts of Irish territory. The presented GRP map can also be used as a useful tool for land-use planning and mitigation strategies adopted by the local administration authorities.

7.1 Study Area Description

The study area, which extends on a surface of about 4km^2, is located near Graignamanagh, a town in County Kilkenny, Ireland, which has historical and touristic importance. As shown in Figure 7-1, the measurement site is placed in alluvial deposits (i.e., coarse-textured gravels and sands) of the Barrow valley. Depth of the soil was varying from deep soil at uphill to shallower depth near the shores of the Barrow river (CAAS, 2003). The geological setting of the study area consists of Caledonian Leinster Granite, which, based on the results of previous studies, is often known as the rocks associated with high radon concentration (McAulay & McLaughlin, 1985). Moreover, the Radiological Protection Institute of Ireland has named some towns in County Kilkenny, including Graignamanagh, as areas that may possess high radon levels (McGarry et al., 1997). Considering these, the mentioned area was selected as the case study to firstly identify

areas where indoor radon concentration is likely to be higher to aim at health risk reduction for the inhabitants and secondly to develop a model for accurate predictions of soil-gas radon based explanatory data on a local scale.

Figure 7-1: Satellite image of the study area with the location of the soil gas radon testing sites and airborne radiometric survey points

7.2 Materials and Methods

7.2.1 Airborne Radiometric Data

Ideally, a GRP estimation is derived from radon soil gas concentrations (SGR) (Kropat et al., 2017). An alternative method to detect the radon in the ground is to use airborne gamma spectrometry (Smethurst et al., 2017). In Ireland, there are insufficient SGR data to generate useful radon potential maps. However, airborne radiometric data, provided by the Tellus project is available with a high resolution for most of the Irish territories (http://www.tellus.ie). The airborne radiometric survey is carried out by using a low-flying aircraft (flying at 60 m in rural areas and 240 m in urban areas). The data are recorded by a 256-channel gamma spectrometer (Exploranium GR820) covering 0.3–3 MeV (Hodgson and Young, 2016). They are integrated over flying distances of about 50m. The gamma-ray count rates for the energy lines of Potassium (^{40}K), equivalent

uranium (eU, estimated from ^{214}Bi) and equivalent thorium (eTh, estimated from ^{208}Tl) are measured as a result of surveys. Then the obtained count rates which had the unit of count per seconds (cps) were converted to part per million-ppm (eU and eTh), percent (^{40}K) and, nGy h^{-1} (total count) using the standard conversion rate, suggested by Geosoft® (Barberes et al., 2015). The descriptive statistics of equivalent Uranium (eU) and equivalent Thorium (eTh) together with air absorbed dose rates (ADR_{air}) are reported in Table 7-1. The Shapiro-Wilk test (Shapiro & Wilk, 1965) was also applied at a statistically significant level of 0.05 to test the normality of the distribution of radiometric data.

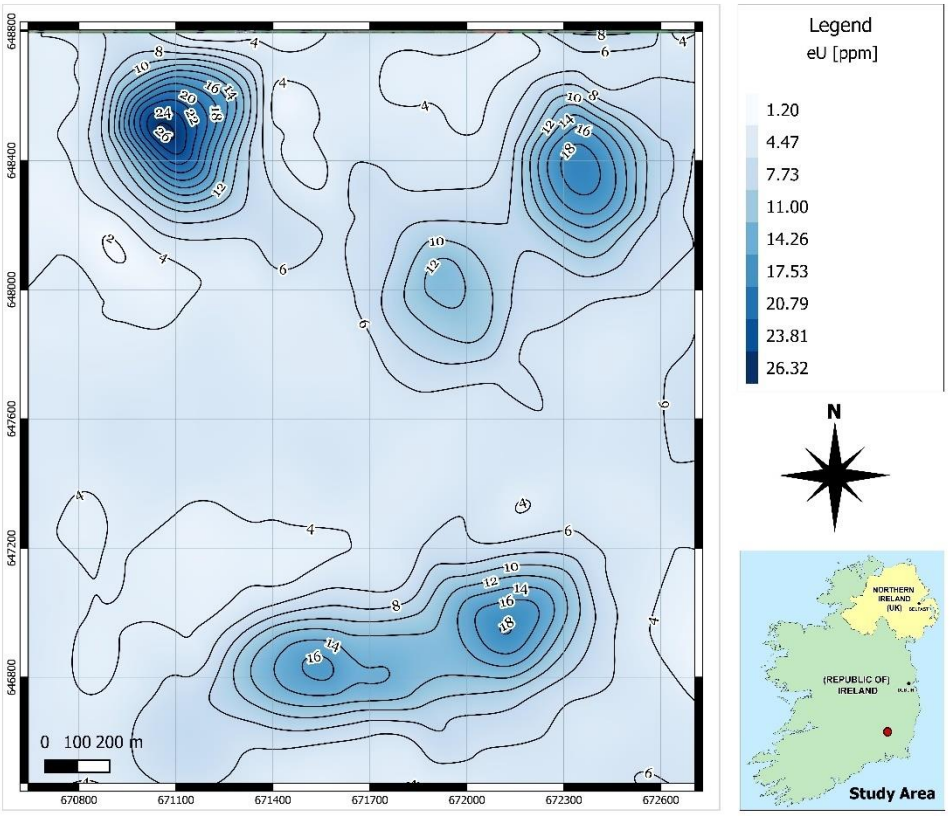

Figure 7-2: Contour map of equivalent uranium concentration (eU)

As shown in Figure 7-1, there are gaps between the airborne survey lines. To predict the radiometric values for the points located within the gap space, the cubic spline interpolation method was utilized in QGIS software. This method is best for gently varying surfaces (e.g., pollution concentrations) (Mitáš & Mitášová, 1988). Using this method, raster maps of smooth surfaces of radiometric data (Figure 7-2 to Figure 7-4) were produced and then the contour lines were generated using the Contour Extraction

tool of QGIS. Finally, the eU, eTh and ADR_{air} values corresponding to each SGR test point location were extracted using the Raster Sampler tool in QGIS.

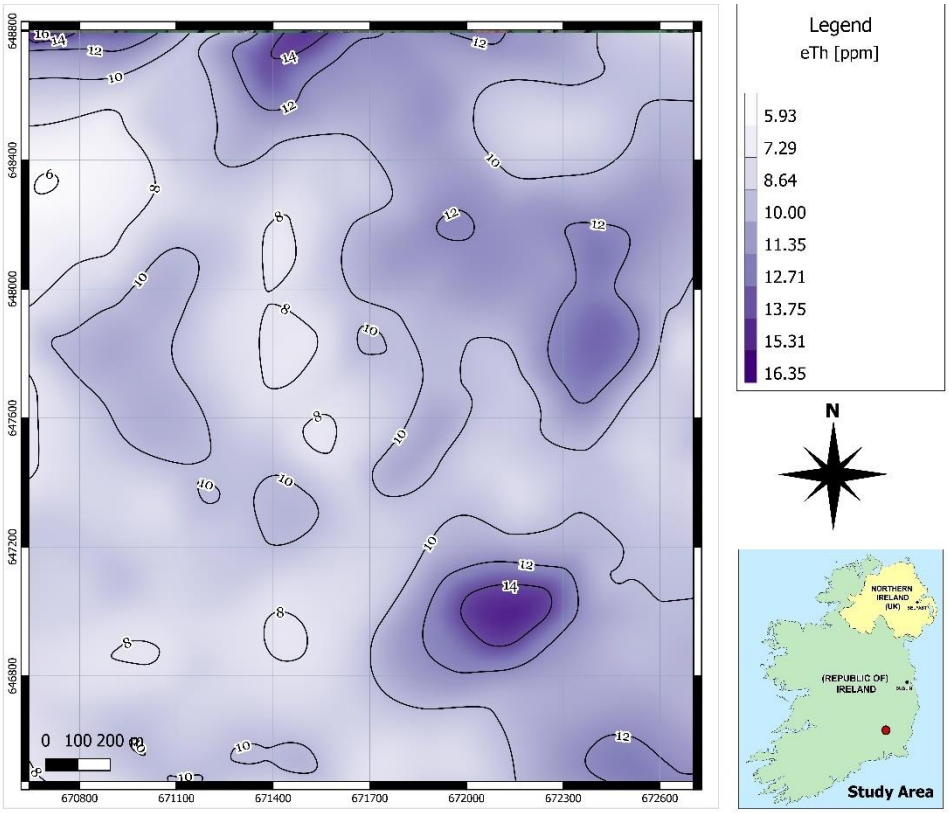

Figure 7-3: Contour map of equivalent thorium concentration (eTh)

Table 7-1: Descriptive statistics of extracted airborne radiometric data and soil gas radon concentrations

Statistic	eU (ppm)	eTh (ppm)	ADR_{air} (nGy h^{-1})	SGR (KBq m^{-3})
Number of data		40		
Minimum	2.42	7.53	124.81	5.60
Maximum	17.37	13.54	214.45	236.00
1st Quartile	4.44	8.60	150.62	57.90
Median	4.94	9.61	154.65	74.30
3rd Quartile	5.47	10.38	159.83	109.25
Mean	5.39	9.63	154.70	87.96
Standard deviation	2.25	1.26	14.14	49.34
Skewness (Pearson)	3.78	0.64	1.50	0.88
Kurtosis (Pearson)	17.44	0.54	6.29	0.64
Geometric mean	5.10	9.55	154.09	71.95
Geometric standard deviation	1.36	1.14	1.09	2.10
Shapiro-Wilk test (W)	0.62 Reject normality (P <0.0001)	0.96 Normal distribution (P=0.22)	0.85 Reject normality (P <0.0001)	0.94 Reject normality (P =0.04)

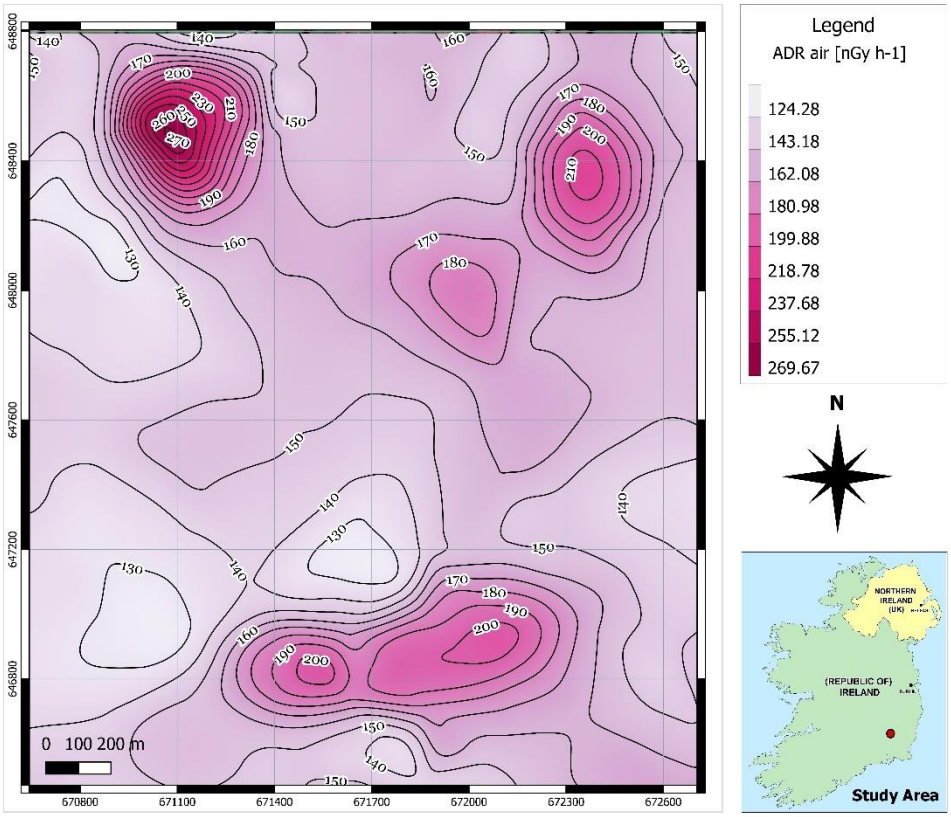

Figure 7-4: Contour map of air absorbed dose rates (ADRair)

7.2.2 Soil Gas Radon and soil Gas Permeability Test

Soil gas radon activity concentrations were measured at 40 measuring sites (see also Fig.1) by using a Radon detector RM-2 in March 2020. Besides, the permeability of soil was determined at each measuring point using RADON – JOK equipment. At selected sites, at the first step, the time required for pumping 2 liters of air from the soil employing negative pressure mechanically created by RADON – JOK, was recorded and depending on the time spent, the soil gas permeability was calculated. In the second step, the soil gas sample was collected from 80 cm depth of the soil through a hollow steel rod using a plastic 150ml-volume syringe and transferred to an evacuated ionization chamber. After a time delay of 15 minutes, the chamber was introduced to the detector and the concentration of radon was measured based on the number of alpha counts that give rise to ionization current in the ionization chamber (Neznal et al., 2004). Both SGR (KBq m^{-3}) and permeability values (m^2) were georeferenced and introduced to the ArcGIS version 10.5 software. Spatial variability of the measured parameters was processed to generate a contour map of SGR using the ordinary Kriging method, which is a geostatistical interpolator that uses randomly distributed measured data to predict values at the un-

sampled locations (Giustini et al., 2019). Descriptive statistics of soil gas radon together with produced contour map are shown in Table 7-1 and Figure 7-5, respectively.

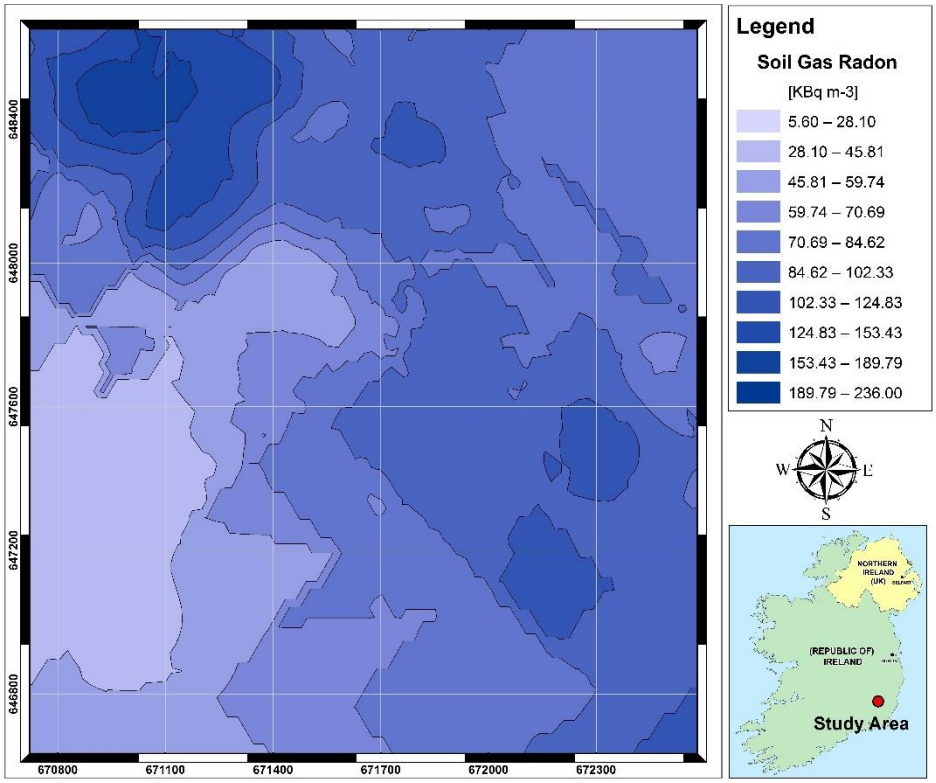

Figure 7-5: Contour map of measured soil gas radon (SGR) activities.

7.2.3 Distance from Fault Lines

The presence of geologic faults increases radon levels on the ground by providing favorable pathways from the source of uranium-rich bedrock units to the surface. Generally, a distance less than 150 m from a major fault may have a more considerable influence on the abnormal increase of radon potential (Drolet & Martel, 2016). On the other hand, the alterations of magmatic and crystalline rocks along the non-active faults may increase the ratio of clay minerals which decreases the permeability and the radon potential (Barnet, 2008). Therefore, the presence of tectonics may not necessarily increase radon potential. As can be seen in Figure 7-1, there is a fault structure with NW-SE orientation in the study area. To evaluate the effect distance from a fault on soil gas radon variations, the distance of each SGR test point from the fault line was calculated. To aim this, the vectorized tectonic structure map (scale 1:100,000) (https://www.gsi.ie/) was first added as input for QGIS software. Then, distance calculations were performed using the Nearest Neighbour join (NNjoin) Plugin.

7.2.4 Geostatistical Model Setting

To evaluate relationships between predictors and the response variable, the Ordinary Least Squared (OLS) regression was employed. OLS is a commonly utilized regression technique for geostatistical modeling of the radon potential (Ciotoli et al., 2017). It is also a starting point for all spatial regression analyses. Equation 7-1 presents the linear function of the repressors, which can predict the response variable based on explanatory variables.

Equation 7-1: $$y = \beta_0 + \beta_1 X_1 + \beta_2 X_2 + ... + \beta_n X_n + \varepsilon$$

where y is the dependent variable predicted, X_i are the explanatory Variables and βi are the coefficients computed by the regression tool, representing the strength and type of relationship between x and y and ε are the residuals, i.e., the unexplained portion of the dependent variables. In this study, equivalent uranium (eU), equivalent thorium (eTh), gas permeability (LogP), Digital Terrain Model (DTM), distance from Fault line (FD) and air absorbed dose rate (ADR_{air}) were considered as predictor variables for the GRP model while considering soil-gas radon (SGR) concentrations as the response variable. The predictor variables in this study are selected based on the explanatory variables investigated in similar research (Ciotoli et al., 2017; Giustini et al., 2019).

To validate the OLS model, the variance analysis and the diagnosing tests of Multicollinearity (by measuring Variance Inflation Factor (VIF) (Kleinbaum et al., 1998)), Heteroscedasticity tests (i.e., Breusch-Pagan and White tests (Breusch & Pagan, 1979; White, 1980)) and Spatial Autocorrelation test (i.e., Durbin-Watson test (Durbin & Watson, 1971)) were performed and the adjusted R^2 value, the coefficient of how much variation in a dependent variable's values is explained by a set of explanatory variables, together with the other statistical parameters and assumptions have been examined.

An adequately specified OLS model (i.e., errors are normal, homoscedastic and independent of the repressors and the linear specification of the model is correct) should meet the following requirements (Ciotoli et al., 2017): a) an adjusted R^2 of 0.50 or higher, b) significance of the β coefficients (p-values that are less than 0.05), c) a VIF of less than 7.5, d) a Jarque-Bera statistics for normality test (p-value greater than 0.10) and e) a spatial autocorrelation test (p-value greater than 0.10). These statistical parameters were

calculated and analyzed for the proposed OLS model by running the XLSTAT add-in within Microsoft Excel media (Addinsoft, 2019).

7.3 Results

7.3.1 Preliminary Statistics

Table 7-1 summarizes the descriptive statistics of airborne radiometric data and the measured soil gas radon (SGR) concentrations. SGR values ranged between 5.60 kBq m^{-3} and 236.00 kBq m^{-3} with a mean value of 87.96 kBq $m^{-3,}$ which is a significantly high value even for an area with a granitic background. The equivalent activity of uranium and thorium ranged from 2.42 to 17.37 ppm and from 7.53 to 13.54 ppm, respectively. The calculated mean value of eU (5.39 ppm) is slightly higher than the average value of uranium in U and Th enriched granitic rocks (5ppm for U and 15ppm for Th (Tzortzis & Tsertos, 2004)). However, the mean calculated eTh (9.63 ppm) was considerably lower than the average Th content in the granite rocks. The mean air absorbed dose rate measured for the study area is almost 2.5 times the population-weighted average absorbed dose rate in the air outdoors from terrestrial gamma radiation of 60 nGy h^{-1} (UNSCEAR, 2000). Comparing the contour maps of eU and air absorbed dose rate (Figure 7-2 and Figure 7-4), it can be understood that high dose rates occurred in the areas where eU concentrations are high. This means that uranium anomalies present in the area (Northern and south-central sectors) may be responsible for higher dose rate values. According to the results of the Shapiro-Wilk test, soil gas radon, eU and ADR_{air} failed to be normally distributed. This can be justified by the presence of local radiometric anomalies (mainly due to the presence of uranium) within the area (Pereira & Neves, 2012) (see also Figure 7-2).

7.3.2 Analysis of the OLS Model

In this study, ordinary least squared regression was used to investigate the mathematical relationship between predictors and the response variable. Equation 7-2 represents the resulting OLS regression formula.

Equation 7-2:

$$SGR = 78.81 - 0.15*(DTM) - 2.87E\text{-}02*(DF) + 12.53*(eU) + 0.53*(ADR_{air}) + 11.31*(eTh) + 18.39*(Log\ P)$$

Where SGR= soil gas radon concentration (kBq m^{-3}), ADR_{air}= air absorbed dose rate (nGy h^{-1}), Log P= permeability of the soil (m^2), eTh = equivalent content of thorium

(ppm), DTM = Digital Terrain Model (m asl.), DF = Distance from the major fault (m), eU = equivalent content of Uranium (ppm).

Table 7-2: Main statistics of the coefficients of the explanatory variables for the OLS model

Source	Coefficient	SE	t	Pr > |t|	VIF
Intercept	78.81	131.03	0.60	0.55	-
DTM	-0.15	0.13	-1.18	0.25	1.44
DF	-0.03	0.03	-1.09	0.28	1.55
eU	12.53	4.77	2.63	**0.01***	4.60
ADR_{air}	0.53	0.79	0.67	0.51	5.01
eTh	11.31	5.46	2.07	**0.05***	1.88
Log P	18.39	6.32	2.91	**0.01***	1.02

*Statistical significant

To avoid using variables that may cause instability in the model, multicollinearity was tested through the Variance Inflation Factor (VIF) statistic before setting the regression model. As shown in Table 7-2, for none of the explanatory variables, the VIF value exceeded the recommended value of 7.5. The result of the regression model analysis (Table 7-2) states that the variables eU, eTh and Log P bring a significant amount of information to explain the variability of the dependent variable (SGR). However, the variables, DTM, DF and ADR_{air} are not consistently significant.

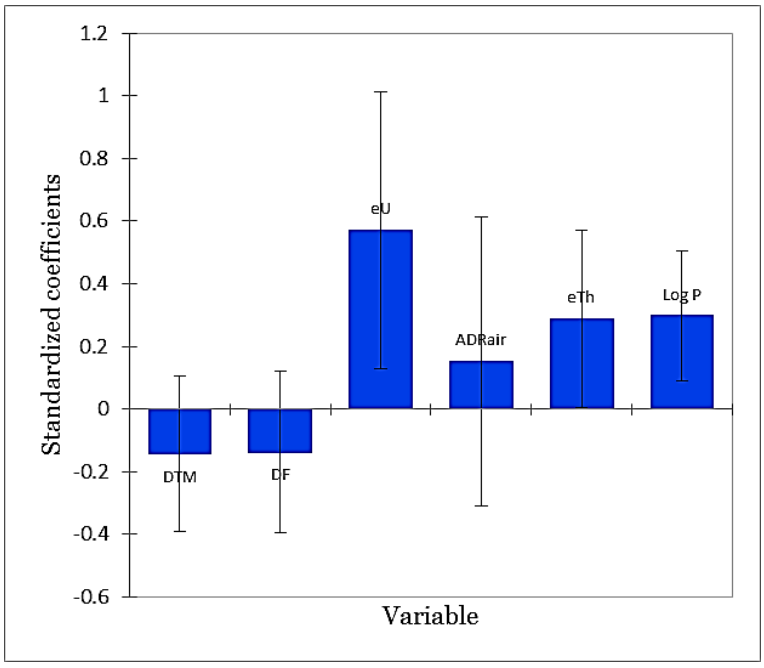

Figure 7-6: The standardized regression coefficients of the explanatory variables (95% confidence interval)

Figure 7-6 shows the chart of standardized regression coefficients of the model. The chart allows us to directly compare the relative influence of the explanatory variables on the

dependent variable and their significance. The higher the absolute value of a coefficient, the more critical the relative influence a variable is. As anticipated, among the significant variables, Log P and eU are found to be the most influential predictors. This can be explained by the fact that these two parameters control the source of radon (as uranium is the parent of radon) and also the mobility of the gas toward the surface.

7.3.3 The Validity of the Model

Table 7-3 summarizes the results of diagnostic tests performed for the proposed OLS regression model. Given the p-value (<0.0001) of the F statistic computed by Fisher's test and given the significance level of 5%, the information brought by the explanatory variables is significantly better than what a basic mean would bring. Given the adjusted R^2, 60% of the variability for the OLS model, it can be concluded that the proposed model explains approximately 60% of the variation in the dependent variable (SGR). The chart in Figure 7-7 visualized the correlation between the measured SGR and predicted values, the regression line (the fitted model R^2= 0.66) and two 95% confidence intervals (i.e. given the assumptions of the linear regression model, residuals should be normally distributed, meaning that 95% of the residuals should be in the interval (-1.96, 1.96)). All values outside this interval are potential outliers. As can be seen in Figure 7-7, no potential outlier value was identified among the measured SGR values. Moreover, the Jarque–Bera statistics value is not significant which indicates that the residuals follow a normal distribution.

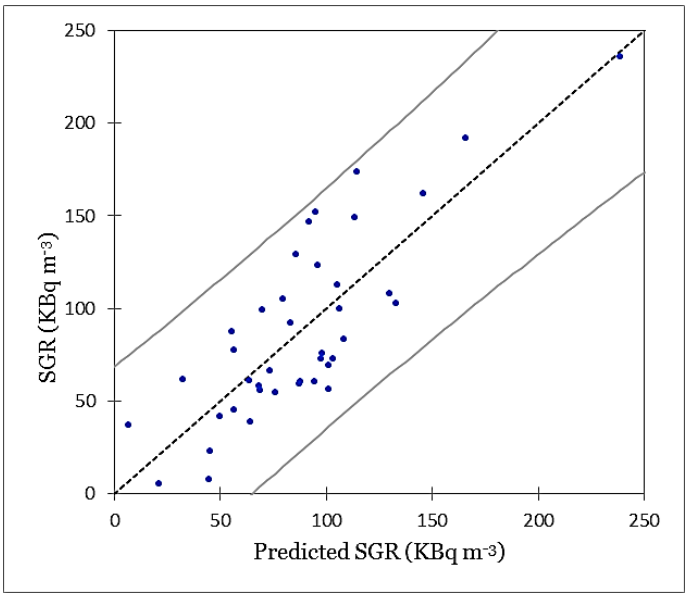

Figure 7-7: Predicted SGR values versus the measured ones (95% confidence intervals).

The Durbin-Watson test is a measure of autocorrelation (also called serial correlation) in residuals from regression analysis; the null hypothesis is no spatial correlation. As the computed p-value for this test is greater than the significance level alpha=0.05, one cannot reject the null hypothesis. Furthermore, the Breusch-Pagan and White tests are used to test heteroscedasticity. As the calculated p-values of these two tests are greater than the significance level alpha=0.05, it can be concluded that residuals are homoscedastic. The abovementioned diagnostic test results demonstrate that the basic assumptions underlying the OLS regression analysis have not been violated.

Table 7-3: The results of diagnostic tests

Parameter	value	p-value
Observations	40	
R^2	0.66	
Adjusted R^2	0.60	
AICs	282.63	
Fisher's F test	10.72 (DoF=6)	<0.0001
Durbin-Watson test (DW)	2.31	0.50
Breusch-Pagan test (LM)	5.95	0.43
White test (LM)	26.97	0.47
Jarque-Bera test	3.06	0.22

7.3.4 Geogenic Radon Potential Mapping

In the previous sections, the relationship between radon-related variables and the soil gas radon concentration was obtained. The geogenic radon potential, i.e., the quantity of radon directly related to the local geology, is defined as the soil gas radon values predicted based on the regression equation, which calculates SGR solely based on predictor variables. To produce the map of the spatial distribution of GRP for the study area, the empirical Bayesian kriging (EBK), an automatic geostatistical interpolator, was used in ArcGIS version 10.5 software. This tool creates prediction surfaces based on restricted maximum likelihood estimation. Additionally, it allows us for uncertainty analysis in the semi-variogram model by the process of data subsetting and simulation to estimate a range of semi-variogram models (Krivoruchko, 2012). In this study, the EBK was employed for three purposes a) for cross-validation of the results, b) to create a GRP prediction surface and c) to estimate the error of predicted values. Table 7-4 shows the results of cross-validation of the predicted values (i.e., the geogenic radon potential) and measured SGR activities. According to this table, the mean prediction error (ME = 1.98) and the mean standardized error (MSE=0.035) are close to zero, indicating that the

interpolation method is unbiased (centered on the true values) and the model is accurate; the average standard error (SE=50.68) is higher than the root mean squared prediction error (RMSE = 48.38), suggesting that the interpolation method slightly overestimates the variability in the predictions (Giustini et al., 2019).

Table 7-4: Results of executing Cross-validation using Empirical Bayesian Kriging

Parameter	value
Count	40
Mean Error	1.98
Root Mean Square Error	48.38
Average Standard Error	50.69
Mean Standardized Error	0.035
Root Mean Square Standardized Error	0.96

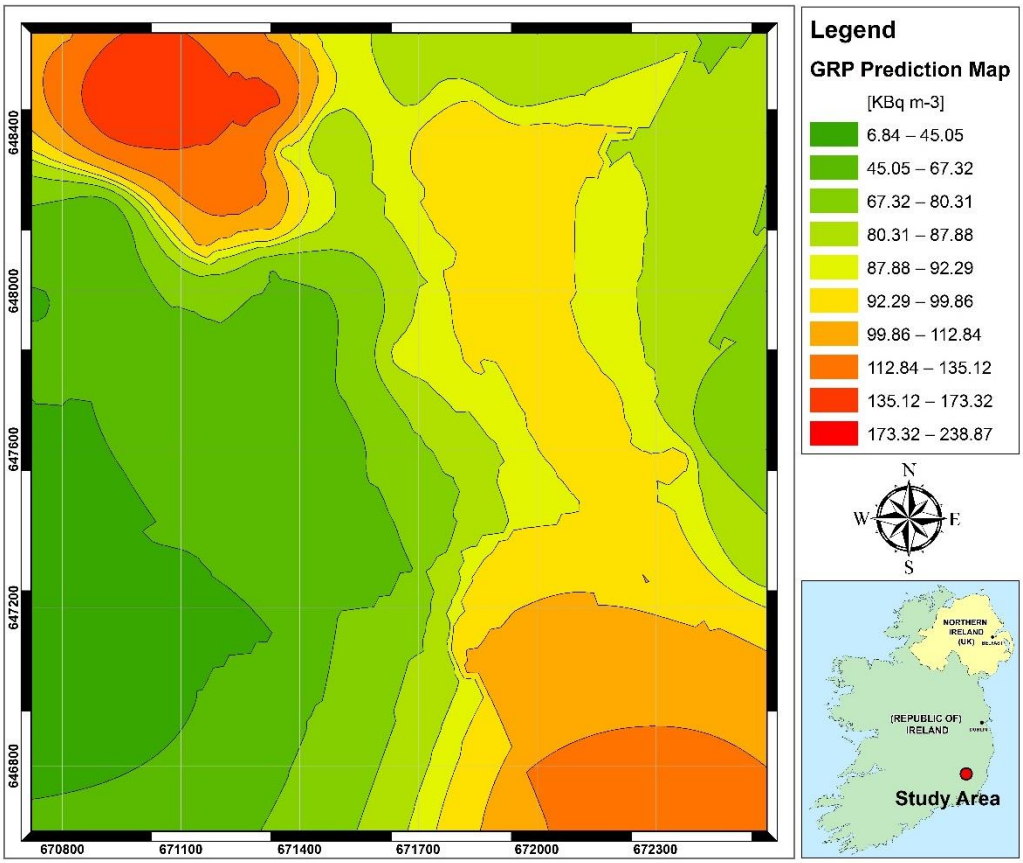

Figure 7-8: Predicted Geogenic Radon (GRP) concentrations.

GRP surface predicted based on the soil gas radon concentrations is shown in Figure 7-8, along with its corresponding prediction standard error surface, which illustrates the amount of uncertainty associated with the predicted SGR value. As shown in Figure 7-8 high GRP values (>85 kBq m^{-3}) can be found in the Eastern and North-western sectors of the study area. Just for the Southwestern part, the GRP is in the low range (50 kBq m^{-3})

and the remaining parts are characterized as medium GRP levels (50 to 85 kBq m^{-3}). The uncertainty of GRP prediction shown in Figure 7-9 is generally in the low to medium range (less than 35 kBq m^{-3}); however, for areas along the borders of the study area, rather high values (up to 52 kBq m^{-3}) can be predicted. A possible source of error in those areas would be an insufficient number of SGR test points that occurred due to sampling limitations (i.e., presence of saturated soil and improper site access).

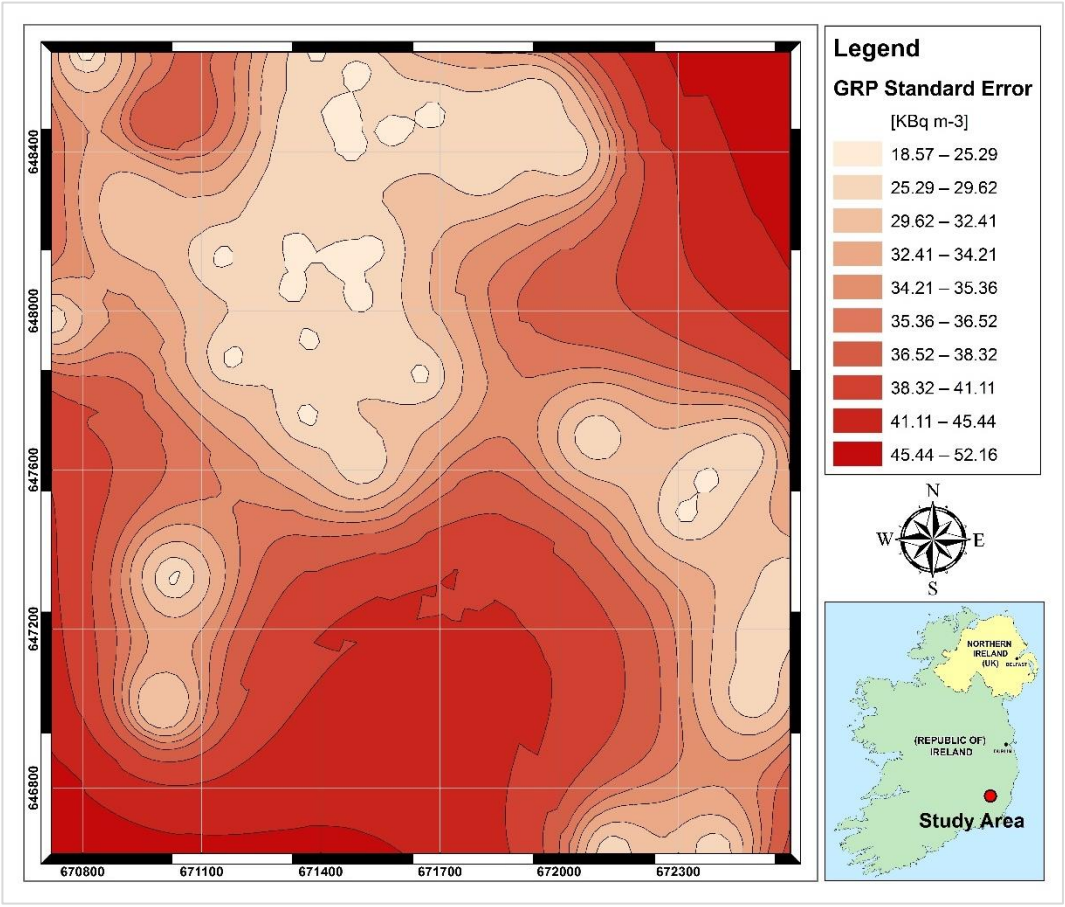

Figure 7-9: Map of GRP prediction error.

7.4 Discussion

A set of radiometric data, geogenic parameters, together with soil gas radon and permeability measurements, were used to model the geogenic radon potential of a granitic area. The proposed model was successful in explaining 60 percent of the variations in the soil gas radon. It is suggested that considering other radon affecting factors in the OLS model would help to increase the goodness of the prediction. The other radon affecting factors mainly include; soil type, grain size, water content, porosity and permeability (Manohar et al., 2013). In this chapter, due to the lack of information about additional parameters (at least on a local scale), we were not able to consider their effects.

Rainfall and precipitation are among the important events which can change near-surface environmental gamma rates by affecting radon progeny ^{214}Pb and ^{214}Bi (Melintescu et al., 2018). Furthermore, water accumulation on the surface of the soil may act as a shield and can prevent radon emission. The accumulation of radon in a stable boundary layer can also have a considerable influence on gamma levels (Mercier et al., 2009). Moreover, hydrological movement at sites with high radon fluxes may represent a source of false alarms about radioactivity levels (Voltaggio, 2011). As mentioned previously, the equivalent uranium concentrations measured in the frame of the Tellus project are estimated from the ^{214}Bi photoelectric peak. Knowing the fact that rainfall events, precipitation, or other meteorological parameters can profoundly affect the detection results of airborne gamma-ray spectrometry and also considering that Ireland is a country in which rainfall and precipitation are frequent. Soils can be saturated during wet seasons; thus, it would be necessary to perform radon background correction for airborne gamma-ray spectrometry results to improve the accuracy of measurement and avoid false alarms (Zeng et al., 2019).

An outlook of Chapter 8

The next chapter expresses the application of natural radioactivity as a quick way for geological assessments. Integrated investigations of radioelements mapping together with radon exhalation rate measurements will be employed to characterize and identify members of a formation having a geological interest (placer deposits of the Punta Serpeddì Formation) and also to constrain possible radiation hazard due to natural radiation induced by radioactive elements contained in heavy minerals accumulated in shallow-marine placer deposits near Dolianova town as well as other areas with similar geological conditions in Sardinia.

8 RADIOLOGICAL ASSESSMENT OF THE HEAVY-MINERAL PLACERS DEPOSITS OF THE PUNTA SERPEDDÌ FORMATION

In this chapter, the presence of heavy minerals, including radionuclides such as ^{238}U and ^{232}Th, in the various outcrops of sedimentary shallow-marine placer deposits of the Punta Serpeddì Formation (Upper Ordovician of SE Sardinia, Italy) has been investigated. To single out the contribution from natural sources to the radon exhalation and total radiation level, a set of laboratory and in-situ experiments were considered. The surface exhalation rate of radon gas was determined with passive discriminative nuclear track detectors (CR-39) in the air column of the depth of 30 to 50 cm in the soil. The soil gas radon concentration of air in soil pores at the depth of 50 cm was also measured in-situ by using an MR1 radon monitor. The concentrations of terrestrial radionuclides (U, Th and K) of soils and the adjoining rocks were measured at the site by using GT-40S – multipurpose gamma-ray analyzer. Soil samples were also taken from measuring points. The porosity of soil was estimated from the samples collected with a brass cylinder. The collected soil samples were introduced to follow up laboratory measurements by GT-40 gamma-ray spectrometer to monitor the activity concentration of radioisotopes. The integration of radionuclide mapping and radon exhalation measurements was found to be a very useful tool to characterize radiological properties of the Punta Serpeddì formation and also to assess people's exposure level to natural radiation, in terms of dose rates and potential indoor radon, especially when the studied materials are used as building and construction materials.

8.1 Introduction

Heavy metal placer deposits tend to have higher concentrations of naturally occurring radionuclides of the uranium and thorium families in the crystal structure of their resistant minerals (i.e. titaniferous minerals, tourmaline) and some other radioactive species (i.e. zircon, monazite)(Pistis et al., 2018). The accumulation of heavy minerals in these deposits occurred as a result of gravity separation during aerodynamic or hydrodynamic processes in marine environments (Hughes et al., 2000). Subsequently, the superposition of mineral contents due to the several sea-level cycles of different frequencies leads to significant enrichment of minerals containing the naturally occurring radionuclides (i.e. ^{232}Th, ^{238}U and ^{40}K). The origin and distribution of naturally occurring radionuclides depend on the distribution of the rocks from which they originate and on the geological processes which concentrate them (Sabatino et al., 2019). Those materials derive from weathering processes of the continental rocks, mostly of volcanic, plutonic, metamorphic and sedimentary origin and thus have a broad compositional range. Their concentration depends on hydrodynamic conditions like sediment influx from the hinterland, wave energy and its velocity, longshore current and wind speed, which control the littoral transport, sorting and deposition of placer minerals in suitable locales (Sabatino et al., 2019).

This chapter is focused on the activity determination of ^{238}U and ^{232}Th decay chains radioisotopes and primordial ^{40}K as well as soil gas radon activity and exhalation rate monitoring in the storm-dominated placer deposits of the Punta Serpeddì Formation in the Variscan basement of Sardinia. The results of this work, have value not only from the geological point of view but also they can be used to direct future investigations concerning radioactivity background levels to gain a better evaluation of possible health effects on the population living in Dolianova, SE Sardinia and also in other regions with similar geological conditions.

8.2 Geological Description of Study Area

The study area (with an area of 1.8 km^2) is located near Dolianova, a town in the territory of Parteolla, in the south-east of Sardinia. The geology of the study area consists of fine to coarse-grained lithic wackes containing intercalations of conglomerates, microconglomerates and siltstones belonging to the Punta Serpeddı` Formation (Upper

Ordovician with a 60 to 140 m thickness) (Pistis et al., 2016, 2018). This formation rests on the ‘‘Porfidi Grigi’’ volcanic rocks and is overlain by the Tuviois formation (Pavanetto et al., 2012) (Figure 8-1).

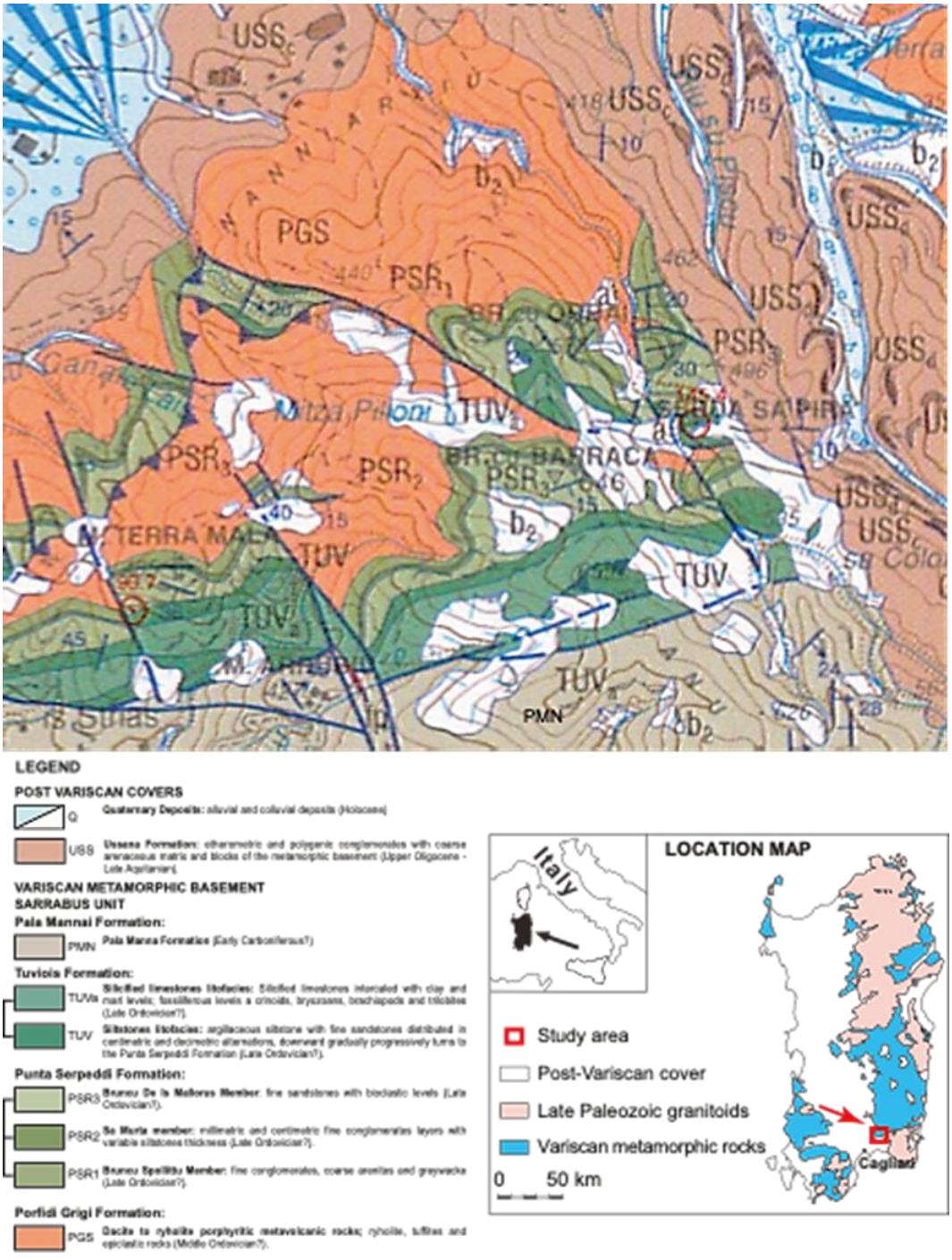

Figure 8-1: The geological map of the study area (Barca et al., 2005)

As shown in Figure 8-1, the Punta Serpeddı` Formation can be subdivided into three main members: a) Bruncu Spollittu; represented by coarse- to very coarse-grained sandstones,

b) Sa Murta; consist of siltstones and coarse-grained to conglomeratic sandstones and c) Bruncu de Is Mallorus. Based on the investigations by Pistis et al., 2016, 2018 regarding the sedimentological (facies, sequence stratigraphy) on the three mentioned members and petrographic analyses combined with outcrop gamma-ray logging, it was found that the placers are mainly abundant in the Sa Murta and Bruncu de Is Mallorus members and are scattered in the Bruncu Spollittu member. The main source-areas of the heavy minerals supply are the underlying "Porfidi Grigi" volcanic rocks. (Pistis et al., 2018)

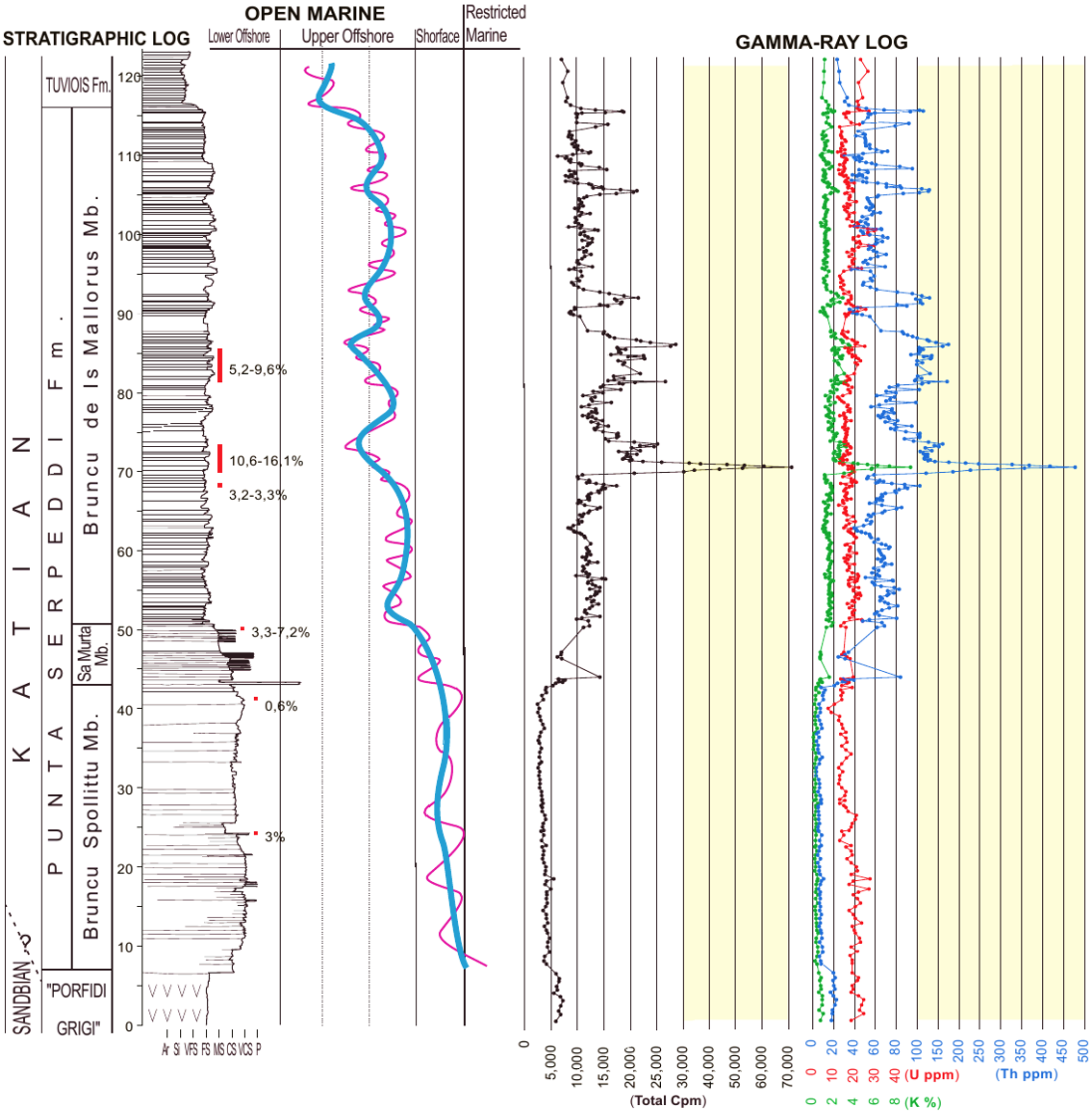

Figure 8-2: Heavy mineral contents of samples from different sections (vertical red line) studied in the Sarrabus area; gamma-ray spectral logs: total counts (cpm), K (%), U and Th (ppm). Taken from (Pistis et al., 2018)

8.3 Materials and Methods

The naturally occurring radionuclides (^{232}Th, ^{238}U and ^{40}K), as well as radon and its progenies, can be employed as tracers of the mineralogical properties of placer deposits and geological processes indicators of transport and sorting (Anjos et al., 2006; Baskaran, 2016). In this study, a multidisciplinary approach - including the use of several laboratory and in-situ testing instruments, was considered for the mineralogical and geochemical characterization of the heavy-mineral placers deposits.

8.3.1 In-situ Tests

8.3.1.1 Detection of Activity Concentrations of Radionuclides and Attributed Dose Rates of Rocks and Soils

To distinguish between the radiological properties of different formations located in the Study area, a total of 12 test points were selected (please see Figure 8-3 and Table 8-1); five from Bruncu de Is Mallorus (PSR3) member, three from Bruncu Spollittu (PSR1) member of both belonging to Punta Serpeddì Formation, three from Ussana formation (USS) and one from Tuviois formation (TUV).

Figure 8-3: Satellite map of the study area overlapped by the topographic contours showing the location of test points/soil gas radon measuring sites

Table 8-1: The location of test points and the attributed geological formation.

Geological Formation	Code	Latitude	Longitude	Altitude
Punta serpeddì -Bruncu de Is Mallorus	IM-1	39.36439	9.229973	435.8m
	IM-2	39.36422	9.229851	442.3m
	IM-3	39.3642	9.229763	445.0m
	IM-7	39.36414	9.230128	458.7m
	IM-8	39.36342	9.231139	452.8m
Punta serpeddì -Bruncu Spollittu	BS-4	39.36457	9.2295	434.5m
	BS-5	39.36481	9.229063	444.6m
	BS-6	39.36541	9.229919	423.3m
Tuviois	TV-9	39.36259	9.231054	494.3m
Ussana	US-10	39.36366	9.23217	479.3m
	US-11	39.3649	9.231433	466.7m
	US-12	39.36608	9.230456	453.5m

At each point location, a hole with 30-50 cm depth and 20-30 cm diameter was dug and at bottom of the hole, the activity concentration K, U and Th together with attributed dose rate were measured for 300s by using GT-40S gamma-ray analyzer (Figure 8-4 and Figure 8-5). Then, using the same instrument, the natural radionuclide concentrations at the surface of the nearby embedded rocks were determined.

Figure 8-4: natural activity detection at the test point location (left) and the rocks belonging to the Punta Serpeddì Formation (right).

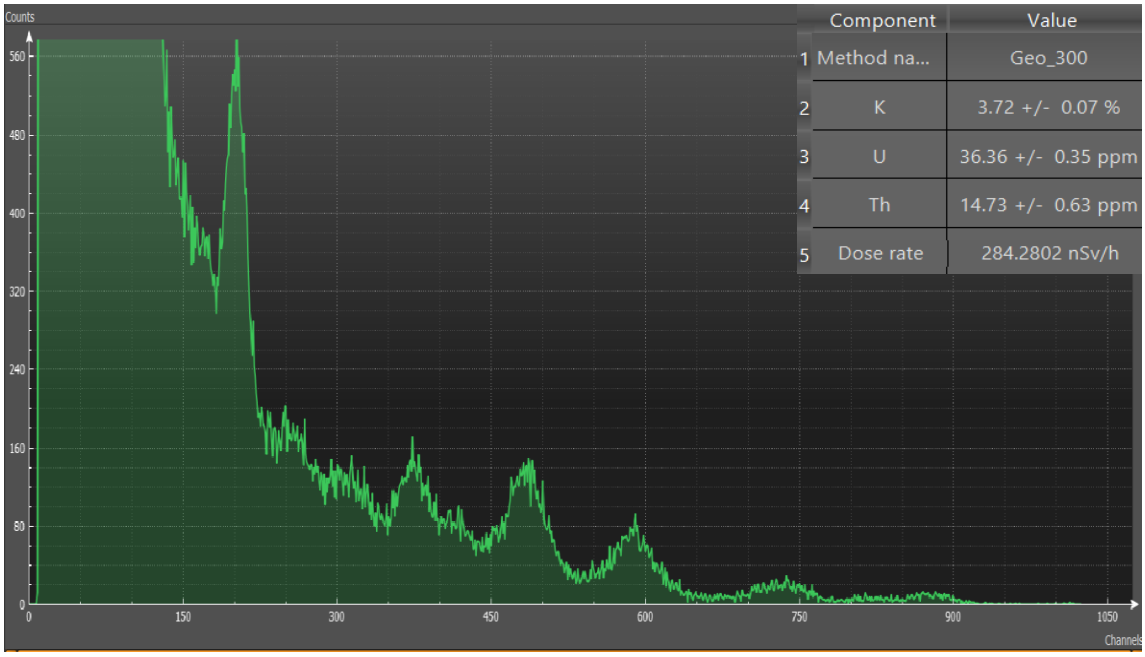

Figure 8-5: An example of a spectrum and the calculated activity of radioactive components by using GT40S-Geoview software.

8.3.1.2 Radon Exhalation Rate Measurement

After measurement of the activity concentration of the terrestrial radionuclide at the bottom of the excavated holes, plastic cans with the volume of two litters were located inside the pitch while an alpha-sensitive solid-state nuclear track detector (CR-39) was fixed on the inner upper surface of the can (Figure 8-6). Then the pitch was fully covered by the soil that was excavated during the digging. The sensitive lower surface of the detector is thus freely exposed to the emergent radon exposed from the soil surface and accumulated in the can so that it was capable of recording the alpha particles resulting from the decay of radon in the Can. After the exposure for 30 days, the detectors from all the Cans were retrieved and were etched in 2.5N NaOH at 80 ^{o}C for a period of 70 min in a constant temperature water bath for the revelation of tracks (Mahur et al., 2015). After the chemical treatment, the visual counting of alpha particle tracks was carried out utilizing an optical microscope (Al-Nuzal et al., 2019). Finally, the mean activity of radon during the exposure time was calculated using the number of alpha tracks identified on each detector.

The radon exhalation rate from the soil, E_{Rn} is Bq m^{-2} h^{-1}; can be determined by the following formula (Abu-Jarad, 1988; Vasidov, 2014):

Equation 8-1: $E_{Rn} = A_m \lambda K(t)(V / S)$

where A_{mn} is the mean radon activity (Bq m^{-3}); k is the decay constant (h^{-1}); V is the volume of the chamber or can (m^3); S is the surface area (m^2); K (t) is the effective time and is calculated by:

Equation 8-2: $$K(t) = t \Big/ \left[t + (e^{-\lambda t} - 1) / \lambda \right]$$

Where t is the exposition time (h).

Figure 8-6: Installation of the passive radon detector can

Besides testing the surface radon exhalation rates, we collected samples using a brass cylinder for determination index properties of soil, in particular specific gravity of soil solids, dry unit weight and water content. From these data, the porosity of the soil was calculated. Then samples were immediately put in plastic bags and sealed. Then weighed and oven-dried for 24 hours with a temperature of 105 ^{o}C. By using the mass difference between dry and wet samples the porosity was calculated.

8.3.1.3 Soil Gas Radon Monitoring

The soil gas radon concentration was measured at four test point locations using an MR-1 (the active method) connected with the Soil kit accessory (Figure 8-7). Although the recommended depth of the soil gas radon testing is 80 cm, because of the presence of gravelly soil, the measurement was carried out at levels of 50 cm below the ground level. For this purpose, an auger instrument was employed to dig the hole. Then the top of the

hole was covered and the radon activities were measured for 20 minutes at two-minute intervals (Figure 8-8). For each test point, the average recorded value was reported.

8.3.2 Laboratory Experiments

8.3.2.1 Gamma-ray Spectrometry

Gamma-ray measurements were taken in the laboratory of the Department of geology and chemical science of The University of Cagliari. A GT-40S gamma-ray analyzer incorporated into a Pb shielding collimator was employed for radionuclide detections (Figure 8-9). The instrument was calibrated through 300 grams of the reference material placed inside plastic containers. The samples to be measured were prepared in the same containers. A counting time of 900 seconds was considered to obtain most the accurate gamma-ray spectra of the samples. The monitoring and analysis results were displayed in a color graphic manner and the activities/content of gamma emitters were automatically determined based on the obtained spectra. Then the radionuclide activity concentrations were being subjected to the weight correction.

Figure 8-7: Active soil gas radon measurement with an MR-1 instrument

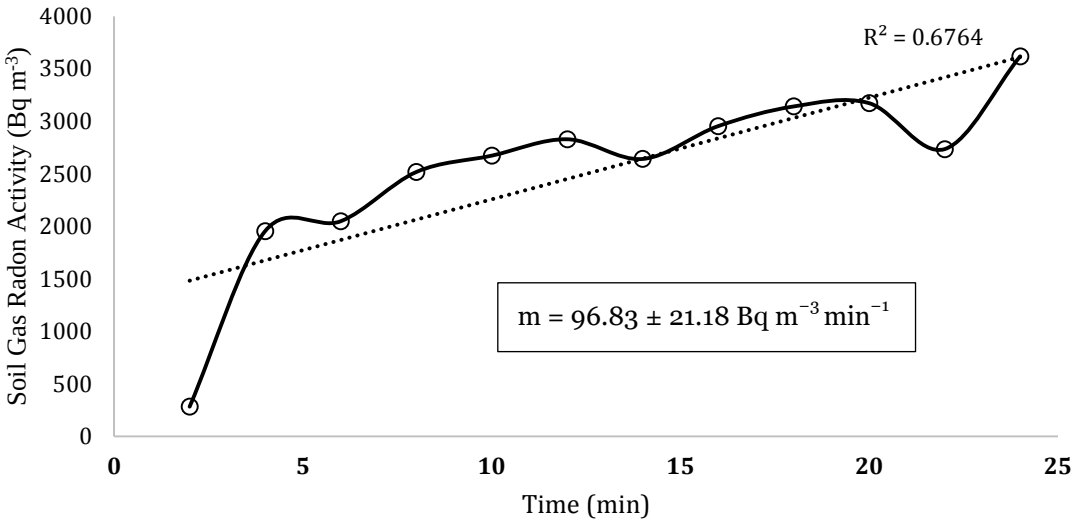

Figure 8-8: Radon activity growth during the soil gas radon testing and the calculated slope of the concentration increase- Test point IM-1.

Figure 8-9: The GT-40S gamma-ray spectrometer incorporated into the Pb shielding collimator and a sample prepared for testing.

8.4 Results and Discussion

The results of radionuclide content measurements at the bottom of the pitch (code: in-situ), on the surface of nearby rocks (code: Rock) and in the collected soil samples (code: Lab) are stated in Table 8-2 to

Table 8-4. As shown in these tables the activity of K ranges between 2.77 and 5.74 (%). U activities range between 0.48 and 15.31ppm. The minimum and maximum Th concentrations are 6.53 and 216.35 ppm, respectively. The values obtained here are in

agreement with the results of the previous surveys carried out by Meloni et al., 2020 using the RS-230 gamma-ray instrument. The correlation between radionuclide concentrations (K, U and Th) measured in-situ (both at the bottom of the pitch and nearby rocks) and in the laboratory are evaluated in Figure 8-10 and Figure 8-11. As can be seen, the values measured in-situ are well correlated (R^2= 0.93 for Th values and R^2=0.52 for U contents). This is can be explained by the fact that similar radiochemical properties were anticipated for the soils that originated from the same rock formation because the soils develop as a result of the weathering of materials on the earth's surface, including the mechanical breakup of rocks and the chemical weathering of minerals. The results of in-situ radioelements determination are correlated with the values observed in the laboratory. In other words, the concentration of U and Th measured at the bottom of the pitch and in the collected soil samples show a good correlation (R^2= 0.92 for Th values and R^2=0.85 for U contents).

Table 8-2: Results of radioactivity detections at the bottom of the pitch

Code	D-rate	K± error		U± error		Th± error	
	nSv h-1	%		ppm		ppm	
IM-1	326.28	3.05	0.12	8.83	0.64	85.26	1.53
IM-2	302.15	3.22	0.11	8.16	0.56	73.96	1.33
IM-3	356.96	3.70	0.12	8.73	0.61	93.21	1.47
BS-4	93.27	3.10	0.05	1.74	0.22	11.37	0.49
BS-5	110.56	4.21	0.06	1.47	0.25	13.26	0.55
BS-6	139.14	3.84	0.07	2.65	0.31	23.06	0.70
IM-7	501.06	3.29	0.15	10.14	0.81	149.30	2.01
IM-8	155.37	3.33	0.09	3.51	0.38	30.28	0.89
TV-9	132.35	5.08	0.07	2.50	0.27	14.20	0.59
US-10	123.27	3.16	0.06	2.58	0.28	19.82	0.63
US-11	125.40	3.01	0.06	2.53	0.28	22.18	0.63
US-12	138.20	4.68	0.07	2.67	0.30	19.00	0.68

Table 8-3: Results of radioactivity detections on the surface of nearby rocks

Code	D-rate	K± error		U± error		Th± error	
	nSv h^{-1}	%		ppm		ppm	
IM-1	275.04	3.65	0.10	6.86	0.47	69.00	1.12
IM-2							
IM-3	491.08	3.75	0.16	11.25	0.82	146.24	2.01
BS-4	105.92	4.87	0.06	0.48	0.24	9.07	0.55
BS-5	95.27	4.30	0.06	1.57	0.25	6.53	0.54
BS-6	144.95	5.09	0.07	3.26	0.30	17.78	0.65
IM-7	680.62	3.60	0.21	15.31	1.12	216.35	2.79
IM-8	246.37	2.77	0.10	5.67	0.49	63.13	1.19
TV-9	124.71	4.11	0.07	2.51	0.28	16.19	0.63
US-10							
US-11							
US-12							

Table 8-4: Results of radioactivity detections in the collected soil samples

Code	D-rate	K± error		U± error		Th± error	
	nSv h^{-1}	%		ppm		ppm	
IM-1	10.91	3.97	0.57	13.22	2.94	50.78	5.04
IM-2	11.68	4.30	0.60	9.92	3.09	46.29	5.29
IM-3	10.26	4.68	0.51	8.00	2.67	50.90	4.72
BS-4	7.77	4.52	0.40	4.37	2.11	29.80	3.56
BS-5	8.14	4.34	0.40	7.03	2.08	32.74	3.51
BS-6	7.51	4.36	0.38	7.65	2.02	30.47	3.32
IM-7	9.44	3.81	0.46	10.51	2.44	64.74	4.27
IM-8	7.47	3.72	0.38	8.35	2.05	26.65	3.37
TV-9	7.53	5.74	0.42	5.65	2.17	29.26	3.62
US-10	6.46	3.86	0.34	5.95	1.77	23.43	3.04
US-11	7.88	4.67	0.41	9.69	2.12	33.78	3.64
US-12	7.25	5.24	0.36	3.90	1.81	28.44	3.21

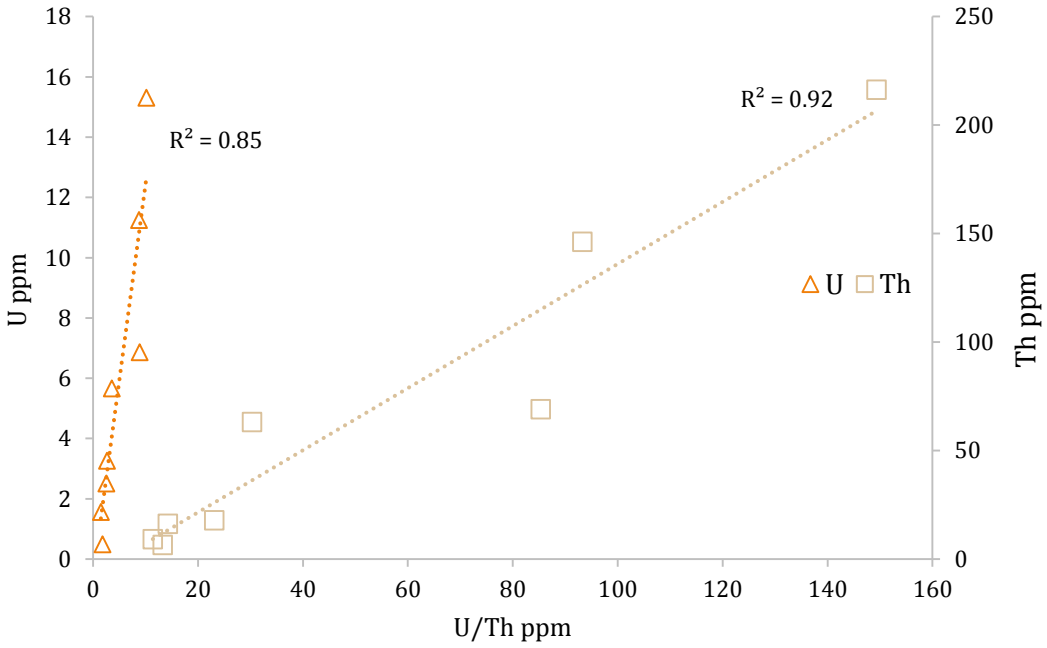

Figure 8-10: The correlation between U and Th contents measured in the collected soil samples and detected in-situ at the bottom of the pitch.

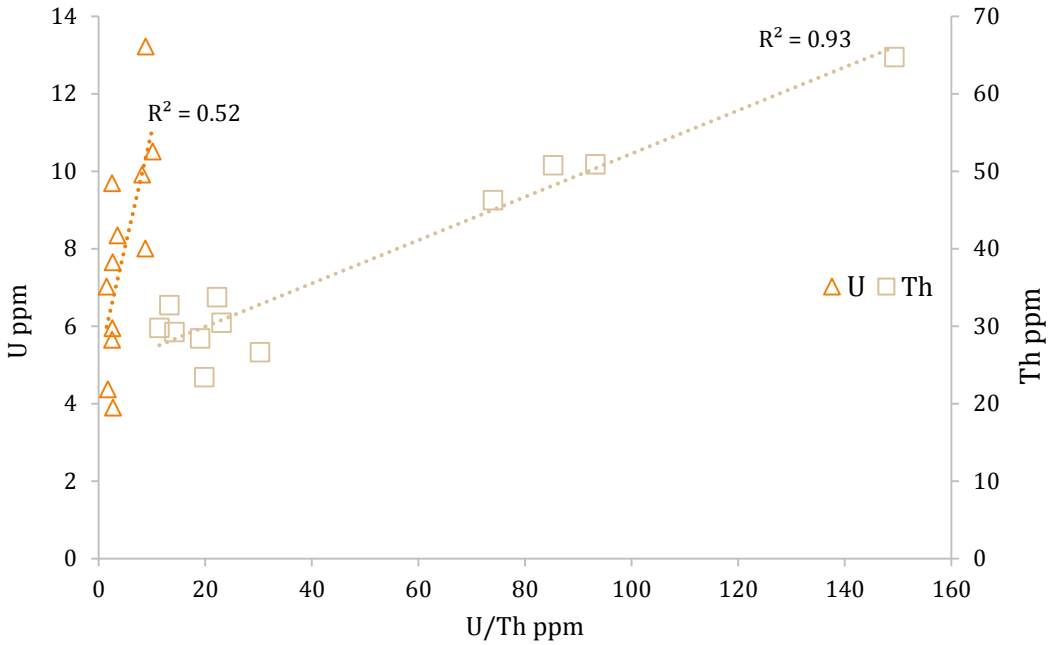

Figure 8-11: The correlation between U and Th contents measured on the surface of nearby rocks and detected in-situ at the bottom of the pitch.

Table 8-5 shows the results of soil gas radon (SGR) testing and measurement of radon exhalation rate (E_{Rn}) from the soil surface. The porosity of the soils in different test points is reported as well. According to this table, the SGR activities range between 704.50 and 2547 Bq m^{-3}. Considering the measured uranium values, the obtained SGR activities are lower than anticipated levels (see Wattananikorn et al., 2008). Theoretically, the soil gas radon is related to ground uranium concentration by the following equation (Soonawala & Telford, 1980):

Equation 8-3: $$SGR = 370adu/n$$

where SGR is the soil radon concentration in pci/litter, u is the ground uranium content in ppm, a is the emanation coefficient, d is the density in g/cc and n is the porosity. As the porosity and density of the soil samples are calculated, based on Equation 8-3 it would be possible to estimate the radon emanation coefficients. As shown in Table 8-5 the calculated emanation coefficients are very low (0.02-0.03). The emanation coefficient of radon depends on several mineralogical aspects such as lattice structure, porosity, grain shape and elemental composition (Ishimori et al., 2013). In our case, it seems that as the uranium-bearing minerals of the soils are present in the crystal form, only a small fraction of radon, generally those are close to the surface of soil grains can escape from the lattice

structure. Because considering the mean uranium concentration of the soil (7.8 ppm), a higher mean soil gas radon (SGR) concentration rather than 1.5 KBq m^{-3} was anticipated. There is also a correlation between the SGR concentrations and the measured value of uranium at the bottom of the pitch. (See Figure 8-12)

Table 8-5: Results of Soil gas radon testing and soil gas radon exhalation rate measurements

Code	Emanation coefficient	Porosity	Active Soil Gas Radon Measurements (Bq m^{-3})				Soil Gas Exhalation Rate			
			Min	Max	Mean	±SD	A_m± SD (Bq m^{-3})		E_{Rn}± SD (Bq m^{-2} h^{-1})	
IM01	0.02	0.24	281.9	3618.6	2546.89	849.09	870	251	55.38	15.98
IM02	0.03	0.18	1219.4	1594.4	1461.63	110.59	2149	474	136.79	30.17
IM03		0.25					1215	199	77.34	12.63
BS04		0.10					920	194	58.56	12.35
BS05		0.08					739	197	47.04	12.54
BS06		0.28					1936	312	123.23	19.86
IM07	0.03	0.18	1297.5	2000.6	1580.31	200.97	1362	187	86.69	11.9
IM08		0.52					1460	302	92.93	19.22
TV09	0.02	0.53	429.9	1078.7	704.5	174.85	6299	925	400.94	58.88
US10		0.49					6221	628	395.98	39.94
US11							5116	391	325.64	24.89
US12		0.52					4482	435	285.29	27.69

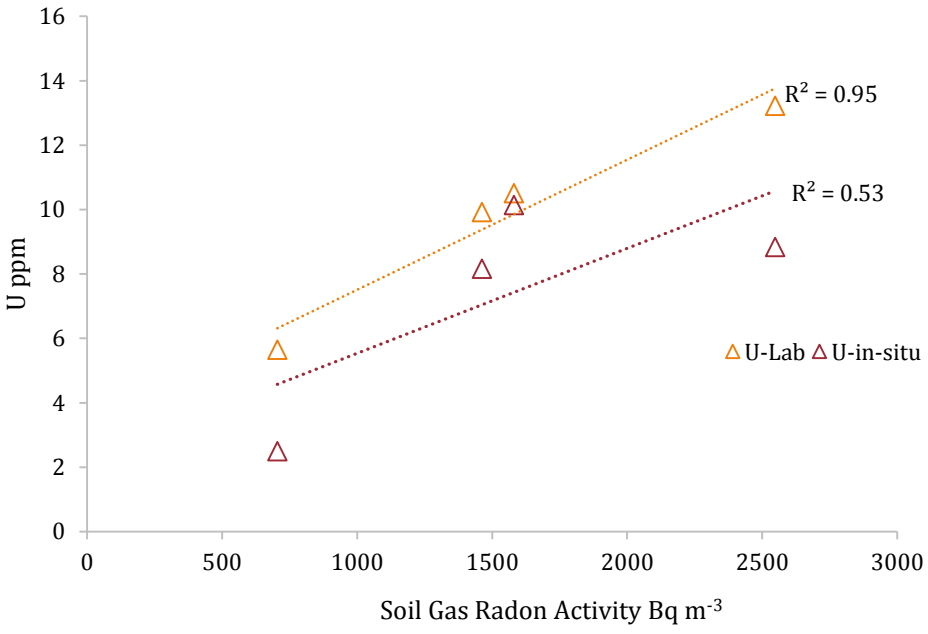

Figure 8-12: Correlation between uranium contents (measured in collected soil samples and in-situ at the bottom of the pitch) and the Soil Gas Radon activity

The mean activity concentration of radon exhaled from the soil surface and the calculated radon exhalation rate (E_{Rn}) are reported in Table 8-5. According to this table, the minimum, mean and maximum radon exhalation rate due to the exposure of the plastic detectors during a 34 days interval are 47.07, 173.81 and 400.94 Bq m^{-2} h^{-1}. Comparing these values with average E_{Rn} of soils from countries with relatively high radon exhalation rates (e.g. Czech, Mean E_{Rn} = 750 Bq m^{-2} h^{-1})(Barnet, 2008), it can be understood that the radon exhalation rates of the tested soils represent lower radon release potential.

The correlation between uranium contents and the measured E_{Rn} is evaluated in Figure 8-13. According to that although there was a good correlation between U levels and the emanated soil gas radon (Figure 8-12), there is no correlation between the uranium contents and the radon exhalation rates. This is because the radon flux and exhalation can be controlled not only by U contents but also by radon diffusion and advection processes. According to Figure 8-14, in the case of this study, the radon exhalation rate of soils significantly depends on the porosity.

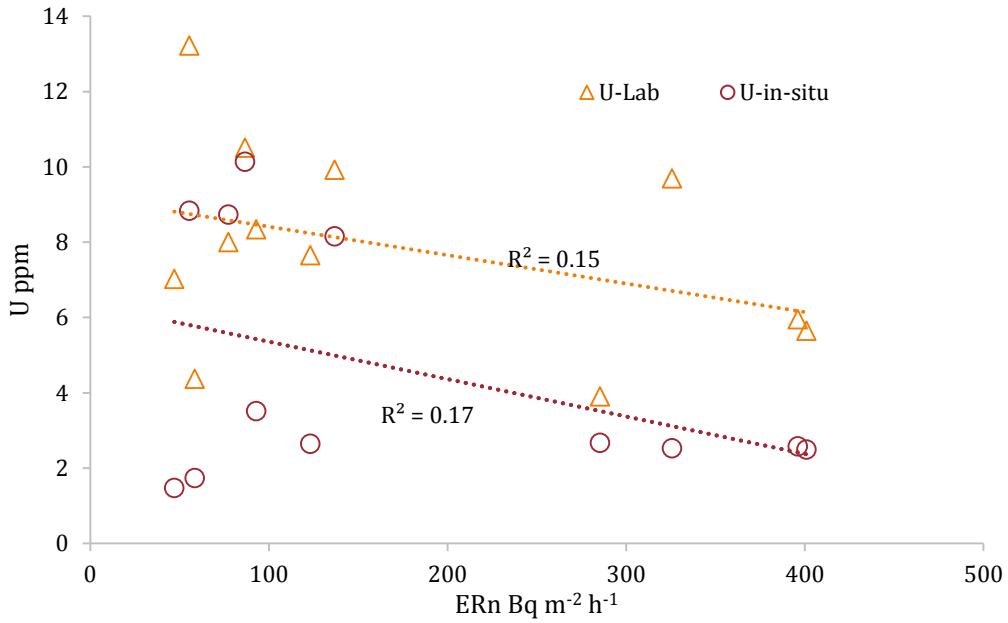

Figure 8-13: Correlation between uranium contents (measured in collected soil samples and in-situ at the bottom of the pitch) and the measured exhalation rates

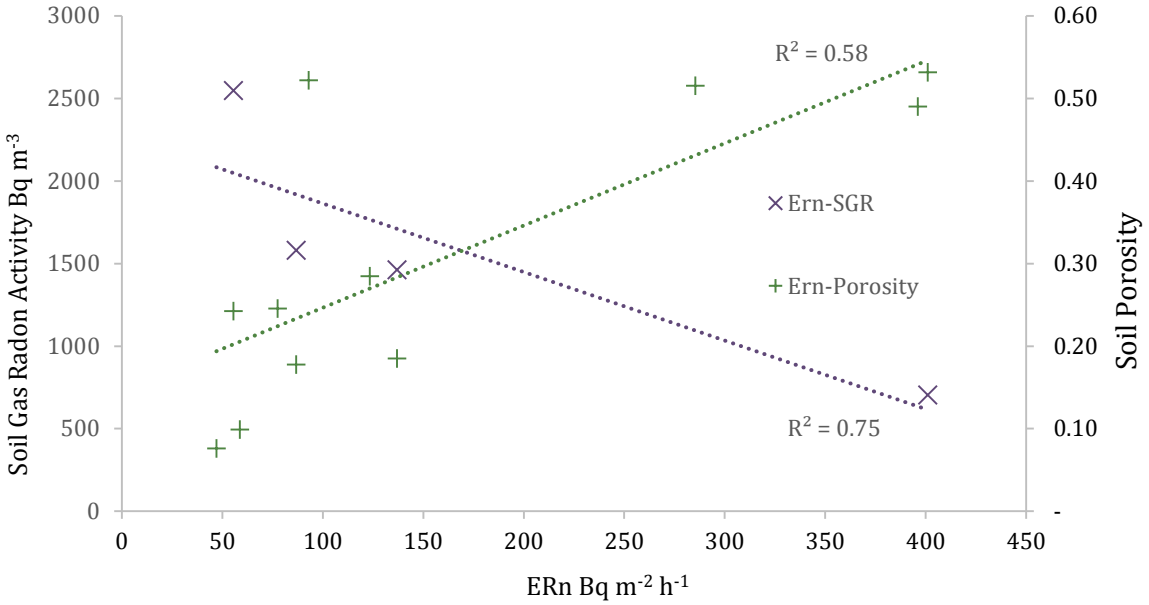

Figure 8-14: Correlation between radon exhalation rate with emanated soil gas radon and porosity of the soil.

In the chart of Figure 8-15, the mean value of the radiogenic parameters (K, Th, U, SGR and E_{Rn}) are calculated for the different geological formations of the study area. According to this chart the highest U, Th and emanated soil gas radon mean values are observed in Punta Serpeddì-Is Mallorus. The second highest values can be attributed to the other member of the Punta Serpeddì formation (i.e. Spollittu). This is because these two members of the Punta Serpeddì formation are the hosts of uranium and thorium bearing minerals. The amounts of K were slightly lower in Is Mallorus, however, it was not possible to distinguish between the K varieties of the studied formations. The results obtained here are in agreement with previous studies carried out in the study area (Pistis et al., 2016, 2018).

The highest U values were observed in the two members of the Punta Serpeddì formation (Is Mallorus and Spollittu). However, the radon exhalation rate of Tuviois and Ussana formations were found to be higher than those two members. This is might be because of the presence of factors that facilitates the mobility of radon from the source to the soil surface (e.g. higher porosity) in Tuviois and Ussana formations.

According to the Neznal criterion (see also section 6.2.9) (Neznal et al., 2004), the low soil gas radon levels (maximum 4 KBq m^{-3}) measured in-situ represent low to medium (for higher permeability rates of soil) risk geogenic radon potential. It is noteworthy that the studied rock materials might have a commercial interest to be used as building and

construction materials. In the case of being used for these purposes, they can be considered as a secondary source of radon and especially thoron exposure as the thorium values observed here are relatively high.

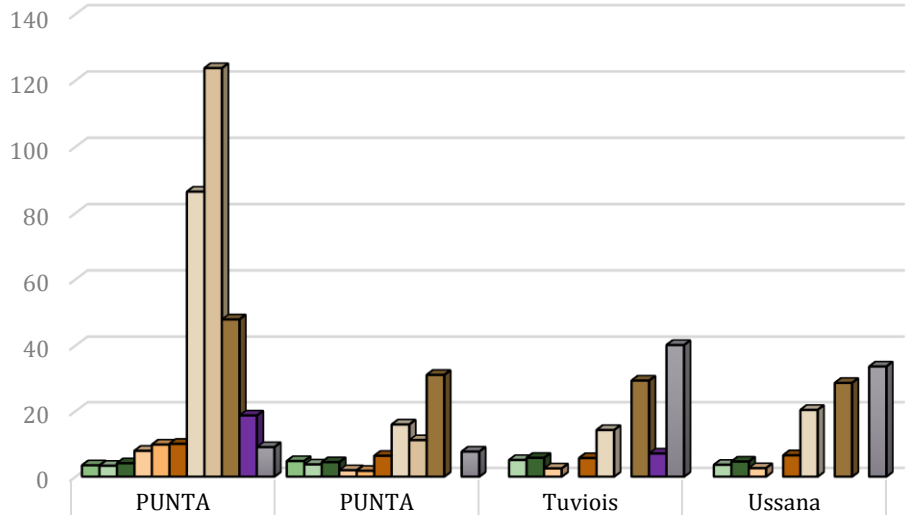

	PUNTA SERPEDDÌ - Bruncu de Is Mallorus	PUNTA SERPEDDÌ - Bruncu Spollittu	Tuviois	Ussana
K-Rocks (%)	3.44	4.75		
K-Insitu (%)	3.32	3.72	5.08	3.62
K-Lab (%)	4.09	4.41	5.74	4.59
U-Insitu (ppm)	7.87	1.95	2.50	2.59
U-Rocks (ppm)	9.77	1.77		
U-Lab (ppm)	10.00	6.35	5.65	6.52
Th-Insitu (ppm)	86.40	15.90	14.20	20.33
Th-Rocks (ppm)	123.68	11.13		
Th-Lab (ppm)	47.87	31.00	29.26	28.55
SGR (HBq m-3)	18.63		7.05	
ERn (DaBq m-2 h-1)	8.98	7.63	40.09	33.56

Figure 8-15: Mean values of radio-parameters classified according to geological formations of the study area

Finally, the radionuclide content detection (U and Th), as well as the measurement of soil gas radon concentrations, were found to be a useful tool to distinguish between the radiogenic behaviors and radiological characterization of the heavy-mineral placers deposits of the Punta Serpeddì formation. Furthermore, the radon exhalation rates were found to be significantly affected by topsoil properties. This point should be considered while studying the radon release potentials because it can significantly affect the perception of the geogenic radon potential of an area.

9 CONCLUSIONS

This thesis presented a predictive map of Geogenic Radon Potential for the Sardinian region and also a methodology in which geogenic information such as; geological features, radiometric characteristics, soil physical properties and soil gas radon activities were employed to develop accurate and high precision GRP models.

In order to map the GRP of Sardinia two approaches were considered a) Extrapolation of soil gas radon data measured at similar German and Czech geotypes and b) Scoring the radon potential using a cross-tabulation matrix consisting of local geogenic data (uranium content of rocks). The second approach was found to be more reliable than the first one, as even rocks classified in the same category, from the lithological point of view, may have different compositions of the accessory phases, which may have very different U contents and radon release potentials. And also, considering that rocks can hold U enrichments according to the geodynamic, stratigraphic, environmental and geochemical features, climatic conditions and (mainly for the sedimentary rocks) the composition of the source areas which feed the sedimentary basins. Thus, we can deduce that the different geological evolutions linked to the paleogeography of the geological regions do not allow to completely exporting the radon-related measurements carried out in other geological regions without carrying out the measurements for the evaluation of the contents of the Rn producing elements. Therefore preliminary, a geogenic potential map has to take into account the local geological condition and the geodynamic environment from which they were derived. According to this the map produced through the second approach was preferred.

The proposed GRP map of Sardinia was later examined in three ways; 1) comparison with independent indoor radon data 2) investigation of the association between the complementary test results and the estimated radon potential and 3) evaluation of the ability to justify the occurrence of enhanced radon concentrations.

A rather good correlation (R^2=0.53) was found between the GRP categories and the geometric mean indoor radon concentration of Sardinian post offices. Besides, the predicted GRP levels together with corresponding anthropogenic factors were used as

input of the ANOVA model to predict indoor radon activity in workplaces of a University in Sardinia. It was found that integration of GRP categories, ventilation rate, ambient gamma dose rate, floor level and building materials in the model was successful to explain 81 percent of the variations in the observed indoor radon concentrations.

The natural radioactivity levels and the radon production rates of the black shale formation of Villasalto district (introduced as an area with a high radon level based on the proposed GRP map) were investigated. High concentrations of uranium and subsequently high radon exhalation rates were observed in field and laboratory tests.

The presence of bedrocks with medium to high predicted GRP levels (i.e. shales from Genna Muxerra formation), was found to be the main source of elevated indoor radon in a dam in southwestern Sardinia. In other words, water passing through the bedrock transports a considerable amount of sediments containing uranium-bearing minerals. The water penetrates to the gallery of the dam through joints and cracks. Outgassing of radon from the water flowing in the drainage canal and its accumulation due to poor ventilation was found to be the most probable reason for the enhanced indoor radon level.

The visiting research period in Ireland mainly focused on increasing the knowledge on the major controllers of radon and thoron release potentials and production of geogenic radon maps with higher resolution and better accuracy.

To better understand which of the geogenic variables are more significant in the GRP mapping process, a detailed investigation was carried out to study natural radioactivity levels and radon and thoron exhalation rates in a legislatively designated “high radon” area based on existing indoor radon measurements. Indoor radon concentrations, airborne radiometric data, and stream sediment geochemistry were collated and a set of soil samples were taken from the study area. While sampling, the ambient dose rates were also measured at 1m above the ground level using a handheld radio dosimeter. The collected samples were introduced to laboratory testing of radon and thoron exhalation rates. The resultant data were classified based on geological and soil type parameters. Geological boundaries were found to be robust classifiers for radon exhalation rates ($E^{222}Rn$) and radon-related variables whilst, soil type classification could better differentiate thoron exhalation rates ($E^{220}Rn$) and correlated variables. Radiometric data and radon/thoron exhalation rates for soil sample sites were found to be correlated (R^2=0.55 for $E^{222}Rn$ vs. eU and 0.57 for $E^{220}Rn$ vs. eTh). Based on the correlation

achieved, linear models were developed to predict the radon and thoron exhalation rates of the study area. Based on the produced map of radon exhalation rates, a small prone area was selected for further study and additional soil gas radon and soil permeability tests were carried out. Airborne radioelement concentrations (i.e. eU and eTh), air absorbed dose rate, distance from the major fault, soil permeability, and digital train model were assumed as main predictors and soil gas radon was considered as the response value of a geostatistical (i.e. an ordinary least squared regression) model. Through diagnostic tests, the validity of the developed model was evaluated. Empirical Bayesian Kriging, an interpolator tool, was used to produce the high-resolution geogenic radon potential map and also to estimate the uncertainty of predictions.

Furthermore, two complementary research are included in this thesis 1) a study of secondary source of radon in Sardinia and also 2) an investigation of further application (i.e. geological explorations) of radon monitoring and natural radioactivity detection. The overall characterization of the dimension stones mostly used in the Sardinian territory and widely exported worldwide, the radon exhalation rates and the natural radioactivity of eighteen selected samples were estimated. The indoor radon accumulation was simulated for a reference room made of Pietra di Serrenti, which showed the higher value of radon exhalation rate. Despite the hypothesis of poor ventilation, the model proved that radon concentration remains below the reference level of 300 Bq m^{-3} established by the 2013/59/Euratom Directive, revealing the absence of a substantial risk in dwellings and public buildings where the use of the natural stones under investigation is significant.

As an application of radon and gamma-ray mapping for radiogenic assessments, radon and its parent's element, U activities together with Th concentrations were used to distinguish between the heavy minerals bearing placer deposits located in an area in southeastern Sardinia. Elevated levels of U, Th and soil gas radon activity were observed in Is Mallorus (a member of Punta Serpeddì formation) in which the main constituents of the placer assemblages (e.g. zircon and monazite) were accumulated.

9.1 Implications and Limitations

The geogenic map produced in this study would be considered as one of the first sources of information that give the possibility to characterize areas for radon risk in Sardinia especially where indoor radon measurements are not available. This thesis work can be also used to increase public awareness about natural radioactivity and radon risk in

Sardinia and Ireland. It can be employed as help for decision-making and management guidance to be used by the government, radiation protection and public health authorities. The developed GRP map can be efficiently used for targeting follow-up radon measurements in priority areas.

Recently, high-resolution GRP maps are in high demand. A multivariate methodology was introduced in this thesis which gives more precise information about radon potential on a local scale. This methodology can be used for any area where the requisite data are available. Soil gas radon data, radiometric surveys and permeability measurements were employed to develop the accurate GRP maps. The main limitation of this work was that the above-mentioned data are scarce for the Sardinian region. Therefore, an integration of the geogenic information was used to derive a rough estimate of the Sardinian GRP. Another limitation that we encountered was that there is no unified methodology for geogenic radon mapping. Every country has its own approach. Therefore we had to define a general workflow of a multivariate classification approach to construct the geogenic map of Sardinia based on the geogenic data.

The third limitation was for validation of the proposed geogenic map. We were able to test the prediction power only for some hot spot points. But systematic field and laboratory measurements over large areas were necessary to better examine the workability of the map.

9.2 Recommendations for Future Work

To cover the limitations previously mentioned, the authors would like to suggest the following work to be considered in the future:

1) to carry out a more systematic radon investigation related to the larger territory rather than just some points. In this regard, airborne radiometric surveys (even drone-based) and soil gas radon monitoring coupled with permeability testing would give the most representative data on geogenic radon potentials.

2) To use robust methods (e.g. machine learning) to model geogenic radon. In such models, both measured radon data (i.e soil gas and radiometric), as well as other geogenic quantities, would be analyzed to achieve more realistic values of geogenic radon potential.

3) Through the proposed GRP map of Sardinia some radon priority areas have been identified. For radioprotection and mitigation purposes, it is strongly suggested to carry out further indoor radon tests, especially in homes and schools.

REFERENCES

A. Elzain, A.-E. (2016). Measurements of Indoor Radon Levels and Dose Estimation and Lung Cancer Risk Determination for Workers in Health Centres of Some Towns in the Sudan. *American Journal of Modern Physics*, *5*(4), 51. https://doi.org/10.11648/j.ajmp.20160504.12

Abu-Jarad, F. A. (1988). Application of nuclear track detectors for radon related measurements. *International Journal of Radiation Applications and Instrumentation. Part D. Nuclear Tracks and Radiation Measurements*, *15*(1), 525–534. https://doi.org/https://doi.org/10.1016/1359-0189(88)90195-1

Adams, J. A. S., & Weaver, C. E. (1958). Thorium-to-uranium ratios as indicators of sedimentary processes: example of concept of geochemical facies. *AAPG Bulletin*, *42*(2), 387–430.

Addinsoft. (2019). *XLSTAT statistical and data analysis solutions*. https://www.xlstat.com.

Al-Azmi, D., Okeyode, I. C., Alatise, O. O., & Mustapha, A. O. (2018). Setup and procedure for routine measurements of radon exhalation rates of building materials. *Radiation Measurements*, *112*, 6–10. https://doi.org/10.1016/j.radmeas.2018.03.001

Al-Jarallah, M. (2001). Radon exhalation from granites used in Saudi Arabia. *Journal of Environmental Radioactivity*, *53*(1), 91–98.

Al-Nuzal, S. M. D., Al-Obaidy, A.-H. M. J., & Amin, S. A. (2019). Alpha radioactivity level along Tigris River sediments in Baghdad governorate area by using CR-39 SSNTD's. *Applied Water Science*, *9*(7), 149. https://doi.org/10.1007/s13201-019-1027-4

Algeo, T. J., & Heckel, P. H. (2008). The Late Pennsylvanian midcontinent sea of North America: a review. *Palaeogeography, Palaeoclimatology, Palaeoecology*, *268*(3–4), 205–221.

Amaral, P. G. Q., Galembeck, T. M. B., Bonotto, D. M., & Artur, A. C. (2012). Uranium

distribution and radon exhalation from Brazilian dimension stones. *Applied Radiation and Isotopes*, *70*(4), 808–817. https://doi.org/10.1016/j.apradiso.2011.10.010

Anchuela, Ó. P., Frongia, P., Di Gregorio, F., Sainz, A. M. C., & Juan, A. P. (2018). Internal characterization of embankment dams using ground penetrating radar (GPR) and thermographic analysis: A case study of the Medau Zirimilis Dam (Sardinia, Italy). *Engineering Geology*, *237*, 129–139.

Anjos, R. M., Veiga, R., Macario, K., Carvalho, C., Sanches, N., Bastos, J., & Gomes, P. R. S. (2006). Radiometric analysis of Quaternary deposits from the southeastern Brazilian coast. *Marine Geology*, *229*(1), 29–43. https://doi.org/https://doi.org/10.1016/j.margeo.2006.03.001

Appleton, J. D., Doyle, E., Fenton, D., & Organo, C. (2011). Radon potential mapping of the Tralee–Castleisland and Cavan areas (Ireland) based on airborne gamma-ray spectrometry and geology. *Journal of Radiological Protection*, *31*(2), 221. https://doi.org/10.1088/0952-4746/31/2/002

Appleton, J. D., & Miles, J. C. H. (2010). A statistical evaluation of the geogenic controls on indoor radon concentrations and radon risk. *Journal of Environmental Radioactivity*, *101*(10), 799–803. https://doi.org/10.1016/j.jenvrad.2009.06.002

Appleton, J. D., Miles, J. C. H., Green, B. M. R., & Larmour, R. (2008). Pilot study of the application of Tellus airborne radiometric and soil geochemical data for radon mapping. *Journal of Environmental Radioactivity*, *99*(10), 1687–1697. https://doi.org/10.1016/j.jenvrad.2008.03.011

ARPAS. L'Agenzia regionale per la protezione dell'ambiente della Sardegna (2019). *Carta della Permeabilità dei substrati della Sardegna 1:25000*.

Arpas, L'Agenzia regionale per la protezione dell'ambiente della Sardegna., settore Monitoraggio Ambientale Dipartimento Geologico, V. (2016). *"CLASSIFICAZIONE DEL TERRITORIO REGIONALE CON INDIVIDUAZIONE DELLE AREE A RISCHIO RADON"* .

Aru, A., Baldaccini, P., Delogu, G., Dessena, M. A., Madrau, S., Melis, R. T., Vacca, A., & Vacca, S. (1990). Carta dei Suoli della Sardegna, in scala 1/250.000. *Assessorato Alla Programmazione e All'assestamento Del Territorio, Centro Regionale*

Programmazione, Dip. Sc. Della Terra, Universitadi Cagliari, Italy.

Arvela, H., Voutilainen, A., Makelainen, I., Castren, O., & Winqvist, K. (1988). Comparison of predicted and measured variations of indoor radon concentration. *Radiation Protection Dosimetry*, *24*(1–4), 231–235.

Ashrafi, S., & Jahanbakhsh, O. (2019). Measurement of natural radioactivity of Iranian granite samples using beta–gamma coincidence spectrometer and maximum likelihood method. *Environmental Earth Sciences*, *78*(15). https://doi.org/10.1007/s12665-019-8434-6

Baiocchi, A., Dragoni, W., Lotti, F., Piacentini, S. M., & Piscopo, V. (2015). A multi-scale approach in hydraulic characterization of a metamorphic aquifer: what can be inferred about the groundwater abstraction possibilities. *Water*, *7*(9), 4638–4656.

Barberes, G., Reis, R., Fonseca, P., & Pimentel, N. (2015). *Airborne Radiometric Survey data processing and interpretation to find Hydrocarbon anomalies in the Carboniferous units of the South Portuguese Zone*.

BARCA, S., DEL RIO, M., PP, D., & others. (1982). *DISCOVERY OF LOWER ORDOVICIAN ACRITARCHS IN THE" POSTGOTLANDIANO" SEQUENCE OF SOUTHWESTERN SARDINIA (ITALY): AGE AND TECTONIC IMPLICATIONS*.

Barca, S., Melis, E., Annino, E., Cincotti, F., Ulzega, A., Orrù, P., & Pintus, C. (2005). Note Illustrative della Carta Geologica d'Italia alla scala 1: 50.000, foglio 557, Cagliari. *Servizio Geologico d'Italia*.

Barceló, D., Fabian, · P, Fiedler, · H, Frank, · H, Giesy, · J P, Hites, R. A., Khalil, M. A. K., Mackay, · D, Neilson, · A H, Paasivirta, · J, Parlar, · H, Safe, S. H., & Wangersky, · P J. (2006). *The Handbook of Environmental Chemistry Volume 5 Water Pollution Part T* (O. Hutzinger · D. Barceló · A. Kostianoy (ed.); T, Vol. 5).

Barnet, I. (2008). Radon in geological environment: Czech experience. *Czech Geological Survey*.

Baskaran, M. (2016). Radon: A Tracer for Geological, Geophysical and Geochemical Studies. In *Radon: A Tracer for Geological, Geophysical and Geochemical Studies*. Springer International Publishing. https://doi.org/10.1007/978-3-319-21329-3

Baucon, A., Corradini, C., Floris, M., Briguglio, A., Cabella, R., Campomenosi, N.,

Piazza, M., & Corriga, M. G. (2020). Life in near-anoxic conditions: A case study of the ichnology and infaunal ecology of Silurian graptolitic black shales from Sardinia, Italy. *Palaeogeography, Palaeoclimatology, Palaeoecology*, *556*, 109889. https://doi.org/https://doi.org/10.1016/j.palaeo.2020.109889

Beretka, J., & Mathew, P. J. (1985). Natural radioactivity of australian building materials, industrial wastes and by-products. *Health Physics*, *48*(1), 87–95. https://doi.org/10.1097/00004032-198501000-00007

Bezzon, G. P., Buso, G. P., Callegari, I., Colonna, T., Guastaldi, E., Mantovani, F., Mariani, S., Massa, G., Rossi Alvarez, C., Shyti, M., & Xhixha, G. (2010). *Preliminary Results for the Characterization of the Radiological Levels of Rocks in Tuscany Region*.

Bigi, S., Beaubien, S. E., Ciotoli, G., D'Ambrogi, C., Doglioni, C., Ferrante, V., Lombardi, S., Milli, S., Orlando, L., Ruggiero, L., Tartarello, M. C., & Sacco, P. (2014). Mantle-derived CO2 migration along active faults within an extensional basin margin (Fiumicino, Rome, Italy). *Tectonophysics*, *637*, 137–149. https://doi.org/10.1016/j.tecto.2014.10.001

Bochicchio, F., Ampollini, M., Antignani, S., Carpentieri, C., Bochicchio, F., Ampollini, M., Carpentieri, C., Caprio, M., Caccia, B., Di Carlo, C., Pozzi, S., Valentini, S., & Venoso, G. (2019). Protection from radon in Italy: past, present and perspectives Radiation effect enhancement with hyperthermia. Glioblastoma treatment. View project Radon survey in Serbia View project PROTECTION FROM RADON IN ITALY: PAST, PRESENT AND PERSPECTIVES. In *Article in Romanian Journal of Physics* (Vol. 64). https://www.researchgate.net/publication/338117411

Bossew, P. (2015). Estimation of radon prone areas through binary classification, part 2: Radon prone geologies. *Journal of Environmental Radioactivity*, *141*, 44–50. https://doi.org/10.1016/j.jenvrad.2014.11.020

Bossew, P., Tollefsen, T., Gruber, V., & De Cort, M. (2013). *The European radon mapping project*. http://inis.iaea.org/Search/search.aspx?orig_q=RN:45020953

Bossew, Peter, Cinelli, G., Ciotoli, G., Crowley, Q. G., De Cort, M., Elío Medina, J., Gruber, V., Petermann, E., & Tollefsen, T. (2020). Development of a Geogenic Radon Hazard Index—Concept, History, Experiences. *International Journal of*

Environmental Research and Public Health, *17*(11), 4134. https://doi.org/10.3390/ijerph17114134

Brenner, D. J. (1994). *Protection against Radon-222 at Home and at Work. ICRP Publication 65*. Taylor & Francis.

Breusch, T. S., & Pagan, A. R. (1979). A Simple Test for Heteroscedasticity and Random Coefficient Variation. *Econometrica*, *47*(5), 1287–1294. http://www.jstor.org/stable/1911963

Bruno, R. C. (1983). Sources of indoor radon in houses: A review. *Journal of the Air Pollution Control Association*, *33*(2), 105–109. https://doi.org/10.1080/00022470.1983.10465550

Bucci, S., Pratesi, G., Viti, M. L., Pantani, M., Bochicchio, F., & Venoso, G. (2011). Radon in workplaces: first results of an extensive survey and comparison with radon in homes. *Radiation Protection Dosimetry*, *145*(2–3), 202–205. https://doi.org/10.1093/rpd/ncr040

Burke, Ó., Long, S., Murphy, P., Organo, C., Fenton, D., & Colgan, P. A. (2010). Estimation of seasonal correction factors through Fourier decomposition analysis—a new model for indoor radon levels in Irish homes. *Journal of Radiological Protection*, *30*(3), 433. https://doi.org/10.1088/0952-4746/30/3/002

CAAS Environmental Services Ltd. (2003). *Landscape Appraisal of County Kilkenny*.

Cardellini, F. (2017). *New experimental activity at ENEA INMRI radon laboratory The second radon-in-field international intercomparison for passive measurement devices: dwellings and workplaces*.

Careddu, N., & Grillo, S. (2015). Rosa Beta granite (Sardinian Pink Granite): A heritage stone of international significance from Italy. *Geological Society Special Publication*, *407*(1), 155–172. https://doi.org/10.1144/SP407.1

Careddu, N, Scanu, M., & Desogus, P. (2018). Map of natural stones from Sardinia. *Global Stone Congress 2018*.

Careddu, Nicola, & Grillo, S. M. (2019). "Trachytes" from Sardinia: Geoheritage and current use. *Sustainability (Switzerland)*, *11*(13). https://doi.org/10.3390/su11133706

Carmignani, L., Oggiano, G., Funedda, A., Conti, P., & Pasci, S. (2016). The geological map of Sardinia (Italy) at 1:250,000 scale. *Journal of Maps*, *12*(5), 826–835. https://doi.org/10.1080/17445647.2015.1084544

Carmignani, L, Cocozza, T., Gandin, A., & Pertusati, P. C. (1982). Lineamenti della geologia dell'Iglesiente-Sulcis. *Memorie Della Societa Geologica Italiana*, *24*, 65–77.

Carmignani, Luigi, Oggiano, G., Barca, S., Conti, P., Salvadori, I., Eltrudis, A., Funedda, A. L., & Pasci, S. (2001). *Geologia della Sardegna (Note illustrative della Carta Geologica della Sardegna in scala 1: 200.000)*.

Carrera, G., Garavaglia, M., Magnoni, S., Valli, G., & Vecchi, R. (1997). Natural radioactivity and radon exhalation in stony materials. *Journal of Environmental Radioactivity*, *34*(2), 149–159. https://doi.org/10.1016/0265-931X(96)00025-2

Chauhan, R. P., & Kumar, A. (2015). A Comparative study of indoor radon contributed by diffusive and advective transport through intact concrete. *Physics Procedia*, *80*, 109–112.

Chen, J. (2019). RISK ASSESSMENT FOR RADON EXPOSURE IN VARIOUS INDOOR ENVIRONMENTS. *Radiation Protection Dosimetry*, *185*(2), 143–150. https://doi.org/10.1093/rpd/ncy284

Chen, J., & Quayle, D. (2019). *An Activity Concentration-Based Proposal for Radon Management in NORM Workplaces*.

Chen, J., Rahman, N. M., & Atiya, I. A. (2010). Radon exhalation from building materials for decorative use. *Journal of Environmental Radioactivity*, *101*(4), 317–322. https://doi.org/10.1016/j.jenvrad.2010.01.005

Chiozzi, P., De Felice, P., Fazio, A., Pasquale, V., & Verdoya, M. (2000). Laboratory application of NaI(Tl) γ-ray spectrometry to studies of natural radioactivity in geophysics. *Applied Radiation and Isotopes*, *53*(1–2), 127–132. https://doi.org/10.1016/S0969-8043(00)00123-8

Cidu, R., Biddau, R., Dore, E., Vacca, A., & Marini, L. (2014). Antimony in the soil--water--plant system at the Su Suergiu abandoned mine (Sardinia, Italy): Strategies to mitigate contamination. *Science of the Total Environment*, *497*, 319–331.

Cinelli, G, Tositti, L., Capaccioni, B., Brattich, E., & Mostacci, D. (2015). Soil gas radon assessment and development of a radon risk map in Bolsena, Central Italy. *Environmental Geochemistry and Health*, *37*(2), 305–319. https://doi.org/10.1007/s10653-014-9649-9

Cinelli, Giorgia, Tondeur, F., Dehandschutter, B., Bossew, P., Tollefsen, T., & De Cort, M. (2017). Mapping uranium concentration in soil: Belgian experience towards a European map. *Journal of Environmental Radioactivity*, *166*, 220–234. https://doi.org/10.1016/j.jenvrad.2016.04.026

Ciotoli, G., Voltaggio, M., Tuccimei, P., Soligo, M., Pasculli, A., Beaubien, S. E., & Bigi, S. (2017). Geographically weighted regression and geostatistical techniques to construct the geogenic radon potential map of the Lazio region: A methodological proposal for the European Atlas of Natural Radiation. *Journal of Environmental Radioactivity*, *166*, 355–375. https://doi.org/10.1016/J.JENVRAD.2016.05.010

Cocco, F., Oggiano, G., Funedda, A., Loi, A., & Casini, L. (2018). Stratigraphic, magmatic and structural features of Ordovician tectonics in Sardinia (Italy): a review. *Journal of Iberian Geology*, *44*(4), 619–639. https://doi.org/10.1007/s41513-018-0075-1

Cosma, C., Moldovan, M., Dicu, T., & Kovacs, T. (2008). Radon in water from Transylvania (Romania). *Radiation Measurements*, *43*(8), 1423–1428. https://doi.org/10.1016/j.radmeas.2008.05.001

Council, N. R. (1999). *Evaluation of guidelines for exposures to technologically enhanced naturally occurring radioactive materials*. National Academies Press.

CRAERD. (1999). *Risk assessment of radon in drinking water*. National Research Council.

Cuccuru, S., Casini, L., Oggiano, G., & Cherchi, G. P. (2012). Can weathering improve the toughness of a fractured rock? A case study using the San Giacomo granite. *Bulletin of Engineering Geology and the Environment*, *71*(3), 557–567. https://doi.org/10.1007/s10064-012-0416-9

D'Angelo, S., Fiorentino, A., Pesci, G., Mazzella, D., & Editoria, I. (2013). *L Istituto Superiore per la Protezione e la Ricerca Ambientale (ISPRA) e le persone che agiscono per suo conto non sono responsabili per luso che può essere fatto delle*

informazioni contenute in questa pubblicazione.

De Vivo, B., Boni, M., Marcello, A., Di Bonito, M., & Russo, A. (1997). Baseline geochemical mapping of Sardinia (Italy). *Journal of Geochemical Exploration*, *60*(1), 77–90. https://doi.org/10.1016/S0375-6742(97)00027-7

Drolet, J. P., & Martel, R. (2016). Distance to faults as a proxy for radon gas concentration in dwellings. *Journal of Environmental Radioactivity*, *152*, 8–15. https://doi.org/10.1016/j.jenvrad.2015.10.023

Drolet, J. P., Martel, R., Poulin, P., Dessau, J. C., Lavoie, D., Parent, M., & Lévesque, B. (2013). An approach to define potential radon emission level maps using indoor radon concentration measurements and radiogeochemical data positive proportion relationships. *Journal of Environmental Radioactivity*. https://doi.org/10.1016/j.jenvrad.2013.04.006

Durbin, J., & Watson, G. S. (1971). Testing for Serial Correlation in Least Squares Regression. III. *Biometrika*, *58*(1), 1–19. http://www.jstor.org/stable/2334313

Durrani, S. A., Ilic, R., & Fleischer, R. L. (1997). Radon: Overview of Properties, Origin, and Transport. In *Radon Measurements by Etched Track Detectors* (pp. 3–20). WORLD SCIENTIFIC. https://doi.org/10.1142/9789812830197_0001

Duval, J. S., Fukumoto, L. E., Fukumoto, J. M., & Snyder, S. L. (2004). Geology and Indoor Radon in Schools of the Palos Verdes Peninsula Unified School District, Palos Verdes Peninsula, California. *US Geological Survey*.

East, B. W. (2014). *The Environmental Behaviour of Radium, Vols 1 and 2, International Atomic Energy Agency, Technical Reports Series No. 310, IAEA, Vienna. ISBN 92 0 125190 4. 1989.*

Elicki, O., & Wotte, T. (2003). Cambroclaves from the Cambrian of Sardinia (Italy) and Germany: Constraints for the architecture of western Gondwana and the palaeogeographical and palaeoecological potential of cambroclaves. *Palaeogeography, Palaeoclimatology, Palaeoecology*, *195*(1–2), 55–71. https://doi.org/10.1016/S0031-0182(03)00302-X

Elío, J., Crowley, Q., Scanlon, R., Hodgson, J., & Long, S. (2017). Logistic regression model for detecting radon prone areas in Ireland. *Science of The Total Environment*, *599–600*, 1317–1329. https://doi.org/10.1016/J.SCITOTENV.2017.05.071

Elío, J., Crowley, Q., Scanlon, R., Hodgson, J., & Zgaga, L. (2018). Estimation of residential radon exposure and definition of Radon Priority Areas based on expected lung cancer incidence. *Environment International*, *114*, 69–76. https://doi.org/10.1016/J.ENVINT.2018.02.025

Elzain, A. E. A. (2017). Radon Monitoring in the Environment. In *Radon*. InTech. https://doi.org/10.5772/intechopen.69902

Erdi-Krausz, G., Matolin, M., Minty, B., & Nicolet, J. (2003). *Guidelines for radioelement mapping using gamma ray spectrometry data: also as open access e-book*. https://research.utwente.nl/en/publications/guidelines-for-radioelement-mapping-using-gamma-ray-spectrometry-

Erdi-Krausz, G., Matolin, M., Minty, B., Nicolet, J. P., Reford, W. S., & Schetselaar, E. M. (2003). *Guidelines for radioelement mapping using gamma ray spectrometry data: also as open access e-book*. International Atomic Energy Agency (IAEA).

EU. (2013). *59/Euratom of 5 December 2013 laying down basic safety standards for protection against the dangers arising from exposure to ionising radiation, and repealing Directives 89/618/Euratom, 90/641/Euratom, 96/29/Euratom, 97/43/Euratom and 2003/122/Euratom*. Euratom.

European Commission. Environment Directorate-General. (2000). *Radiation protection 112 : radiological protection principles concerning the natural radioactivity of building materials*. Office for Official Publications of the European Communities.

Fello, N., Luening, S., Storch, P., & Redfern, J. (2006). Identification of early Llandovery (Silurian) anoxic palaeo-depressions at the western margin of the Murzuq Basin (southwest Libya), based on gamma-ray spectrometry in surface exposures. *GeoArabia*, *11*, 101–118.

Ferreira, A., Daraktchieva, Z., Beamish, D., Kirkwood, C., Lister, T. R., Cave, M., Wragg, J., & Lee, K. (2018). Indoor radon measurements in south west England explained by topsoil and stream sediment geochemistry, airborne gamma-ray spectroscopy and geology. *Journal of Environmental Radioactivity*, *181*, 152–171. https://doi.org/10.1016/J.JENVRAD.2016.05.007

Fleischer, R. L., & Mogro-Campero, A. (1978). Mapping of integrated radon emanation for detection of long-distance migration of gases within the Earth: Techniques and

principles. *Journal of Geophysical Research: Solid Earth*, *83*(B7), 3539–3549. https://doi.org/10.1029/jb083ib07p03539

Foley, M., & others. (2020). *Investigation of radon prevention and mitigation: from radon measurements to specification for soil depressurisation systems*. NUI Galway.

Föllmi, K. B. (2012). Early Cretaceous life, climate and anoxia. *Cretaceous Research*, *35*, 230–257. https://doi.org/https://doi.org/10.1016/j.cretres.2011.12.005

Font Guiteras, L. (2008). *Radon generation, entry and accumulation indoors*. Universitat Autònoma de Barcelona,.

Franklin, J. A. (1979). Suggest methods for determining water content, porosity, density, absorption and related properties and swelling and slake-durability index properties. *Int. J. Rock Mech. Min. Sci. & Geomech. Abstr.*, *16*, 141–156.

Frías-Rojas, M., Sánchez-de-Rojas-Gómez, M. I., Medina-Martínez, C., & Villar-Cociña, E. (2017). *6 - New trends for nonconventional cement-based materials: Industrial and agricultural waste* (H. Savastano Junior, J. Fiorelli, & S. F. B. T.-S. and N. C. M. using I. B. F. C. dos Santos (eds.); pp. 165–183). Woodhead Publishing. https://doi.org/https://doi.org/10.1016/B978-0-08-102001-2.00007-3

Friedmann, H., Baumgartner, A., Bernreiter, M., Gräser, J., Gruber, V., Kabrt, F., Kaineder, H., Maringer, F. J., Ringer, W., Seidel, C., & Wurm, G. (2017). Indoor radon, geogenic radon surrogates and geology – Investigations on their correlation. *Journal of Environmental Radioactivity*, *166*(Pt 2), 382–389. https://doi.org/10.1016/j.jenvrad.2016.04.028

Friedmann, H., Nuccetelli, C., Michalik, B., Anagnostakis, M., Xhixha, G., Kovler, K., de With, G., Gascó, C., Schroeyers, W., Trevisi, R., Antropov, S., Tsapalov, A., Kunze, C., & Petropoulos, N. P. (2017). Measurement of NORM. In *Naturally Occurring Radioactive Materials in Construction: Integrating Radiation Protection in Reuse (COST Action Tu1301 NORM4BUILDING)* (pp. 61–133). Elsevier Inc. https://doi.org/10.1016/B978-0-08-102009-8.00005-0

Geochemistry, S. (2016). *Mark Baskaran*. https://doi.org/DOI 10.1007/978-3-319-21329-3 ISBN

Ghezzo, C., & Orsini, J. B. (1982). Lineamenti strutturali e composizionali del batolite ercinico sardo-corso in Sardegna. *Memorie Della Societa Geologica Italiana*, *24*,

165–181.

Gilmore, G. R. (2008). Practical Gamma-Ray Spectrometry: Second Edition. In *Practical Gamma-Ray Spectrometry: Second Edition*. https://doi.org/10.1002/9780470861981

Gilmore, G. R., & Wiley, J. (2011). *Practical Gamma-ray Spectrometry 2nd Edition*. https://books.google.com/books?hl=en&lr=&id=S0Dy4hjkmmMC&oi=fnd&pg=PT12&ots=CGJtNmtIb8&sig=raumtguu1O5VVCthSCGElHi3nNY

Giustini, F., Ciotoli, G., Rinaldini, A., Ruggiero, L., & Voltaggio, M. (2019). Mapping the geogenic radon potential and radon risk by using Empirical Bayesian Kriging regression: A case study from a volcanic area of central Italy. *Science of the Total Environment*, *661*, 449–464. https://doi.org/10.1016/j.scitotenv.2019.01.146

Grasty, R. L. (1991). Airborne gamma-ray spectrometer surveying. *Tech. Rep., 97*.

Gruber, V., Bossew, P., Cort, M. De, & Tollefsen, T. (2013). The European map of the geogenic radon potential. *Journal of Radiological Protection*, *33*(1), 51–60. https://doi.org/10.1088/0952-4746/33/1/51

Grygar, R. (2016). *GeologyGeology and Tectonic DevelopmentTectonic development of the Czech Republic* (pp. 7–18). https://doi.org/10.1007/978-3-319-27537-6_2

Guida, D., Guida, M., Cuomo, A., Guadagnuolo, D., & Siervo, V. (2013). Assessment and Mapping of Radon-prone Areas on a regional scale as application of a Hierarchical Adaptive and Multi-scale Approach for the Environmental Planning. Case Study of Campania Region, Southern Italy. *WSEAS TRANSACTIONS on SYSTEMS*, *2*.

Harrell, J. A. (1991). *Radon Hazards Associated with Outcrops of Ohio Shale in Ohio - ’] H Cuyahoga ~ Z ~ Pike Co . 222*.

Hassan, N. M., Ishikawa, T., Hosoda, M., Iwaoka, K., Sorimachi, A., Sahoo, S. K., Janik, M., Kranrod, C., Yonehara, H., Fukushi, M., & Tokonami, S. (2011). The effect of water content on the radon emanation coefficient for some building materials used in Japan. *Radiation Measurements*, *46*(2), 232–237. https://doi.org/10.1016/j.radmeas.2010.11.006

Hazen, R. M., Ewing, R. C., & Sverjensky, D. A. (2009). Evolution of uranium and

thorium minerals. *American Mineralogist*, *94*(10), 1293–1311.

Health Canada. (2008). *Guide for Radon Measurements in Public Buildings (Schools, Hospitals, Care Facilities, Detention Centers)*. Minister of Health Canada.

Heckel, P. H. (2008). Pennsylvanian cyclothems in Midcontinent North America as far-field effects of waxing and waning of Gondwana ice sheets. *Resolving the Late Paleozoic Ice Age in Time and Space; Fielding, CR, Frank, TD, Isbell, JL, Eds*, 275–290.

Hodgson, J, Carey, S., & Scanlon, R. (2014). *Developing a new national radon risk map*.

Hodgson, James, & Young, M. (2016a). 2. The Tellus airborne geophysical surveys and results. *Unearthed: Impacts of the Tellus Surveys of the North of Ireland. Dublin. Royal Irish Academy*. https://doi.org/10.3318/978-1-908996-88-6.ch2

Hughes, M. G., Keene, J. B., & Joseph, R. G. (2000). Hydraulic sorting of heavy-mineral grains by swash on a medium-sand beach. *Journal of Sedimentary Research*, *70*(5), 994–1004.

Hurley, B. W. (2009). *Natural Radioactivity in the Geologic Environment*.

IAEA. (1987). *Preparation and certification of IAEA gamma-ray spectrometry reference materials RGU-1, RGTh-U and RGK-1*. International Atomic Energy Agency Vienna.

Ielsch, G., Cushing, M. E., Combes, P., & Cuney, M. (2010). Mapping of the geogenic radon potential in France to improve radon risk management: Methodology and first application to region Bourgogne. *Journal of Environmental Radioactivity*, *101*(10), 813–820. https://doi.org/10.1016/j.jenvrad.2010.04.006

Ippolito, R., & Remmeti, R. (2019). RADON ENTRY MODELS INTO BUILDINGS VERSUS ENVIRONMENTAL PARAMETERS, BUILDING SHAPE AND TYPES OF FOUNDATION. *WIT Transactions on Ecology and the Environment*, *236*, 309–316.

Ishimori, Y., Lange, K., Martin, P., Mayya, Y. S., & Phaneuf, M. (2013). *Measurement and calculation of radon releases from NORM residues*. Iaea.

ISO 11665-1. (2012). *Measurement of radioactivity in the environment-Air: radon-222-Part 2: Integrated measurement method for determining average potential alpha*

energy concentration of its short-lived decay products (ISO 11665-2:2012).

Jánossy, L. (1965). *Theory and Practice of the Evaluation of Measurements*.

Jiranek, M., & Svoboda, Z. (2007). Numerical modelling as a tool for optimisation of sub-slab depressurisation systems design. *Building and Environment*, *42*(5), 1994–2003.

Jobbágy, V., Altzitzoglou, T., Malo, P., Tanner, V., & Hult, M. (2017). A brief overview on radon measurements in drinking water. *Journal of Environmental Radioactivity*, *173*, 18–24. https://doi.org/10.1016/j.jenvrad.2016.09.019

Jürgen H.Schön. (2015). Nuclear/Radioactive Properties. *Developments in Petroleum Science*, *65*, 119–166. https://doi.org/10.1016/B978-0-08-100404-3.00005-6

Karadeniz, Ö., Karakurt, H., & Akal, C. (2015). Natural radionuclide activities in forest soil horizons of Mount IDA/Kazdagi, Turkey. *Environmental Monitoring and Assessment*, *187*(6), 319. https://doi.org/10.1007/s10661-015-4554-y

Kemmer, G., & Keller, S. (2010). Nonlinear least-squares data fitting in Excel spreadsheets. *Nature Protocols*, *5*(2), 267–281. https://doi.org/10.1038/nprot.2009.182

Kemski, J., Siehl, A., Stegemann, R., & Valdivia-Manchego, M. (2001). Mapping the geogenic radon potential in Germany. *Science of The Total Environment*, *272*(1), 217–230. https://doi.org/https://doi.org/10.1016/S0048-9697(01)00696-9

Kemski, J., Siehl, A., & Valdivia-Manchego, M. (1996). Kartierung des geogenen Radon-Potentials in der Bundesrepublik Deutschland. *Bundesministerium Für Umwelt, Naturschutz Und Reaktorsicherheit, Ed. Forschung Zum Problemkreis „Radon “-Vortragsmanuskripte Des 9. Statusgespräches*.

Kemski, J., Siehl, A., & Valdivia-Manchego, M. (1998). Klassifikation des geogenen Radon-Potentials in der Bundesrepublik Deutschland. *Berichte Der Strahlenschutzkommission (SSK) Des Bundesministeriums Für Umwelt, Naturschutz Und Reaktorsicherheit*, *17*, 13.

Ketris, M. P., & Yudovich, Y. E. (2009). Estimations of Clarkes for Carbonaceous biolithes: World averages for trace element contents in black shales and coals. *International Journal of Coal Geology*, *78*(2), 135–148.

Kleinbaum, D., Kupper, L. L., Muller, K., & Nizam, A. (1998). *Dummy variables in regression, in" Applied regression analysis and other multivariable methods". Pacific Grove. CA: Brooks*. Cole Publishing Co.

Kohn, M. J. (2003). Geochemical Zoning in Metamorphic Minerals. *Treatise on Geochemistry*, 229–261. https://doi.org/10.1016/B0-08-043751-6/03176-5

Kovler, K., Friedmann, H., Michalik, B., Schroeyers, W., Tsapalov, A., Antropov, S., Bituh, T., & Nicolaides, D. (2017). Basic aspects of natural radioactivity. *Naturally Occurring Radioactive Materials in Construction*, 13–36. https://doi.org/10.1016/B978-0-08-102009-8.00003-7

Krieger, R. (1981). Radioactivity of construction materials. *Betonwerk Fertigteil Techn*, *47*(5), 468–473.

Kristensen, A. H. (2013). *RADON GAS MIGRATION THROUGH SOIL AND INTO INDOOR ENVIRONMENTS Background*. https://vbn.aau.dk/en/projects/radon-gas-transport-i-jord-og-ind-i-bygninger

Krivoruchko, K. (2012). *Empirical Bayesian Kriging Implemented in ArcGIS Geostatistical Analyst*.

Kropat, G., Bochud, F., Jaboyedoff, M., Laedermann, J. P., Murith, C., Palacios, M., & Baechler, S. (2015). Improved predictive mapping of indoor radon concentrations using ensemble regression trees based on automatic clustering of geological units. *Journal of Environmental Radioactivity*, *147*, 51–62. https://doi.org/10.1016/j.jenvrad.2015.05.006

Kropat, G., Bochud, F., Murith, C., Palacios (Gruson), M., & Baechler, S. (2017). Modeling of geogenic radon in Switzerland based on ordered logistic regression. *Journal of Environmental Radioactivity*, *166*, 376–381. https://doi.org/10.1016/j.jenvrad.2016.06.007

Leonardi, F., Bonczyk, M., Nuccetelli, C., Wysocka, M., Michalik, B., Ampollini, M., Tonnarini, S., Rubin, J., Niedbalska, K., & Trevisi, R. (2018). A study on natural radioactivity and radon exhalation rate in building materials containing norm residues: preliminary results. *Construction and Building Materials*, *173*, 172–179. https://doi.org/10.1016/j.conbuildmat.2018.03.254

Licour, C., Tondeur, F., Gerardy, I., Alaoui, N. M., Dubois, N., Perreaux, R., Gerardy,

N., & Christiaens, D. (2017). 226Ra, 222Rn AND PERMEABILITY OF BELGIAN SOILS IN RELATION WITH INDOOR RADON RISK. *Radiation Protection Dosimetry*, *177*(1–2), 168–172. https://doi.org/10.1093/RPD/NCX163

Lucchetti, C., Briganti, A., Castelluccio, M., Galli, G., Santilli, S., Soligo, M., & Tuccimei, P. (2019). Integrating radon and thoron flux data with gamma radiation mapping in radon-prone areas. The case of volcanic outcrops in a highly-urbanized city (Roma, Italy). *Journal of Environmental Radioactivity*, *202*(September 2018), 41–50. https://doi.org/10.1016/j.jenvrad.2019.02.004

MacDonald Pettit, M. (1996). *Bedrock Geology 1:100,000 Map Series, Geology of Monaghan and Carlingford Sheet 8 and part of Sheet 9*.

Mahur, A. K., Sharma, A., Sonkawade, R. G., Sengupta, D., Sharma, A. C., & Prasad, R. (2015). Measurement of Radon Exhalation Rate in Sand Samples from Gopalpur and Rushikulya Beach Orissa, Eastern India. *Physics Procedia*, *80*, 140–143. https://doi.org/https://doi.org/10.1016/j.phpro.2015.11.088

Manohar, S. N., Meijer, H. A. J., & Herber, M. A. (2013). Radon flux maps for the Netherlands and Europe using terrestrial gamma radiation derived from soil radionuclides. *Atmospheric Environment*, *81*, 399–412. https://doi.org/10.1016/j.atmosenv.2013.09.005

McAulay, I. R., & McLaughlin, J. P. (1985). Indoor natural radiation levels in Ireland. *Science of The Total Environment*, *45*, 319–325. https://doi.org/10.1016/0048-9697(85)90233-5

McGarry, A. T., Fennell, S. G., Mackin, G. M., Madden, J. S., Duffy, J. T., & Colgan, P. A. (1997). *Radon in dwellings the national radon survey Carlow, Donegal, Kildare, Kilkenny, Laois, Leitrim, Longford, Meath, Offaly, Roscommon, Sligo, Waterford, Westmeath and Wexford*.

Melintescu, A., Chambers, S. D., Crawford, J., Williams, A. G., Zorila, B., & Galeriu, D. (2018). Radon-222 related influence on ambient gamma dose. *Journal of Environmental Radioactivity*, *189*, 67–78. https://doi.org/10.1016/J.JENVRAD.2018.03.012

Mercier, J.-F., Tracy, B. L., d'Amours, R., Chagnon, F., Hoffman, I., Korpach, E. P., Johnson, S., & Ungar, R. K. (2009). Increased environmental gamma-ray dose rate

during precipitation: a strong correlation with contributing air mass. *Journal of Environmental Radioactivity*, *100*(7), 527–533. https://doi.org/https://doi.org/10.1016/j.jenvrad.2009.03.002

Missimer, T. M., Teaf, C., Maliva, R. G., Danley-Thomson, A., Covert, D., & Hegy, M. (2019). Natural Radiation in the Rocks, Soils, and Groundwater of Southern Florida with a Discussion on Potential Health Impacts. In *International journal of environmental research and public health* (Vol. 16, Issue 10). NLM (Medline). https://doi.org/10.3390/ijerph16101793

Mitáš, L., & Mitášová, H. (1988). General variational approach to the interpolation problem. *Computers & Mathematics with Applications*, *16*(12), 983–992.

Muñoz, E., Frutos, B., Olaya, M., & Sánchez, J. (2017). A finite element model development for simulation of the impact of slab thickness, joints, and membranes on indoor radon concentration. *Journal of Environmental Radioactivity*, *177*, 280–289.

Muravsky, V. A., Tolstov, S. A., & Kholmetskii, A. L. (1998). Comparison of the least squares and the maximum likelihood estimators for gamma-spectrometry. *Nuclear Instruments and Methods in Physics Research, Section B: Beam Interactions with Materials and Atoms*, *145*(4), 573–577. https://doi.org/10.1016/S0168-583X(98)80555-7

National Research Council. (1999). *Risk assessment of radon in drinking water*. National Academies Press.

Nazaroff, W. W. (1992). Radon transport from soil to air. *Reviews of Geophysics*, *30*(2), 137. https://doi.org/10.1029/92RG00055

Nero, A. V, Gadgil, A. J., Nazaroff, W. W., & Revzan, K. L. (1990). *Indoor radon and decay products: concentrations, causes, and control strategies*.

Neznal, M., Neznal, M., Matolin, M., Barnet, I., & Miksova, J. (2004). *The new method for assessing the radon risk of building sites*. Czech Geological Survey.

Noverques, A., Juste, B., Sancho, M., García-Fayos, B., & Verdú, G. (2020). Study of the influence of radon in water on radon levels in air in a closed location. *Radiation Physics and Chemistry*, *171*, 108761. https://doi.org/10.1016/j.radphyschem.2020.108761

Nuccetelli, C., de With, G., Trevisi, R., Vanhoudt, N., Pepin, S., Friedmann, H., Xhixha, G., Schroeyers, W., Aguiar, J., Hondros, J., Michalik, B., Kovler, K., Janssens, A., & Wiegers, R. (2017). Legislative aspects. In *Naturally Occurring Radioactive Materials in Construction: Integrating Radiation Protection in Reuse (COST Action Tu1301 NORM4BUILDING)* (pp. 37–60). Elsevier Inc. https://doi.org/10.1016/B978-0-08-102009-8.00004-9

Nuccetelli, Cristina, Risica, S., Onisei, S., Leonardi, F., & Trevisi, R. (2017). *Natural radioactivity in building materials in the European Union: a database of activity concentrations, radon emanations and radon exhalation rates*.

O'Connor, C., Currivan, L., Cunningham, N., & Kelleher, K. (2014). *Radiation Doses Received by the Irish Population*. https://inis.iaea.org/search/search.aspx?orig_q=RN:46045338

Örgün, Y., Altinsoy, N., Gültekin, A. H., Karahan, G., & Çelebi, N. (2005). Natural radioactivity levels in granitic plutons and groundwaters in Southeast part of Eskisehir, Turkey. *Applied Radiation and Isotopes*, *63*(2), 267–275. https://doi.org/10.1016/j.apradiso.2005.03.008

Paquette, J. L., Ménot, R. P., Pin, C., & Orsini, J. B. (2003). Episodic and short-lived granitic pulses in a post-collisional setting: Evidence from precise U-Pb zircon dating through a crustal cross-section in Corsica. *Chemical Geology*, *198*(1–2), 1–20. https://doi.org/10.1016/S0009-2541(02)00401-1

Park, J. H., Lee, C. M., Lee, H. Y., & Kang, D. R. (2018). Estimation of seasonal correction factors for indoor radon concentrations in Korea. *International Journal of Environmental Research and Public Health*, *15*(10). https://doi.org/10.3390/ijerph15102251

Park, J. H., Whang, S., Lee, H. Y., Lee, C.-M., & Kang, D. R. (2018). Measurement and modeling of indoor radon concentrations in residential buildings. *Environmental Health and Toxicology*, *33*(1), e2018003. https://doi.org/10.5620/eht.e2018003

Pavanetto, P., Funedda, A., Loi, A., & Matteini, M. (2012). The Ordovician Magmatism puzzle: a preliminary comparison of samples from Calabria and Sardinia volcanites. *Rendiconti Online Della Società Geologica Italiana*, *22*, 174–176.

Pearson, K. (1895). VII. Note on regression and inheritance in the case of two parents.

Proceedings of the Royal Society of London, *58*(347–352), 240–242.

Pereira, A. J. S. C., & Neves, L. J. P. F. (2012). Estimation of the radiological background and dose assessment in areas with naturally occurring uranium geochemical anomalies—a case study in the Iberian Massif (Central Portugal). *Journal of Environmental Radioactivity*, *112*, 96–107. https://doi.org/https://doi.org/10.1016/j.jenvrad.2012.05.022

Pereira, A., Lamas, R., Miranda, M., Domingos, F., Neves, L., Ferreira, N., & Costa, L. (2017). Estimation of the radon production rate in granite rocks and evaluation of the implications for geogenic radon potential maps: A case study in Central Portugal. *Journal of Environmental Radioactivity*, *166*, 270–277.

Pereira, A., Pereira, D., Neves, L., Peinado, M., & Armenteros, I. (2013). Radiological data on building stones from a Spanish region: Castilla y León. *Natural Hazards and Earth System Sciences*, *13*(12), 3493–3501. https://doi.org/10.5194/nhess-13-3493-2013

Pereira, D., Neves, L., Pereira, A., Peinado, M., Blanco, J. A., & Tejado, J. J. (2012). A radiological study of some ornamental stones: The bluish granites from Extremadura (Spain). *Natural Hazards and Earth System Science*, *12*(2), 395–401. https://doi.org/10.5194/nhess-12-395-2012

Perry, S. A., & Team, P. R. I. M. S. (2011). Understanding naturally occurring radioactive material in the Marcellus Shale. *Marcellus Shale*, 1–8.

Pistis, M., Loi, A., & Dabard, M. P. (2016). Influence of relative sea-level variations on the genesis of palaeoplacers, the examples of Sarrabus (Sardinia, Italy) and the Armorican Massif (western France). *Comptes Rendus - Geoscience*, *348*(2), 150–157. https://doi.org/10.1016/j.crte.2015.09.006

Pistis, M., Loi, A., & Dabard, M. P. (2018). Gamma-ray facies in marine paleoplacer deposits of the Punta Serpeddì Formation (Ordovician of SE Sardinia, Italy). *Journal of Mediterranean Earth Sciences*, *10*, 155–158. https://doi.org/10.3304/JMES.2018.007

Primavori, P. (2011). I materiali lapidei della Sardegna. *Sardegna Ricerche; Regione Autonoma Della Sardegna, Ed.; Sainas Industrie Grafiche: Villaspeciosa, Italy*, 261–307.

Puccini, A., Xhixha, G., Cuccuru, S., Oggiano, G., Xhixha, M. K., Mantovani, F., Alvarez, C. R., & Casini, L. (2014). Radiological characterization of granitoid outcrops and dimension stones of the Variscan Corsica-Sardinia Batholith. *Environmental Earth Sciences*, *71*(1), 393–405. https://doi.org/10.1007/s12665-013-2442-8

Ribeiro, F. C. A., Silva, J. I. R., Lima, E. S. A., do Amaral Sobrinho, N. M. B., Perez, D. V., & Lauria, D. C. (2018). Natural radioactivity in soils of the state of Rio de Janeiro (Brazil): Radiological characterization and relationships to geological formation, soil types and soil properties. *Journal of Environmental Radioactivity*, *182*, 34–43. https://doi.org/10.1016/J.JENVRAD.2017.11.017

Ries, H. (1922). *The Clay Deposits of Kentucky: An Economic Consideration of the Pottery, Brick, and Tile Clays, Fire Clays, and Shales of Kentucky, with Notes on Their Industrial Development* (Vol. 8). Kentucky Geological survey.

Ruzer, L. S., & Harley, N. H. (2012). *Aerosols handbook: measurement, dosimetry, and health effects*. CRC press.

Sabatino, G., Di Bella, M., Caridi, F., Italiano, F., Romano, D., Magazù, S., Gnisci, A., Faggio, G., Messina, G., Santangelo, S., Leonetti, F., & Tripodo, A. (2019). Radiological assessment, mineralogy and geochemistry of the heavy-mineral placers from the Calabrian coast (South Italy). *Journal of Instrumentation*, *14*(5). https://doi.org/10.1088/1748-0221/14/05/P05015

Sahoo, B. K., & Mayya, Y. S. (2010). Two dimensional diffusion theory of trace gas emission into soil chambers for flux measurements. *Agricultural and Forest Meteorology*, *150*(9), 1211–1224. https://doi.org/10.1016/j.agrformet.2010.05.009

Sainz Fernández, C., Quindós Poncela, L. S., Fernández Villar, A., Fuente Merino, I., Gutierrez-Villanueva, J. L., Celaya González, S., Quindós López, L., Quindós López, J., Fernández, E., Remondo Tejerina, J., Martín Matarranz, J. L., & García Talavera, M. (2017). Spanish experience on the design of radon surveys based on the use of geogenic information. *Journal of Environmental Radioactivity*, *166*, 390–397. https://doi.org/10.1016/j.jenvrad.2016.07.007

Sakoda, A., Ishimori, Y., Hanamoto, K., Kataoka, T., Kawabe, A., & Yamaoka, K. (2010). Experimental and modeling studies of grain size and moisture content effects

on radon emanation. *Radiation Measurements*, *45*(2), 204–210.

San Alduan, M. T., Ramos, S., & others. (2008). CSN Criteria for radiological protection against exposure to natural radiation. *Alfa. Revista de Seguridad Nuclear y Proteccion Radiologica*, *3*(III), 45–53.

Sarrou, I., & Pashalidis, I. (2017). Radon exhalation from granite countertops and expected indoor radon levels. *Journal of Radioanalytical and Nuclear Chemistry*, *311*(1), 913–916. https://doi.org/10.1007/s10967-016-5108-7

Scheib, C., Appleton, J. D., Miles, J. C. H., Green, B. M. R., Barlow, T. S., & Jones, D. G. (2009a). Geological controls on radon potential in Scotland. *Scottish Journal of Geology*, *45*(2), 147–160. https://doi.org/10.1144/0036-9276/01-401

Scheib, C., Appleton, J. D., Miles, J. C. H., Green, B. M. R., Barlow, T. S., & Jones, D. G. (2009b). Geological controls on radon potential in Scotland. *Scottish Journal of Geology*, *45*(2), 147–160. https://doi.org/10.1144/0036-9276/01-401

Schmoker, J. W. (1981). Determination of organic-matter content of Appalachian Devonian shales from gamma-ray logs. *AAPG Bulletin*, *65*(7), 1285–1298.

Schön, J. (2015). *Physical properties of rocks: Fundamentals and principles of petrophysics*. https://books.google.com/books?hl=en&lr=&id=uckHBgAAQBAJ&oi=fnd&pg=PP1&dq=Physical+properties+of+rocks:+Fundamentals+and+principles+of+petrophysics&ots=Ra0uXyp8Cd&sig=AyqABizgtkMghsDlw4zlNI5G_yE

Schon, J., Geophysics, R. W.-P. and A., & 1997, U. (2015). Physical properties of rocks: Fundamentals and principles of petrophysics. *Basel, Birkhauser Verlag*.

SHAPIRO, S. S., & WILK, M. B. (1965). An analysis of variance test for normality (complete samples)†. *Biometrika*, *52*(3–4), 591–611. https://doi.org/10.1093/biomet/52.3-4.591

Smethurst, M. A., Watson, R. J., Baranwal, V. C., Rudjord, A. L., & Finne, I. (2017). The predictive power of airborne gamma ray survey data on the locations of domestic radon hazards in Norway: A strong case for utilizing airborne data in large-scale radon potential mapping. *Journal of Environmental Radioactivity*, *166*, 321–340. https://doi.org/10.1016/J.JENVRAD.2016.04.006

Soesoo, A., & Hade, S. (2014). BLACK SHALE OF ESTONIA: MOVING TOWARDS A FENNOSCANDIAN-BALTOSCANDIAN DATABASE. *Transactions of Karelian Research Centre of Russian Academy of Sciences: Precambrian Geology*, 103–114.

Soonawala, N. M., & Telford, W. M. (1980). Movement of radon in overburden. *Geophysics*, *45*(8), 1297–1315.

Stoulos, S., Manolopoulou, M., & Papastefanou, C. (2003). *Assessment of natural radiation exposure and radon exhalation from building materials in Greece*. *69*, 225–240. https://doi.org/10.1016/S0265-931X(03)00081-X

Swanson, V. E. (1961). *Geology and geochemistry of uranium in marine black shales: a review*. US Government Printing Office Washington, DC.

Szabó, K. Z., Jordan, G., Horváth, Á., & Szabó, C. (2014). Mapping the geogenic radon potential: Methodology and spatial analysis for central Hungary. *Journal of Environmental Radioactivity*, *129*, 107–120. https://doi.org/10.1016/j.jenvrad.2013.12.009

Szűcs, L., Szilágyi, Z. N., Nagy, Á., Nagy, P., Botos, R., Árva, F., Szabó, N., Rózsa, K., & Párkányi, D. (2018). *Geogenic Radon Potential Short overview Report of EURAMET 16ENV10 MetroRadon*.

Tan, Y., & Xiao, D. (2011). Revision for measuring the radon exhalation rate from the medium surface. *IEEE Transactions on Nuclear Science*, *58*(1 PART 2), 209–213. https://doi.org/10.1109/TNS.2010.2090897

Tedd, K., Misstear, B., Coxon, C., Daly, D., Williams, T. H., Craig, M., & Mannix, A. (2011). *A Review of Groundwater Levels in the South-East of Ireland Review of Groundwater Level Data in the South Eastern River Basin District Environmental Research Centre Report*.

The 2007 Recommendations of the International Commission on Radiological Protection. ICRP publication 103. (2007). *Annals of the ICRP*, *37*(2–4), 1–332. https://doi.org/10.1016/j.icrp.2007.10.003

Thu, H. N. P., Van Thang, N., Loan, T. T. H., Van Dong, N., & others. (2019). Natural radioactivity and radon emanation coefficient in the soil of Ninh Son region, Vietnam. *Applied Geochemistry*, *104*, 176–183.

Tondeur, F., Cinelli, G., & Dehandschutter, B. (2014). Homogenity of geological units with respect to the radon risk in the Walloon region of Belgium. *Journal of Environmental Radioactivity*, *136*, 140–151. https://doi.org/10.1016/J.JENVRAD.2014.05.015

Tóth, G., Jones, A., & Montanarella, L. (2013). *LUCASS Top soil Survey methodology ,data and results*. https://doi.org/10.2788/97922

Tzortzis, M., & Tsertos, H. (2004). Determination of thorium, uranium and potassium elemental concentrations in surface soils in Cyprus. *Journal of Environmental Radioactivity*, *77*(3), 325–338. https://doi.org/10.1016/J.JENVRAD.2004.03.014

UNSCEAR. (2008). UNSCEAR 2008 Report: Sources and effects of ionizing radiation. In *The United Nations Scientific Committee on the Effects of Atomic Radiation*.

UNSCEAR (United Nations Scientific Committee on the Effects of Atomic Radiation). (2000). *Sources and effects of ionizing radation annex B, Exposures from natural radiation sources*.

Valković, V. (2000). *Radioactivity in the environment*. Elsevier Science B.V.

Vasidov, A. (2014). Field measurement of radon exhalation rate from the soil by CR-39 detector. *Journal of Radioanalytical and Nuclear Chemistry*, *302*(2), 919–923. https://doi.org/10.1007/s10967-014-3644-6

Voltaggio, M. (2011). Radon progeny in hydrometeors at the earth's surface. *Radiation Protection Dosimetry*, *150*(3), 334–341. https://doi.org/10.1093/rpd/ncr402

Vukanac, I., Đura, M., Lon, B., & Kolar, P. (2016). *Novel method of measurement of radon exhalation from building materials*. *164*, 337–343. https://doi.org/10.1016/j.jenvrad.2016.08.009

Wattananikorn, K., Emharuthai, S., & Wanaphongse, P. (2008). A feasibility study of geogenic indoor radon mapping from airborne radiometric survey in northern Thailand. *Radiation Measurements*, *43*(1), 85–90. https://doi.org/https://doi.org/10.1016/j.radmeas.2007.04.011

Wedepohl, K. H., Correns, C. W., Shaw, D. M., Turekian, K. K., & Zemann, J. (1969). *Handbook of geochemistry*.

White, H. (1980). *A Heteroskedasticity-Consistent Covariance Matrix Estimator And A*

Direct Test For Heteroskedasticity. https://citeseerx.ist.psu.edu/viewdoc/summary?doi=10.1.1.11.7646

WHO (World Health Organization). (2009). *WHO handbook on indoor radon: a public health perspective.* World Health Organization.

Winkler, R., Ruckerbauer, F., & Bunzl, K. (2001). Radon concentration in soil gas: A comparison of the variability resulting from different methods, spatial heterogeneity and seasonal fluctuations. *Science of the Total Environment*, *272*(1–3), 273–282. https://doi.org/10.1016/S0048-9697(01)00704-5

Xhixha, M., Baldoncini, M., Bezzon, G. P., Buso, G. P., Carmignani, L., Casini, L., Callegari, I., Colonna, T., Cuccuru, S., Guastaldi, E., Fiorentini, G., Mantovani, F., Massa, G., Mou, L., Oggiano, G., Puccini, A., Rossi Alvarez, C., Strati, V., Xhixha, G., & Zanon, A. (2014). *A Detailed Gamma-ray Survey for Estimating the Radiogenic Power of Sardinian Variscan Crust*. http://inis.iaea.org/Search/search.aspx?orig_q=RN:45114777

Xhixha, M. K., Albèri, M., Baldoncini, M., Bezzon, G. P., Buso, G. P., Callegari, I., Casini, L., Cuccuru, S., Fiorentini, G., Guastaldi, E., Mantovani, F., Mou, L., Oggiano, G., Puccini, A., Alvarez, C. R., Strati, V., Xhixha, G., & Zanon, A. (2016). Uranium distribution in the Variscan Basement of Northeastern Sardinia. *Journal of Maps*, *12*(5), 1029–1036. https://doi.org/10.1080/17445647.2015.1115784

Yalcin, S., Gurler, O., Akar, U. T., Incirci, F., Kaynak, G., & Gundogdu, O. (2011). Measurements of radon concentration in drinking water samples from Kastamonu (Turkey). *Isotopes in Environmental and Health Studies*, *47*(4), 438–445.

Young, M., Knights, K., Smyth, D., Glennon, M., Scanlon, R., & Gallagher, V. (2016). 3. The Tellus geochemical surveys, results and applications. In *Royal Irish Academy*. https://doi.org/10.3318/978-1-908996-88-6.ch3

Zanin, Y. N., Zamirailova, A. G., & Eder, V. G. (2016). Uranium, thorium, and potassium in black shales of the Bazhenov Formation of the West Siberian marine basin. *Lithology and Mineral Resources*, *51*(1), 74–85.

Zeng, C., Lai, W., Feng, X., Fan, C., Wu, J., & Gu, R. (2019). Overview of Radon Background Correction Technology for Airborne Gamma Spectrometry. *IOP Conference Series: Earth and Environmental Science*, *281*(1).

https://doi.org/10.1088/1755-1315/281/1/012002

Zhang, L., Lei, X., Guo, Q., Wang, S., Ma, X., & Shi, Z. (2012). Accurate measurement of the radon exhalation rate of building materials using the closed chamber method. *Journal of Radiological Protection*, *32*(3), 315.

END OF THESIS

White Pages

Modelling of Geogenic Radon in Sardinia and Health risk Assessment

PhD thesis of Mirsina Mousavi Aghdam